Bias Correction of Global Circulation Model Outputs Using Artificial Neural Networks

A Dissertation
Presented to
The Academic Faculty

by

Sanaz Moghim

In Partial Fulfillment
of the Requirements for the Degree
Doctor of Philosophy in the
School of Civil and Environmental Engineering

Georgia Institute of Technology
August 2015

Bias Correction of Global Circulation Model Outputs Using Artificial Neural Networks

Approved by:

Dr. Rafael L. Bras, Advisor
School of Civil and Environmental Engineering
Georgia Institute of Technology

Dr. Aris P. Georgakakos
School of Civil and Environmental Engineering
Georgia Institute of Technology

Dr. Jingfeng Wang
School of Civil and Environmental Engineering
Georgia Institute of Technology

Dr. Kuo-lin Hsu
School of Civil and Environmental Engineering
University of California, Irvine

Dr. Yi Deng
Earth and Atmospheric Sciences
Georgia Institute of Technology

Date Approved: April 1, 2015

This thesis is dedicated to my wonderful parents (Mohammad and Manijeh) and my lovely sister (Mona), as well as my family and friends. Their love and support have given me extraordinary strength to accomplish my goal.

ACKNOWLEDGEMENTS

I would like to thank Dr. Rafael L. Bras who taught me how to be an independent researcher and also strong enough to overcome difficulties and problems.

I would like to acknowledge my committee, Dr. Aris P. Georgakakos, Dr. Jingfeng Wang, and Dr. Kuo-lin Hsu from the school of Civil and Environmental Engineering, and Dr. Yi Deng from the Earth and Atmospheric Sciences. In particular, I would like to thank Dr. Aris P. Georgakakos for his great guidance, support, and encouragements during this work. He has given me a considerable amount of his time and care to guide me to complete this thesis.

I am grateful to my professors in the Georgia institute of Technology and the University of the California, Irvine, particularly to Dr. Soroosh Sorooshian for all his willingness to help. I want to extend my thanks to my colleagues in Dr. Bras' group particularly Shawna L. McKnight and Ryan G. Knox for their help during my Ph.D.

I am thankful to all of my friends. I would like to thank several individuals for their friendship and help along my way: Mina Taheri, Elena Elnaz Morcelin, and her amazing family.

I express my sincere thanks to my family, especially my awesome parents Mohammad and Manijeh and my lovely sister Mona for their love, kindness, and support. They have given me more than I can repay. They have been my main motivation in every step of my life, and I truly could not overcome difficult life challenges without them.

TABLE OF CONTENTS

Page

LIST OF TABLES

LIST OF FIGURES

SUMMARY

Climate studies and effective environmental management plans require accurate and unbiased climate datasets. Global model outputs are subject to model errors, which need to be corrected. This study develops a new bias correction approach using Artificial Neural Networks (ANN). A three layer feedforward neural network is employed to reduce the biases of climate variables (temperature and precipitation) over northern South America, extending from 80°W to 35°W (longitude) and from 23°S to 12°N (latitude). Air and skin temperature, specific humidity, net longwave and shortwave radiation are used as inputs for the bias correction of temperature. Precipitation at lag zero, one, two, and three, and the standard deviation from 3 by 3 neighbors around the pixel of interest are the inputs into the ANN bias correction of precipitation. The data are provided by the Community Climate System Model (CCSM3).

The proposed model relies on a supervised learning approach (back propagation generalized delta rule, BPGDR) to construct a functional relationship between the input-output. This relationship learns the error structure by training the inputs with observations (targets) to understand prediction biases. The predictive capacity of the ANN (generalization ability) confirms that the network can perform well with new and unseen datasets without any need for re-training. Results show that the trained ANN can markedly reduce the estimation error and improve the correlation and probabilistic structure of the bias-corrected variables. The ANN outperforms linear regression (LR), which is used for comparison purposes.

The ability of the regression models to regionalize the study domain is investigated by defining the minimum number of training pixels necessary to achieve a good level of bias correction performance over the entire domain. Results confirm that it is possible to identify regions in terms of physical features such as land cover, topography, and climatology over which the trained models at a few pixels can do well. The number of training pixels (model calibrations) depends on the accuracy criterion and physical features of the domain.

CHAPTER 1

INTRODUCTION

1.1. Motivation

Numerical models are essential tools that allow us to fill space-time observational gaps and to simulate present and future dynamics of the Earth's climate. General Circulation Models (GCMs) are key numerical tools to simulate land-ocean-atmosphere interactions and to study short- and long-term climate changes. However, the outputs of these models are often subject to random and structural errors (biases), mainly due to inadequate knowledge and simplified parameterization of the underlying physics. Thus, prior to using outputs of climate models into land-surface hydrologic models, bias removal is an essential step. In this study, we seek to develop a methodology that could improve estimates of the surface temperature and precipitation. The methodology is illustrated by operating on outputs from one of the GCMs called the Community Climate System Model (CCSM3) over northern South America.

1.2. Brief Introduction to the Study Domain

This study looks at northern South America extending from 80°W to 35°W (longitude) and from 23°S to 12°N (latitude), see Figure 1.1. The region is covered by different land uses such as forest, pasture, agriculture, bare land, and mountain. Different topographic and vegetation patterns of the region and adjacent oceans are the main drivers to control the weather system over the area. One of the landforms of the domain is the Andes Mountains along the west coast of the region, the longest mountains with a maximum peak of about 6,962 m (22,841 ft.) above sea level. The mountains act as a barrier to atmospheric flow, which causes different climate and weather patterns over the

east and the west side of the mountains. On the west side of the mountains, the westerly Southern Pacific Gyre controls the climate of the area and on the east side, the subtropical Atlantic and the Southern Polar Gyre influence the climate. Another landform is the Amazon Basin with the largest tropical rainforest in the world, covering about 40 percent of South America. The Amazon River and its tributaries, considered the largest reservoir of freshwater and the second longest river in the world, rise in the Andes Mountains and drain into the Atlantic Ocean. The humidity and temperature are generally high over the basin. Diabatic heating process over the Amazon Basin and central Brazil and deviation of the easterly trade winds to the zone of the convergence by the Andean topography control the climate over the basin (Figueroa et al., 1995). They argued that the South American Convergence Zone (SACZ) consisting of the westerly air mass of the Amazon and the easterly subtropical south Atlantic air mass, is closely tied to the ecosystem of the Amazon Basin.

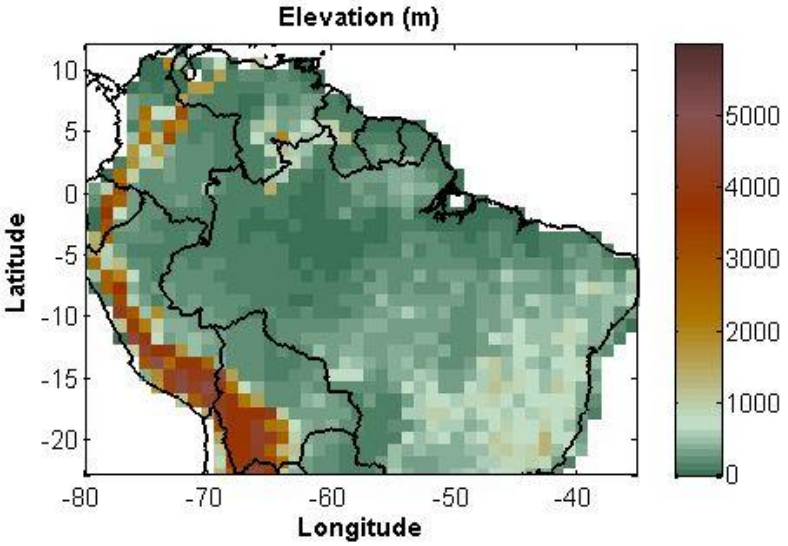

Figure 1.1. Study domain extending from 80°W to 35°W (longitude) and from 23°S to 12°N (latitude).

Different climate, land cover, and orography conditions over South America result in high diversity of animals and plants species, and thriving the Earth-life systems. Figure 1.2 shows the South America land use classification by the Olson Global Ecosystem Framework (Olson, 1994).

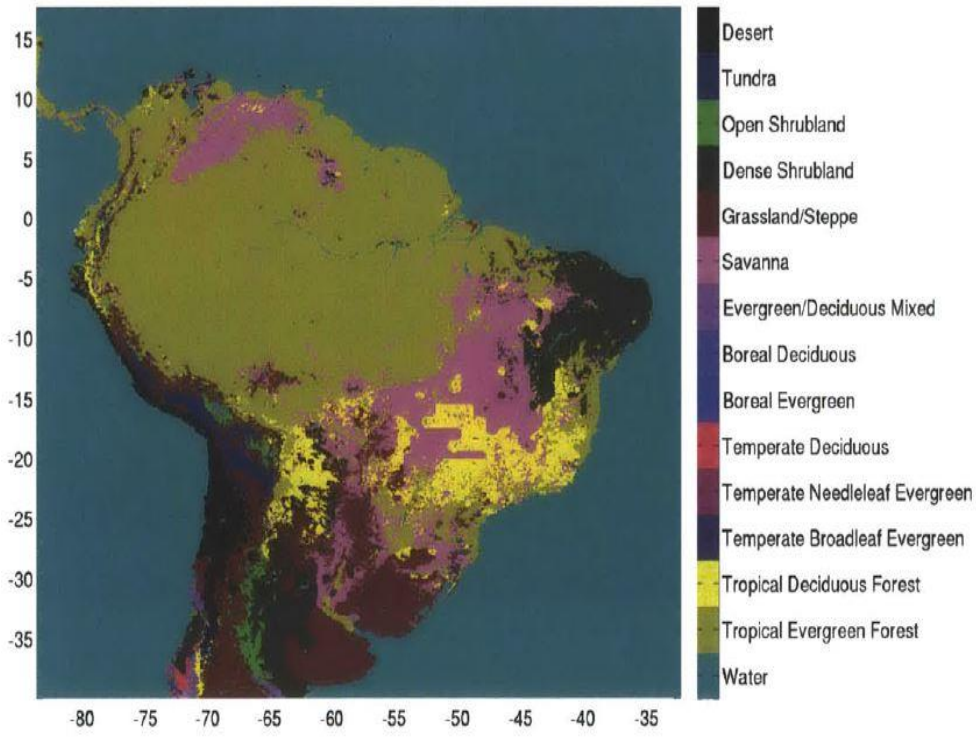

Figure 1.2. Land classification of South America from the DisCover database, EROS center (Olson, 1994).

Changes on the land use and vegetation types can alter climatological parameters including light absorption capability, reflectivity (albedo), net surface radiation, and leaf area index (LAI). These changes influence the drag force on winds, planetary boundary layer, vertical transport of heat, momentum and water vapor flux, evaporation, precipitation, and total runoff rate. This relationship between the climate and ecosystem has been investigated by many studies (Shukla, 1990; Wang, 2000, among others).

The Amazon rainforest has a significant impact on the hydrological climate of the region. Climate and land cover changes in the Amazon Basin, the largest tropical forest

and reservoir of freshwater and carbon in the world can influence the entire world's ecosystems and is of paramount importance for climate and ecosystem studies (Cochrane and Barber, 2009). The Amazon rainforest stores about 40 percent of the global carbon of the terrestrial biomass (Dixon, 1994). Over the past decades, the rate of deforestation has increased mostly over an arc on the southeastern region, largely for the purpose of developing cattle pasture, agricultural lands, and infrastructure. The Amazon lost 6 and 15 percent of the forest in 1988 and 2001, respectively (Skole and Tucker, 1993; Instituto Nacional de Pesquisas Espaciais, INPE, 2003). Figure 1.3 shows annual forest loss in the Amazon during 2001-2012 (Butler, 2006).

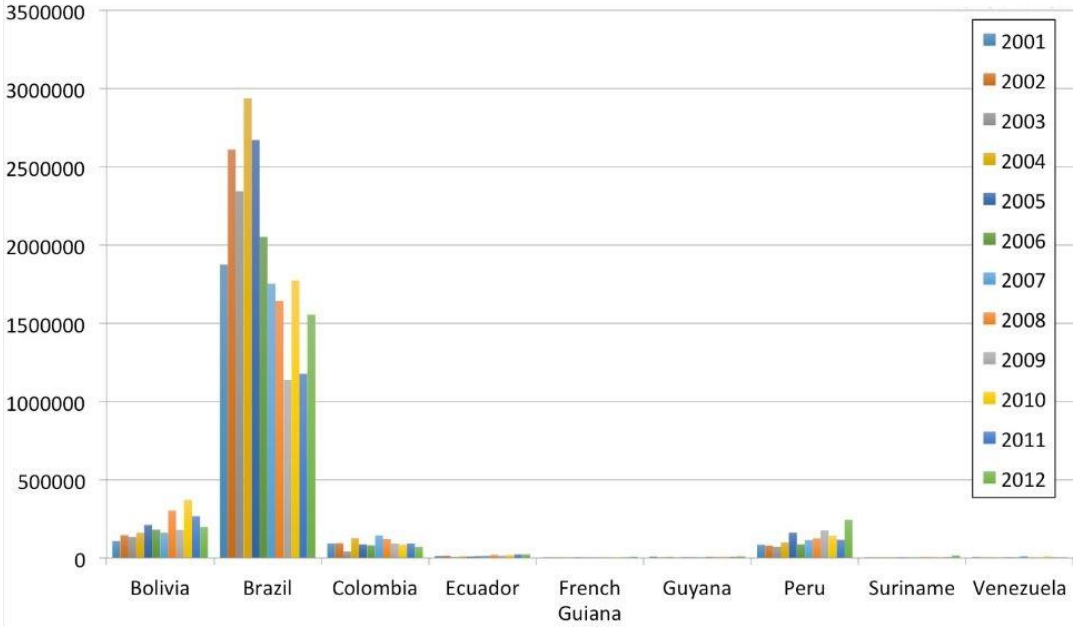

Figure 1.3. Annual forest loss (ha) in the Amazon, 2001-2012 (Butler, 2006).

Although an accurate estimate of deforestation rate is difficult, large degraded patches of the basin can be observed using remote sensing tools. Deforestation changes the ecosystem of the Amazon basin and influences the land-atmospheric circulation. Deforestation also increases the risk of fire and drought over the region. The Amazon basin has been experiencing severe drought and fire in the past decades. Although deforestation impacts the frequency and severity of the droughts, the droughts in the

basin are mainly related to variations in the ocean temperature, in particular the El Niño-Southern Oscillation (ENSO) and the Atlantic Multi-decadal Oscillation (AMO) (Bagley et al., 2014). High sea surface temperature in the North Atlantic Ocean is recognized as the main driver of the severe droughts in 2005 and 2010 (Marengo et. al., 2011), which increased the fire frequency. Past studies using satellite data over Amazonia provide evidence that the intensity and frequency of the droughts in this region are increasing in a way that can change the structure of the entire Amazonian ecosystem (e.g., Bush et al., 2008; Aragao et al., 2008, among others).

In summary, this domain is of primary interest for climate and ecosystem scientists because of

- The diversity in the topography and the vastness and richness of the species and resources.
- The significant impact of change of climate and land cover over the domain on the entire world's ecosystems (Cochrane and Barber, 2009).

1.3. Brief Introduction to the Datasets

This section describes the datasets used in the study, including the Community Climate System Model (CCSM3) dataset, the bias-corrected National Centers for Environmental Prediction (NCEP) Reanalysis data, and the Climate Research Unit data (see Table 1.1).

1.3.1. Community Climate System Model (CCSM3) Dataset

Climate models are key tools to study short- and long-term climate changes under different scenarios. The Community Climate System Model (CCSM3) is one of the Global Climate Models/General Circulation Models (GCMs), which is used to numerically simulate land-atmosphere-ocean circulation. CCSM3 was developed by the

University Corporation for Atmospheric Research (UCAR) and maintained by the National Center for Atmospheric Research (NCAR). CCSM3 is a well-established model and has been successfully used for simulating the impacts of land-use changes on climate (Collins et al., 2006). This model includes the Community Land Model (CLM), which has dynamic vegetation growth, death, and succession (Bonan and Levis, 2006). The frequencies of CCSM3's outputs are 6-hourly, daily, monthly, and annually from IPCC AR4 simulations (publicly available at www.cgd.ucar.edu/ccr/strandwg/ccsm_6hr_data.html). Forty two variables are available for these scenarios at 1 to 26 vertical pressure levels, with spatial resolution of about 1.4° (T85). The CCSM3 outputs represent different scenarios including 20th century (20C3M) for the period 1900-1999, climate change commitment (Commit), IPCC SRES A1B (SRESA1B), IPCC SRES B1 scenario (SRESB1), IPCC SRES A2 scenario (SRESA2), and IPCC SRES A1FI scenario (SRESA1FI), all for 2000-2099. For detailed descriptions of different greenhouse gases emission scenarios, the reader is referred to the Special Report on Emission Scenarios (SRES) by the IPCC Working Group III (Nakicenovic et al., 2000). This work uses one emission scenario "A2", which is identified as one of the marker scenarios by the IPCC. A2 is based on a "worse-case scenario" with increases of CO2 by factors of four to five over 2000-2099 (Li et al., 2010). This scenario provides a high rate of warming based on model ensembles (Meehl et al., 2007) and has been widely used for different climate change assessments including the North American Regional Climate Change Assessment Program, NARCCAP (Mearns et al., 2009). The 6-hourly instantaneous and monthly air temperature (T), skin temperature (TS), specific humidity (Q), longwave (LW) and shortwave (SW) radiation, surface pressure (PS), horizontal winds (u, v), and precipitation (P) are used in this study for two time periods: historical period 1901-1999 (20^{th} century), and SRESA2 future projection for 2000-2013. Here T, u, v, and Q are chosen from the first pressure level of CCSM3 (992.56 mb), while the other variables are selected at the surface level.

1.3.2. Meteorological Forcing Dataset

The Meteorological Forcing Dataset is a bias-corrected NCEP (National Centers for Environmental Prediction) Reanalysis product (Sheffield et al., 2006). The NCEP Reanalysis uses the Numerical Weather Prediction (NWP) model to represents the physical process of the earth's atmosphere. The NCEP also incorporates data assimilation of the past data and observations in an analysis/forecast system to provide global dataset in 6-hourly, daily, and monthly temporal resolution in 17 pressure levels and 28 sigma levels. Sheffield et al. (2006) downscaled the 2-degree NCEP reanalysis product to 1-degree resolution and then combined it with observation-based datasets such as those from the Global Precipitation Climatology Project (GPCP) and Climatic Research Unit (CRU) to remove the potential biases in the NCEP data. Bilinear interpolation with adjustment for difference of elevation is used to disaggregate 2° NCEP temperature to 1° spatial resolution. Sheffield et al. showed that the NCEP underestimates mean annual temperature compared to the Climate Research Unit (CRU) data. They argued that the biases in the temperature are related to the parameterization of the surface water budget. To match monthly average of the NCEP temperature with the corresponding CRU ones, they used a shifting adjustment approach based on the difference between the monthly average of the NCEP and CRU temperature. To adjust the monthly mean diurnal temperature range to the corresponding CRU ones the scaling adjustment of the diurnal cycle of temperature is used (The detailed description of the method is provided in Chapter 2). Sheffield et al. (2006) created this 1° bias-corrected meteorological forcing dataset (referred to hereafter as MFD) for the purpose of improving the results of land-surface models. This product is publicly available at hydrology.princeton.edu/data.php and can be used as a ground truth benchmark in the absence of long term observations. Since it is almost impossible to find fine resolution observations (6-hourly) for all grids of the study domain and we want to correct the biases of 6-hourly temperature, MFD temperature is used as a reference.

1.3.3. Climate Research Unit (CRU) Dataset

The gridded Climate Research Unit dataset is recognized as one of the most valid records of the climate observations, which are widely used by the climate research community. The dataset is produced by the Climate Research Unit in the school of the Environmental Sciences and the Tyndall Centre in the University of the East Anglia, United Kingdom (Jones and Harris 2014). This dataset is compiled from more than 4000 weather stations around the world. The thin-plate splines method as a function of longitude, latitude, and elevation is used to interpolate station data. The results are evaluated by cross validation and compared with other climatologies (New et al., 1999). The denser station network can capture well the spatial variability of the climate. The data are reported monthly at spatial resolution of 0.5° for all land masses excluding Antarctica. There are different versions of the CRU datasets with different temporal coverage. The newest one is CRU TS3.22, which covers the longest time period from 1901 to 2013 (Harris et al., 2013, 2014). The data are publicly available at http://www.cru.uea.ac.uk/cru/data/hrg/. The new version corrected some discontinuity in the data and incorporated more stations. Since the CRU dataset is considered as one of the valid long term observations and we want to correct the biases of monthly precipitation, CRU precipitation is used as the true observation.

Table 1.1. General information of the datasets.

Dataset	**Variable**	**Spatial Resolution**	**Temporal resolution**
CCSM3	T, TS, Q, LW, SW, P, PS, u, v	1.4°× 1.4° (T85)	6-hourly
MFD	T	1°	6-hourly
CRU	P	0.5°	Monthly

1.4. Outline of Thesis

To develop a new approach to reduce the biases of the climate variables, this work poses the following questions:

- Does the proposed approach improve all statistics including mean square error, bias, and also correlation and distribution structure of the climate variables of interest?
- Does the proposed approach have generalization ability to perform well with new and unseen datasets?
- Does the proposed approach have ability to regionalize the study domain?
- Is the proposed approach efficient or in other words, does the proposed approach use a reasonable number of observations to construct a robust model between the input-output?

To address these questions, this dissertation is developed as follows:

- We discuss previously used methods to correct biases and their advantages in Chapter 2.
- Artificial Neural Networks (ANN), the nonlinear regression that is used for bias correction is explained in Chapter 3.
- Chapter 4 applies the framework explained in Chapter 3 to correct the biases of temperature and precipitation, pixel by pixel over the study domain.
- The potential of the regionalization of the model is evaluated in Chapter 5.
- Chapter 6 summarizes the results and conclusions of this study and recommends potential future work.
- Appendix A explains a new algorithm for retrieving hourly records of surface temperature based on the maximum entropy production and the half-order derivative/integral models. This result is not directly related to the central bias

correction objective of this thesis but arose from the interest to develop high temporal resolution datasets.

- Appendix B provides the results of bias-corrected temperature and precipitation in two GCMs using Equidistant Cumulative Distribution Function method (EDCDF).
- Additional figures regarding results of bias-corrected temperature and precipitation by the regression models are provided in Appendix C.
- Locations (latitude and longitude) of the training pixels in the delineated domains are presented in Appendix D.

CHAPTER 2

STATISTICAL BIAS CORRECTION METHODS

2.1. Biases in the Models

The Earth's climate has shaped the history of biological and cultural evolution and the geographical distribution of humans. Almost all of the man-made and natural systems such as water supplies, agriculture, forestry, fisheries, human settlements, industries, energy, and financial services are sensitive to climate change (Harding et al., 2011). Since our observational knowledge is limited in space and time, accurate numerical simulations and predictions are necessary to understand and forecast the consequences of climate change. Different numerical models such as global (General Circulation Model, GCM) and regional (Regional Climate Model, RCM) models can represent the underlying physics of the land-atmosphere-ocean interactions. Although the models allow us to fill space-time observational gaps and to simulate present and future dynamics of the Earth's climate, their outputs are often subject to random and structural errors (biases). The inevitable biases are model dependent and may arise due to our inadequate knowledge, oversimplification of the governing equations, deficient parameterization of the underlying physics, and calibration errors. Due to the highly nonlinear nature of the underlying governing equations, the errors are typically amplified in space-time (Dai, 2006). Although the models have been improved over time, the biased outputs of these models are still a matter of significant concern in climate studies (Dai 2001a, b, 2006; Solomon et al., 2007). For example, Sun et al., (2005) concluded that "most GCMs overestimate the frequency of light precipitation and underestimate the intensity of heavy precipitation." Dai et al., (2001) also reported unrealistic simulations of the tropical precipitation regimes by the Community Climate System Model (CCSM).

Chang et al. (2007) illustrated a pattern in CCSM3 with cold and warm biases in the northern and southeastern Tropics, respectively. Bonan and Levis (2006) used the Dynamic Global vegetation Model (DGVM) to evaluate the biases in the CCSM3. They reported severe dry bias in the CCSM precipitation over the eastern United States and Amazonia, which produced biases in the simulation of vegetation. They also showed an underestimation of the global forest cover (e.g. evergreens over the tropic), indicating that the simulated soil moisture was low. The biases in the model influence the sensitivity analysis. It was shown by Castillo and Gurney (2012) that CCSM3 coupled with the DGVM was not able to explore the sensitivity of the biophysical climate to the tropical deforestation due to a warm dry bias in the model over the Amazon basin. The relatively flat annual cycle of the CCSM evapotranspiration (ET) with overestimation and underestimation during the wet and dry seasons was reported by Malhi et al. (2002); Nobre et al. (1996); Werth and Avissar (2004). The biases in the annual cycle of the ET lead to an unrealistic behavior of the hydrological cycle such as rain, evaporation, surface runoff, and drainage over the Amazon basin (Lawrence, 2007). They concluded that less frequent small- to medium-size rain events and underestimation of the photosynthesis were the two main consequences of the biased ET. We can conclude that the biased inputs to the models affect the outputs and the analysis studies. As a result, the biases are of critical concern to the end users, especially for those involved in climate change studies.

2.2. Bias Correction Methodology

The biased forcings from the models can significantly impair outputs of other models such as land surface hydrologic models and hence any related risk management and strategic planning (see e.g., Sharma et al., 2007; Hansen et al., 2006; Feddersen and Andersen, 2005, among other studies). Thus, prior to using outputs of the climate models

as inputs into the land-surface hydrologic models, bias removal is an essential step. Due to the underlying natural nonlinearities and complexities of the governing equations of the models (GCMs), intrinsic bias correction within the model structure may not be practically feasible. Biases of the climate variables are commonly reduced using statistical and dynamical approaches.

2.2.1. Dynamical Bias Correction

Dynamical bias correction methods can correct intrinsic biases within the model structure. They are capable of producing physically consistent climate variables. Dynamical bias correction can involve data assimilation to improve the modeled outputs and forecast skills by using various kinds of observations (radar, satellite, station). The optimally estimated state of the system is obtained at each analysis step, which combines observations and numerical modeled outputs minimizing a cost function. A cost function typically measures departures:

1) From the observations, weighted by an observational error covariance.
2) From the background field, weighted by a background error covariance.

For comprehensive and systematic descriptions of the data assimilation the reader is referred to "Atmospheric Modeling, Data Assimilation, and Predictability" by Kalnay (2003) and to "Atmospheric Data Analysis" by Daley (1993). Although data assimilation techniques improve the results by combining the model and the data, they require dealing with high dimensional matrices, which is computationally expensive. Therefore, assumptions, approximations, and simplification of the methods are required, which produce additional uncertainties and errors in the results. In addition to the various assumptions required for data assimilation, computation of the global minimum of the cost function and the uncertainty associated with the error covariance are the two big challenges for the users. These difficulties of the dynamical methods, in particular

computational costs, generally hamper their applicability for climate-scale bias correction problems.

2.2.2. Statistical Bias Correction

The main idea of the statistical bias correction method is to develop a statistical relationship between modeled and observed variables over the same historical period and then use the constructed relationship for the modeled projection. Diagnostic statistical methods commonly use the statistics of the observations (mean, variance, and distribution) to detect and remove biases from the model predictions. In these approaches the statistics of the modeled data are improved by re-scaling to the statistics of the corresponding observation. The widely-used statistical methods follow:

2.2.2.1. Delta Change Method

The Delta change method (linear scaling) is one of the most well-known statistical approaches that shifts or re-scales the mean of the modeled data based on the mean of the observations obtained from a historically selected baseline period. In this approach the error is identified by taking the difference between the mean of the modeled and observed values over a specific time period (baseline). The mean error obtained over the baseline period is used for bias correction over the prediction phase. Ines and Hansen (2006) used a simple multiplicative shift method to remove the biases from the mean monthly GCM precipitation outputs x^i in month i as follows:

$$x_{adj}^{i} = x^{i} \times \frac{\bar{x}^{i}{}_{obs}}{\bar{x}^{i}{}_{GCM}} \tag{2.1}$$

where x_{adj}^{i} is the bias-corrected monthly precipitation, $\bar{x}_{GCM}^{i}$ denotes the long-term monthly mean rainfall obtained from the GCM outputs, and $\bar{x}_{obs}^{i}$ refers to the corresponding monthly mean of the observations. The simple multiplicative scheme removes the mean monthly bias of the modeled precipitation but the biases of the intensity, frequency, and inter-annual variability of the precipitation were not adjusted.

Ines and Hansen (2006) used the bias-corrected GCM precipitation to drive crop simulation models. They concluded that the overall prediction of the yields can be improved mainly by improving the mean bias of precipitation through the delta change method.

Sheffield et al. (2006) constructed a 50-year bias-corrected, 3-hourly and 1° meteorological forcing dataset to drive land surface modeling. They used the delta change method and the CRU dataset as the observations to improve the biases of the NCEP-NCAR reanalysis precipitation and temperature as follows:

- **Precipitation:** The accuracy of the gauge-based precipitation is influenced by the wind and solid precipitation (Goodison et al., 1998). Adam and Lettenmaier (2003) provided a global adjustment ratios dataset to correct the gauge under-catch, which can increase the global precipitation about 12 percent. Sheffield et al. (2006) adjusted the monthly CRU precipitation by the adjustment ratios before using them as the observation. Then they used the same multiplicative scheme to re-scale the monthly total NCEP precipitation ($P_{NCEP,Mon}$) to the corresponding observation ($P_{CRU,Mon}$) as

$$\tilde{P}_{NCEP,3hr} = \frac{P_{CRU,Mon}}{P_{NCEP,Mon}} \times P_{NCEP,3hr} \quad (2.2)$$

  where $P_{NCEP,3hr}$ is 3-hourly NCEP precipitation and $\tilde{P}_{NCEP,3hr}$ denotes the bias corrected 3-hourly values.

- **Temperature:** Sheffield et al. (2006) used an additive adjustment scheme to match the monthly mean NCEP temperature ($T_{NCEP,Mon}$) to the corresponding observation one ($T_{CRU,Mon}$) as

$$\tilde{T}_{NCEP,3hr} = \left(T_{CRU,Mon} - T_{NCEP,Mon}\right) + T_{NCEP,3hr} \quad (2.3)$$

where $T_{NCEP,3hr}$ and $\tilde{T}_{NCEP,3hr}$ are 3-hourly NCEP temperature before and after bias correction, respectively. This adjustment scheme assured that the monthly mean CRU temperatures were properly conserved in the corresponding NCEP ones. Furthermore, they re-scaled the diurnal cycle of temperature for each day so that the monthly mean NCEP diurnal temperature range ($DTR_{NCEP,Mon}$) matched the corresponding CRU ones ($DTR_{CRU,Mon}$) as

$$\tilde{T}_{NCEP,3hr} = \tilde{T}_{NCEP,Daily} + \frac{DTR_{CRU,Mon}}{DTR_{NCEP,Mon}} \times (\tilde{T}_{NCEP,3hr} - \tilde{T}_{NCEP,Daily}) \qquad (2.4)$$

where $\tilde{T}_{NCEP,Daily}$ is the bias-corrected daily NCEP temperature, which remains fixed.

Horton et al. (2011) provided bias-corrected projected temperature and precipitation by using a variation of the delta change method. The data is used for decision support of stakeholders as part of the New York City's climate change adaptation plans. He used 16 GCMs with three different emission scenarios to find the mean change of the three time slices of a 30-year modeled projection (2010-2039; 2040-2069; 2070-2099) relative to a 30-year modeled baseline (1970-1999). The results showed a significant increase in the frequency of the extreme events (coastal flooding and heat events), which highlighted the importance of long-term adaptation and mitigation planning. Hay et al. (2000) used the delta change method to project bias-corrected precipitation, maximum and minimum of temperature from the Hadley Centre Coupled Model, version 2 (HadCM2) to drive a hydrologic model (U.S. Geological Survey's, USGS, Precipitation-Runoff Modeling System, PRMS) over three basins in the United States. They concluded that projection of the modeled variables onto the observations using the delta change method leads to a realistic runoff simulation. The skill of the method depends on the ability of the GCMs to simulate the variables.

The main advantage of the delta change method is its simplicity and computational efficiency. This method assumes that the difference between the historical (baseline) modeled and observed values remains the same for the projection, which is not verifiable. As is evident, this method adjusts only the mean of the modeled data without any correction of the higher order error statistics.

Schmidli et al. (2006) modified the linear scaling method to correct the biases of the precipitation not only in the mean but also in frequencies and intensities of the wet days. This method called the Local Intensity Scaling (LOCI) method has two steps. In the first step, a threshold is determined such that a number of wet days in the model exceeding this threshold matches the number of wet days in the observation. Then to adjust a wet day frequency, the days with precipitation smaller than the threshold are identified as dry days. In the second step, the intensities of the wet day precipitation (P_{adj}^{m}) are adjusted as

$$P_{adj}^{m} = P_{w}^{m} \times \frac{\overline{P_{w}^{o}}}{\overline{P_{w}^{m}} - P_{wdt}^{m}} \tag{2.5}$$

where P_{w}^{m} is wet day modeled precipitation ($P_{w}^{m} \geq P_{wdt}^{m}$), P_{wdt}^{m} is a threshold for model wet day, $\overline{P_{w}^{m}}$ denotes the long-term monthly mean wet day intensities from the model, and $\overline{P_{w}^{o}}$ refers to the corresponding monthly mean of the observations.

Leander and Buishand (2007) used a power transformation to correct the mean and coefficient variation (CV) of the precipitation as

$$P_{adj}^{m} = a \times (P^{m})^{b} \tag{2.6}$$

where a and b are parameters. The modeled precipitation (P^{m}) is transformed to the adjusted precipitation (P_{adj}^{m}). Parameter b is determined such that the CV of the adjusted precipitation matches the CV of the observed one through iterative procedure (Brent, 1971). In other words, b is estimated such that

$$\frac{\sigma(P_{adj}^{m})}{\overline{P_{adj}^{m}}} = \frac{\sigma(P^{o})}{\overline{P^{O}}} \tag{2.7}$$

where σ is the standard deviation. Parameter a is determined such that the mean of the adjusted precipitation matches the mean of the observed one ($\overline{P_{adj}^{m}} = \overline{P^{o}}$). The adjusted precipitation has the same mean and CV with the observed ones. For temperature the mean and standard deviation can be adjusted by shifting and scaling as (Leander and Buishand, 2007; Shabalova et al., 2003; Chen et al., 2011a,b)

$$T_{adj} = \left[(T^{m} - \overline{T^{m}}) \times \frac{\sigma(T^{o})}{\sigma(T^{m})} + \overline{T^{m}}\right] + [\overline{T^{o}} - \overline{T^{m}}] \quad (2.8)$$

where T^{o} is observed temperature and T^{m} is modeled temperature. The first part in Eq. 2.8 scales the variance of temperature and the second part adjusts the mean of the temperature values relative to the observation ones.

The adjustment factors used in the correction of mean and variance of precipitation and temperature values in the above approaches are assumed not to change in the future. Teutschbein and Seibert (2012) used the methods discussed above to correct the biases of precipitation and temperature from the regional climate model (RCM) simulations in two periods; one is 1961-1990 (control run) and the other is 2021-2050 under the A1B scenario. All methods improved the mean modeled temperature and precipitation while the methods exhibited different skills in adjusting higher moments such as variance. They used uncorrected and bias-corrected precipitation to drive a conceptual streamflow model HBV (Bergström, 1976) over five catchments in Sweden. They found that the simulated streamflow with bias-corrected precipitation matches the observed one well.

2.2.2.2. Cumulative Distribution Function Method (CDF)

The so-called quantile-based mapping method (CDF matching) maps the cumulative distribution function (CDF) of the biased model outputs onto the distribution of observations (Panofsky and Brier, 1968; Cayan et al., 2008; Hayhoe et al., 2004; Maurer and Hidalgo, 2008). The approach imposes the following equivalence:

$$F_{OBS}(y) = F_{MOD}(x) \tag{2.9}$$

where $F(\cdot)$ denotes the CDF of the observations (OBS) and the modeled (MOD) outputs. From where the bias corrected model output is obtained:

$$x_{adj} = F_{OBS}^{-1}\left(F_{MODh}(x)\right) \tag{2.10}$$

where x_{adj} is the bias-corrected model output while F_{MODh} denotes the CDF of the historical modeled simulations. Figure 2.1 illustrates a schematic of the CDF method for correction of the bias at an arbitrary point ($x = 3.5$, solid circle, selected for illustration purposes).

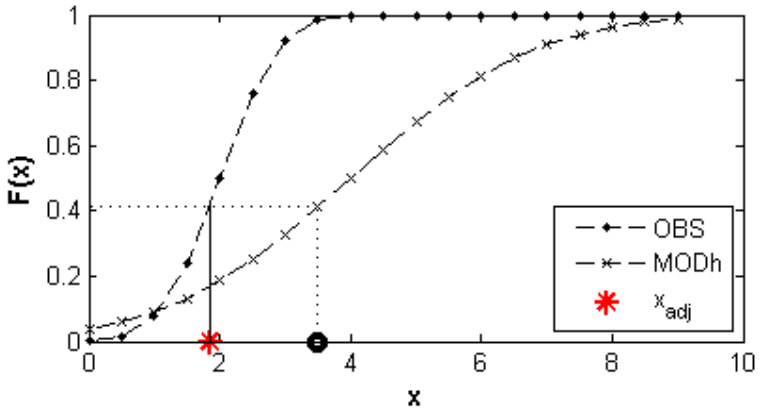

Figure 2.1. Illustration of the CDF method for correction of the bias at $x = 3.5$ (solid circle). Dashed line is the cumulative distribution function (CDF_{OBS}) for the observation, cross-dashed line is the cumulative distribution function (CDF_{MODh}) for the historical modeled variable, and solid star is an adjusted value (x_{adj}) based on the CDF method.

The CDFs and their inverse can be estimated by fitting a distribution function to the data empirically or theoretically through parameter estimation. The theoretical distribution function fitted to the historical data is more likely to capture the extreme values of the projection compared to the empirical one. Note that the biases associated with the estimates of the parameters of the theoretical distribution can influence the results of the bias correction method.

Ines and Hansen (2006) used the CDF method to correct the biases of the daily GCM precipitation to drive simulations of maize yield at the Katumani station in Kenya. They fitted the Gamma distribution to the data to map the modeled CDF of precipitation to the observed one. They compared the bias-corrected results with the ones obtained by the delta change method. Although the delta change method can correct the biases of the monthly and total rainfall better than the CDF method, it cannot improve the biases of the intensity and frequency of the precipitation. They concluded that all bias correction methods improved the crop growth and the yield simulations. They also showed that although the mean bias of precipitation was the main source of the bias in the maize simulations, the bias in the time structure of precipitation caused an underestimation of the maize yields at the location.

Piani et al. (2010) used the quantile-based mapping approach to remove the biases of the daily precipitation in a regional climate model (DMI-HIRHAM version 5) over Europe. They fitted a two-parameter Gamma distribution to the precipitation data (1961-1970) to formulate Equation (2.9) between the modeled and observed values. The method was validated during 1991-2000. They indicated that the bias correction method improved not only the mean and the intensity of precipitation but also the drought and heavy precipitation indices for the both calibration and validation periods. Baigorria et al. (2007) used the CDF method to reduce the biases of the climate outputs from the Florida State University/Center for Ocean-Atmospheric Prediction Studies (FSU/COAPS) regional model. They used raw and bias-corrected climate variables to drive the CERES-Maize crop model at three stations in the Southeastern USA including Alachua (Florida), De Kalb (Alabama), and Tift (Georgia). They applied Gamma, Beta, and Gaussian CDF to the precipitation, incoming solar radiation, and temperature (T_{min}, T_{max}) values, respectively. They concluded that the bias correction of the variables improved the monthly statistics of the results, number and the length of the dry spells, while the time of occurrences of the dry spell were not well predicted.

Wood et al. (2004) evaluated the effect of bias correction of the climate variables from the NCAR-DOE Parallel Climate Model (PCM) and RCM outputs on hydrologic simulation. The two main approaches, the statistical downscaling method and the bias correction and spatial downscaling method (BCSD), were used to post-process the climate data to drive the Variable Infiltration Capacity model (VIC) over the Columbia River Basin (CRB) of the U.S. Pacific Northwest (PNW) region. For the downscaling step, they used a linear interpolation (LI) and spatial disaggregation (SD) method. For the bias correction step (BC), they established an empirical quantile-based relationship or function between modeled data (average temperature and total precipitation) and corresponding observations from Maurer et al. (2002) for the period of 1975-1995 (B06.22 simulation). The established function was used for a future period (2040-2060) under a Business As Usual (BAU) scenario. Since the future distribution of temperature differed from the historical one, they removed the temperature shift. Thus, the difference between the mean monthly future temperature and the corresponding historical one was removed before bias correction and then added after the process of the bias correction. They assumed that the variability of the projected variables is similar to the historical ones, while the mean changes. They compared the results of the hydrologic simulations using downscaled climate data and bias-corrected, downscaled data as inputs to the VIC. They concluded that the downscaled data without bias correction produced biases in the hydrologic simulation and the bias correction was a necessary step to reasonably model hydro-climatological simulations.

Maurer et al. (2010) downscaled NCEP/NCAR reanalysis temperature and precipitation to drive the hydrologic model (VIC) over California for two different periods: 1950–1976 (calibration period) and 1977–1999 (validation period). They used a quantile-mapping bias correction method before statistical downscaling. They indicated that the bias correction improved the skill of the downscaling and predicted stream flow.

The CDF approach implicitly corrects the biases of the future modeled outputs by using the CDF of the model historical simulations, which assumes to be the same as that of the CDF of the model predictions. Notice that this method can adjust not only the mean but also the distribution of the model simulations and higher order statistics. This method is simple, effective, and has been successfully reported for bias correction in many climate studies (Cayan et al., 2008; Hayhoe et al., 2004; Maurer and Hidalgo, 2008; among many others). As is evident, one of the main drawbacks of this approach is that it implicitly assumes stationarity of the state variable of interest, which might be unrealistic (Solomon et al., 2007; Milly et al., 2008).

2.2.2.3. Equidistant CDF Method (EDCDF)

The quantile-based method (CDF) uses the CDFs of the historical model outputs (CDF_{MODh}) and the corresponding observation ones (CDF_{OBS}). The method is able to improve all moments (the mean and the higher statistics) of the data during the time that the CDFs and the transfer function are constructed (historical period). The constructed transfer function is proper for another period if the change in the distributions is not significant.

In light of available climate model predictions, Li et al. (2010) extended the CDF matching approach for bias correction of climatic predictions by partially accounting for the distribution of the model projections in the CDF matching process. The modified version of the CDF matching approach, called equidistant CDF (EDCDF), uses CDF information of the model predictions (CDF_{MODp}) in addition to the current CDFs (historically modeled and observed data). The idea is to find an incremental adjustment based on the historical data for any given model prediction. This adjustment is based on the difference between the CDF of observations and outputs of historical simulations (Δ) for a given percentile of the model outputs x as follows:

$$\Delta = F_{\mathrm{OBS}}^{-1}\left(F_{\mathrm{MODp}}(x)\right) - F_{\mathrm{MODh}}^{-1}\left(F_{\mathrm{MODp}}(x)\right) \tag{2.11}$$

$$x_{adj} = x + \Delta \tag{2.12}$$

where x_{adj} is the bias-corrected modeled outputs, $F(\cdot)$ is the CDF of the observations (OBS), the historical model simulations (MODh), and the prediction model outputs (MODp). Figure 2.2 illustrates the EDCDF method for correction of the bias at an arbitrary point ($x = 3.5$, solid circle, selected for illustration purposes).

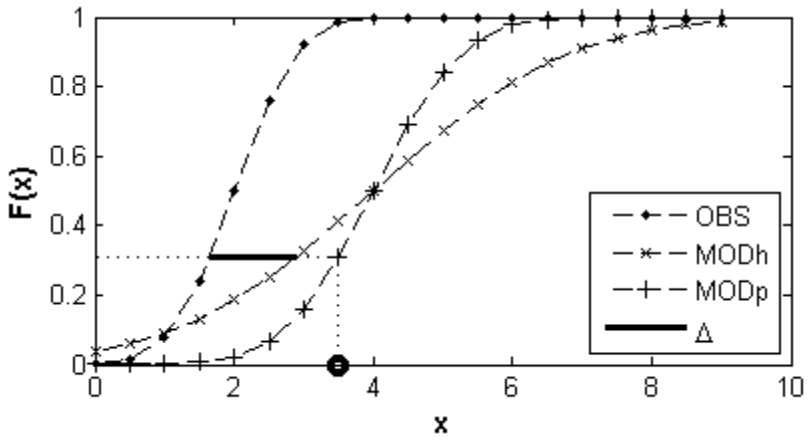

Figure 2.2. Illustration of the EDCDF method for correction of the bias at $x = 3.5$ (solid circle). Dashed line is the cumulative distribution function (CDF_{OBS}) for the observations, cross-dashed line is the cumulative distribution function (CDF_{MODh}) for the historical modeled variable, and plus-dashed line is the cumulative distribution function (CDF_{MODp}) for the future modeled variable, and the thick solid line is an adjustment (Δ) for the EDCDF method according to Eq. 2.11.

Specifically, the biased model projections (x) are inverted via their estimated CDF to obtain their uniformly distributed counterparts in the probability space. Then these random values are used by the CDFs of the historical observations and the model simulations to obtain the estimated bias for the climate variable of interest. The idea is to find an adjustment function (transfer function) based on the difference between the historically modeled and observed data (Δ) in a distribution sense and then apply it to reduce the biases of the modeled values during the entire historical and future periods.

When F_{MODp} is close to F_{MODh} (see Eqs. 2.10 to 2.12), the results of the EDCDF method are very similar to the CDF method.

Li et al. (2010) corrected biases of modeled temperature and precipitation over the Northern Eurasian Earth Science Partnership Initiative (NEESPI) using the EDCDF method. The modeled data were from the Parallel Climate Model (PCM1) for 20th century (20C3M) and future under the Special Report on Emissions Scenarios A2 (2001-2099). They used a four-parameter beta distribution and a mixed gamma distribution to fit on the temperature and precipitation values, respectively. Basically they modified the CDF method by incorporating the distribution of the model projections in addition to the distribution of the historical model and observation used in the CDF method. As a result, they concluded that the EDCDF method performs better than the CDF method, in particular for heavy tailed distributions in the presence of abundant extreme values in the temperature and precipitation fields. The assumption for the EDCDF method is that the transfer function linking observations and model outputs remains time invariant. Thus, the incremental differences between the CDFs of the observations and historical model outputs at each percentile (Δ) can be used for bias correction purposes of the entire period.

As part of this effort we used the EDCDF method to reduce the biases of temperature and precipitation from the Community Climate System Model (CCSM3) and the Regional Climate Model driven by the Hadley Centre Coupled Model (RegCM3) over Amazonia for the Andes-Amazon Project (http://www.oeb.harvard.edu/faculty/moorcroft/andes-amazon/). Adjustments were also made on specific humidity and downwelling longwave radiation to avoid inconsistency between those variables and bias-corrected temperature values. The results are provided in Appendix B.

2.2.2.4. Joint Variable Spatial Downscaling Method (JVSD)

Zhang and Georgakakos (2012) followed the BCSD approach by Wood et al. (2004) and developed the Joint Variable Spatial Downscaling (JVSD) technique as a new statistical method for downscaling and bias correction. In this approach, the historical analogue approach was used for downscaling and a functional relationship between the joint statistics of the historical GCMs outputs and coincident observations was employed for bias correction purposes over the Apalachicola-Chattahoochee-Flint river basin (ACF) in the southeast US. They divided GCM temperature and precipitation from 1950 to 2099 into the three periods:

- 1950-1999 as the historical period (CON)
- 2000-2049 as the first future period (FUT1)
- 2050-2099 as the second future period (FUT2)

They used a differencing process to remove seasonality and trend as

$$\Delta x_t = \nabla_l(x_t) \tag{2.13}$$

where x is a climate variable (temperature and precipitation) from the observation or the model, Δx is the increment of the variable, t is the number of the month, and ∇_l is a differencing operator with lag l calculated as

$$\nabla_l(x_t) = x_t - x_{t-l} \tag{2.14}$$

They compared:

1) Joint distributions of the actual CON modeled temperature and precipitation with the corresponding ones from FUT1.
2) Joint distributions of the actual CON modeled temperature and precipitation with the corresponding ones from FUT2.
3) Joint distributions of the increment of CON modeled temperature and precipitation with the corresponding ones from FUT1.
4) Joint distributions of the increment of CON modeled temperature and precipitation with the corresponding ones from FUT2.

The results indicated that although the joint distributions of the actual variables for the CON, FUT1, and FUT2 were different, the joint distributions of the increments were very close for the three different periods (CON, FUT1, FUT2). It was concluded that the joint distributions of the increments of the variables are stationary and a constructed transfer function based on the historical increments (CON) can be used for the bias correction of the increments in the future time (FUT1 and FUT2). They found the best performance with the first order differencing and 12 month lag (l = 12). Thus, they used a 12-month differencing process to create a stationary joint cumulative distribution function of the increments of the variables (e.g., joint CDFs of the increments of temperature and precipitation). The biases were removed based on the mapping of the stationary joint distribution of the increments of the climate variables to corresponding increments of the observed ones. Each point on the contours of the joint probability distribution indicated the joint frequency of the two variables (e.g., temperature and precipitation). Joint frequencies of the GCM distribution were mapped onto the corresponding observed ones (with the same joint CDF) based on the minimum Euclidean distance between the GCM and observed contours (d) in the probability space as (Fig. 2.3)

$$d = \sqrt{x^2 + y^2} \tag{2.15}$$

where x and y are the distances between the marginal CDFs of the variables (temperature and precipitation). When the biases of the increments were removed, they were inverted to the actual values.

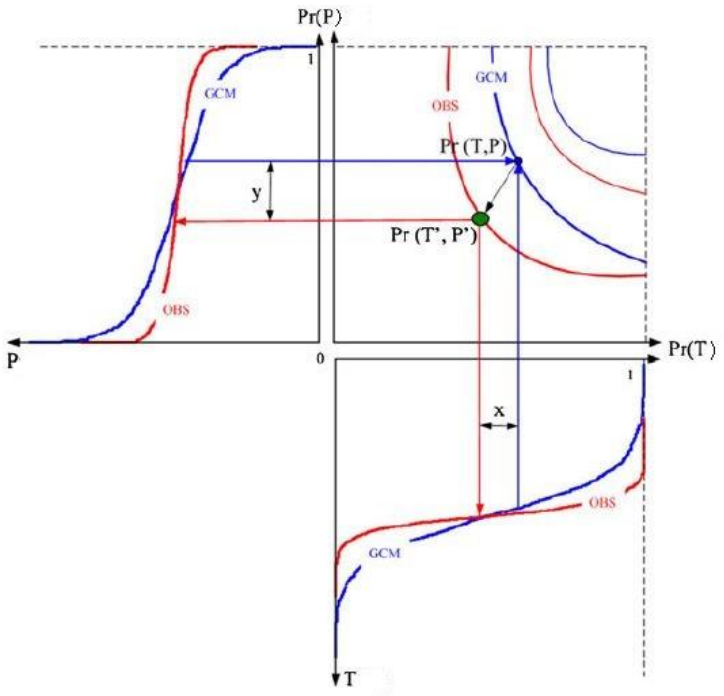

Figure 2.3. The schematic joint CDF mapping in the probability space (Zhang and Georgakakos, 2012). Top-right plot shows the joint distribution of temperature (T) and precipitation (P). Top-left and bottom-right plots are the marginal distribution of P and T, respectively. The red and blue contours refer to the observation (OBS) and the GCM, respectively. x and y are the distances between the marginal CDFs of the variables (temperature and precipitation, respectively).

Zhang and Georgakakos (2012) concluded that the JVSD approach has a distinct advantage over the BCSD and dynamical methods. The advantage of the JVSD is that the method can downscale and correct the biases of the variables of the interest consistently at the same time. The JVSD can consider the co-variability of the climate states by modeling their joint distribution, which can produce the consistent dataset. When the correlation between the two state variables is negligible, the BCSD and the JVSD methods perform similarly. As one of the key assumptions, the JVSD method assumes that the joint distributions of the incremented variables in the historical and future time are identical. This has been shown to be valid for several GCMs.

2.3. Summary and Conclusions

Bias correction approaches are commonly based on statistical relationships (transfer functions) between the modeled and observed variables, which are constructed during the historical period. Then the constructed function is applied to correct the biases of the modeled variables in the projection period. The statistical methods assume that the underlying relationship for the historical time is valid for the projection, which cannot be guaranteed. The consistency between the climate variables can deteriorate with statistical bias correction. As we explained, this deficiency was addressed and resolved to some extend by some proposed methods (Sheffield et al., 2006; Zhang and Georgakakos, 2012). Although this family of statistical approaches cannot completely address the underlying physics and variability of the climate, they have considerable computational advantages over the dynamical approaches.

The probability matching methods (e.g. CDF, EDCDF, JVSD) adjust different quantiles of the modeled distribution according to the corresponding quantiles of the observed distribution, while the modeled value at a certain quantile may not coincide with the observed value of that quantile. Thus, effective implementation of the probability matching methods requires high correlations between the modeled and the observed climate variables. This is consistent with the results obtained by Chen et al. (2013). They compared the sensitivity of the different bias correction methods including mean-based (delta change) and distribution-based (quantile mapping) approaches on hydrological simulation. They used precipitation from four RCM provided by the NCEP over 10 river basins in the North America to drive the conceptual rainfall-runoff model, HSAMI developed by Hydro-Quebec. To evaluate the performance of the bias correction methods, they compared the simulated streamflow using raw and bias-corrected precipitation. They concluded that the distribution-based bias correction method outperformed the mean-based bias correction approach. The quantile mapping approach was not able to correct the biases of precipitation over the five watersheds. It was due to

the fact that there was a low temporal consistency between the time series of the modeled and observed precipitation.

The performance of the bias correction method varies with the different models and study locations. Note that even if the distribution-based methods can adjust the mean and higher statistics of the time series of the variables, they are not able to improve the temporal structure of the variables. This study attempts to define an approach that is able to remove the biases of the variables and improve the temporal sequence of them relative to the observations. We develop a data driven approach that allows obtaining bias-corrected estimates of the climate variables (air temperature and precipitation) via a supervised statistical learning approach. To account for the model errors and in particular biases, the method should be able to:

- Learn from available information.
- Adapt.
- Be generalizable to perform well when the observation is not available.

These features exist in regression models (linear and nonlinear). Our effort tries to improve the estimates of air temperature and precipitation, provided by the Community Climate System Model (CCSM3), using Artificial Neural Network (ANN) as a nonlinear regression method. We compare the results with the linear regression method. In the subsequent chapter, the fundamentals and the mathematical structure of the ANN will be explained.

CHAPTER 3

ARTIFICIAL NEURAL NETWORKS

3.1. Introduction

Machine learning is defined as a "field of study that gives computer the ability to learn (train) without being explicitly programmed" (Simon, 2013). Training, which is identified with biological systems, is the process of learning through experiences, examples, and adaptation (Schalkoff, 1990). The brain is able to store and integrate experiences and previous information and also organizes itself. This ability allows the brain to predict new situations, which is known as a generalization capability. The parallel structure of the brain is fault tolerant and self-organized and also it has ability to adapt to the changes of the environment, which offers a similar artificial neural architecture to solve various tasks. An Artificial Neural Network (ANN), a biologically motivated idea, consists of an interaction of computational elements or units. ANN imitates the abilities of the human brain including storing information, learning, and training to produce a (hopefully) correct response to new or unseen situations (Schalkoff, 1997). ANN seems to be suitable for:

- Complex problems with high-dimensional space.
- Problems with flawed and missing data.
- Problems with unknown or complicated relationships between the variables.

Functional approximation and pattern recognition/classification are the two main applications of ANNs. A list of illustrative examples is (Schalkoff, 1997):

- "Image processing and computer vision including image matching and compression; processing of time-varying images.

- Signal processing including seismic signal analysis.
- Pattern recognition including satellite and radar signal analysis; speech and fingerprint identification; character and handwriting analysis.
- Medicine including electrocardiographic analysis; diagnosis of various diseases; medical image processing.
- Military systems including undersea mine detection; radar clutter classification; tactical speaker recognition; target tracking.
- Financial systems including stock market analysis; real estate appraisal; credit card authorization; securities trading.
- Planning, control, and search including parallel implementation of constraint satisfaction problems (CSPs); system control; robotics.
- Artificial intelligence including implementation of computer programs such as expert systems.
- Power systems including system state estimation; fault detection and recovery; load forecasting; security assessment."

Formulating neural networks with many unknown parameters, without any clear guideline to the design of the model structure, is a big challenge. Despite the fact that ANN models are not able to represent underlying physical equations of the process, they have been widely used in various fields because:

- ANNs are known as universal approximators. In other words, ANNs are almost capable to approximate any continuous input and output mapping (Hornik, 1989, 1991).
- ANNs are able to identify complex and nonlinear relationships between predictors and response variables (nonlinear input-output mapping).
- Parallel structure of the ANNs results in fast computations.

- ANNs can be trained when observations are available and generalized to future situations.

The first concepts and characteristics of the ANN were explained by Rosenblatt (1959); Widrow and Hoff (1960); Minsky and Papert (1969). A classic paper by McCulloch and Pitts in 1943 combined neurophysiology and mathematical logic to explain fundamental logic of the ANN model. The physical and mathematical concepts of the neural network are explained in the following sections.

3.2. Fundamental Concepts behind Neural Networks

The structure of the ANNs is inspired by biological neural systems and is composed of artificial neurons (nodes) in multiple layers. The behaviour of a neural system that consists of billions of microscopic biological processing neurons (Churchill, 1986) is represented at a macroscopic scale. Neurons (nerve cells) and glia (glial cells) are two classes of cells in the nervous system, which perform processing and support functions, respectively. The neuron consists of three main components as (Kandel, 1991) (see Figure 3.1)

1) The cell body (soma) with a diameter of about 50 μm is made up of the nucleus and perikaryon.
2) The axon in a shape of a tube with a diameter of about 0.2 to 20 μm mainly generates the signals and transfers them to other neurons.
3) Dendrites in the shape of trees are connected to the axon of the other neurons by synaptic connections (synapses) to amplify the transmission of the impulse between the neurons. They act as a neuron's input. Synaptic activity is a complicated process to pass chemical and electrical signals from one neuron to another. A single neuron has about 10^3 to 10^4 synapses.

Transmitted signals are integrated in the soma to increase or decrease the electrical potential of the cell, which is called an action potential or nerve impulse. The magnitude of the action potential can increase and decrease (or stop increasing) by excitatory and inhibitory neurotransmitters, respectively. The action potential typically has a spiked signal so the frequency of the action corresponds to the electrical potential of the soma. If the potential is below the threshold, no response is generated and if the potential rises above the threshold (the magnitude of the potential is not important), the neuron responds. This is known as the firing of the neuron.

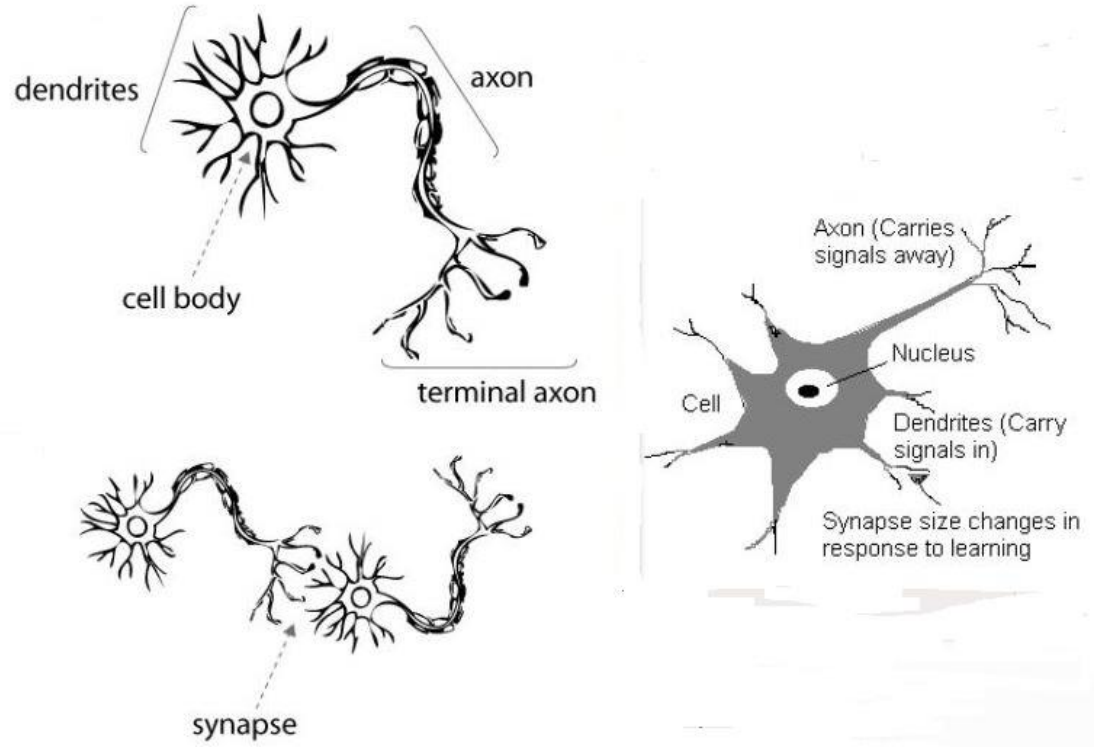

Figure 3.1. A typical biological neuron (Maltarollo, 2013; Galkin 1836).

The biological mechanisms of creative information-processing suggest the basic principles for artificial neural networks, although ANNs are not able to model all the complexity (Churchland and Sejnowski, 1993). To process the signals, the structure of an ANN consists of three main parts:

1) The input layer consists of the input nodes connected to the input variables.

2) Hidden layers (one or more) consist of the hidden nodes (units).

3) The output layer consisting of the output nodes that deliver the output variables.

A three-layer ANN (sometime called two-layer) including one input, hidden, and output layer is a widely-used structure for many applications (see Figure 3.2).

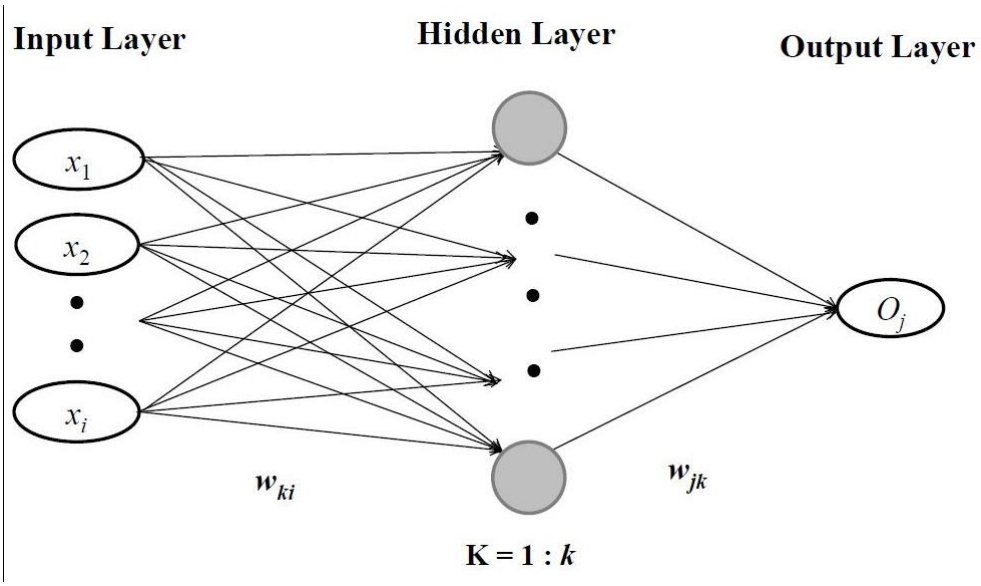

Figure 3.2. A model of a three-layer ANN. x_i and O_j refer to input and output variables, respectively. w_{ki} and w_{jk} are connected weights from input layer (i) to the hidden layer (k) and from hidden layer to the output layer (j), respectively. i, k, and j denote number of the nodes in the input, hidden, and output layers, respectively.

ANNs are constructed by a number of units (artificial neurons/nodes) in the layers that are connected by weights (synapses) in different forms (feedforward and recurrent neural networks). The weights determine an effective magnitude of contributed information between nodes. The weights in the feedforward network are connected in only one forward direction while the weights in the recurrent network are connected in a directed cycle (see Figure 3.3). The most widely used ANN is the feedforward neural network, FNN (Rumelhart et al., 1995; Maier and Dandy, 1998). FNNs are known as universal approximators (Kolmogorov, 1957; Sprecher, 1965; Lorentz, 1976; Hecht-

Nielsen, 1987; Hornik, 1989) and have been applied successfully in many hydrological applications such as rainfall modeling (Dawson and Wilby, 1998; Hsu et al., 1995) river flow modeling (Cheng et al., 2005; Joorabchi et al., 2007) flood forecasting (Chau et al., 2005), and water quality modeling (Muttil and Chau, 2006; May and Sivakumar, 2009).

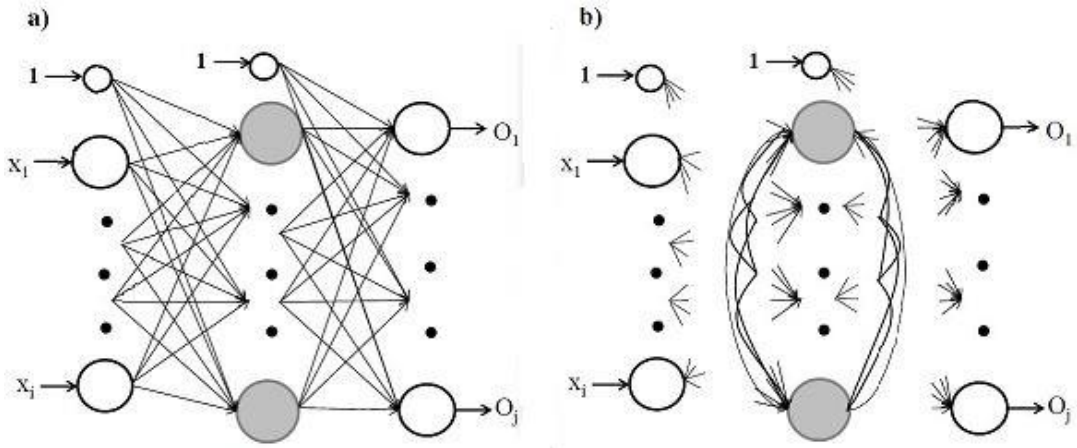

Figure 3.3. A two-layer: (a) feedforward network (FNN) and (b) recurrent network (RNN).

The non-biological concepts that are used to construct the computational structure of ANNs are the reason for the descriptor "artificial". A comparison between biological and artificial neurons is summarized in Table 3.1 (Schalkoff, 1997).

Table 3.1. Comparison of a biological and an artificial neuron (Schalkoff, 1997).

Biological	**Artificial**
Neuron cell	Unit
Synapse	Interconnection weight
Excitatory input	(Large) positive interconnection weight
Inhibitory input	(Large) negative interconnection weight
Activation by (spiking) frequency	Activation (transfer) function
Range of activation limited by cell physics	Range of activation limited by squashing function

ANNs are useful because:

- Neural systems are able to train, adapt, and self-organize information.
- The neural system can establish an implicit computational function and structure by training process.

3.3. Mathematical Fundamentals of Neural Networks

Artificial neural networks use an inherent feature of the biological neural systems: "the interconnection of a massively parallel array of processing elements (units) with variable parameters" (Schalkoff, 1997). Each unit shares a part of the computational effort to provide an overall result. ANN is characterized by the stimulus-response (S-R) process to learn the right response for each input through training. Since the internal computation of the ANN is not known or quantified, the network is called a black-box computational strategy. The strategy does not require detailed understanding of the internal network. The essence of a black-box method is establishing a relationship between input and output. A mathematical neural network typically involves a set of n-dimensional, nonlinear equations to characterize the network operation, structure, characteristics of the units or nodes (e.g. weight, number of the hidden nodes), training, and activation function. A simplified mathematical model of the ANN is a general functional representation between inputs (x) and outputs (y) as

$$y = f(x) \tag{3.1}$$

where $f(\cdot)$ denotes the functional mapping. Function $f(\cdot)$ in ANN is called a transfer function (activation function), which can be linear or nonlinear. Some common linear transfer functions are (see Figure 3.4):

- Hard-Limit (threshold, Bi-Level) Function as

Hard-Limit Function	$\begin{cases} f(x) = 1 & x > 0 \\ f(x) = 0 & x \leq 0 \end{cases}$
Symmetric Hard-Limit Function	$\begin{cases} f(x) = 1 & x > 0 \\ f(x) = 0 & x = 0 \\ f(x) = -1 & x < 0 \end{cases}$

- Piecewise Linear Function as

Piecewise Linear Function	$\begin{cases} f(x) = 1 & x \geq 1 \\ f(x) = x & 0 \leq x < 1 \\ f(x) = 0 & x < 0 \end{cases}$
Symmetric Piecewise Linear Function	$\begin{cases} f(x) = 1 & x > 1 \\ f(x) = x & -1 \leq x \leq 1 \\ f(x) = -1 & x < -1 \end{cases}$

- Pure Linear Function as $f(x) = x$.

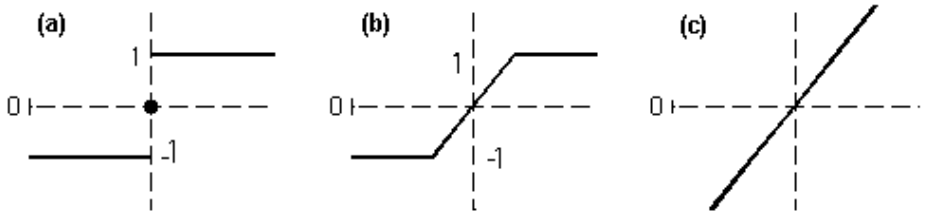

Figure 3.4. Common linear transfer functions. (a) Symmetric Hard-Limit Function, (b) Symmetric Piecewise Linear Function, and (c) Pure Linear Function.

The widely used nonlinear transfer functions are (see Figure 3.5):

- Radial Basis Function (RBF), which is based on the distance of the inputs from the origin (O). A typical kind of the RBF is in the Gaussian format as

$$f(x) = exp\left[-\frac{\|x-O\|^2}{2\sigma^2}\right] \tag{3.2}$$

The detailed descriptions and applications of the RBF can be found in the papers by Broomhead and Lowe (1988); Chng (1996); Heiss and Kampl (1996).

- Sigmoid Function with an "S" shape, generally includes

  - Log-Sigmoid (Logistic) Function $f(x) = \frac{1}{1+e^{-x}}$ (3.3)

  and

  - Tan-Sigmoid Function as $f(x) = \frac{2}{1+e^{-2x}} - 1$ (3.4)

  The sigmoid functions are monotonically increasing, continuous, differentiable, and bounded between 0 and 1 for the logistic function and between -1 and 1 for the hyperbolic tangent function.

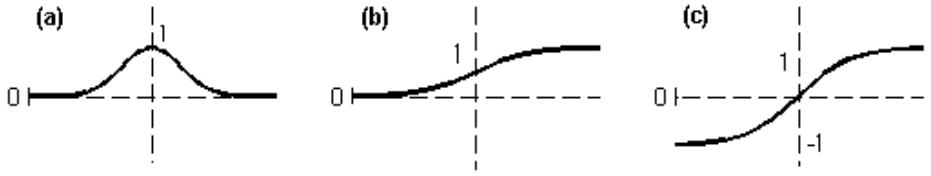

Figure 3.5. Common nonlinear transfer functions. (a) Radial Basis Function, (b) Log-Sigmoid Function, and (c) Tan-Sigmoid Function.

The transfer function converts the summation of the synaptic weights vector, $\underline{w}$, and inputs vector, $\underline{x}$, to a corresponding output vector as

$$y = f\left(\sum \underline{\boldsymbol{w}}.\underline{\boldsymbol{x}}\right) \quad (3.5)$$

The inputs are multiplied by synaptic weights and then fed to the first hidden layer. If the signal (stimulus) is above a threshold, the output is produced (the neuron fires). An activated function has usually a spiked shape in which the frequency is proportional to

the strength of the stimuli. The sigmoid-type functions are the most common activation functions (transfer function or threshold function) to transfer the summation of the weighted inputs into the next hidden layer (Funahashi, 1989; White, 1990; Hecht-Nielsen, 1990; Blum and Li, 1991; Takahashi, 1993; Hsu et al., 1995). The same process occurs in the other layers until the results of the last hidden layer reach the output layer.

The weights (parameters of the ANNs) are determined by minimizing the following quadratic error function (E) over the network weights iteratively in each iteration (epoch):

$$\boldsymbol{E} = \frac{1}{2}\left[Tar_j - O_j(\underline{\boldsymbol{w}}, \underline{\boldsymbol{x}})\right]^2 \tag{3.6}$$

where O_j is the output form the output layer, Tar_j is the corresponding target, and the other parameters have been defined previously (see Figure 3.2). The process that adjusts the weights of the network in response to the set of inputs and targets values is called training or learning phase. The training phase is a type of teaching process to correct or adjust the parameters of the system iteratively among the past steps to achieve a desired performance in the next iteration. Furthermore, after training, the internal structure of the network is able to self-organize to react properly to the unseen inputs. This feature is called generalization capability. There are two main learning procedures: supervised and unsupervised learning. The goal of the unsupervised learning, uses inputs (without the desired output), is to find a structure or pattern in the data. This learning algorithm organizes the data such that inputs with similar properties are in the same cluster. For instance, the unsupervised algorithm is used in the "Google news" to group a set of news articles into the subsets with the same story. The unsupervised learning can be used for pre-processing, clustering of the data, and reduction of the dimensionality of the input space. The Kohonen self-organizing (Kohonen, 1982, 1987, 1988) and the adaptive resonance theory (ART) (Carpenter and Grossberg, 1987a,b) are two examples of the unsupervised learning.

The objective of supervised learning, uses a set of input-output, is to learn the relationship between the inputs and the desired outputs. Supervised learning uses deterministic approaches such as the back propagation (Rumelhart et al., 1986), the Hebbian methods (Cline, 2003) or stochastic approaches such as genetic (Kitano, 1994) and simulated annealing (Kirkpatrick et al., 1989; Hinton and Sejnowski, 1986) methods. The most common supervised training algorithm is the back propagation generalized delta rule (BPGDR), which employs a gradient search strategy (Rumelhart et al., 1986; Rocha et al., 2005). The BPGDR has been applied as a weight optimizer in many ANN applications since 1990 because of its numerical efficiency (Hagan and Menhaj, 1994). The goal of the BPGDR is to minimize a cost function (error function) based on the difference between the modeled and desired outputs. The BPGDR includes the following steps:

a. Initialize the weights randomly.
b. Find a summation of the weighted inputs from the input layer to the first hidden layer for each unit, called net activation of unit k (net_k) as

$$net_k = \sum_i w_{ki} x_i \tag{3.7}$$

where i, k refer to the input nodes and hidden nodes, respectively (see Figure 3.2).

c. Activate the summation of the weighted inputs by transfer function f as

$$O_k = f_k(net_k) \tag{3.8}$$

where O_k is the output of unit k and the input to the next layer (here output layer).

d. Repeat steps b and c to get to the last layer (output layer).
e. Estimate the error function (Eq. 3.6).
f. Adjust the weights by minimizing the error function and propagating the error backward to the network (starting from the output layer).

In the BPGDR algorithm, a gradient descent optimization technique, the parameters (weights) are adjusted by moving in the direction of the gradient of the error function (Eq. 3.6) relative to the weight vector. The algorithm imposes the following equivalence for the network with three layers (see Figure 3.2):

$$\nabla E\left(\underline{w}\right) = \left(\frac{\partial E}{\partial w_{11}}, \dots, \frac{\partial E}{\partial w_{k1}}, \dots, \frac{\partial E}{\partial w_{ki}}, \dots, \frac{\partial E}{\partial w_{jk}}\right) = 0 \tag{3.9}$$

where ∇ is the gradient or differential operator. i, k, and j refer to the nodes in the input, hidden, and the output layers, respectively. As we can see, the error space is n-dimensions (n = number of the weights). At each iteration, the weights are updated and the total adjusted weights define the new direction of moving on the error space for the next iteration. The moving on the error space (adjustments of the weights) continues till the error function converges to the minimum value. This complex and high dimensional problem is computationally expensive. To overcome this issue, the scaling parameter (between zero and one) called learning rate η is used to determine a magnitude of learning (change of the error relative to the weight change) in each iteration. The BPGDR algorithm can be formulated as follows:

I. For the weights that are connected to the output nodes (output weights):

$$\Delta w_{jk} = \eta \frac{\partial E}{\partial w_{jk}} = \eta \frac{\partial E}{\partial net_j} \cdot \frac{\partial net_j}{\partial w_{jk}} = \eta \frac{\partial E}{\partial O_j} \cdot \frac{\partial O_j}{\partial net_j} \cdot \frac{\partial net_j}{\partial w_{jk}} \tag{3.10}$$

where $\delta_j = \frac{\partial E}{\partial net_j}$ is the sensitivity of the error on the net activation of unit j. On the right side of Eq. 3.10, the first part can be computed as

$$\frac{\partial E}{\partial O_j} = \frac{\partial\left[\frac{1}{2}(Tar_j - O_j)^2\right]}{\partial O_j} = -\left(Tar_j - O_j\right) \tag{3.11}$$

the second part as

$$\frac{\partial O_j}{\partial net_j} = \frac{\partial f_j(net_j)}{\partial net_j} = f_j'(net_j) \tag{3.12}$$

and the last part as

$$\frac{\partial net_j}{\partial w_{jk}} = \frac{\partial(\sum_k w_{jk} O_k)}{\partial w_{jk}} = O_k \tag{3.13}$$

where O_k is the output from unit k in the hidden layer.

So to correct the output weights, Eq. 3.10 leads to

$$\Delta w_{jk} = \eta \left(Tar_j - O_j\right) f_j'(net_j)\, O_k \tag{3.14}$$

II. For the weights that are connected to the hidden nodes (hidden weights):

$$\Delta w_{ki} = \eta \frac{\partial E}{\partial w_{ki}} = \eta \frac{\partial E}{\partial net_k} . \frac{\partial net_k}{\partial w_{ki}} = \eta \frac{\partial E}{\partial O_k} . \frac{\partial O_k}{\partial net_k} . \frac{\partial net_k}{\partial w_{ki}} \tag{3.15}$$

where $\delta_k = \frac{\partial E}{\partial net_k}$. The outputs of hidden nodes are used as the inputs to the output layer so the hidden weights have indirect effect on the error function. As a result, the first part of Eq. 3.15 on the right side, can be computed as

$$\frac{\partial E}{\partial O_k} = \frac{\partial E}{\partial net_j} . \frac{\partial net_j}{\partial O_k} = \delta_j w_{jk} \tag{3.16}$$

and the second part of Eq. 3.15 can be expressed as

$$\frac{\partial O_k}{\partial net_k} = \frac{\partial f(net_k)}{\partial net_k} = f_k'(net_k) \tag{3.17}$$

and the last part is the input from unit i in the input layer as

$$\frac{\partial net_k}{\partial w_{ki}} = \frac{\partial(\sum_i w_{ki} x_i)}{\partial w_{ki}} = x_i \tag{3.18}$$

So to correct the hidden weights, Eq. 3.15 leads to

$$\Delta w_{ki} = \eta\, \delta_j w_{jk}\, f_k'(net_k)\, x_i \tag{3.19}$$

The process of updating the random weights starts from the output layer (see Eq. 3.14) and then moves backward to update the hidden weights (see Eq. 3.19). The backpropagation adjustment of the weights stops when the minimum error function is achieved.

Design of the ANN model is a complicated and iterative task. A proper performance of the ANN demands a suitable structure (e.g., number of the nodes and the way that they are connected), suitable learning algorithm (e.g., transfer function, training function, learning rate), and a proper set of weights. The size of the model affects the generalization ability of the network. A very small network is not trained well and a very large one attempts to model the noise. In a large network, the number of degrees of freedom (unknown parameters) far exceeds the number of the training samples so overtraining (over-fitting) occurs, which means that the network models the training samples well (memorization ability) but the performance of the model during the validation is poor. However the availability of large training samples and the training algorithm does not guarantee a solution to any ANN application, the quality of the training data and algorithm has a significant impact on the results.

3.4. Hydrologic Applications of ANNs

Artificial neural networks (ANNs) have been widely used in the hydrology and modelling of water resource systems (see, ASCE Task Committee on Application of the Artificial Neural Networks in Hydrology, 2000). Maier et al. (2010) reviewed 210 journal papers from 1999-2007 that developed ANN models for the purpose of flow prediction (quantity and quality) in the river system. The focus of the majority of the papers was on the water quantity variable (e.g., discharge, water level) and a few studies focused on the water quality variable (e.g., salinity, sediment). Most ANNs used feedforward network and the gradient-based method for the architecture and training algorithm of the model, respectively. Maier et al. (2010) argued that although many studies described the use of ANNs, only a few of them focused on the optimal structure of the ANN model. Their statements agree with the results obtained by Maier and Dandy (2000) who reviewed 43 papers, focused on the use of the ANN for the prediction of water resources variables

such as rainfall, discharge, runoff coefficient, water level, salinity, PH, and algal/cyanobacteria concentration. They explained different approaches that were used to find the unknowns in the network such as the structure of the ANN, the choice of the performance criteria, the inputs, hidden nodes and their topology, training algorithm, and transfer functions. They argued that a useful comparison between different approaches is not possible because the details of the ANN modelling are not well described.

Hsu et al. (1996) compared three different formulations including autoregressive moving average with exogenous inputs, ARMAX, a conceptual rainfall-runoff model (Sacramento soil moisture accounting model, SAC-SMA), and a nonlinear model (three-layer feedforward ANN) to model rainfall-runoff at the Leaf River basin near Collins, Mississippi. They used 35 different combinations of the inputs in the ANN and the ARMAX model. Nodes were added to the hidden layer until the desired performance of the network was achieved. The sigmoid function was chosen as a transfer function. They used two training algorithms, simplex nonlinear optimization (Nelder and Mead, 1965) and linear least square (Scalero and Tepedelenlioglu, 1992) to train the hidden and output layers, respectively. They concluded that the ANN model outperforms the other models. They also argued that the ANN model may not be considered as a substitute for the conceptual model because the ANN is not able to represent the physical internal structure of the problem.

Hsu et al. (1999) estimated rainfall from remotely sensed data using an ANN model over the Japanese Islands. They used visible (VIS) and infrared (IR) imagery from the Geostationary Meteorological Satellite (GMS) at 0.25° by 0.25° resolution (Arkin and Xie, 1994). The inputs to the model were VIS and IR brightness temperatures at each individual pixel, mean and standard deviation around the pixel of the 3 by 3 and 5 by 5 VIS and IR brightness temperatures of the surrounding pixels. They used a modified counterpropagation neural network (MCPN) as the architecture of the model. The counterpropagation neural network (CPN) consists of two parts; part one is to categorize

the inputs and provide the clusters in the hidden layer and part two is to establish a function between the clusters and the outputs (Hecht-Nielsonn, 1990). The first part uses an unsupervised clustering technique called the self-organizing feature map (SOFM) (Kohonen, 1982) and the second part uses a supervised linear mapping called a Grossberg Linear Network (GLN) (Grossberg, 1969) as the training algorithms. The SOFM classifies inputs into the groups, which are connected to the nodes in the hidden layer. The GLN trained the network to construct a linear relationship between determined clusters and outputs. The inputs in the same cluster produce one output so the accuracy of the function directly depends on the number of hidden nodes, which are identical to the number of the clusters. One alternative to increase the accuracy of the function without increasing the number of hidden nodes is using the MCPN. The MCPN incorporates all inputs in the clusters to estimate different outputs. Hsu et al. (1999) concluded that the MCPN can provide a reasonable spatial and temporal pattern of the rainfall over a small region, where the model was trained. They also showed that the parameters of the model need to be adjusted and updated when the model is used over different regions with different physical regimes. Hsu et al. (1996, 1999) used the MCPN model to develop the PERSIANN algorithm (Precipitation Estimation from Remotely Sensed Information using Artificial Neural Network) to estimate precipitation. Inputs to the model are infrared and microwave images of the satellite, radar, ground-based, and rain gages data.

Liong et al. (2000) used an ANN model to forecast water level of the Dhaka river, Bangladesh. They used water levels at eight upstream stations as inputs to the model, 30 nodes as hidden nodes, sigmoid function as the transfer function, and back propagation as the training method. The sensitivity analysis on the inputs showed that using all upstream stations added redundant and dependent information. Thus, they eliminated three out of eight chosen inputs, which resulted in an efficient model (lower cost in time and memory usage).

Kuok et al. (2010) used a three-layer feedforward neural network to model rainfall-runoff in the Sungai Bedup Basin, Sarawak, Malaysia. Taormina et al. (2012) used three-layer feedforward neural network to simulate hourly groundwater level in the Lagoon of Venice, Italy. The 0, 1, 2, and 3 lags of rainfall and evapotranspiration and 1, 2, 3, 4 lags of water level were used as inputs with four hidden nodes to estimate current water level. The activation and training functions were hyperbolic tangent and the back propagation algorithm, respectively. The results suggested that the proposed model can be used as an alternative to physical modeling in simulating the groundwater level and fill-in missing water level data. They used lags of precipitation and runoff as inputs to the model to estimate current runoff. The optimal configuration of the model consisted of 0, 1, 2, and 3 lags of precipitation and 1, 2, and 3 lags of runoff (inputs to the model) and 100 nodes in the hidden layer (hidden nodes). The particle swarm optimization PSO (Clerc, M., and J. Kennedy, 2002), an iterative search-space method, was used to train the network. They concluded that the PSO-based training algorithm performed well in modeling rainfall-runoff processes.

Wu and Chau (2006) used a genetic algorithm-based artificial neural network (ANN-GA) to predict the flood at the Yangtze River, China. The GA determined the optimal parameters of the model. The inputs to the model were water levels at the upstream station (Luo-Shan station) and the output was the downstream water level at Han-Kou station. The three hidden nodes were chosen though a trial and error procedure. They concluded that although the ANN-GA model added more parameters and computational time, it provided good accuracy in performance without an over-fitting problem.

Muttil and Chau (2006) used a three-layer feedforward neural network and genetic programing (GP) to model algal blooms in Tolo Harbor, Hong Kong. The objective of the model was to predict one-week lead time of chlorophyll-a using significant inputs. In the first step, they chose inputs based on a priori knowledge of the

system. They tried nine input variables, recognized as the dominant factors on the algal dynamics, including: chlorophyll-a (Chl-a), total inorganic nitrogen (TIN), phosphorus (PO_4), dissolved oxygen (DO), secchi-disc depth (SD), water temperature (Temp), daily rainfall (Rain), daily solar radiation (SR), and daily average wind speed (WS) with a time lag of 7-13 days. The trial and error procedure determined 6 hidden nodes as the best number of the nodes in the hidden layer. The GP identified the most efficient input variables. The results showed that although Chl-a, PO_4, DO, TIN, and SD were the most proper inputs from nine initially selected inputs, the models can predict the long-term trends of algal biomass well by using Chl-a as the only input.

The past studies indicate that ANN modeling is able to construct valid relationships between inputs and outputs by choosing a proper set of inputs and structure. The structure of the ANN cannot explain the underlying physics of the problem as well as physical models. As a result, ANN modeling is a viable alternative for problems with a complex and unknown input-output relationship. In the following chapters we assess the potential of the ANN to reduce the biases of the climate variables including temperature and precipitation.

CHAPTER 4

BIAS CORRECTION OF CLIMATE VARIABLES USING AN ARTIFICIAL NEURAL NETWORK

4.1. Introduction

It is well understood that there is no perfect mathematical model that can completely represent and resolve underlying physical processes of land-atmosphere-ocean interactions. Complexity of the governing equations, simplified parameterizations, and calibration uncertainties in the GCMs typically cause imperfect outputs, which contain errors. The biased climate outputs influence analysis studies and impact assessments. Since the GCM's outputs are used to drive other models such as hydrologic and ecosystem models, the biased forcing can add uncertainty to the results. Thus, the biases of the outputs need to be corrected. The basic idea for bias correction is to find a sufficiently flexible and adaptive approach that is able to learn from available information to develop a predictive function, which performs well for the projection period. We use an Artificial Neural Network (ANN) approach to learn the error structure from the historical outputs and corresponding observations. Then the trained network can be used to reproduce bias-corrected predictions. As we explained in Chapter 3, ANN can be described as a set of stimuli-response (S-R) (Schalkoff, 1997). The overall characteristics of the network can be represented as,

$$r_i = f(\underline{s_i}, \underline{w}, a_c) \tag{4.1}$$

where r_i is a response (output), $\underline{s_i}$ is a stimuli (input), $\underline{w}$ denotes the interconnection weights between the nodes, and a_c is a combination of unknown characteristics of the network including structure of the network, number of the hidden layers and nodes,

transfer function, training algorithm, and learning rate. In this study, the response is the bias-corrected climate variables (temperature and precipitation), and the stimuli includes a set of proper meteorological variables, which needs to be determined. In the subsequent sections, we describe the overall experimental set-up of the employed ANN to determine a_c for the two climate variables of interest, temperature and precipitation.

4.2. Experimental Setup of the ANN

The performance of an ANN depends on two major factors: (1) quality of the training dataset, and (2) architecture of the employed ANN. Quality and dependency of the predictors (inputs) to the response variables (outputs) are essential elements of an effective ANN. The architecture of ANNs is also a determining factor on their performance. A smaller network with few neurons and hidden layers severely restricts the network learning ability while a larger network with too many neurons and hidden layers typically leads to over-fitting and poor generalization of the network. Determination of the characteristics of the network follows.

4.2.1. Determination of the Training Set

An ANN constructs a mathematical mapping function between input-output using a training set including input and target values (observations). Note that a proper training set enables the network to identify an existing function that maps inputs to the desired outputs. Irrelevant and redundant inputs cause an erroneous, ineffective, and large network without notable predictive capacity (Lachtermacher and Fuller, 1994; Taormina et al., 2012). The choice of a suitable set of the input-output depends on a-priori knowledge of an existing relationship between them. The following section describes the training set used for temperature and precipitation.

4.2.1.1. Temperature

The primary goal of the network is to reduce the biases of the surface air temperature (T). Thus, a bias-corrected time series of T is set as the output of the ANN model. The input vectors include the raw temperature and physically relevant climate variables (predictors) that have impact on the error of temperature. We examined different combinations of the CCSM outputs as the inputs (predictors) to the ANN model, including: (1) air temperature T, (2) skin temperature TS, (3) specific humidity Q, (4) downward longwave radiation LW_d, (5) downward shortwave radiation SW_d, (6) net radiation R_n, (7) net longwave radiation LW_n, (8) net shortwave radiation SW_n, (9) surface pressure PS, (10) precipitation P, and (11) horizontal winds u, v. The network is trained in response to the target (observation), which is the MFD, bias-corrected reanalysis NCEP surface air temperature (see Subsection 1.3). Dependent and unnecessary inputs influence the performance of the network, in particular for the validation period, and generally negatively impact the generalization capability of the model. Unnecessary inputs also increase the complexity, uncertainty of the model, computational time, and memory usage (Maier et al., 2010). We used a stepwise approach to determine the best set of the inputs. In this approach, the network starts with the minimum number of the inputs (one) and the model is trained. In each step, one variable is added to the input vector and the model is re-trained. The process of adding variables continues until the desired performance of the network is achieved or the performance of the network stops improving (Masters, 1993; Maier and Dandy, 1998). Although an evaluation of all possible combination of the inputs is not feasible, we examined a large set of different combinations of the aforementioned predictors as inputs to the ANN model. We selected the minimum number necessary inputs, which are expected to have impact on the target variable (T). In the first step, we started with only one input (T or TS or Q or LW_n or SW_n or R_n or P or PS) and trained the network separately. The best performance among the one variable input was obtained using T as

the input. In the next step $TS, Q, R_n, LW_n, SW_n, PS, P, u, v$ were added to the input vector (T) one at a time and the same process was repeated. The best performance was obtained by adding TS and Q to the existing input T. In the next step we trained the network by adding $R_n, LW_n, SW_n, PS, P, u, v$ to the existing inputs (T, TS, Q). The performance of the model did not improve by adding $PS, P, u,$ or u. Among different components of radiation ($LW_d, SW_d, R_n, LW_n, SW_n$) adding net longwave and shortwave radiation to the inputs (T, TS, Q) improves the performance of the network. Adding a new variable to the selected set of inputs (T, TS, Q, LW_n, SW_n) did not influence the performance of the network. As a result, variables T, TS, Q, LW_n, SW_n are selected as the proper set of inputs to the network for the bias correction of temperature through the rest of the study and the results are presented accordingly.

4.2.1.2. Precipitation

Here the objective of the network is to provide bias-corrected precipitation so a bias-corrected time series of P is selected as the output of the network. We use the CRU precipitation (see section 1.3) as the target to train the network. To find an appropriate set of inputs that has impact on the precipitation error, we again used the stepwise approach. Adding variables (e.g., $T, TS, Q, LW_n, SW_n, R_n, PS, u, v$) to the raw precipitation (original model precipitation) did not improve the performance of the network. The best performance of the network is achieved when precipitation is selected as a predictor for itself. This is consistent with the results obtained by Hidalgo et al., (2008). Since we found that the best predictor of precipitation is itself, we examined the effect of adding time-lagged precipitation to the input. The performance of the network improves when zero, one, two, and three lags of precipitation ($P, P_{t-1}, P_{t-2}, P_{t-3}$) are used as inputs. The improvement of the network stops after a lag time larger than three. Since the variability of precipitation can be large over time and space, we also checked the performance of the

network when information from surrounding pixels is added to the existing inputs. To do that, the mean and standard deviation of precipitation from the surrounding pixels (n = 3, 5, or 7) are added to the input set as

$$\mu^{nbyn} = \frac{1}{N} \sum_{i=1}^{N} P_i \tag{4.2}$$

and

$$\sigma^{nbyn} = \sqrt{\frac{1}{N} \sum_{i=1}^{N} (P_i - \mu^{nbyn})^2} \tag{4.3}$$

where N is the total number of the surrounding pixels. The network showed the best improvement when the standard deviation of precipitation from 3 by 3 neighbors around the pixel of interest (σ^{3by3}) is added to the inputs. As a result, we use ($P_t, P_{t-1}, P_{t-2}, P_{t-3}, \sigma_t^{3by3}$) as the best set of inputs to the network to correct the biases of precipitation throughout this study.

4.2.2. Determination of the ANN's Architecture

The architecture of the network includes geometry, the number of the hidden layers, nodes, and also the way that they are connected. In general, the network should have sufficient hidden nodes to accurately approximate the desired mapping function, nevertheless an excessively large number of nodes results in overtraining (over-fitting) and lack of generalization ability of the network. Currently there is no well-established methodology for optimal design of the ANN architecture. Optimal structure of the network is mainly determined using prior information about the problem at hand and trial and error procedures. Since the performance of the model varies with different architectures of the ANN, a selection of an appropriate structure of the model is essential.

As we explained in Chapter 3, there are two main kinds of neural networks, FNN (Feedforward Neural Network) and RNN (Recurrent Neural Network). We found the

FNN as a proper network for our application. The FNN is the most common network in many water resources applications because

- The FNN outperforms the RNN in many practical problems (Khotanzad et al., 1997) and in particular for the forecasting of climate variables (Maier and Dandy, 2000).
- The FNN is more efficient than the RNN in processing time (Masters, 1993; Hochreiter and Schmidhuber, 1997).

Hornik et al. (1989) concluded that FNNs with one hidden layer and enough nodes (degrees of freedom) are able to approximate any function. Adding hidden layers significantly increase the uncertainty, parameters of the model, computational time, and memory usage. Thus, we use a feedforward ANN (FNN) with one hidden layer to correct the biases of T and P in this study.

Once the network is selected, we need to determine an optimal number of hidden nodes, which is one of the big challenges in neural network studies (Maren et al., 1990; Rojas, 1996). The optimal number of hidden nodes is the minimum number of nodes that can represent the underlying function between the input and the output. More hidden nodes result in more complicated mapping function, which can affect the generalization ability of the network. The optimal number of hidden nodes is generally determined by the following algorithms (Bebis and Georgiopoulos, 1994):

- The pruning algorithm: In the pruning algorithm, a large enough network is selected in the first step to insure that the network constructs a mapping function between the input and the output. Then in the next steps redundant nodes are removed until the desired performance is achieved. The initial size of the network is suggested by Hecht-Nielsen (1987), Huang and Huang (1991). For more

comprehensive descriptions of the pruning algorithm, the reader is referred to Reed (1993) and Castellano et al. (1997).

- The constructive algorithm: The constructive algorithm moves in the opposite direction to the pruning algorithm. The algorithm starts with the smallest network (e.g. one hidden node) and then the hidden nodes are added one at a time until the performance of the network stops improving. For more comprehensive descriptions of the constructive algorithm, the reader is referred to Chen et al. (1997), Kwok and Yeung (1997).

Since the pruning algorithm has more uncertainties and unknown parameters, it has more difficulties finding an optimal network than the constructive algorithm (Bebis and Georgiopoulos, 1994). Furthermore, the pruning algorithm is computationally expensive. Here, the optimal number of hidden nodes is determined by the constructive algorithm presented in a number of studies (Hirose et al., 1991; Setiono and Hui, 1995; Fahlman and Lebiere, 1990, among many others). The constructive algorithm is based on a search approach. We start with a pre-specified minimum number of hidden nodes and sequentially add one node at a time and re-train the network. At each step with a fix number of nodes, the algorithm controls the performance of the network and finally chooses the number of nodes based on the chosen error criteria. It is worthwhile to mention that, in general, networks with concise structure provide better generalization and processing speed and also they require less storage than complicated networks (Castellano et al., 1997; Bebis and Georgiopoulos, 1994). Details to identify a proper number of hidden nodes for each climate variable (T and P) are described in section 4.3.

4.2.3. Determination of the Training Algorithm

Once the network is established, a set of weighted inputs is required to transfer between the layers through a training algorithm to deliver a valid output. A training algorithm, including the transfer and training function, processes the inputs in the network and adjusts the weights continually, based on a cost function (see Eq. 3.6).

4.2.3.1. Transfer Function

As we explained in Chapter 3, a transfer function (activation function) is the analog of the potential to activate a neuron, which represents a frequency relationship between the input and the output. Hornik (1991) showed that "the mapping power of the ANN is not inherent in the choice of a specific activation function; rather it is the multilayer feedforward structure that leads to the general function approximation capability." Nevertheless, some transfer functions can be more appropriate for certain types of applications. The sigmoidal functions are the most common transfer functions in the water resource applications due to their computational efficiency. In the process of optimization, the convergence to the optimal solution is faster in the network with the sigmoidal functions due to the smoothness of the error surface (Rumelhart, 1995; Durbin and Rumelhart, 1989). The main consideration to choose a transfer function is that the function should meet requirements for the training algorithm. For instance, in the BPGDR training algorithm, the transfer functions need to be differentiable (see section 3.3). Sigmoidal-type (logistic and hyperbolic tangent functions) and linear functions are among commonly used transfer functions in the FNNs that satisfy this requirement.

Although, in general, the performance of the network using a logistic transfer function is similar to the ones using a hyperbolic tangent function, using the hyperbolic tangent as a transfer function increases learning speed and generalization ability of the network (Maier and Dandy, 1998). This is consistent with the results obtained by Kalman

and Kwasny (1992). Therefore, one hidden layer FNN with hyperbolic tangent-linear transfer functions for hidden-output layers is used to construct a model to reproduce bias-corrected temperature and precipitation.

4.2.3.2. Training Function

The mapping ability of the FNN is related to the sequence of the transformations that transfer the input space (input layer) to the functional space (hidden layers), and then to the last layer (output layer). A transformation of the effective weighted information between the nodes in the input, hidden, and output layers is essential to achieve a desired input-output relationship. To find a best set of weights (parameters of the network) we train the network with the target (observation) by minimizing the objective function (see Eq. 3.6). Then the network can learn the relationship between the input and the output. The process of learning or training is analog to parameter estimation. Since we want to establish a function between the inputs and the desired outputs, supervised learning is used. In this study the BPGDR, as a supervised learning method, is used for optimizing the FNN for both temperature and precipitation variables (for detailed descriptions of the BPGDR method, the reader is referred to Section 3.3). The BPGDR method is known as the most common algorithm for the training of the FNN (Maier and Dandy, 2000). Since the BPGDR algorithm operates based on the gradient of the transfer function, the function needs to be continuous and differentiable. The sigmoid-type functions used in this study meet the requirement of the algorithm. A well trained network is able to produce reasonable outputs using a set of independent inputs, which are not used during the training process. To improve this generalization ability of the network, the technique called early stopping (cross validation) is used (Stone, 1974; Hecht-Nielsen, 1990; Hassoun, 1995; Amari et al., 1997). In this technique the network is trained by the training dataset and the trend of the error is monitored over an independent dataset

(validation set) during the training. In the beginning of the process, the error reduces in both training and validation datasets. The training terminates when the error in the validation set starts to rise. This early stopping avoids memorization in the network and it enhances the generalization capability.

4.3. Evaluation of the Network to Reduce the Biases of the Variables

Having defined the ANN, including training set, architecture, and the training algorithm, we evaluate the capability of the constructed ANN to reduce the biases of the CCSM temperature and precipitation in the subsequent subsections. The performance of the CCSM to simulate climate variables differs for different months/seasons and location. In other words, systematic errors in environmental models are often space-time dependent quantities with seasonal and geographical variations (Moghim et al., 2015). As a result, it is advantageous to correct the biases of the model for each month or season individually.

4.3.1. Temperature

Previous efforts at bias correction of climate model outputs have been mostly concentrated on monthly temporal scales (Wood et al., 2004; Li et al., 2010; Zhang and Georgakakos, 2012). We intend to develop an effective methodology to reduce biases in the modeled temperature on a much finer temporal resolution (6-hour). To train and test the network, the 6-hourly historical CCSM data (ANN input) and MFD temperature (ANN target) from 1970 to 2008 are divided into two periods:

I) 1970-1988 as a training dataset to adjust the ANN synoptic weights (calibration).

II) 1989-2008 as a testing dataset to study the performance of the trained network (validation).

In Section 4.2, we determined an appropriate set of input, geometry, training algorithm, and number of the hidden layer for the network. Figure 4.1 shows a schematic diagram of the proposed ANN for bias correction of temperature.

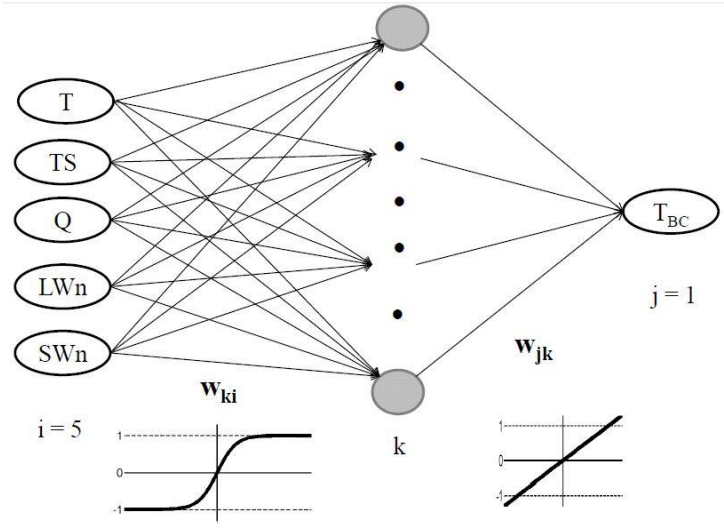

Figure 4.1. The proposed feedforward network (FNN). The inputs of the network are: surface air temperature (T), skin temperature (TS), specific humidity (Q), net longwave radiation (LWn), and net short wave radiation (SWn); while the output is the bias-corrected surface air temperature (T_{BC}). Here, w_{ki} and w_{jk} denote the weights connecting the input layer (i) to the hidden layer (k) to the output layer (j), respectively.

The number of hidden nodes and the learning rate are two parameters that still need to be determined. Since the ANN is a nonlinear regression model with many unknown parameters, a trial and error procedure is a viable alternative to find unknown parameters. The detailed descriptions of the process are explained for an arbitrary geographical location P (latitude: 14.71°S, longitude: 45°W) in the study domain (red circle in Figure 4.2) and for the month of March. We study the role of the chosen number of the hidden nodes and the learning rate on the performance of the proposed ANN for this location.

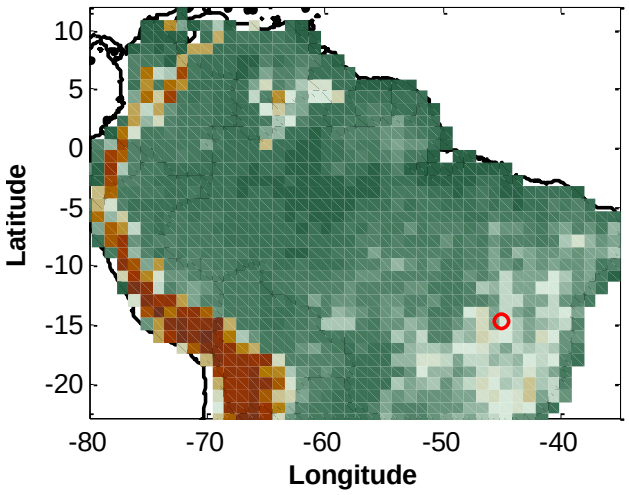

Figure 4.2. The study domain extending from 80°W to 35°W (longitude) and from 23°S to 12°N (latitude). The red circle illustrates the geographical location P.

As explained previously, to find the optimal number of hidden nodes, we use the constructive algorithm (Kwok and Yeung, 1997b) and we choose 0.01 as a first guess for the learning rate (η). It is worth noting that a similar learning rate is often reported in ANN applications in water resources studies (e.g., Tamura and Tateishi, 1997; Kuligowski and Barros, 1998a, b). In the first step, we start with 5 hidden nodes and then given the prescribed characteristics of the network (α_c in Eq. 4.1) we use the training dataset to train the network for the calibration period to find a set of weights that satisfy a desired response relative to the target. In the next steps we add hidden nodes one at a time and each time we re-train the network. The number of the hidden nodes varies from 5 to 35. To evaluate the performance of the network with different hidden nodes, we calculate the mean squared error and correlation between the estimated ANN outputs and corresponding observations for both calibration and validation as:

- Mean squared error (MSE): Expected value of the squared error between targets (Tar) and estimated outputs (O) as

$$MSE = E[(Tar - O)^2] \tag{4.4}$$

where $E(\cdot)$ denotes the expectation operator.

- Pearson correlation coefficient (ρ): Linear correlation between Tar and O as

$$\rho = \frac{E[(Tar - E[Tar])(O - E[O])]}{\sqrt{E[(Tar - E[Tar])^2]\, E[(O - E[O])^2]}} \quad (4.5)$$

Figure 4.3 compares the performance of the ANN with different hidden nodes.

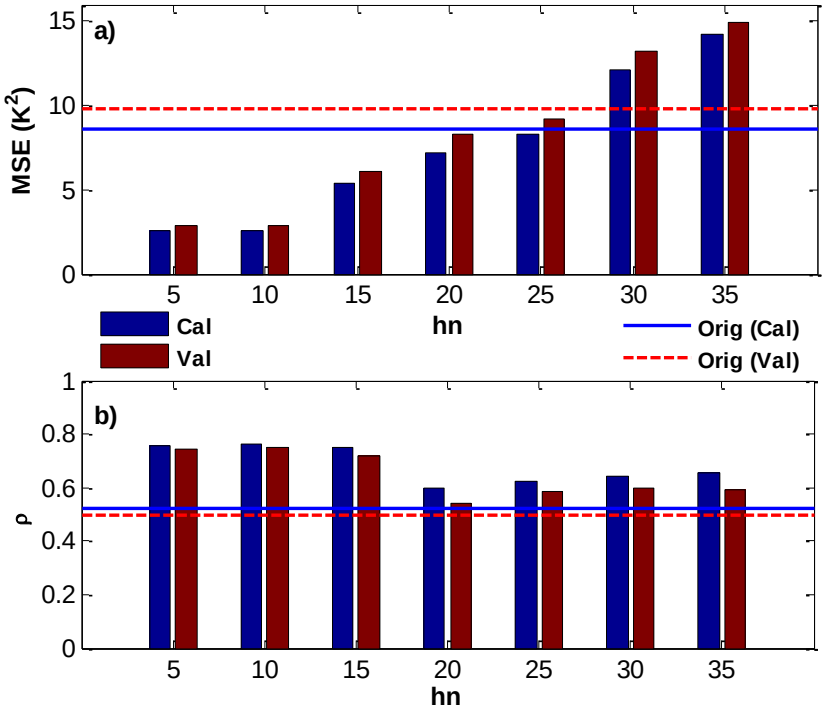

Figure 4.3. Performance of the ANN for different number of the hidden nodes, hn. (a) The mean squared error, MSE and (b) correlation of the ANN outputs with the targets, ρ. The blue bars show the statistics for the calibration (March 1970-1988) and red bars denote the results for the validation (March 1989-2008) at location P. The blue solid and red dashed lines denote the statistics between the input (original temperature) and target values for the calibration (Cal) and validation (Val), respectively.

The horizontal lines in Figure 4.3 correspond to the MSE and correlation between original input temperature (CCSM) and target values (solid lines for the calibration and dashed lines for the validation). Clearly, the bars below the lines in Figure 4.3a and above the lines in Figure 4.3b show the ranges of the hidden nodes that improve the results in the MSE and correlation sense, respectively. As we can see, although the network with 5

to 25 hidden nodes can reduce MSE, 5 and 10 hidden nodes result in a lowest MSE. When the number of hidden nodes exceeds 25, the MSE is not improved by the network (see Figure 4.3a). For the selected number of hidden nodes, the network can improve the correlation as all of the bars are above the reference lines. The highest correlation is obtained using 5, 10, and 15 hidden nodes (see Figure 4.3b). The above results indicate that ANNs with 5 and 10 hidden nodes perform well both in terms of the MSE and correlation. Although the trained network with a few number of hidden nodes (e.g., $hn = 5$) can improve the MSE and correlation structure of the temperature (see Figure 4.3), it is observed that the outputs may be an overly smooth representation of the underlying process with reduced variability. To assure that the ANN outputs preserve sufficient variability of the temperature time series and the results are not overly smooth, we use signal-to-noise ratio (SNR) metric as

$$SNR = \frac{\sigma_T}{|\sigma_T - \sigma_O|} \tag{4.6}$$

where σ_O and σ_T are standard deviations of the ANN outputs and targets, respectively. Clearly, higher values of the presented SNR metric denote that the target standard deviation is better preserved by the network outputs. It is seen that increasing the number of hidden nodes increases the standard deviation of the network outputs. The results of the obtained SNR for different number of hidden nodes are shown in Figure 4.4, which implies that hn =10 yields the best SNR.

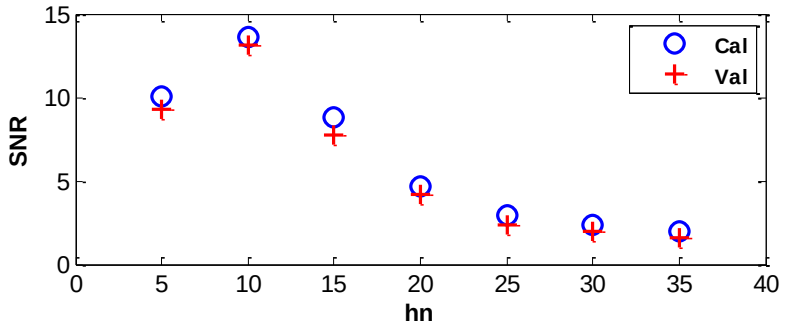

Figure 4.4. Signal-to-noise ratio (SNR) for different hidden nodes, hn. The blue circles denote the calibration period (March 1970-1988) and the red crosses denote the validation period (March 1989-2008) at location P.

A close scrutiny of Figure 4.3 reveals that the ANN with 5 and 10 hidden nodes leads to low MSE and good correlation. We also see in this figure that the correlation is not very sensitive to the number of hidden nodes. Figure 4.4 leads to the conclusion that the ANN with 10 hidden nodes can preserve well the standard deviation of the target compared to other selected number of hidden nodes. Thus, we select $hn = 10$ for which the MSE is sufficiently small, while correlation and signal-to-noise ratio are near their maximum positions.

As previously mentioned, in all of the above calculations we set the learning rate $\eta = 0.01$. This parameter determines the step size in the steepest descent optimization algorithm for obtaining the optimal weights of the network. A small learning rate slows down the training process and a large learning rate may cause the network to oscillate around the optimal solution. Figure 4.5 compares the mean squared error and correlation of the ANN outputs with different learning rates for $hn = 10$.

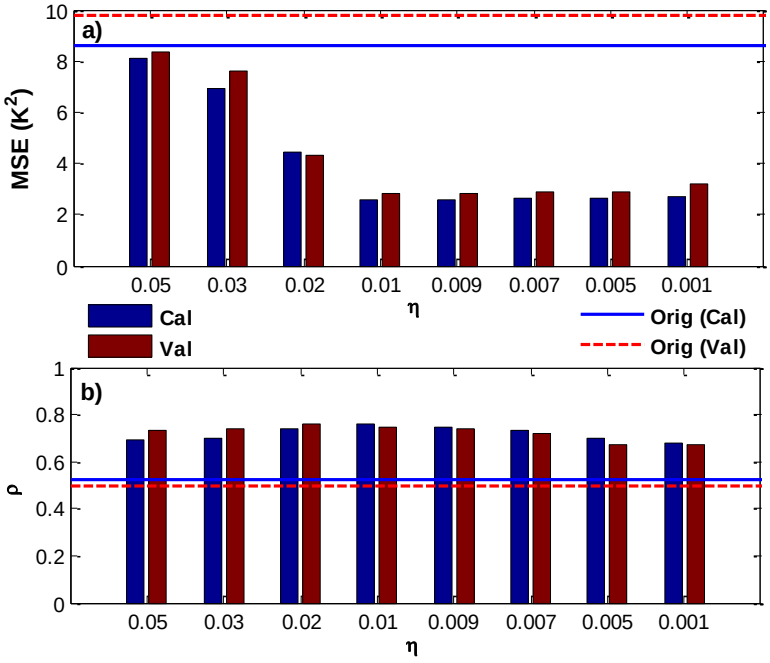

Figure 4.5. Same as Fig. 4.3 but for different learning rates, η.

As we can see, the network with different ranges of learning rate (in particular smaller than 0.01) can improve the results in terms of both MSE (bars are below the reference lines in Fig. 4.5a) and correlation metrics (bars are above the reference lines in Fig. 4.5b). This can indicate that the learning rate $\eta = 0.01$ would be a reasonable choice in our study.

The performance of the proposed ANN with $hn = 10$ and $\eta = 0.01$ is illustrated through scatter plots in Figure 4.6 at location P.

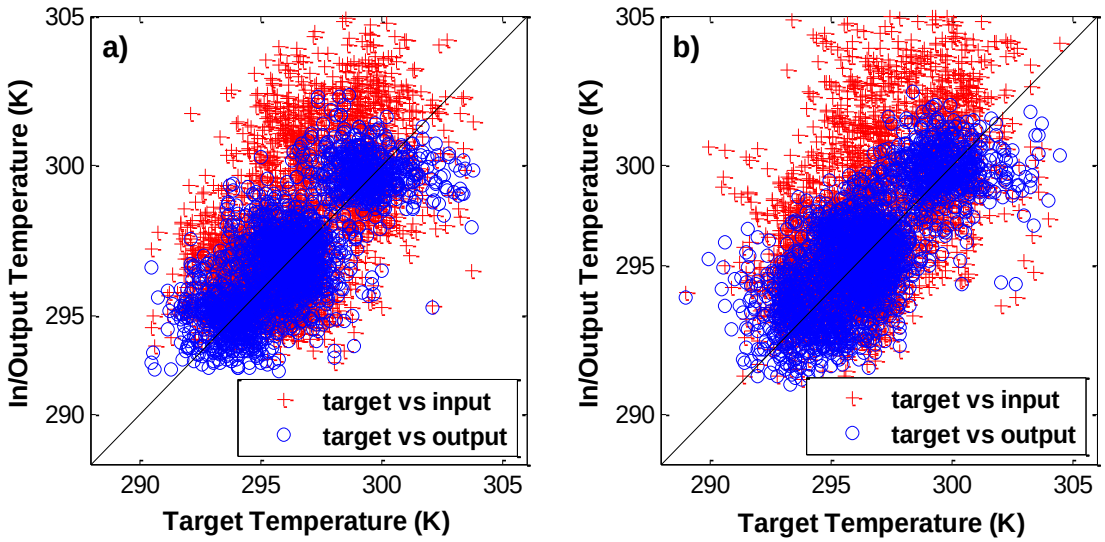

Figure 4.6. Target vs input temperature before bias correction (the red crosses) and target vs ANN output temperature (the blue circles) at location P for the (a) calibration (March 1970-1988) and (b) validation (March 1989-2008).

Figure 4.6 shows that the ANN temperature is in close agreement with the target ones. The correlations between the MFD and CCSM temperatures before bias correction (target-input) are 0.52 and 0.50, while these values are improved to 0.76 and 0.75 by the ANN model in the calibration and validation periods, respectively. The results indicate that the trained network noticeably increases the original correlations and improves estimates of air temperature. To shed more light on the performance of the ANN

approach in a distribution sense, the cumulative distribution function (CDF) of the MFD (target) and ANN (output) temperature values are illustrated in Figure 4.7 at location P.

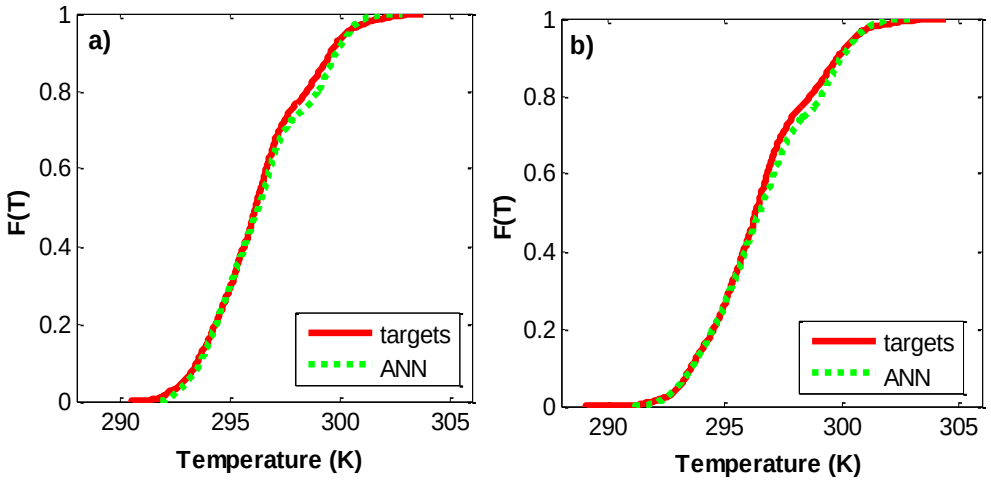

Figure 4.7. CDFs of temperature at location P for the (a) calibration (March 1970-1988) and (b) validation (March 1989-2008). Red solid and green dashed lines denote targets and ANN outputs, respectively.

It is evident from Figure 4.7 that the ANN outputs can preserve the probabilistic structure of target temperatures and the CDF of the ANN outputs follow the CDF of the target closely. As we explained in Chapter 2, the CDF and EDCDF methods are the main quantile-based mapping approaches, which are widely used for bias correction of the variables. Below we compare the performance of the CDF, EDCDF, and regression approaches (linear regression LR and nonlinear regression ANN) to correct the biases of the CCSM temperature. To evaluate the performance, the following statistical metrics are used:

I. MSE (see Eq. 4.4)

II. Bias: Expected value of the absolute error between Tar and O as

$$Bias = E[|Tar - O|], \tag{4.7}$$

III. ρ (see Eq. 4.5)

IV. Kolmogorov-Smirnov test (KS): is a measure of differences between the cumulative distribution functions CDF, which determines the capability of an

estimated distribution to approximate a target distribution. The smaller the values of KS the closer are the CDFs.

Table 4.1. compares the performance of the CDF, EDCDF, LR and ANN approaches at location P.

Table 4.1. Performance of the CDF, EDCDF, LR, and ANN in terms of the mean squared error (MSE), Bias, correlation (ρ), and Kolmogorov-Smirnov test (KS) for the calibration, Cal (March 1970-1988) and validation, Val (March 1989-2008) at location P. "In" refers to the input temperature before bias correction.

T	MSE		Bias		ρ		KS	
	Cal	**Val**	**Cal**	**Val**	**Cal**	**Val**	**Cal**	**Val**
In	8.59	9.77	2.30	2.40	0.52	0.50	0.17	0.19
CDF	5.31	5.56	1.85	1.88	0.50	0.49	0.004	0.03
EDCDF	5.25	5.95	1.84	1.93	0.50	0.48	0.005	0.02
LR	3.67	4.01	1.52	1.60	0.70	0.70	0.04	0.05
ANN	2.58	2.82	1.24	1.33	0.76	0.75	0.032	0.03

The regression methods (LR and ANN) can decrease MSE and Bias more than the distribution-based methods in both calibration and validation periods. The nonlinear regression method (ANN) outperforms linear regression in improving MSE/Bias and also correlation. The ANN improves the MSE by 70% and 71% and increases the original correlation by 46% and 50% for the calibration and validation periods, respectively. In comparison the improvements in the MSE from the LR are 57% and 59% and the improvements of the correlation are 35% and 40% in the calibration and the validation, respectively. The results show that the distribution-based methods are not able to improve the correlation of the temperature time series. To quantify the difference between the estimates in a distribution sense, the KS is provided on the last column of Table 4.1. The smaller KS obtained from CDF and EDCDF methods indicate that estimates resulting

from those methods are closer to the distribution of the target values. The CDF and EDCDF methods are, after all, based on the mapping of the distribution of the variables onto the observed ones at each quantile. However while the quantile-based mapping methods outperform the regression models in the sense of KS for the calibration period, KS is similar for all methods in the validation period. The closeness of the improvements in the calibration and the validation periods by the regression methods indicates that the trained model has the generalization capability to perform well in the validation period and hence is more desirable than the CDF and EDCDF methods.

Up to this point, we have shown that the regression models are able to reduce the biases of model temperature and improve the structure of the data. Now, the linear regression (LR) and the developed ANN (Fig. 4.1) is trained and tested pixel by pixel for the entire domain extending from 80°W to 35°W (longitude) and from 23°S to 12°N (latitude) (see Figure 4.2). The 6-hourly CCSM data (inputs) and MFD temperature (target) from 1970 to 2008 are divided into two separate datasets for each individual month: 1970-1988 as a training period (calibration) and 1989-2008 as a testing period (validation). For a complete assessment of the regression models' performance, we calculate the percent improvement (Imp) of each statistic as

$$ImpA = \frac{(A_{orig} - A_{out})}{A_{orig}} \tag{4-8}$$

where A refers to the statistics (either MSE, Bias, ρ, or KS). A_{orig} denotes statistics of the original CCSM temperature relative to the observations and A_{out} denotes statistics of the regression models outputs (LR and ANN) relative to the observations.

Figures 4.8 to 4.24 show the statistics MSE, Bias, ρ, and KS resulting from the LR and ANN models during the validation period (1989-2008). The corresponding figures for the calibration period (1970-1988) are provided in Appendix C.

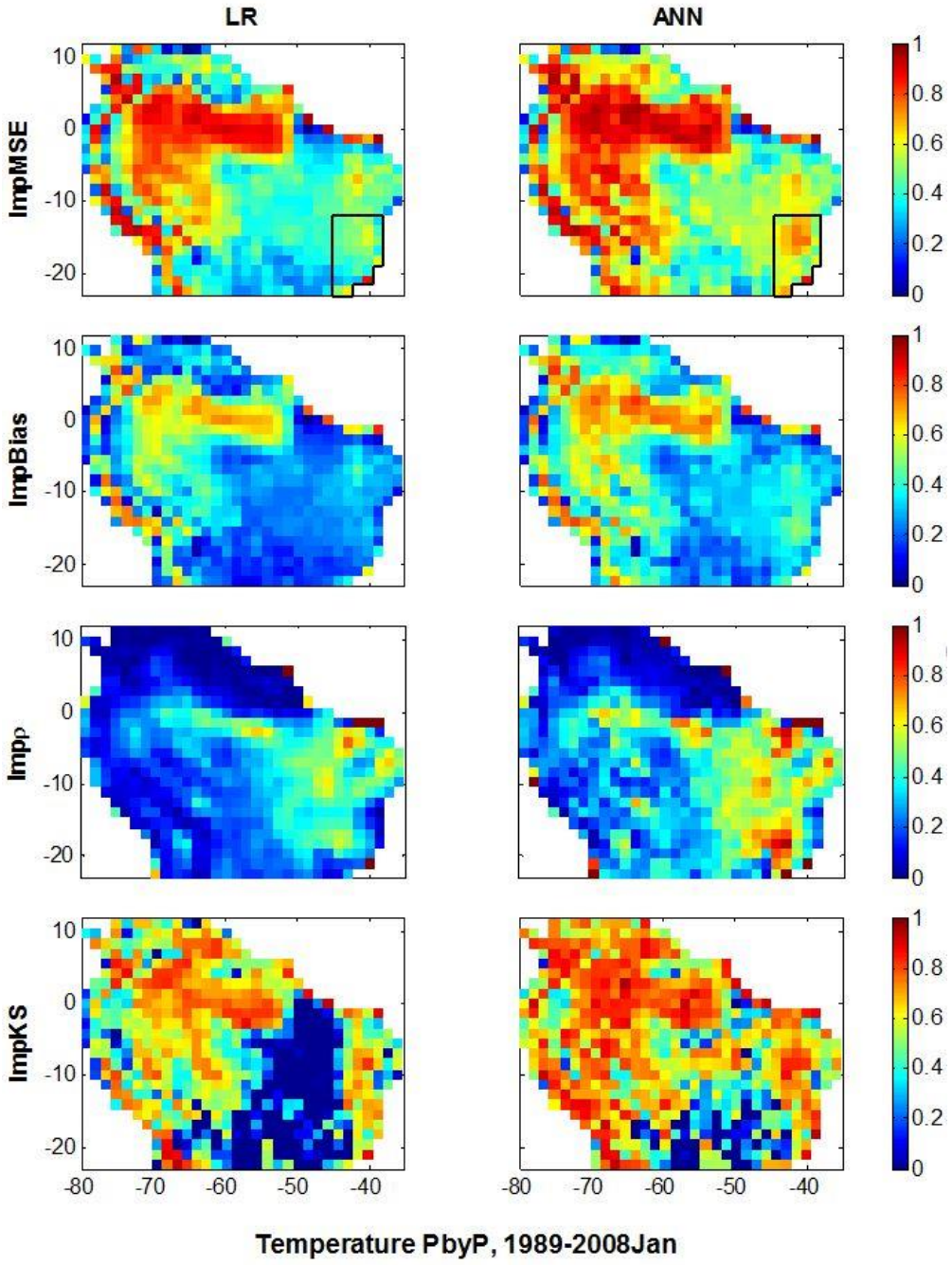

Figure 4.8. From top-to-bottom: Improvements of the MSE (ImpMSE), Bias (ImpBias), ρ (Impρ), and KS (ImpKS) by the linear (LR) and nonlinear (ANN) methods for the validation (Jan 1989-2008).

Figure 4.8 shows that the regression models can reduce the mean square error and the biases for the month of January. The most significant improvements in MSE by both models, LR and ANN, (shown with the red color in the first row in Fig. 4.8) occur over

areas of the domain where CCSM3 fails to simulate temperature well. Indeed, errors in the CCSM3 temperature over those areas are high, and can be improved by the regression models well. The correlation of the estimated field with the targets is improved by the regression models in particular by the ANN (see over the southeast of the study domain in the third row in Fig. 4.8). The blue color over the northern and western parts of the domain, in the third row of the figure, shows the area with high original correlation (on average 0.75). The LR and particularly ANN are able to improve even those high correlations. The KS is improved considerably by the ANN. The better performance of the ANN over some areas such as the southeast of Brazil is evident (see the polygon bounded by the black line in Fig. 4.8). Figure 4.9 compares the improvements of MSE, Bias, ρ, and KS by LR and ANN over the southeast of Brazil (the polygon in Figure 4.8).

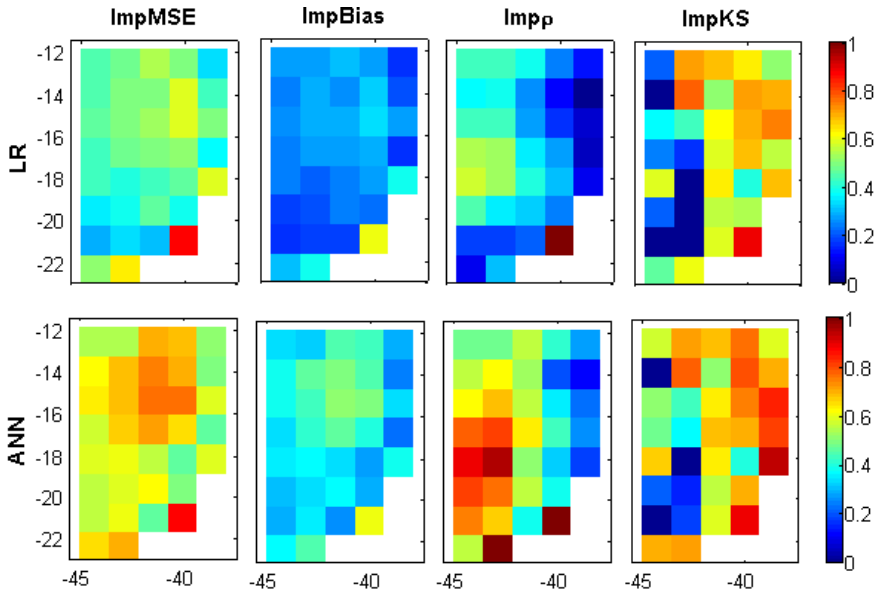

Figure 4.9. Same as Fig. 4.8 but for the region bounded by the black box in Fig. 4.8.

The average improvements of the MSE, Bias, ρ, and KS over this part of domain by LR are 47%, 26%, 31%, and 44%, respectively and the corresponding ones by the ANN are 61%, 37%, 55%, and 55%, respectively. The results indicate that although the LR and ANN improve the results, the ANN generally outperforms the LR in all statistics.

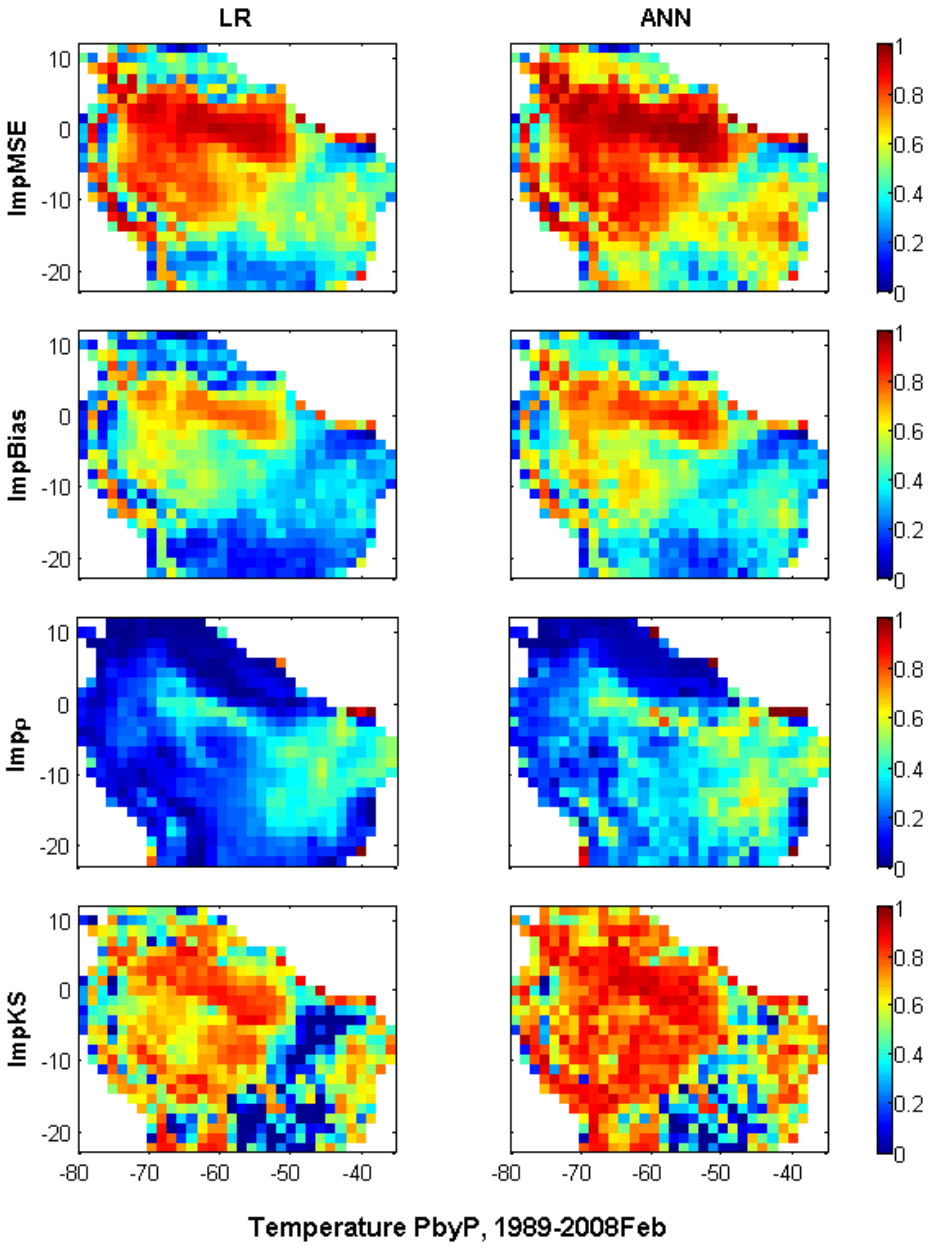

Figure 4.10. Same as Fig. 4.8 but for February.

The same pattern of improvements in statistics is observed over the month of February. The ANN outperforms the LR particularly in terms of ρ and KS statistics. The similarity of improvements in both calibration (shown in Appendix C) and validation periods indicate that the trained ANN has generalization capability.

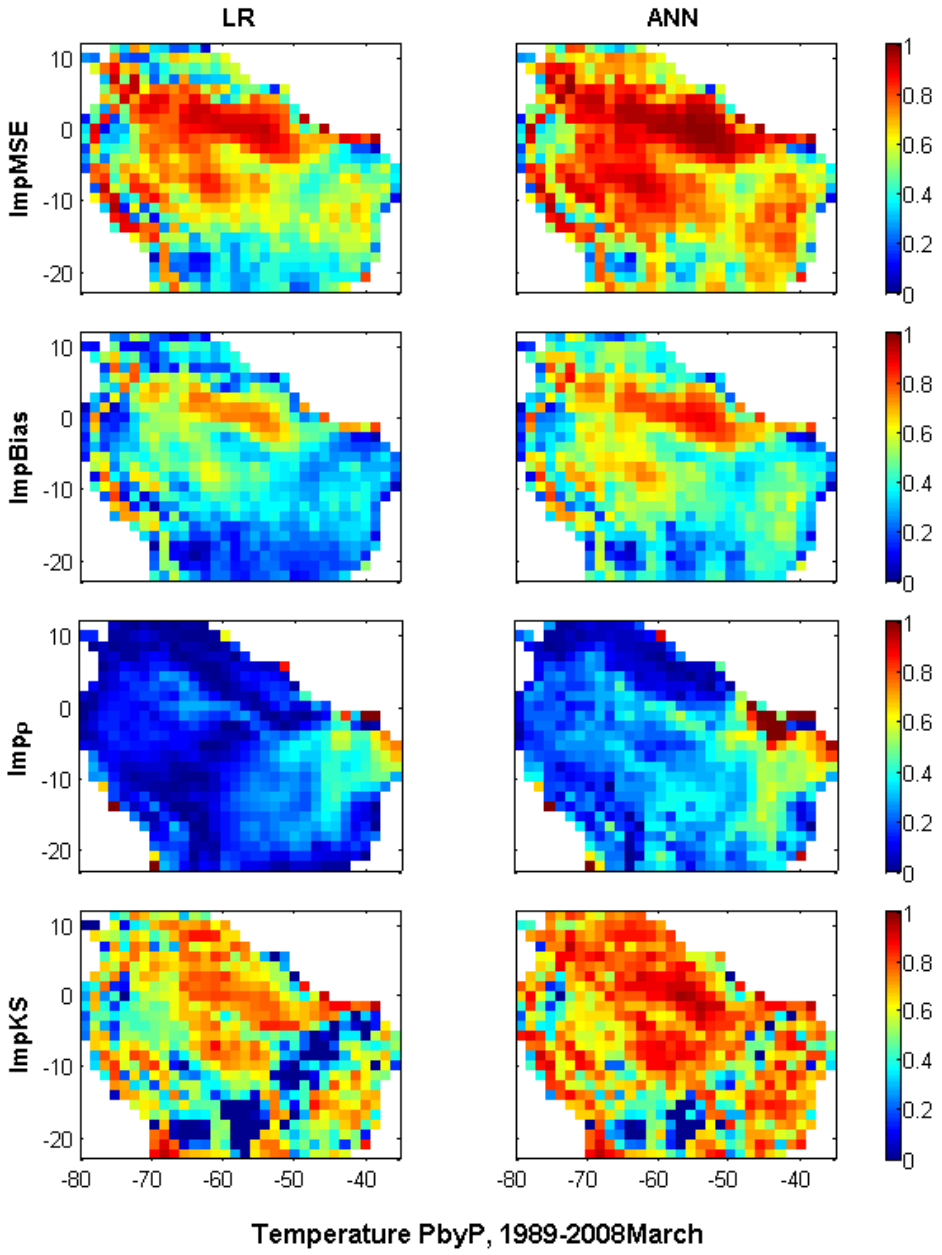

Figure 4.11. Same as Fig. 4.8 but for March.

Figure 4.11 shows that the ANN is consistently better than LR in improving the MSE, Bias, ρ, and KS for most pixels in the study domain during the month of March. The results show that the regression methods, in particular ANN, can increase the correlation of temperature even when the original correlation is low.

Figure 4.12 shows the original MSE, Bias, ρ, and KS (between biased temperature and the target) during the month of April. CCSM3 simulates temperature poorly over the west coast, southern, and northern parts of the domain during April (see Figure 4.12).

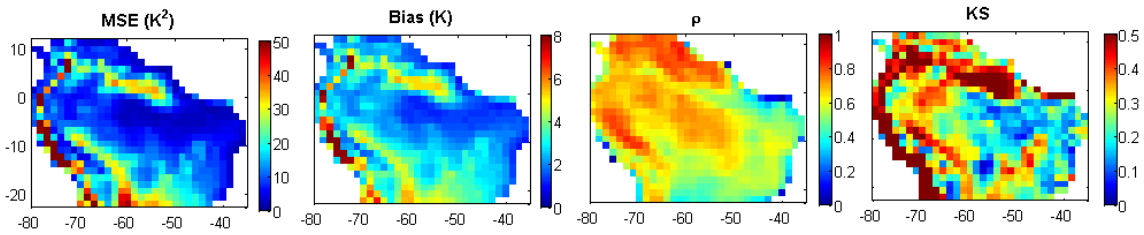

Figure 4.12. From left-to-right: The MSE, Bias, ρ, and KS between the target and the input temperature before bias correction in month April.

The large error of temperature is remarkably improved by the ANN for the month of April (Fig. 4.13). The regression models can improve the MSE and Bias over the west coast and the northern part of the domain more than over the south. This can be due to the fact that the original correlation of the input temperature with the target (third column in Fig. 4.12) is higher over the western and the northern parts of the domain than over the southern parts. Since the ANN is a data driven approach, a high correlation between inputs and targets is an important factor to construct a proper relationship between the input-output. It is clear that the ANN is able to decrease the KS over almost all pixels considerably. Note that the ANN outperforms LR over the entire domain.

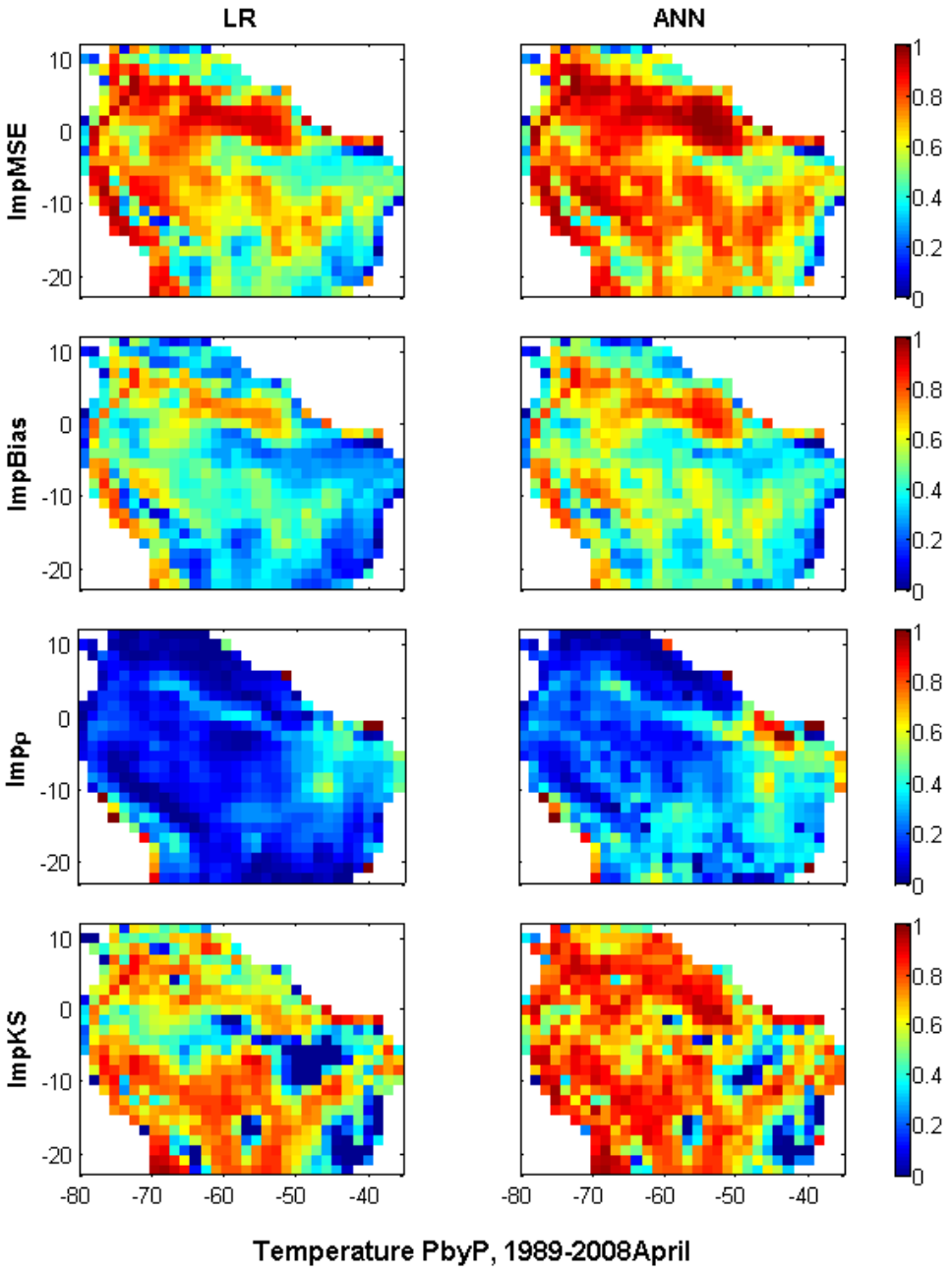

Figure 4.13. Same as Fig. 4.8 but for April.

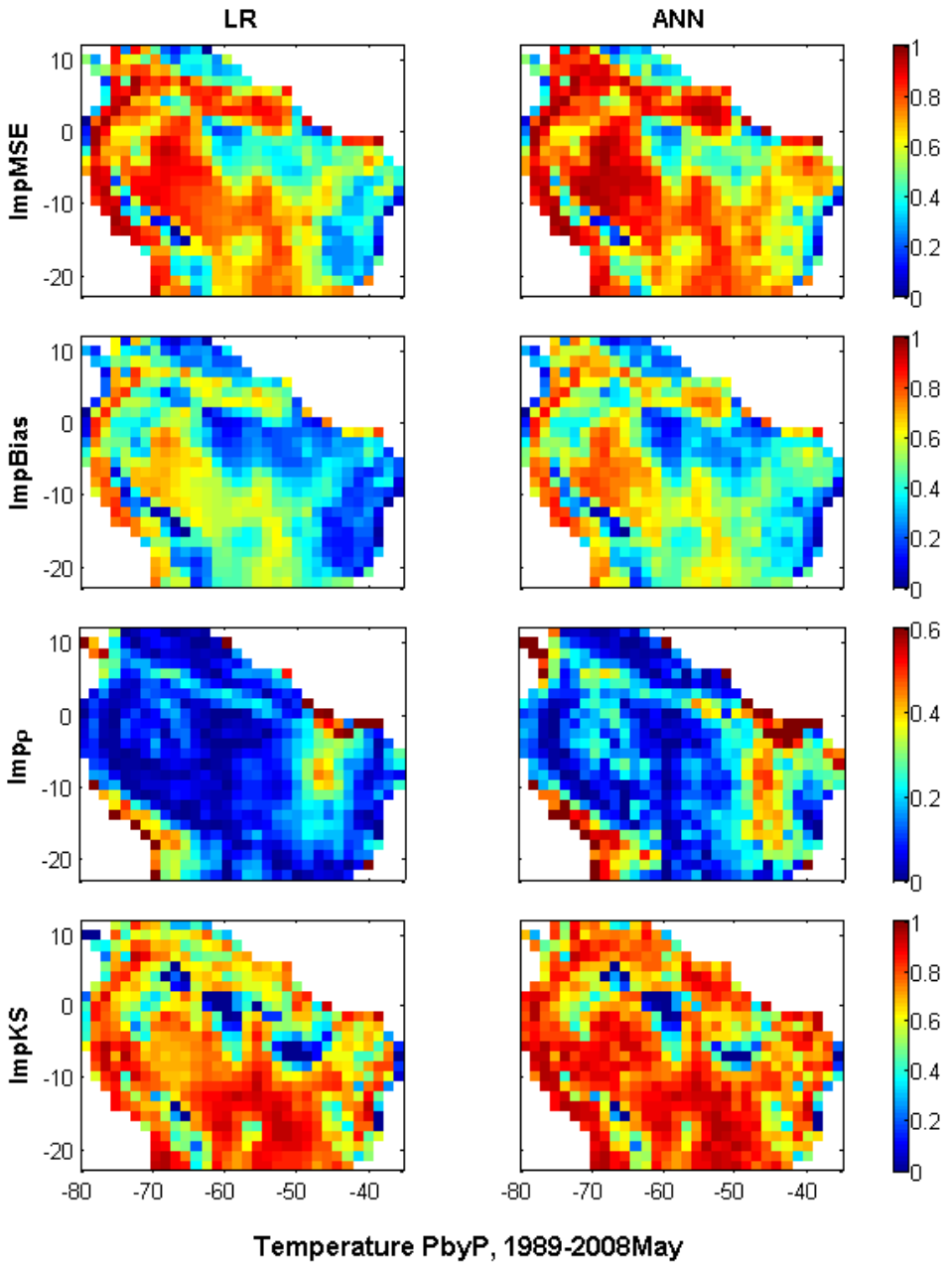

Figure 4.14. Same as Fig. 4.8 but for May.

Similarly to the month of April, the large errors are remarkably reduced by the regression models all over the domain during the month of May. The average domain improvements of the MSE, Bias, ρ, and KS by the LR are 73%, 48%, 11%, 70%, respectively and by the ANN are 78%, 54%, 20%, 78%, respectively.

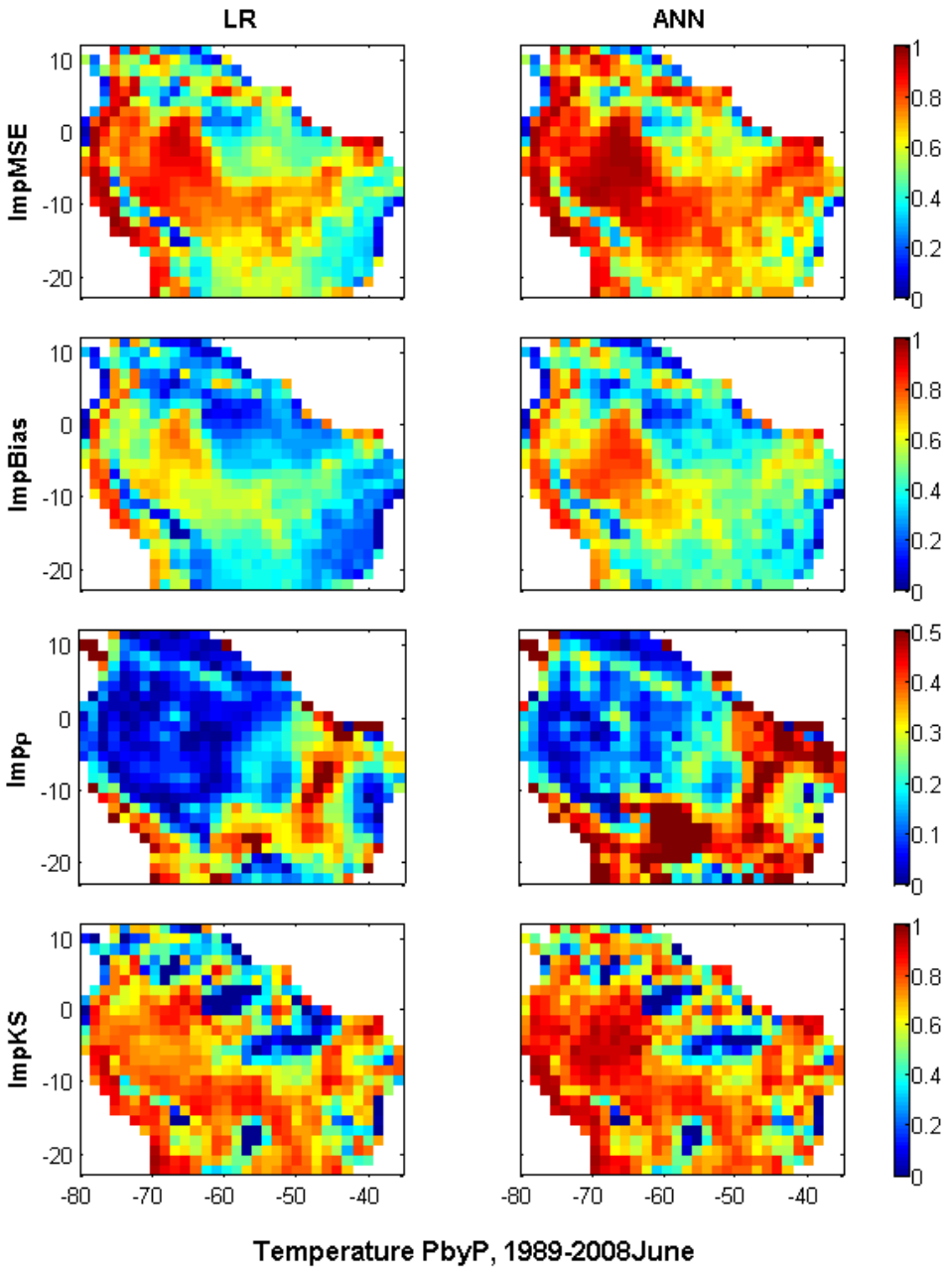

Figure 4.15. Same as Fig. 4.8 but for June.

Figure 4.15 shows that the regression models can reduce high errors over the west coast and center of the domain for the month of June (regions are covered by the red color in the first row). The smaller error over the east coast and northern of the domain can be also improved by the regression models. The lower original correlations over the

southern part of the domain are increased considerably by the regression model, in particular by the ANN.

Figure 4.16 shows the original MSE, Bias, ρ, and KS (between biased temperature and the target) during the month of July. The larger original error occurs over the western and southern part of the study domain. Most parts of the domain have large original ρ and the smaller original ρ is over the southern part of the domain.

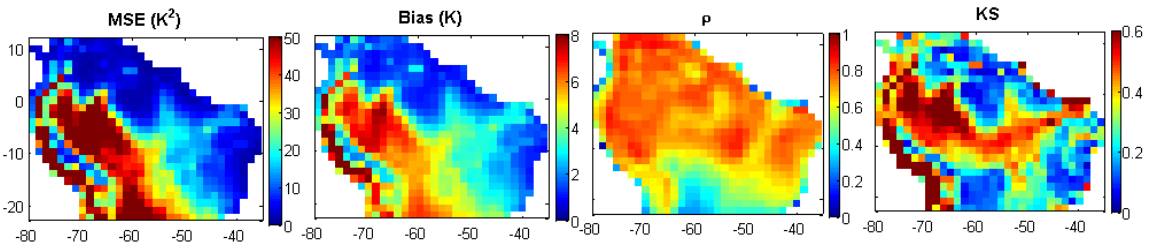

Figure 4.16. Same as Fig. 4.12 but for month July.

Figure 4.17 shows the improvements of the statistics by the regression models in month of July. The pattern of improvements of MSE is similar to the pattern of original MSE. In other words, the most significant improvements of MSE occur over the regions where the original MSE is high (western part of the domain, see Fig. 4.16). Also there is a similarity between the pattern of improvements in ρ and original correlation. Indeed, the most significant improvements of ρ occur over the regions where the original ρ is small (see the light blue on the southern part of the domain in the third column of Fig. 4.16 and the red color in the third row of Fig. 4.17). The smaller original correlation over the south than the western part of the domain leads to smaller improvements of the MSE by the regression methods over the south. This can indicate that the regression models show better performance in improving the error over the pixels that have higher original correlation (covered with the red color in the third column of Fig. 4.16) and in general a higher original correlation between the input-target leads to a better performance of the regression models in improving the errors.

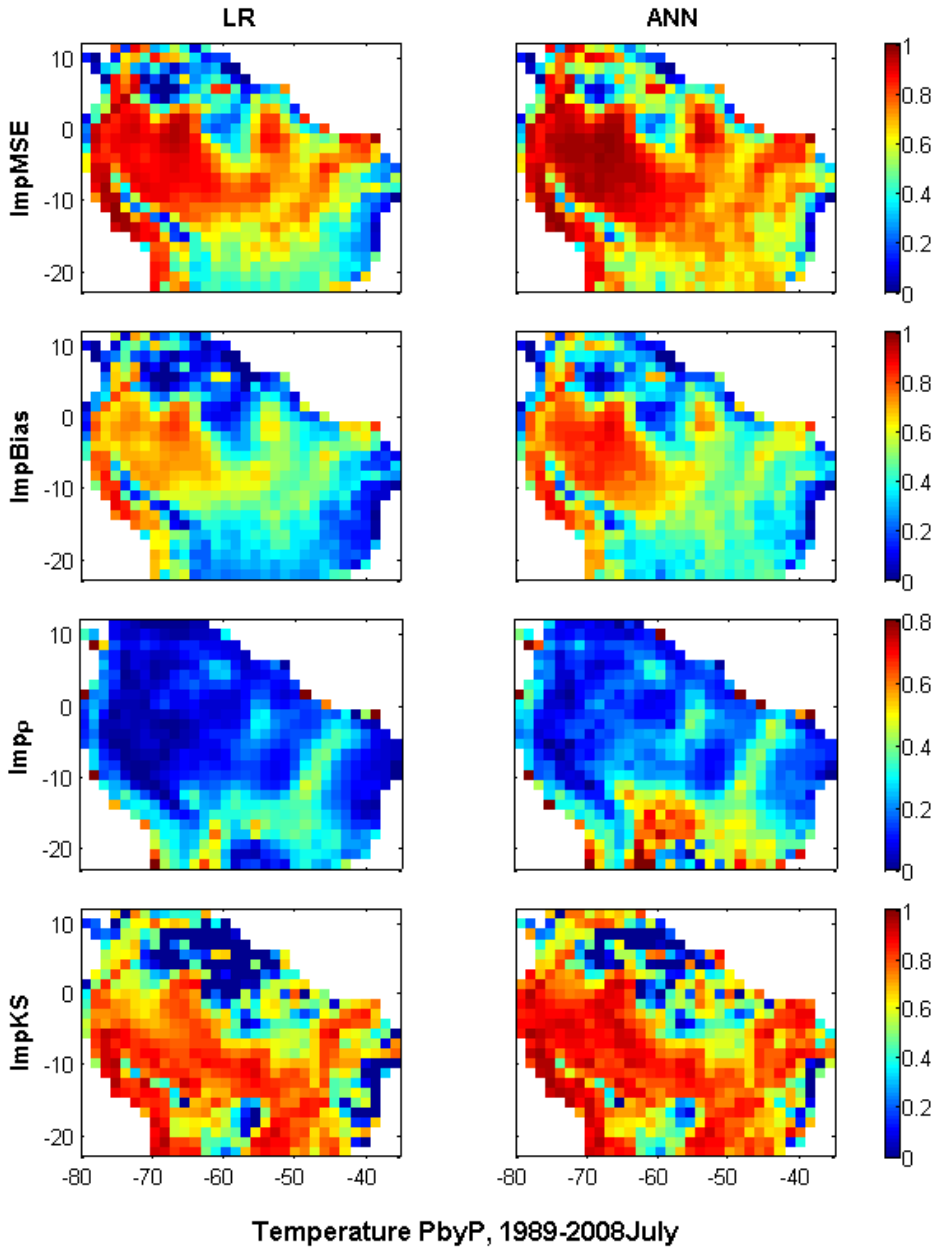

Figure 4.17. Same as Fig. 4.8 but for July.

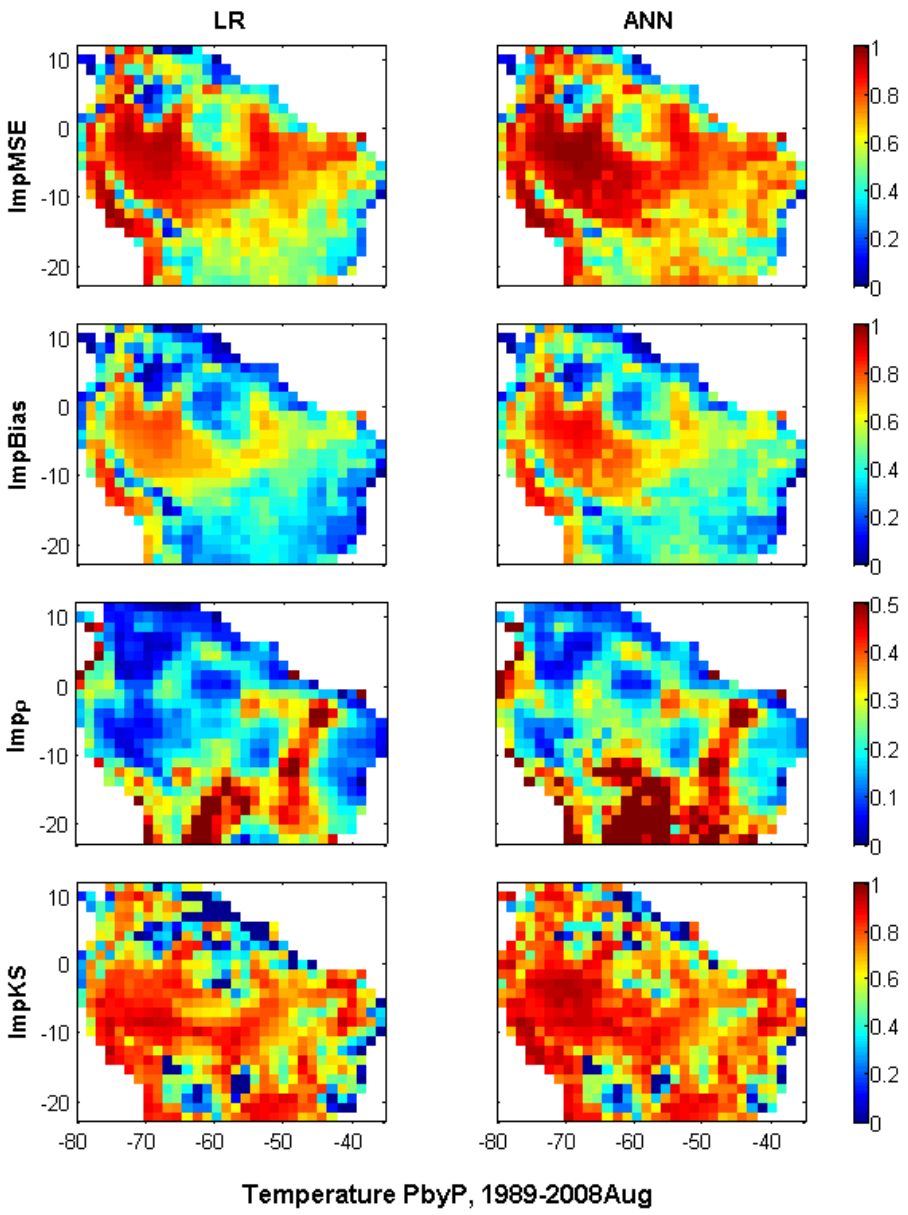

Figure 4.18. Same as Fig. 4.8 but for August.

The pattern of improvements during August and July is similar, which can indicate that the skill of CCSM3 to simulate temperature depends of the validity of the schemes and parameterizations used in each season and location. Large errors over the majority of the domain require bias correction for the climate models outputs (CCSM3). The results show that the regression methods have ability to improve the results in terms of the MSE, Bias, ρ, and KS.

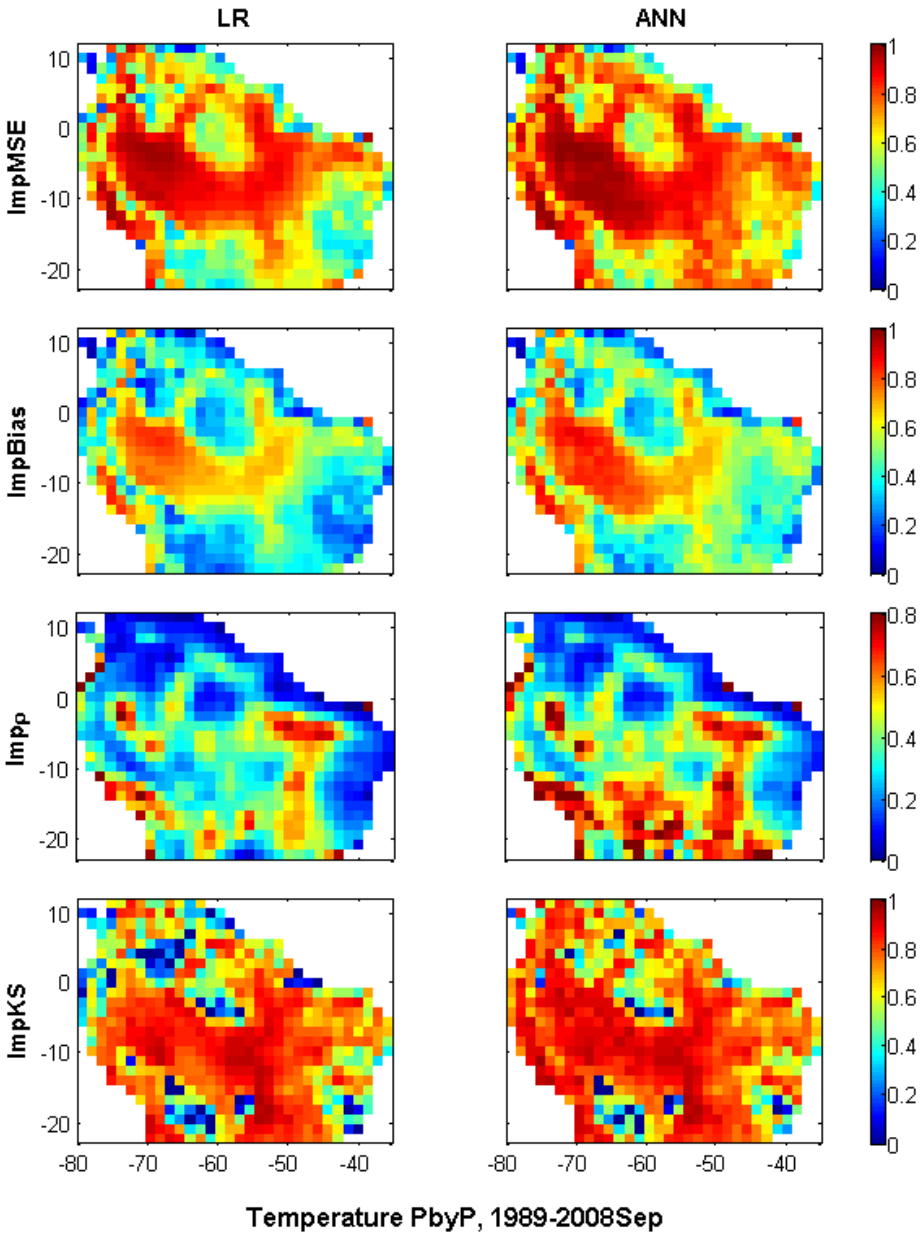

Figure 4.19. Same as Fig. 4.8 but for September.

The maximum domain average of the MSE and Bias occurs during September ($24.64K^2$ and $3.68K$, respectively). Accordingly this month has the highest domain average improvements of the MSE, Bias, and KS by the LR and ANN among all months. The overall domain average improvements of the MSE, Bias, and KS by the LR are 74%,

51%, and 70%, respectively and the corresponding improvements by the ANN are 81%, 58%, and 78% in month September.

Figure 4.20 illustrates the original MSE, Bias, ρ, and KS (between biased temperature and the target) during October. The figure shows that the patterns of the original MSE, Bias, ρ, and KS are quite similar in October. In other words, the regions with large errors have large KS and small ρ and vice versa.

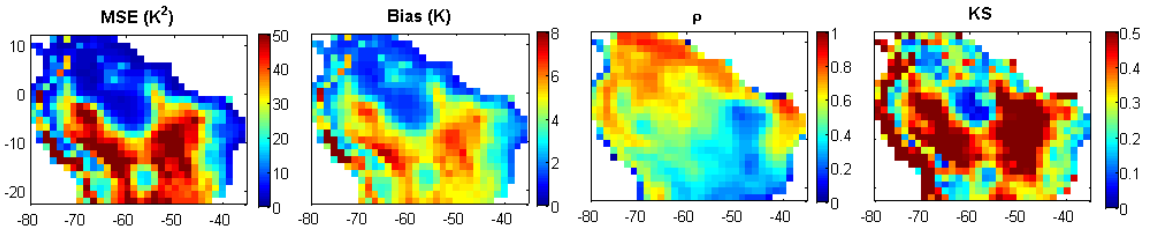

Figure 4.20. Same as Fig. 4.12 but for month October.

The large MSE, Bias, and KS are considerably improved by the regression models for the month of October (see Fig. 4.21). Furthermore, the models, in particular the ANN, are able to increase the correlation of temperature. The overall domain average of improvements of MSE, Bias, ρ, and KS by the LR are 73%, 50%, 22%, and 68%, respectively and the corresponding improvements by the ANN are 79%, 56%, 33%, and 77% respectively. Although the performance of the LR seems comparable with the ANN, the ANN clearly does better over some parts of the study domain (see polygon bounded by the black line in Fig. 4.21). For the region bounded by the black polygon over the eastern of Brazil, the LR improves the MSE, Bias, ρ, and KS by 54%, 33%, 42%, and 52% on average, respectively while the ANN improves them by 70%, 46%, 56%, and 69%, respectively.

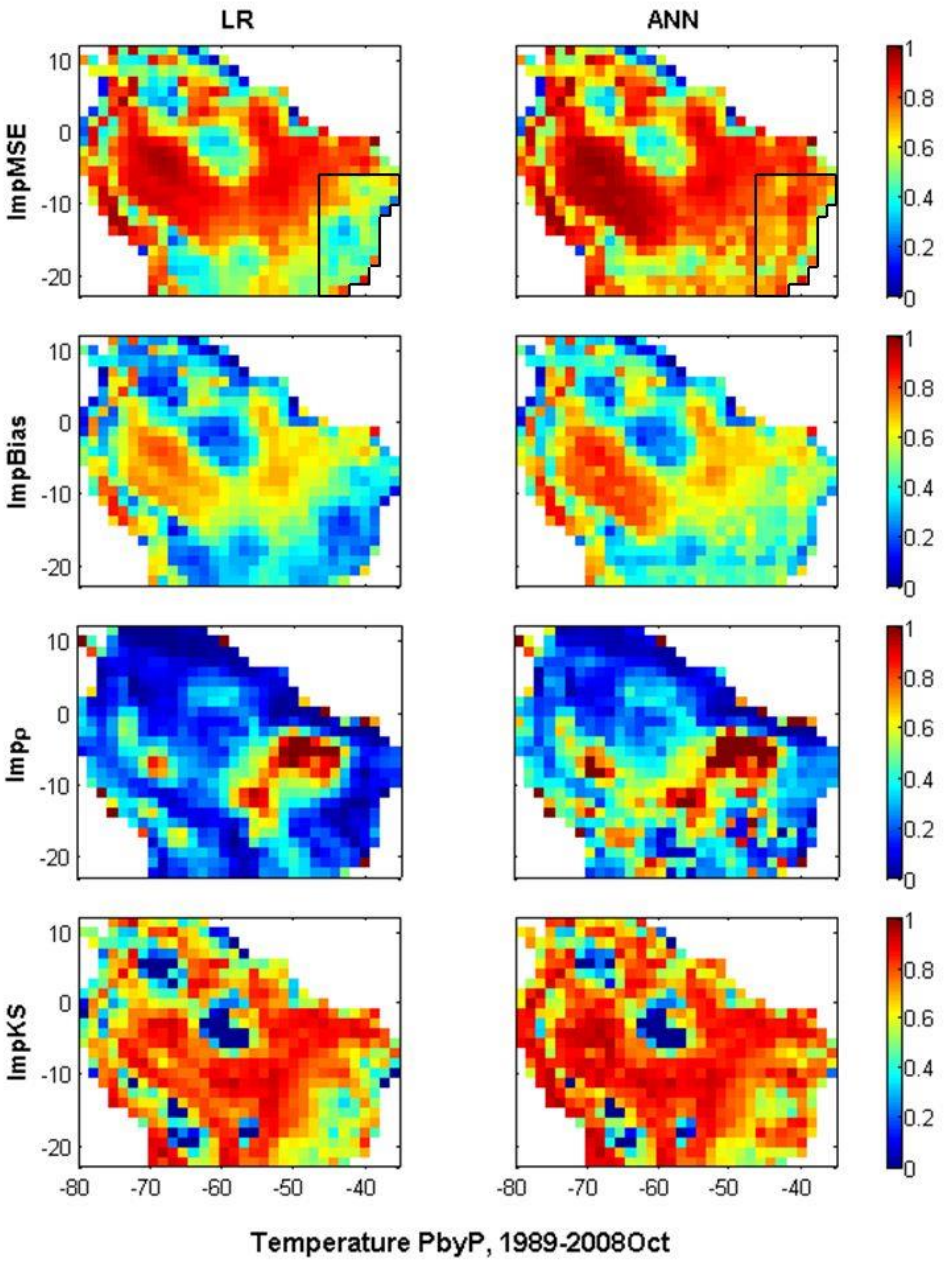

Figure 4.21. Same as Fig. 4.8 but for October.

Thus, the results indicate that the ANN model can be trained during the calibration period by the input-target set better than the LR model.

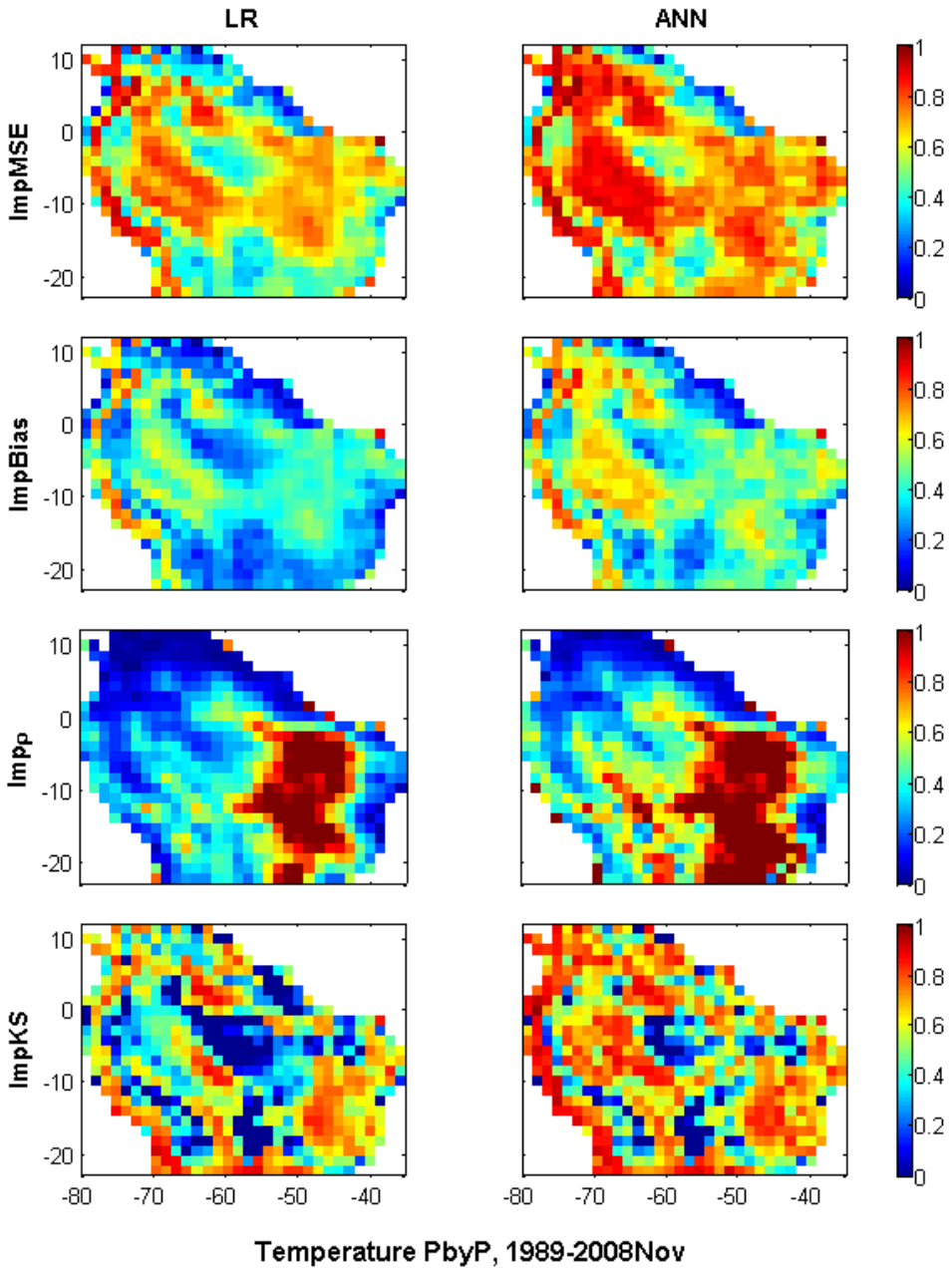

Figure 4.22 Same as Fig. 4.8 but for November.

The highest domain average improvement of the ρ by the LR and ANN occurs during the month of November (33% and 46%, respectively). The better performance of the ANN is obvious almost all over the study domain. The range of improvements in all statistics for both models is similar in the calibration (shown in Appendix C) and the validation periods, which indicates the robustness of the models.

Figure 4.23 shows the original MSE, Bias, ρ, and KS (between biased temperature and the target) during December. Although the regression models improve all statistics, ANN shows better performance than LR (see Fig. 4.24).

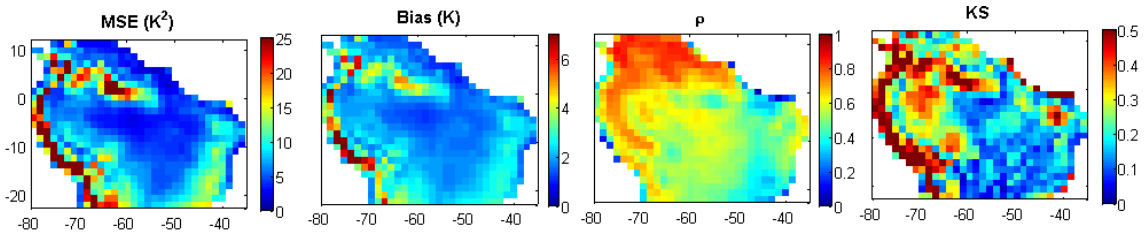

Figure 4.23. Same as Fig. 4.12 but for month December.

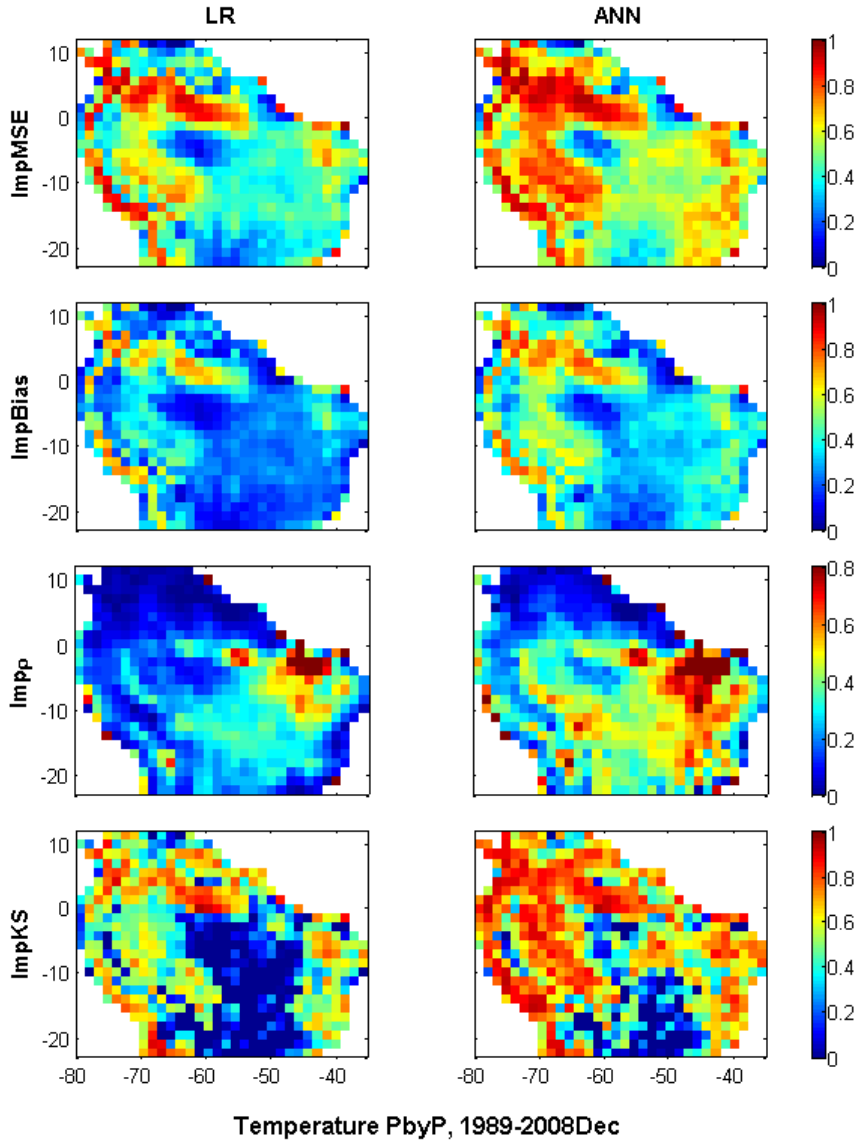

Figure 4.24. Same as Fig. 4.8 but for December.

A close scrutiny of Figures 4.23 and 4.24 indicates that when the original MSE (between biased temperature and the target) is large and the original correlation is also high, the LR has a comparable performance with the ANN (see red color in the first row in Fig. 4.24). While the ANN outperforms the LR over the regions that the original correlation is low (e.g., see the eastern part of the domain). The ANN is able to construct a reliable relationship between the input-output even for the pixels that have low original correlation.

The LR and ANN models are able to improve not only the error of temperature but also the correlation of temperature time series. They also can improve temperature in term of KS. In general, ANN is the best in improving the statistics for all months. Table 4.2 summarizes the overall domain average percent improvements of the statistics by the LR and ANN in both calibration and validation periods for all months.

Table 4.2. Domain average percent improvements of MSE (ImpMSE), Bias (ImpBias), ρ (Impρ), and KS (ImpKS) for calibration, Cal (1970-1988) and validation, Val (1989-2008).

Month		**ImpMSE**		**ImpBias**		**Impρ**		**ImpKS**	
		Cal	**Val**	**Cal**	**Val**	**Cal**	**Val**	**Cal**	**Val**
Jan	**LR**	66	64	41	39	21	23	60	51
	ANN	73	70	47	45	30	32	73	67
Feb	**LR**	70	69	45	44	21	20	67	60
	ANN	77	76	52	51	31	29	77	73
March	**LR**	66	66	41	41	15	16	68	57
	ANN	76	76	51	51	28	29	78	70
April	**LR**	72	68	47	44	17	17	71	60
	ANN	79	77	55	53	26	27	81	73
May	**LR**	74	73	49	48	13	11	78	70
	ANN	79	78	55	54	22	20	84	78
June	**LR**	73	72	49	49	17	16	78	67
	ANN	81	80	57	56	27	27	84	75
July	**LR**	75	72	52	49	16	15	76	64
	ANN	81	79	59	56	24	23	83	74
Aug	**LR**	75	73	53	50	19	19	78	64
	ANN	81	78	59	56	25	25	85	75
Sep	**LR**	76	74	53	51	30	27	77	70
	ANN	84	81	61	58	38	33	83	78
Oct	**LR**	77	73	53	50	25	22	76	68
	ANN	83	79	60	56	37	33	82	77
Nov	**LR**	67	64	43	41	33	33	63	53
	ANN	77	73	52	50	46	46	74	68
Dec	**LR**	64	59	39	35	24	21	56	47
	ANN	73	69	48	44	36	33	74	68

We also look at the correlation length in both S-N and W-E directions, centered at latitude = 6.3°S and longitude = 60.47°W (see Figs. 4.25, 4.26).

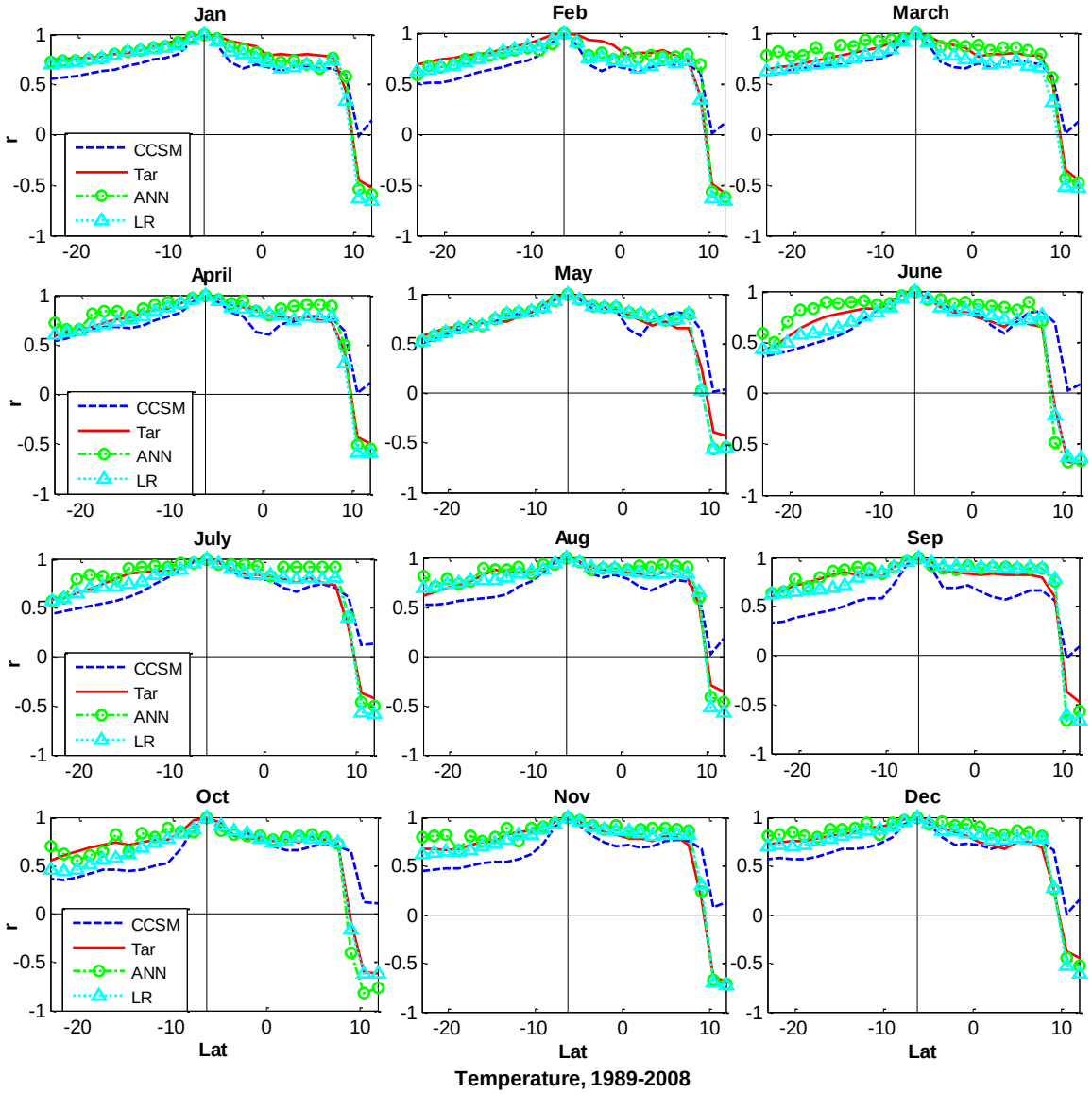

Figure 4.25. The correlation in the S-N direction, centered at latitude = 6.3°S and longitude = 60.47°W for the validation (1989-2008). r is spatial correlation. Blue dashed lines refer to CCSM, red solid lines refer to target, green dash-dot lines with circle markers refer to ANN outputs, and the cyan dotted line with triangle markers refer to LR outputs.

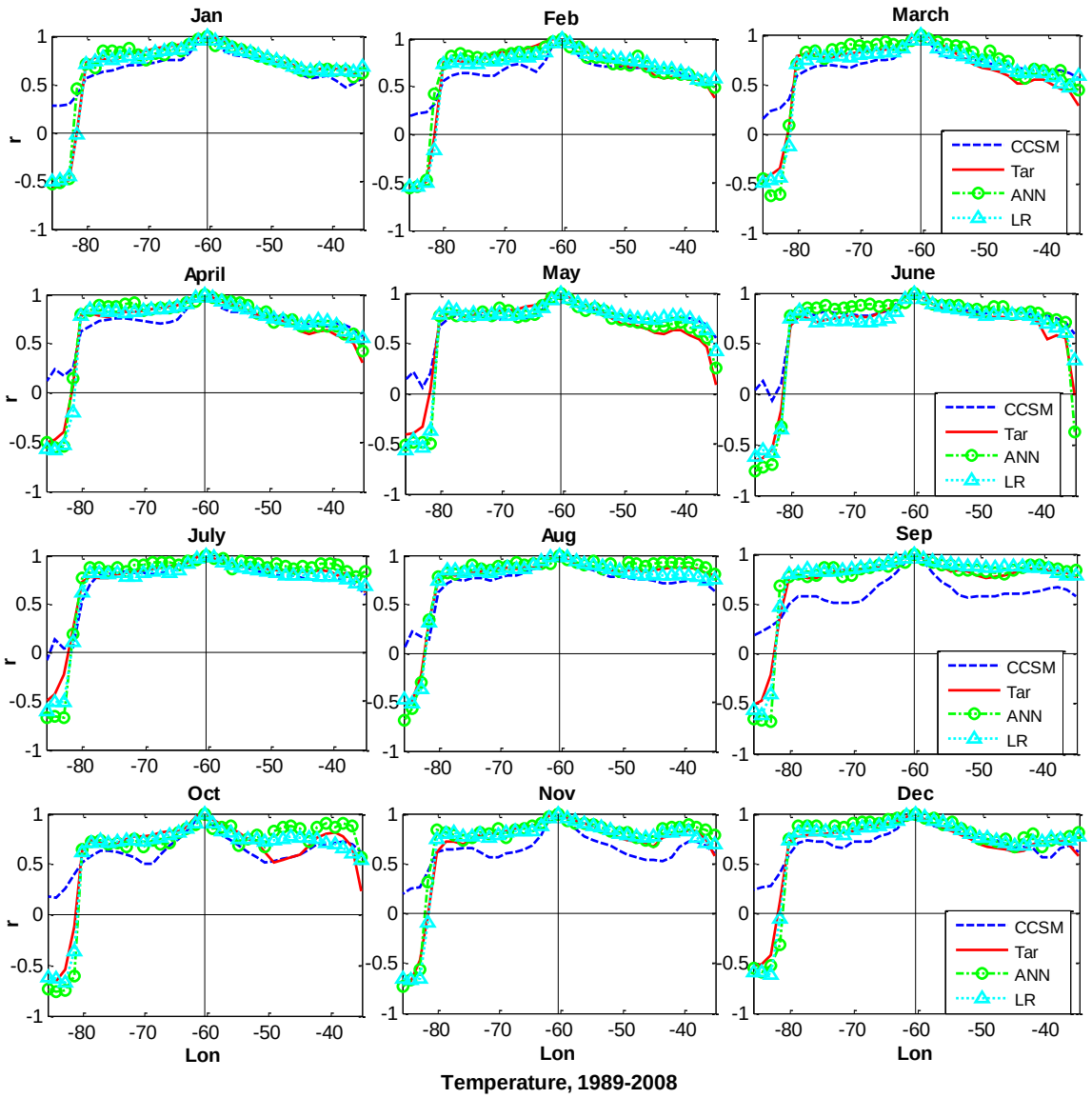

Figure 4.26. Same as Fig. 4.25 but for the W-E direction.

Results show a close agreement between the regression model outputs (LR and ANN) and targets. This can confirm that however the regression models correct the biases of temperature pixel by pixel, the spatial correlation of bias-corrected temperature can be conserved in the study domain.

4.3.2. Precipitation

The direct bias correction of precipitation at fine scale (e.g., 6-hour) is not feasible because there are many zero values (dry hours) that makes it difficult for ANN to construct a proper relationship between the input-output. Many studies have corrected biased precipitation values at a monthly scale (Chen et al., 2013; Teutschbein and Seibert, 2012; Berg et al., 2003, among many others). To correct the biases of precipitation, we use seasonal historical CCSM precipitation (input to the ANN) and CRU precipitation (ANN target) from 1901 to 2013. The training set (the CCSM and CRU precipitation) is divided into two independent periods to check the validity of the trained network:

I) 1901-1956 as a calibration period, used to train the network.
II) 1957-2013 as a validation period, used to study the performance of the trained network.

In Section 4.2, we determined an appropriate training set, architecture, and the training algorithm of the network for the purpose of bias correction of precipitation values. Figure 4.27 shows a schematic diagram of the proposed ANN to reproduce bias-corrected precipitation.

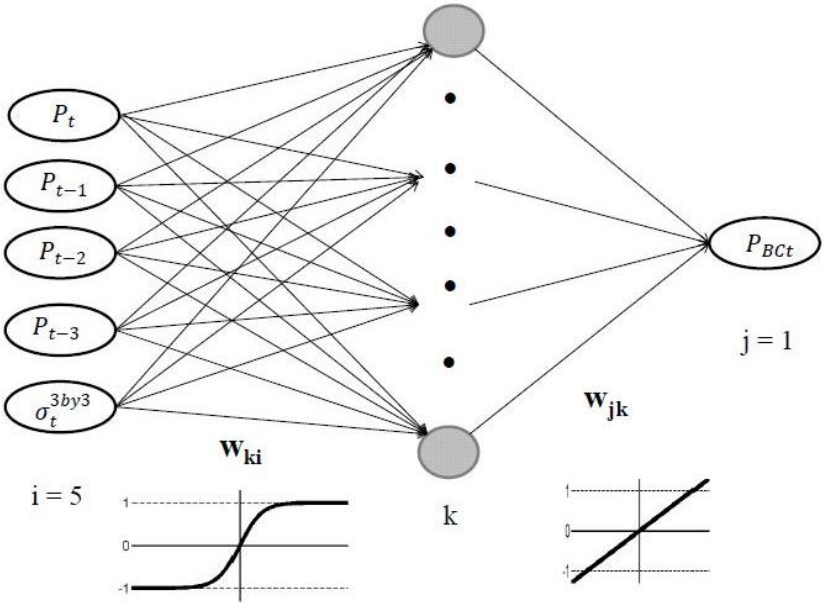

Figure 4.27. The proposed feedforward network (FNN). The inputs of the network are: current precipitation (P_t), one time lag precipitation (P_{t-1}), two time lag precipitation (P_{t-2}), three time lag precipitation (P_{t-3}), and the standard deviation of precipitation from the 3 by 3 neighboring pixels (σ_t^{3by3}) at the current time; while the output is the current bias-corrected precipitation (P_{BCt}). w_{ki} and w_{jk} denote the weights connecting the input layer (i) to the hidden layer (k) to the output layer (j), respectively.

Following we discuss the selection of the number of hidden nodes and the learning rate required to train the network. The detailed description of the procedure is provided for location P (red circle in Fig. 4.2) for the season MAM (March, April, May). For temperature, we showed that the performance of the developed network was not very sensitive to different values of η and $\eta = 0.01$ was a good choice in the network. Therefore, here in the first step we fix η at 0.01, we start with 5 hidden nodes and we train the network. In the next steps, we add hidden nodes one at a time and re-train the network. The number of hidden nodes varies from 5 to 11. The performance of the network using different hidden nodes is shown in Figure 4.28, using MSE and ρ of the results for the calibration and the validation periods.

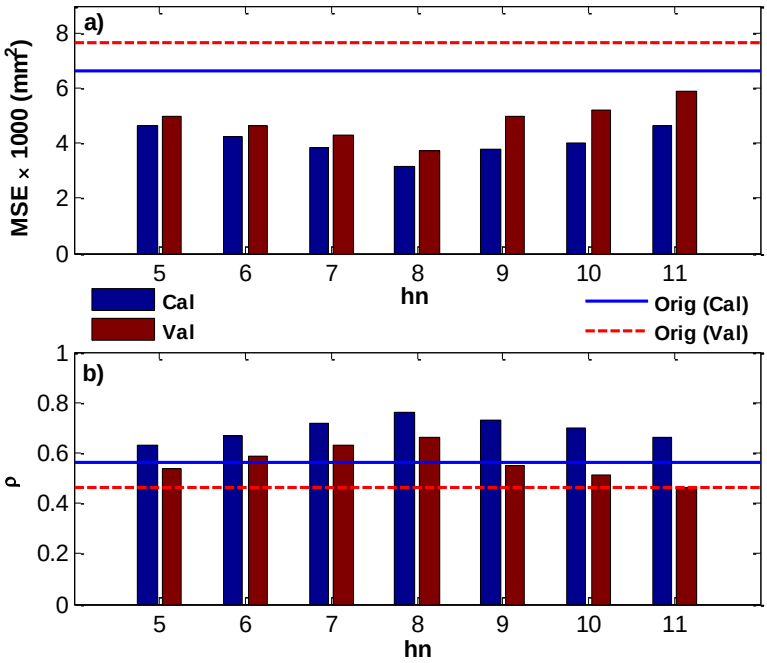

Figure 4.28. Performance of the ANN for different number of the hidden nodes, hn. (a) The mean squared error, MSE and (b) correlation of the ANN outputs with the targets, ρ. The blue bars show the statistics for the calibration (MAM 1901-1956) and the red bars denote the results for the validation (MAM 1957-2013) at location P. The blue solid and red dashed lines denote the statistics between the input (original precipitation) and target values for the calibration (Cal) and validation (Val), respectively.

The bars below and above the horizontal lines in Figure 4.28a and 4.28b show the range of hidden nodes that are able to improve the original MSE and correlation between the CCSM and observed precipitation, respectively (the solid line refers to the calibration period and the dashed line refers to the validation period). As we can see all hidden nodes are able to reduce the original MSE and increase the correlation, while the network with 8 hidden nodes leads to the smallest MSE and the highest correlation in both calibration and validation. A close scrutiny of Figure 4.28 reveals that the performance of the network in the calibration and the validation periods is close when we use a fewer number of hidden nodes. In addition, larger number of hidden nodes increases complexity of the model, computational time, and memory usage in the process of weight optimization. Thus, the optimal network is the one that performs well with a fewer

number of hidden nodes. For this study, the results indicate that 8 nodes are the minimum number of hidden nodes that the network needs to get the smallest MSE and the highest correlation for both calibration and validation periods. To assure that the network with 8 hidden nodes does not reduce the temporal variability of precipitation, we compare the SNR of the ANN outputs using different number of hidden nodes (Fig. 4.29).

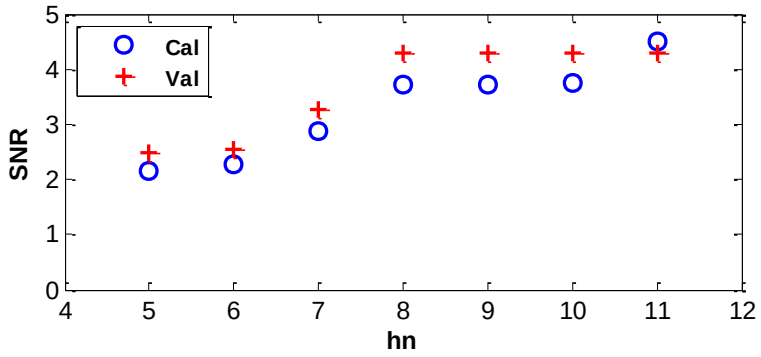

Figure 4.29. Signal-to-noise ratio (SNR) for different hidden nodes, hn. The blue circles denote the calibration period (MAM 1901-1956) and the red crosses denote the validation period (MAM 1957-2013) at location P.

The results of the obtained SNR for different number of hidden nodes illustrate that 8 hidden nodes lead to a higher SNR than 5, 6, or 7 nodes. On the other hand, the temporal variability of the outputs is not very sensitivity to the number of hidden nodes when the number of nodes exceeds 7, particularly for the validation period. In summary, we set $\eta = 0.01$ and we select $hn = 8$ for which the MSE and correlation are in their minimal and maximal positions, respectively. Now we study the sensitivity of the network using different learning rates. Figure 4.30 compares the mean squared error and correlation of the ANN outputs ($hn = 8$) for different learning rates.

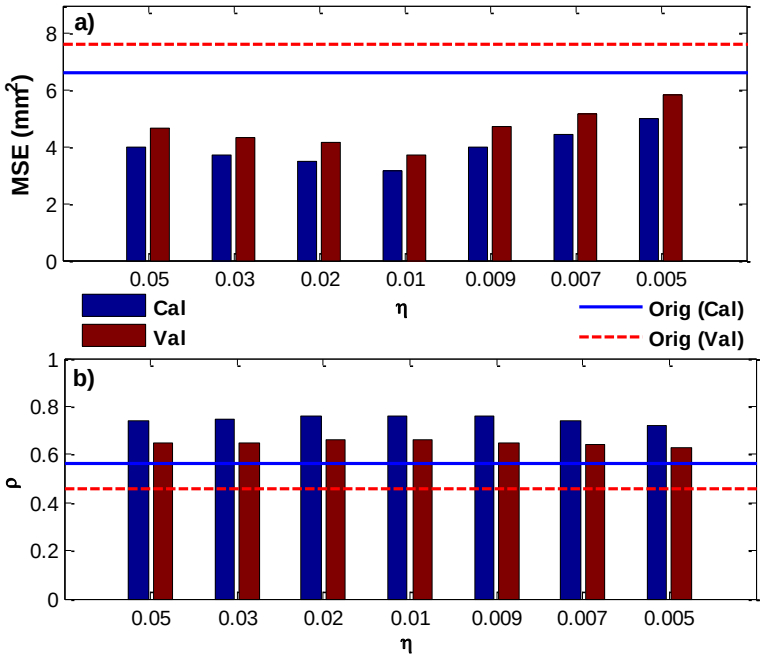

Figure 4.30. Same as Fig. 4.28 but for different learning rates, η.

As we can see, the performance of the network is not very sensitive to the learning rate since the network with different ranges of learning rates can improve the results in both terms of the MSE (bars are below the reference lines in Figure 4.30a) and correlation metrics (bars are above the reference lines in Figure 4.30b). On closer inspection of the figure, the MSE is larger for the learning rate smaller than 0.01 and $\eta = 0.01$ leads to the smallest MSE. To this end, we use $\eta = 0.01$ as the best choice to train the network.

We conclude that $\eta = 0.01$ and $hn = 8$ are reasonable choices for our network to reduce the biases of precipitation values. The performance of the developed model is illustrated through scatter plots in Figure 4.31 at location P.

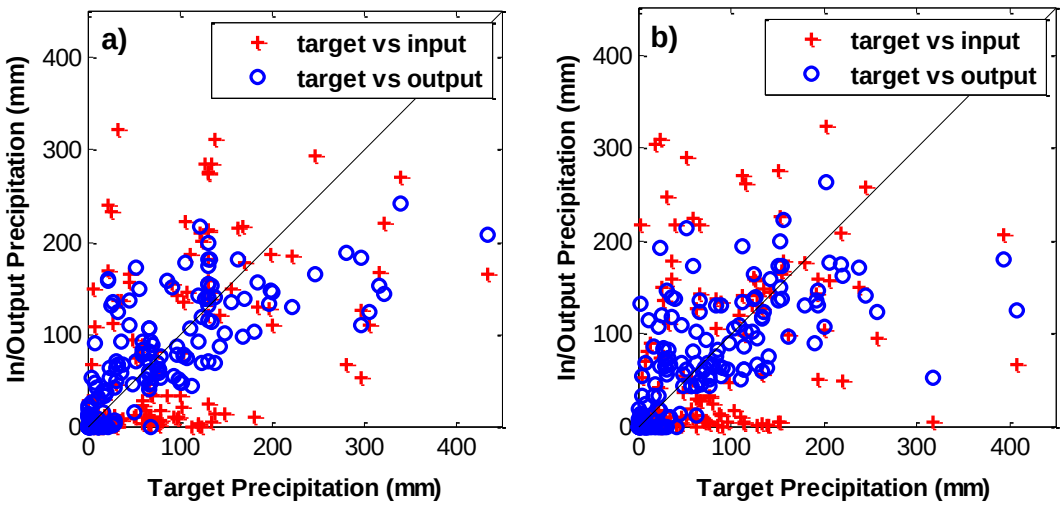

Figure 4.31. Target vs input precipitation before bias correction (the red crosses) and target vs ANN output precipitation (the blue circles) at location P for the (a) calibration (MAM 1901-1956) and (b) validation (MAM 1956-2013).

Figure 4.31 shows a close agreement between the ANN output precipitation and targets. The correlations between the CRU and CCSM precipitation before bias correction (target-input) are 0.56 and 0.46, while these values are improved to 0.76 and 0.66 by the ANN model in the calibration and validation periods, respectively. The results indicate that the ANN improves estimates of precipitation. Figure 4.32 illustrates the performance of the ANN approach in a distribution sense.

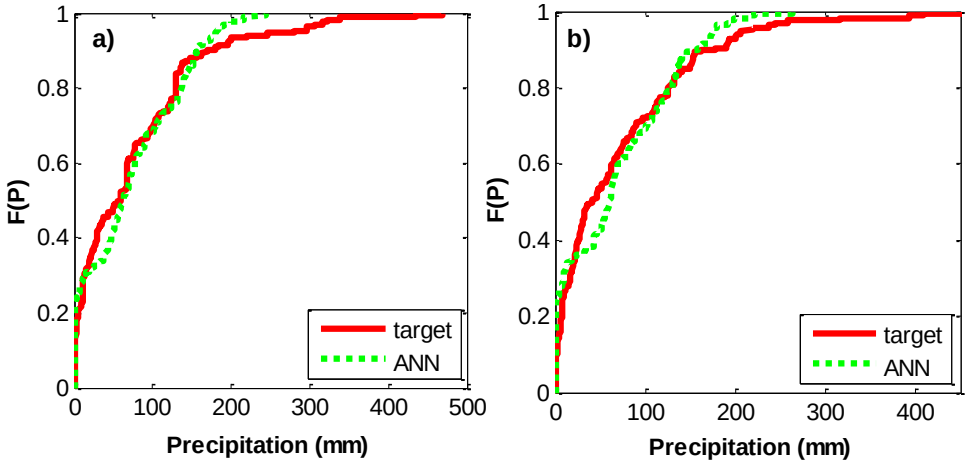

Figure 4.32. CDFs of precipitation at location P for the (a) calibration (MAM 1901-1956) and (b) validation (MAM 1957-2013). Red solid and green dotted lines denote targets and ANN outputs, respectively.

The CDF plot shows that although the ANN does not include any distribution mapping technique, it can preserve the probabilistic structure of the target; the CDF of the ANN outputs follows the CDF of the target closely. For a complete assessment of the ANN model, we use linear regression model and the most widely used distribution-based approaches such as the CDF and EDCDF methods to correct the biases of the CCSM precipitation at location P. A full statistical comparison between all of these methods is presented in Table 4.3.

Table 4.3. Performance of the CDF, EDCDF, LR, and ANN in terms of the mean squared error (MSE), Bias, correlation (ρ), and Kolmogorov-Smirnov test (KS) for the calibration, Cal (MAM 1901-1956) and validation, Val (MAM 1957-2013) at location P. "In" refers to the input precipitation before bias correction.

P	**MSE**		**Bias**		$\boldsymbol{\rho}$		$\boldsymbol{KS}$	
	Cal	**Val**	**Cal**	**Val**	**Cal**	**Val**	**Cal**	**Val**
In	6609	7652	55	56	0.56	0.46	0.24	0.27
CDF	7459	8532	54.97	58.28	0.51	0.40	0.06	0.09
EDCDF	7337	8695	54.53	57.99	0.51	0.40	0.05	0.07
LR	4130	4910	42.17	43.54	0.67	0.54	0.12	0.12
ANN	3166	3711	36.09	37.65	0.76	0.66	0.10	0.12

The results in Table 4.3 indicate that the regression methods, in particular ANN, can decrease the MSE/Bias and increase correlation considerably. The ANN improves the MSE by 52% and 51%, while it increases the original correlation by 36% and 43% for the calibration and validation periods, respectively. The improvements of the MSE by the LR are 37% and 36% and the improvements of the correlations are 20% and 17%, for the calibration and validation periods, respectively. The distribution-based methods are not able to improve the Bias in the validation period nor MSE and correlation in both calibration and validation periods. This is due to the fact that the distribution-based

approach is based on the mapping of the historical modeled variables onto the observed ones at each percentile. Since the modeled value at a certain quantile may not coincide with the observed value of that quantile, this mapping approach does not guarantee a reduction in the MSE or an increase in the correlation of the results. Although the smaller KS for the CDF and EDCDF methods shows that these methods outperform the regression models in a distribution sense for the calibration period, all methods show a comparable performance in a distribution sense for the validation period (KS for all methods are close in the validation). As a result, the quantitative measures in Table 4.3 confirm that the ANN method outperforms the other approaches particularly in the validation period. This generalization capability of the network is vital since the main objective of the proposed method is to construct a trained network that performs well on a new set of inputs.

Given that the regression models are able to improve not only precipitation error but also correlation and the probabilistic structure of precipitation relative to the target, we use the linear regression (LR) and the developed ANN (Fig. 4.27) to reduce the biases of precipitation pixel by pixel for the entire domain extending from 80°W to 35°W (longitude) and from 23°S to 12°N (latitude) (see Fig. 4.2). The seasonal CCSM precipitation (input) and the corresponding CRU precipitation (target) from 1901 to 2013 are divided into two separate datasets for each season: March, April, May (MAM); June, July, August (JJA); September, October, November (SON); December, January, February (DJF). Data from 1901-1956 are used to train the model in the calibration period and data from 1957-2013 are used to test the performance of the trained model in the validation period. The performance of the regression models to improve the statistics of the results during the validation period is illustrated in the Figures below. The corresponding figures for the calibration periods are provided in Appendix C.

Figure 4.33 illustrates the original MSE, Bias, ρ, and KS (between biased precipitation and the target) in season MAM. The figure indicates that CCSM3 can simulate precipitation well over most part of Brazil (smaller MSE and KS as well as higher correlation). CCSM3 does not perform well over the west coast and the northeast of the domain (larger MSE).

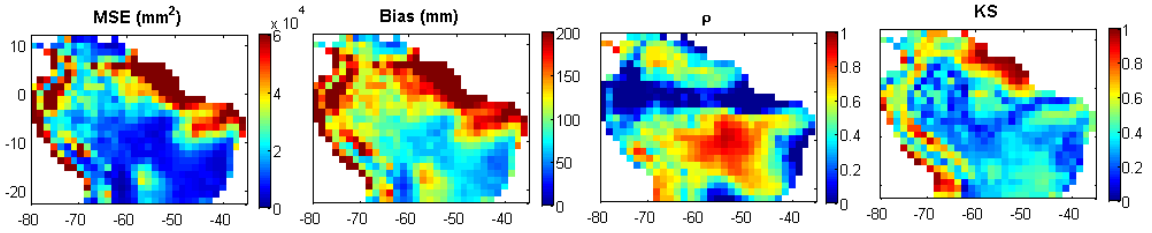

Figure 4.33. From left-to-right: The MSE, Bias, ρ, and KS between target and input precipitation before bias correction in season MAM.

Figure 4.34 shows improvements of the MSE, Bias, ρ, and KS by the LR and ANN in season MAM. The figure shows that the LR and ANN models are able to improve the results for all pixels in the study domain. Smaller improvements of the error or KS over some regions (shown with the blue color in Fig. 4.34) are due to the fact that the original error or KS between the input and the target is small (see Fig. 4.33). The original correlation over most parts of the domain is high (see red color in Fig. 4.33), but it can still be improved by the regression models particularly by ANN. The regression models can significantly increase very low correlation (see the red color in the third row in Fig. 4.34). While the LR shows a comparable performance to the ANN, the ANN yields better results in terms of MSE, Bias, ρ, and particularly KS during season MAM.

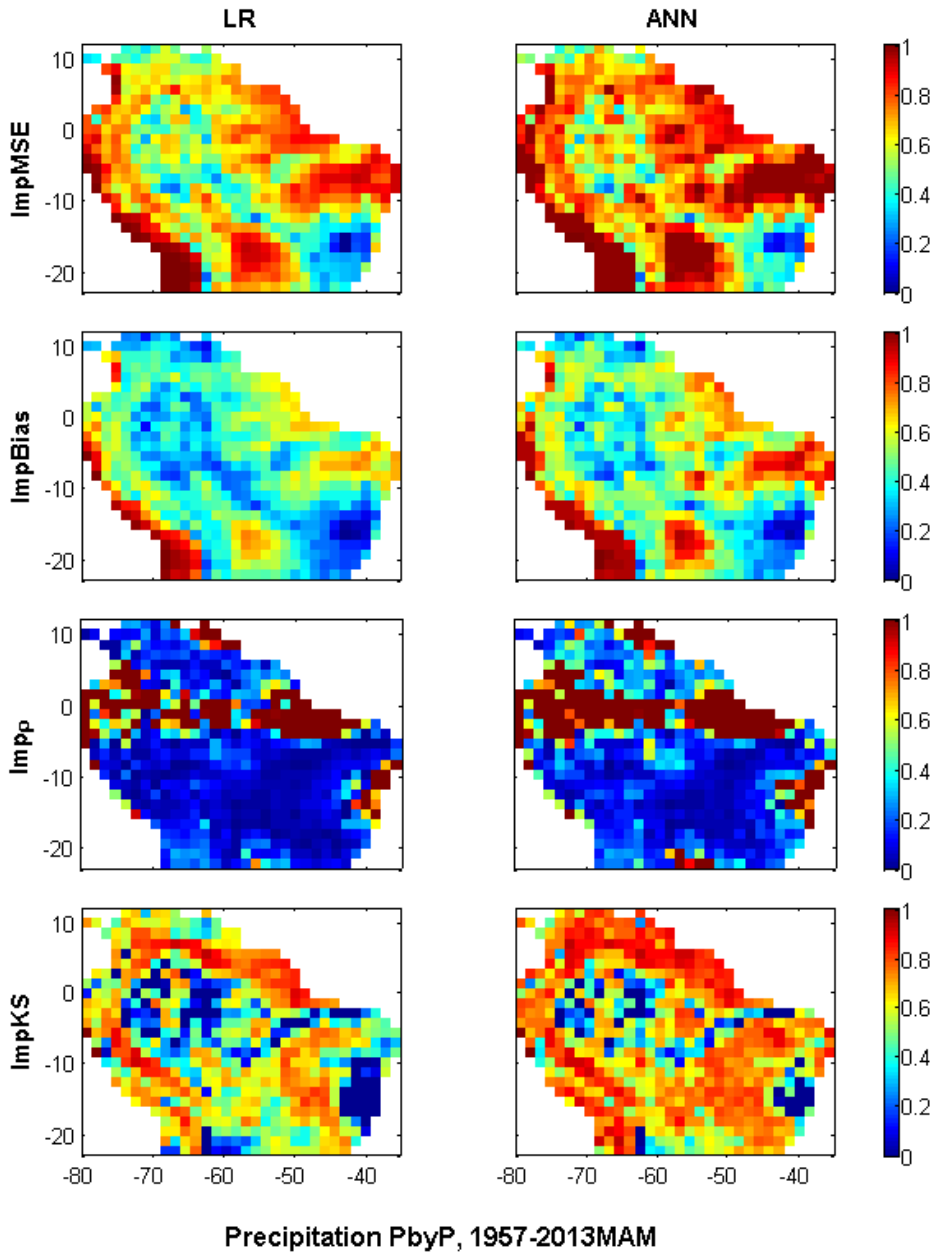

Figure 4.34. From top-to-bottom: Improvements of the MSE (ImpMSE), Bias (ImpBias), ρ (Impρ), and KS (ImpKS) by the linear (LR) and nonlinear (ANN) methods for the validation (MAM 1957-2013).

The original MSE, Bias, ρ, and KS (between biased precipitation and the target) in season JJA is shown in Figure 4.35. As we can see, CCSM3 shows a large error in precipitation over the northwest of the domain. The correlation is very low almost all over the domain.

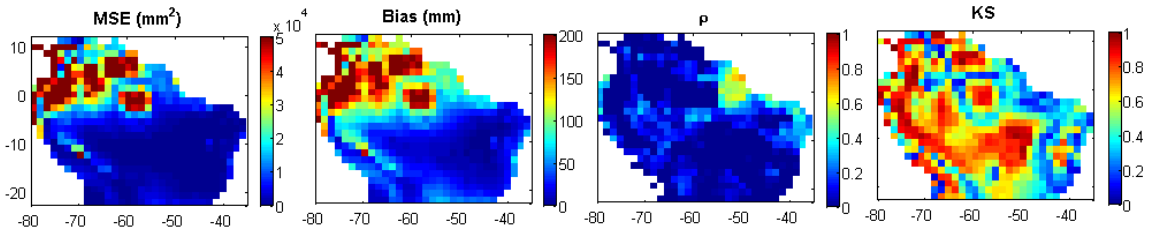

Figure 4.35. Same as Fig. 4.33 but for JJA.

All statistics are improved by the LR and the ANN (see Fig. 4.36). The overall domain average improvements of the MSE, Bias, and KS in season JJA by the LR are 51%, 38%, and 35%, respectively and the corresponding improvements by the ANN are 58%, 45%, and 49%, respectively. The lowest domain average improvements of the MSE, Bias, and KS occur in this season, JJA. This can be due to the fact that the minimum domain average of the original correlation occurs in this season (domain $\bar{\rho}$ = 0.16). A high correlation between the input and target is an important factor in establishing a proper relationship between the input-output. It is clear, though, that the correlation is still significantly improved by the LR and ANN all over the domain (see the red color on the third row in Fig. 4.36). The domain average improvement of the ρ by the LR and ANN is 570% and 770%, respectively.

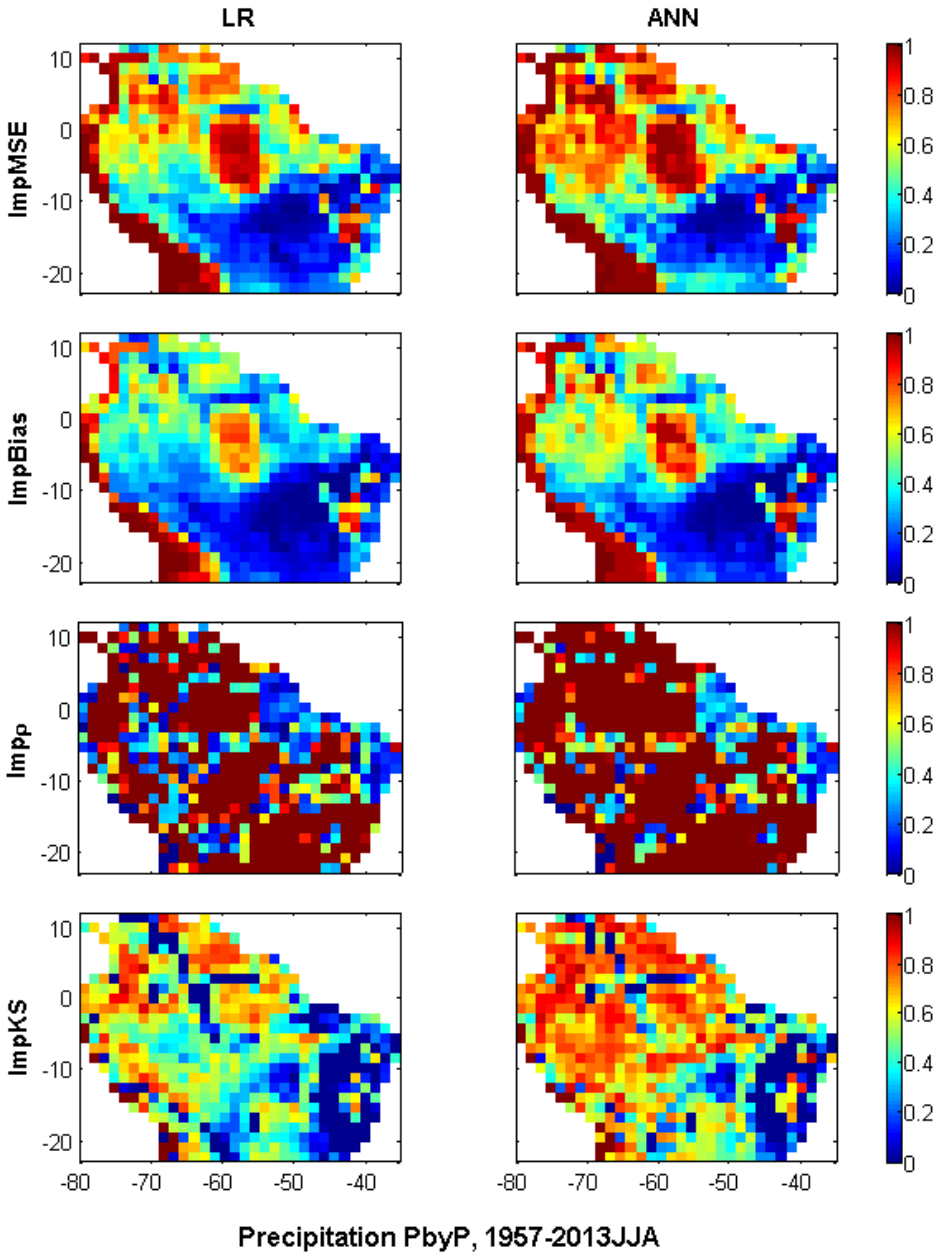

Figure 4.36. Same as Fig. 4.34 but for JJA.

Figure 4.37 illustrates the original MSE, Bias, ρ, and KS (between biased precipitation and the target) in season SON.

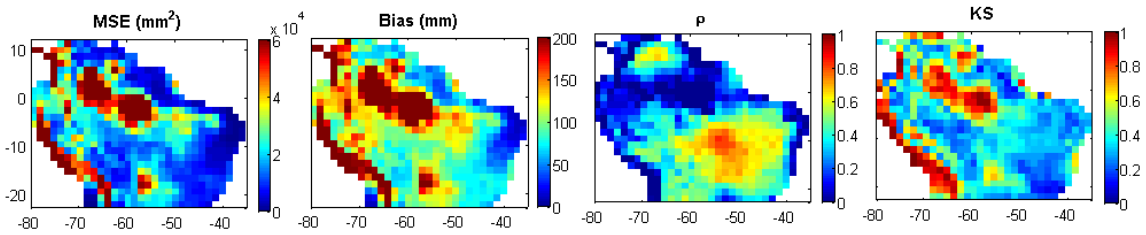

Figure 4.37. Same as Fig. 4.33 but for SON.

Scrutiny of Figures 4.33, 4.35, and 4.37 demonstrates that in each season the highest error occurs over the region that has the maximum rain. This indicates that CCSM3 underestimates high rates of precipitation, which can be improved by the LR and ANN models (see Fig. 4.36). We can see a similar pattern in Figures 4.37 and 4.38, meaning that the higher improvements of the MSE, KS, and ρ occur over the region that has larger MSE, KS, and smaller ρ, respectively. Figure 4.38 shows that although the ANN and LR have a comparable performance in improving the error in season SON, the ANN outperforms the LR in improving ρ and KS. The LR and ANN are able to improve the low original correlation (shown with the blue color in the third column in Fig. 4.37). Similar improvements of the statistics in both calibration (see Appendix C) and validation periods reveal that the trained model has the ability to perform well when the observation is not available.

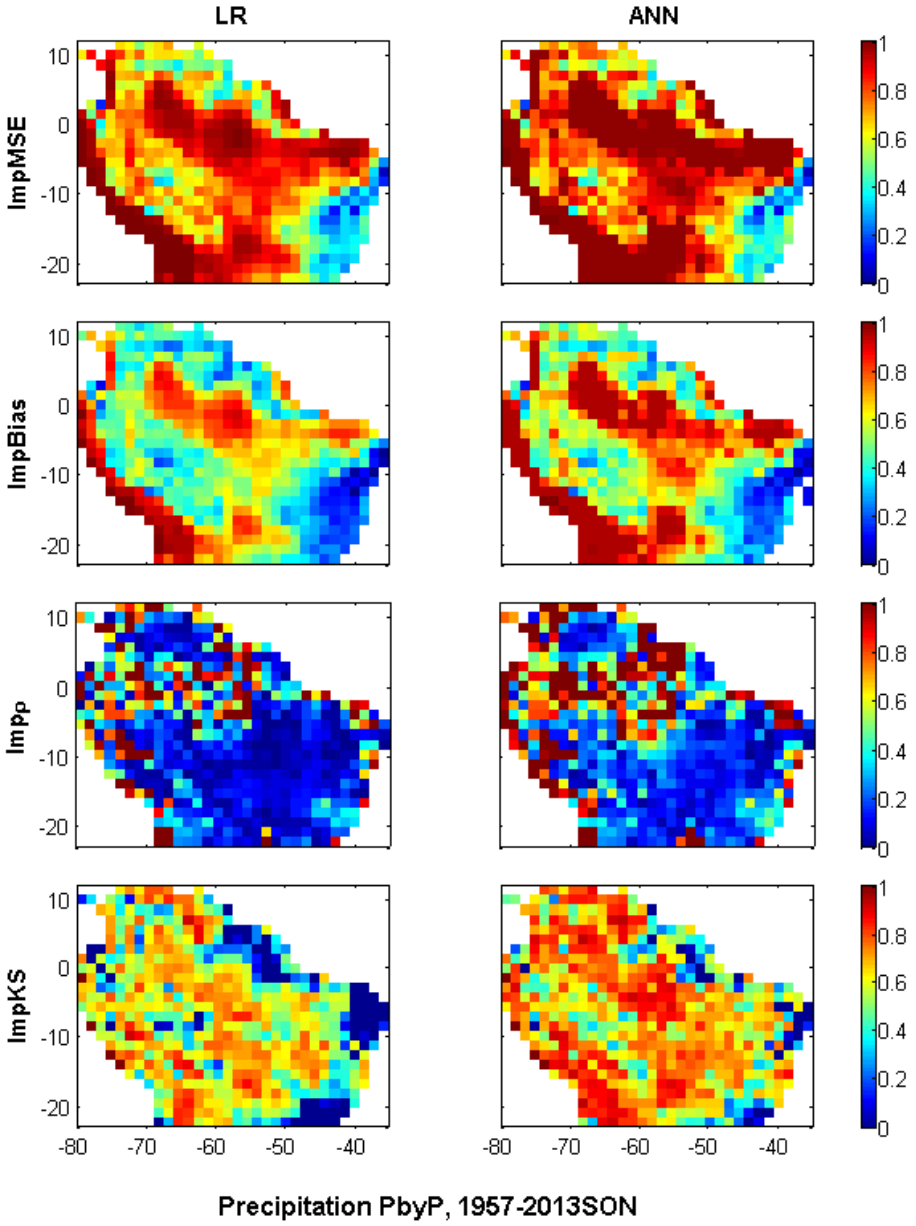

Figure 4.38. Same as Fig. 4.34 but for SON.

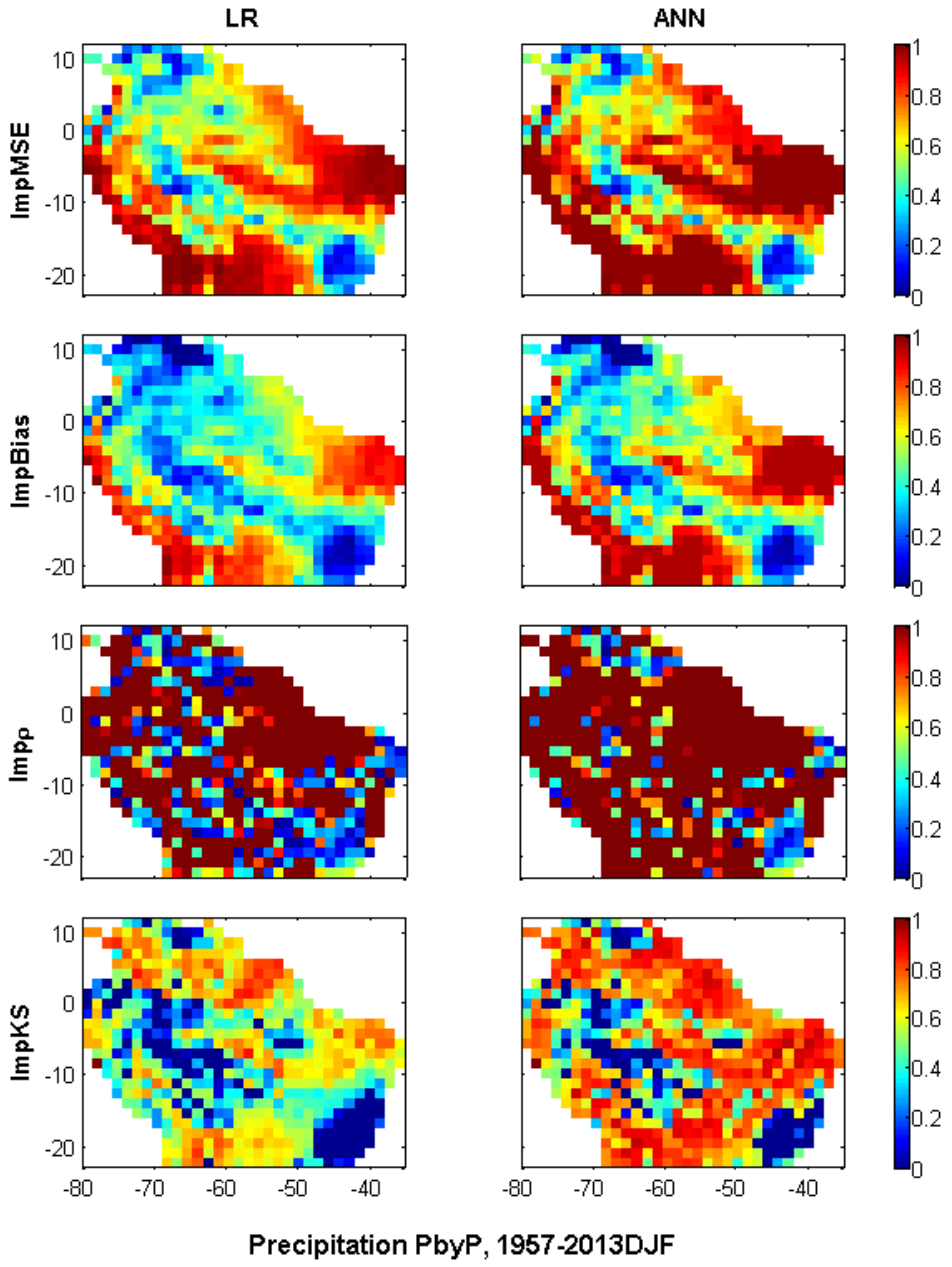

Figure 4.39. Same as Fig. 4.34 but for DJF.

Figure 4.39 shows that the regression models, particularly ANN, improve MSE, Bias, ρ, and KS over the domain during season DJF. The maximum domain average of the original MSE and Bias (between input and target precipitation) occurs in season DJF (44671mm^2 and 161.81mm, respectively). The overall domain average improvements of the MSE, Bias, and KS by the LR are 67%, 50%, and 39%, respectively and the

corresponding improvements by the ANN are 75%, 60%, and 56% for this season. The original correlation in this season is low, which can be increased by the regression method. The domain average improvement of ρ is 759% and 874% by the LR and ANN, respectively.

The results indicate that the regression models, particularly ANN, can reduce the biases of the CCSM3 precipitation, and improve the precipitation time series in the correlation and distribution sense. This improvement is more dominant when the original error is large. Table 4.4 summarizes the overall domain average percent improvements of the statistics by the LR and ANN models for both calibration and validation periods in all seasons.

Table 4.4. Domain average percent improvements of the MSE (ImpMSE), Bias (ImpBias), ρ (Impρ), and KS (ImpKS) for calibration, Cal (1901-1956) and validation, Val (1957-2013).

Season		**ImpMSE**		**ImpBias**		**Impρ**		**ImpKS**	
		Cal	**Val**	**Cal**	**Val**	**Cal**	**Val**	**Cal**	**Val**
MAM	**LR**	74	66	55	47	121	191	57	44
	ANN	82	75	65	56	155	222	74	61
JJA	**LR**	58	51	42	38	341	570	36	35
	ANN	65	58	50	45	511	770	50	49
SON	**LR**	74	69	56	51	136	89	54	45
	ANN	80	75	64	59	168	140	69	60
DJF	**LR**	76	67	59	50	797	759	56	39
	ANN	83	75	69	60	886	874	72	56

We also look at the correlation length in both S-N and W-E directions, centered at latitude = 6.3°S and longitude = 60.47°W (see Figs. 4.40, 4.41).

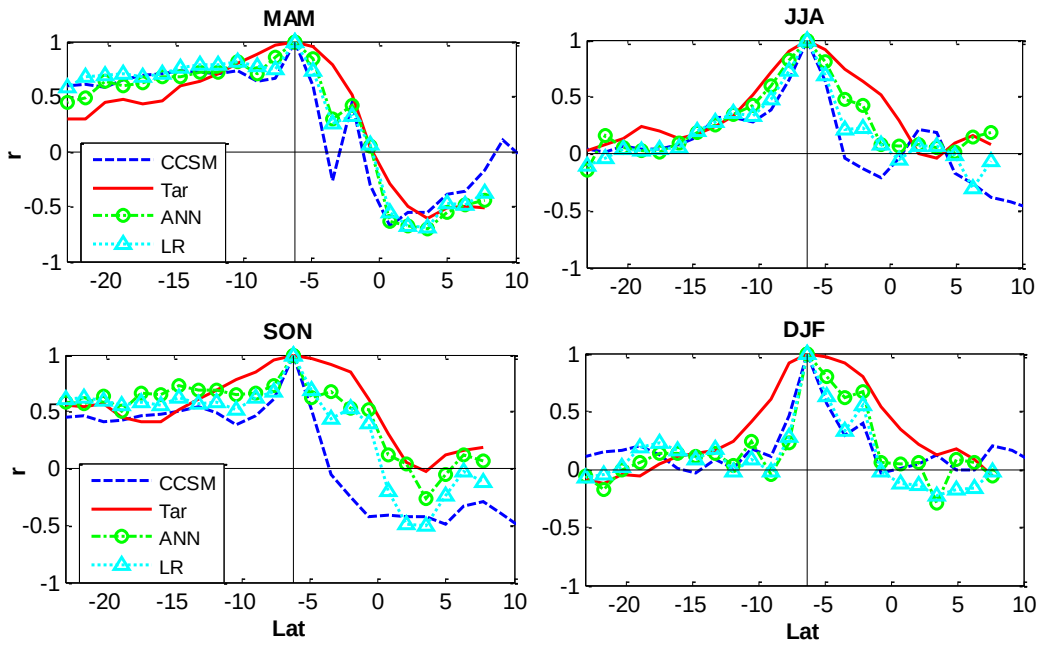

Figure 4.40. The correlation length in the S-N direction, centered at latitude = 6.3°S and longitude = 60.47°W for the validation (1957-2013). r is spatial correlation. Blue dashed lines refer to CCSM, red solid lines refer to target, green dash-dot lines with circle markers refer to ANN outputs, and the cyan dotted line with triangle markers refer to LR outputs.

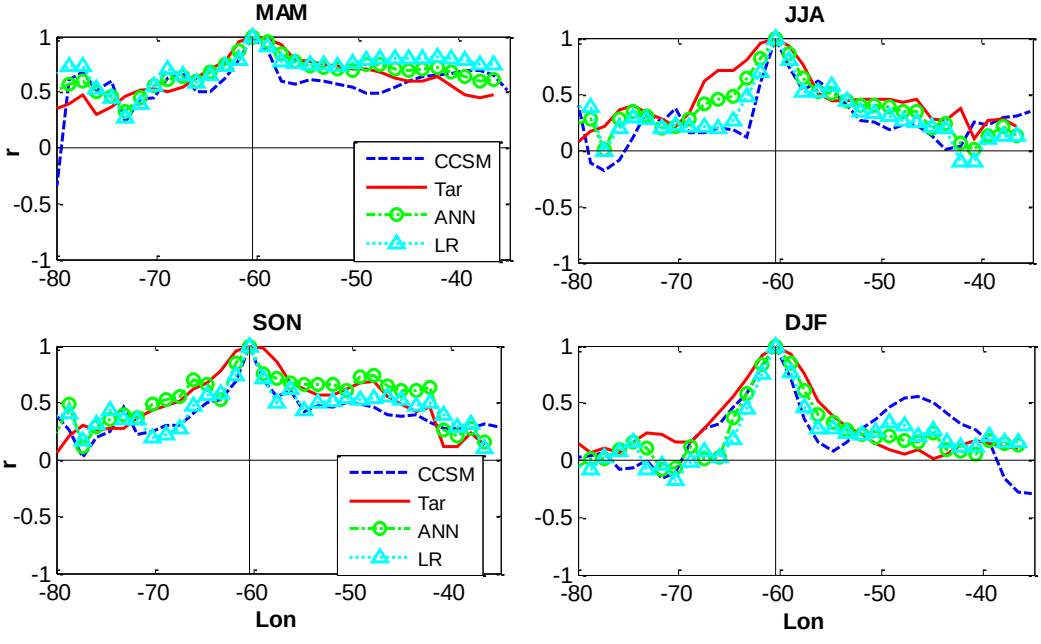

Figure 4.41. Same as Fig. 4.40 but for the W-E direction.

Results show that the spatial correlation of bias-corrected precipitation can be better conserved in the longitude direction than the latitude direction.

4.4. Summary

Large errors in temperature and precipitation values over the domain in all months/seasons are evident. The overall highest and lowest domain average errors for temperature occur in the months of September and December, respectively. In general, the skill of CCSM3 in simulating temperature over the west coast, western Brazil, and the southern part of the domain is weak in all months. In some months (e.g., Jan., Feb.), large errors extend to the north and the southeast of the domain, and in some months (e.g., Sep., Oct.) to the center of the domain.

The overall highest and the lowest domain average errors for precipitation occur in seasons DJF and JJA, respectively. CCSM3 shows a poor performance in simulating precipitation over the west coast.

A one hidden layer feedforward neural network with hyperbolic tangent-linear transfer functions for hidden-output layers was used to reproduce bias-corrected temperature and precipitation. Proper sets of inputs including T, TS, Q, LW_n, SW_n and $P_t, P_{t-1}, P_{t-2}, P_{t-3}, \sigma_t^{3by3}$ were used as inputs to the neural networks for the bias correction of temperature and precipitation, respectively. Including the standard deviation of precipitation from 3 by 3 neighbors around the pixel of interest (σ_t^{3by3}) as the input can improve the magnitude of the precipitation error. It can also adjust the variance of precipitation at each pixel relative to the neighbors. Note that we also tried lag-time temperature, mean, and standard deviation of temperature from 3 by 3 neighbors around the calculation pixel as the inputs to the network. But the best performance of the network was achieved using T, TS, Q, LW_n, SW_n as the inputs. This can be due to the fact that precipitation is more variable than temperature in time and space.

We compared the ANN results with the LR ones. The results showed that both regression models (LR and ANN) have the ability to improve the results in all terms of MSE, Bias, ρ, and KS not only in the calibration period but also in the validation period. Good performance of a model in the validation period indicates that the trained model can be generalized to an unseen dataset. ANN performs consistently better than LR in correcting the biases of temperature and precipitation and specifically in improving ρ and KS. The time-domain average improvements of the MSE, Bias, ρ, and KS for temperature are 76.33%, 52.5%, 29.75%, and 73% by the ANN, respectively and 68.92%, 45.08%, 20%, and 60.92% by the LR, respectively. The time-domain average improvements of the MSE, Bias, and KS for precipitation are 70.75%, 55%, and 56.5%, by the ANN, respectively and 63.25%, 46.5%, 40.75% by the LR, respectively.

The two regression models are able to increase performance even when original correlation of precipitation with the target was very small, which is not possible by the quantile-based mapping approach. Note that unlike the quantile-based mapping approach, the regression models do not directly take into account any specific information about the distribution of the underlying variables and they focus on improving lump error metrics. Although the distribution mapping approach generally outperforms the regression model in the distribution sense for the calibration period, their performance in the distribution sense are comparable to the regression method for the validation period (see Tables 4.1, 4.3).

The results confirm that the ANN model that is trained in response to the targets (observations) during the historical period has capability to generalize for the projection time. The trained ANN can improve all statistics such as MSE, Bias, ρ, and KS for the entire period.

The biases of temperature and precipitation are corrected independently. Figure 4.42 shows the cross-correlation between the monthly temperature and precipitation,

broken up by the season for the original CCSM, target, LR outputs, and ANN outputs during 1970-2008.

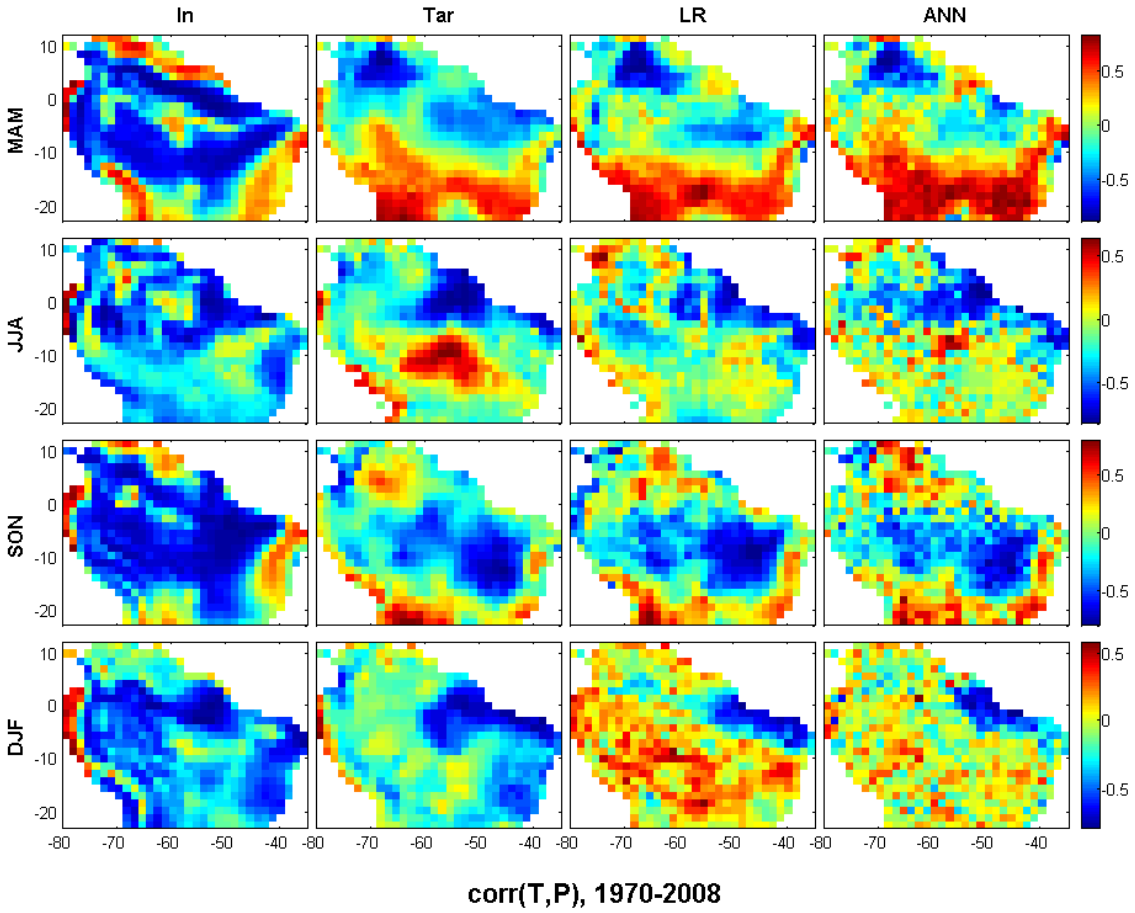

Figure 4.42. From left-to-right panels: The cross-correlation between the monthly temperature and precipitation, broken up by the season for the original CCSM (In), target (Tar), LR outputs, and ANN outputs during 1970-2008, respectively.

The patterns of the cross-correlation between T and P in targets and regression model outputs are similar, particularly during MAM, JJA, and SON. The difference in the patterns is evident during DJF.

CHAPTER 5

REGIONALIZATION OF THE ARTIFICIAL NEURAL NETWORK FOR BIAS CORRECTION OF TEMPERATURE AND PRECIPITATION

5.1. Introduction

Statistical bias correction methods such as the proposed ANN model are inferred relationships between inputs and outputs. They are based on available observations, which are limited in time and space. To be useful, the bias correction methods need to be generalizable and have predictive ability beyond the set of observations. In Chapter 4, we assessed the generalization ability of the ANN model in time (temporal generalization) by dividing the datasets into two independent periods (the calibration and validation periods). In this case, targets (observations) were available for all pixels in the study domain and we corrected the biases pixel by pixel by calibrating the model at each pixel. The results revealed that the trained ANN model performs well for both calibration and validation periods. A related question is whether the ANN model is useful over locations in space where observations are not available. In other words, does the ANN model have spatial generalization skill? In this Chapter, we use a regression approach to delineate regions over the study domain (see Fig. 4.2) that have common error behaviour and hence biases could be corrected with a regional model calibrated at a certain number of the pixels (training pixels).

5.2. Delineation of the Study Domain

The performance of CCSM3 in simulating temperature and precipitation varies with different physical features of the regions (e.g., topography, land cover, and climatology over the domain). The climate model could show similar systematic errors over "homogeneous" regions, i.e., regions with similar features. To correct the biases of the variables in each region, the ANN model can be trained with a limited number of pixels (training pixels) and then applied to the rest of the pixels (validating pixels) in that region. In what follows, we identify the pixels (minimum possible number) that are representative of larger regions and could be used as training pixels to predict the climate response elsewhere in the region. This identification exercise is done using Linear Regression (LR) because it has markedly lower computational cost and smoother regional behavior than the ANN.

5.2.1. Temperature

The goal of the regionalization is to identify a finite number of calibrations (training pixels) that would result in a response sufficiently close to the performance of the model calibrated at all domain pixels. Following is a description of how is this achieved using the month of March as an example.

First, we determine a pixel that has the largest bias in the study domain and, use the defined LR model (see section 4.2.1.1) for that pixel to find a proper set of weights. Then we use the calibrated LR model over all pixels in the domain (validating pixels) to correct the biases of temperature. Differences between the bias-corrected temperature and the targets (biases) are calculated at all pixels in the domain so a map of error is constructed. In the map, validating pixels that achieve a desired performance are defined as improved pixels. Then we find the new maximum bias over the domain and construct a relationship between the input-output using the LR model for that pixel (training pixel). The established relationship is applied for all pixels in the study domain. As a result, a

new error map including improved pixels is generated using the new training pixel. We repeat and continue the procedure until all pixels in the domain reach a pre-specified performance criterion. Each training pixel has an area of influence where the performance goal is achieved. These areas of influence may overlap, which can be combined to form one domain (see D1, D2, D3, D4, and D5 in Figure 5.1). In this case, the training pixel that performs best is used as the index pixel for the ambiguous areas.

Three performance criteria are explored. They are defined as reaching 70%, 80%, and 90% performance when using the model based on observations in every pixel (see Chapter 4). So pixels are identified as improved validating pixels when their biases are smaller than:

$$\begin{cases} 1.3 \times Bias_{PbyP} & For\ 70\%\ performance \\ 1.2 \times Bias_{PbyP} & For\ 80\%\ performance \\ 1.1 \times Bias_{PbyP} & For\ 90\%\ performance \end{cases} \quad (5.1)$$

where $Bias_{PbyP}$ is the bias between the bias-corrected temperature and the target, when the biases are corrected pixel by pixel (see Chapter 4). Figures 5.1, 5.2, and 5.3 show the delineation of the study domain and the corresponding training pixels for each domain in March for 70%, 80%, and 90% performances, respectively.

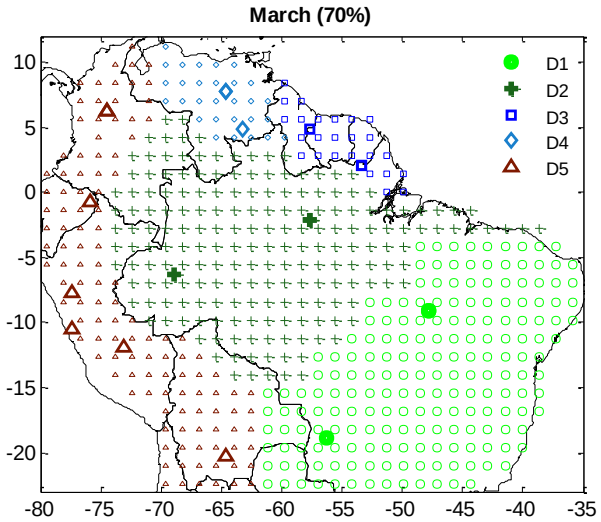

Figure 5.1. Delineation of the study area into five domains for 70% performance; D1 is over the southeast (circle), D2 over the central (cross), D3 over the northeast coast (square), D4 over the north (diamond), and D5 over the western of the study domain (triangle). Larger marker symbols denote training pixels in the delineated domains.

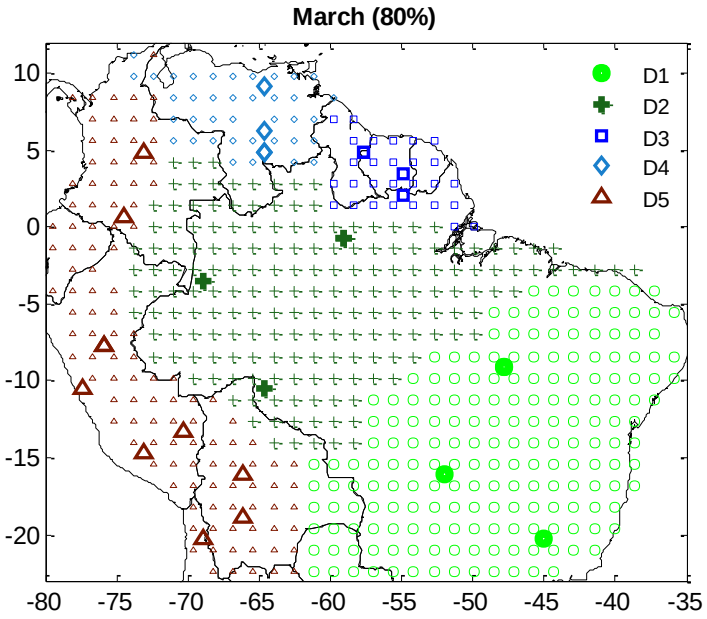

Figure 5.2. Same as Fig. 5.1 but for 80% performance.

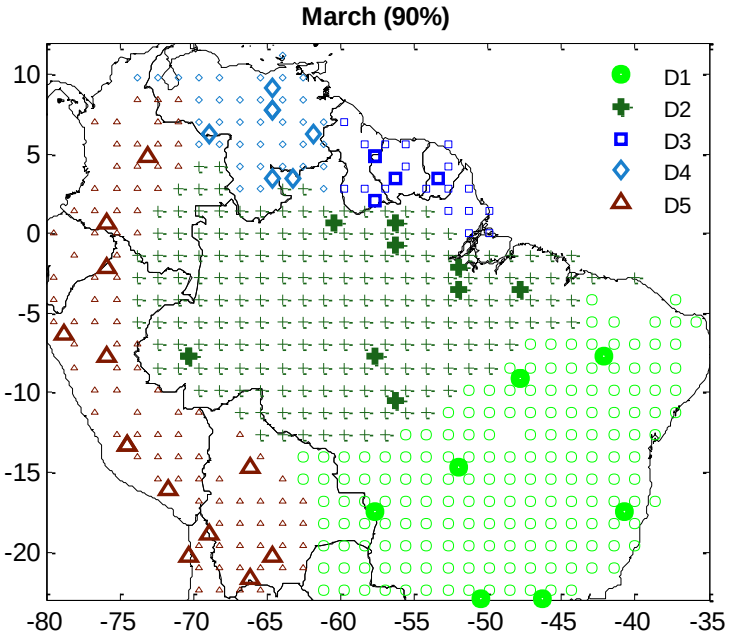

Figure 5.3. Same as Fig. 5.1 but for 90% performance.

Locations (latitude and longitude) of the training pixels in the delineated domains (D1, D2, D3, D4, D5) for 70%, 80%, and 90% performances are presented in Appendix D.

The results indicate that a small number of training pixels in each domain can be used to achieve a desired performance of the model to correct the temperature biases in other pixels of the domains. The training pixels shown in the figures above can be considered as the minimum number of training pixels that are required to get a desired performance at the validating pixels (VlP). There are some pixels that cannot reach the desired performance using the defined training pixels (TrP). Biases of temperature over those pixels are improved when they are selected as the training pixels for themselves (hereafter called Independent TrP, IndTrP). The IndTrPs do not have any symbols of circle, cross, square, diamond, or triangle (see blank space in Figs. 5.1, 5.2, or 5.3). The number of IndTrPs for 70%, 80%, and 90% performances is 39, 46, and 87, respectively. The performance of the regionalization in terms of number of training pixels versus validating pixels over the study domain for the three levels of performance is further illustrated in Figure 5.4.

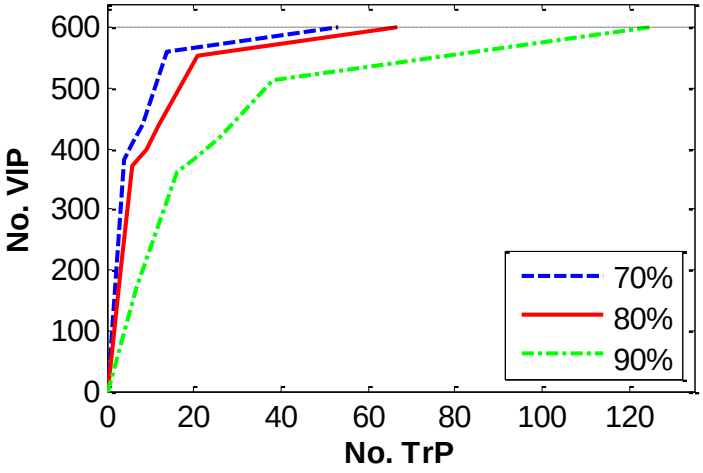

Figure 5.4. The performance curve. A comparison between the numbers of training pixels (No. TrP) vs. validating pixels (No. VlP) over the study domain for 70% (green dash-dot line), 80% (red solid line), and 90% (blue dashed line) performances in March.

As we can see, the required number of training pixels to cover the validating pixels is close for performances of 70% and 80%. The 90% performance needs about twice as

many training pixels as the 80% performance. The number of independent training pixels increases noticeably from 80% to 90% performance relative to the increase when going from the 70% to 80% performance levels. The results show that the total number of training pixels (including IndTrP) required to calibrate the model for bias correction of temperature over the entire study domain (600 pixels) is 53, 67, and 125 for 70%, 80%, and 90% performance levels, respectively. This indicates that performance can be satisfactory using a small number of observations to derive the bias correction models.

Now that the results in March confirm that the study domain can be delineated and a small number of training pixels is sufficient to generalize the model over the delineated domains, we assess the model skill for the other months. The desired performance level used for the following results is 80%. Figures 5.5 to 5.15 show the training pixels in the delineated domains (D1, D2, D3, D4, D5) for all months. Locations (latitude and longitude) of the training pixels are provided in Appendix D.

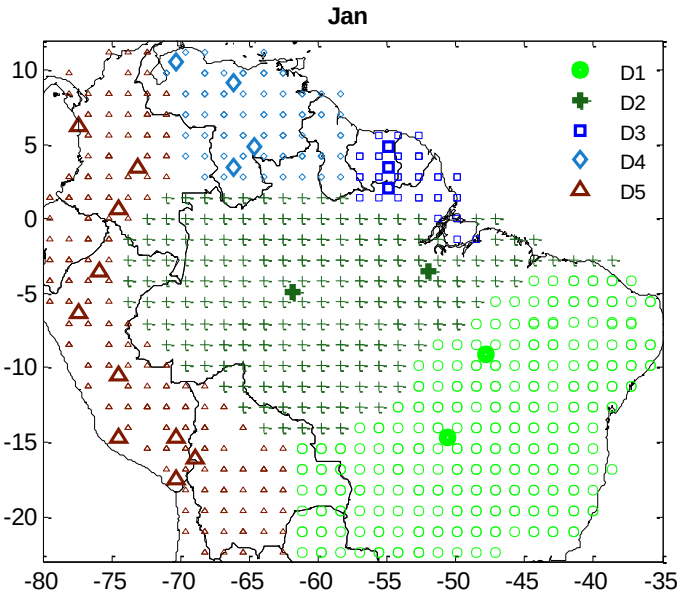

Figure 5.5. Same as Fig. 5.2 but for January.

The minimum number of training pixels (excluding IndTrP) needed to validate all domain pixels are during March and January (21 training pixels). In January, domains D1, D2, D3, D4, and D5 need 2, 2, 3, 4, and 10 training pixels, respectively. The number of independent training pixels is 43. The number of training pixels for D1, D2, D3, D4, and D5 is 2, 2, 6, 4, and 10, respectively in February (Fig. 5.6). The number of independent training pixels is 41 in this month.

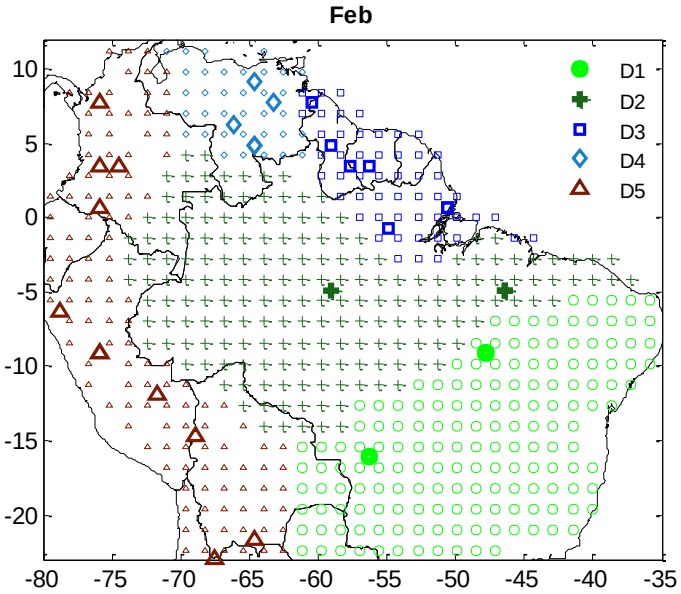

Figure 5.6. Same as Fig. 5.2 but for February.

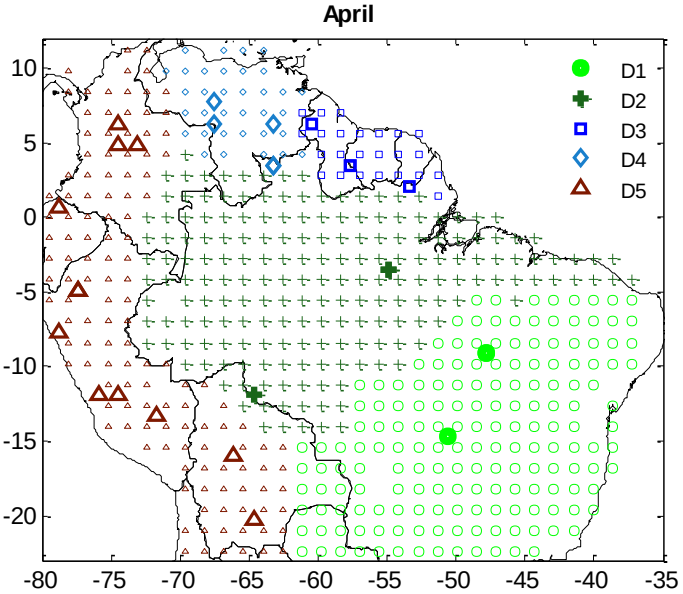

Figure 5.7. Same as Fig. 5.2 but for April.

Figure 5.7 shows that D1, D2, D3, D4, and D5 need 2, 2, 3, 4, and 11 training pixels, respectively in April. The number of independent training pixels is 46 in this month. The figure indicates that fewer numbers of training pixels is required to validate more number of pixels in homogeneous domains such as D1 and D2.

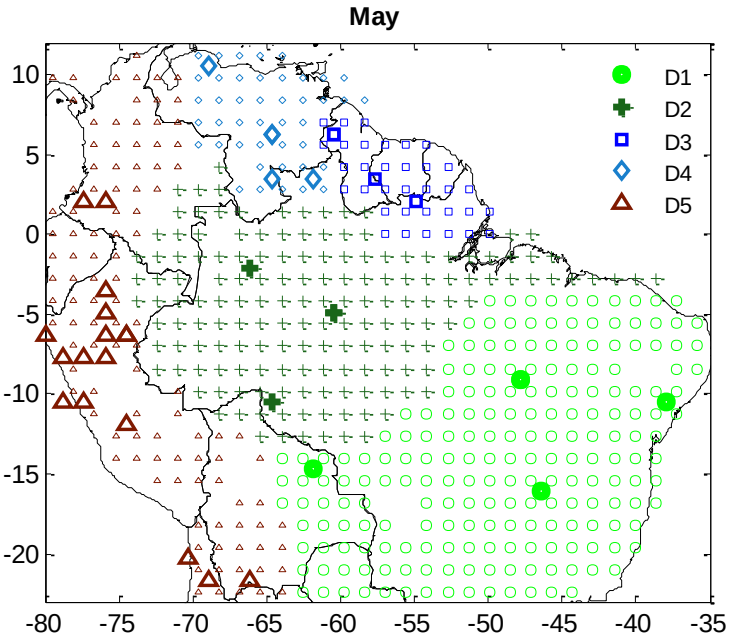

Figure 5.8. Same as Fig. 5.2 but for May.

The maximum number of training pixels (excluding the IndTrP) occurs in May (30 training pixels) compared to the other months. In other words, more training pixels are required to calibrate the model for bias correction of temperature at the validating pixels in the delineated domains for the month of May. The required minimum number of training pixels in D1, D2, D3, D4, and D5 is 4, 3, 3, 4, and 16, respectively. The number of independent training pixels is 52 in this month. The increase in the number of the training pixels is more evident in D5, which is a heterogeneous domain. The results can indicate that the delineated domains and the density of the corresponding training pixels are linked to the physical features of the domains such as land cover and topography. The detailed assessment of this interconnection is studied in section 5.3.

June has the maximum number of independent training pixels (59 IndTrP). In other words, the elected training pixels are not able to validate those 59 pixels (Fig. 5.9). Thus, the only alternative to correct the temperature values at those pixels is to construct a proper relationship between the input-output using observations over those pixels. D1, D2, D3, D4, and D5 need 4, 3, 2, 2, and 12 training pixels, respectively.

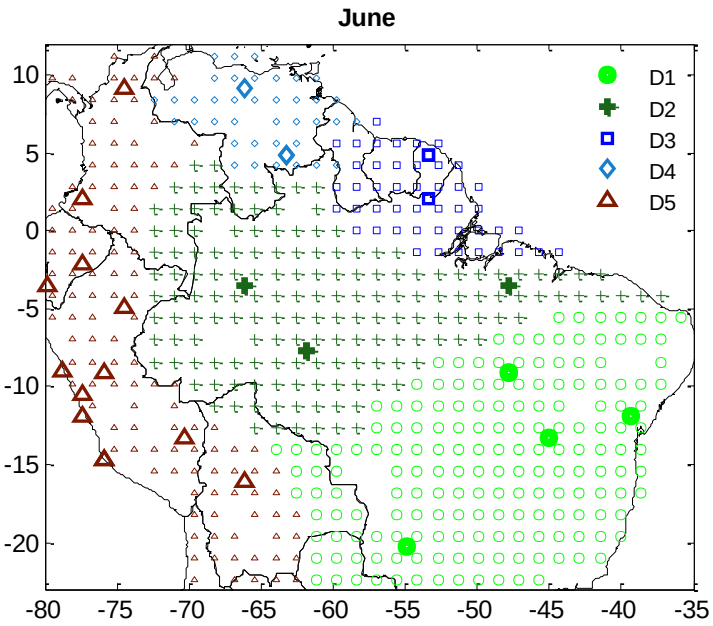

Figure 5.9. Same as Fig. 5.2 but for June.

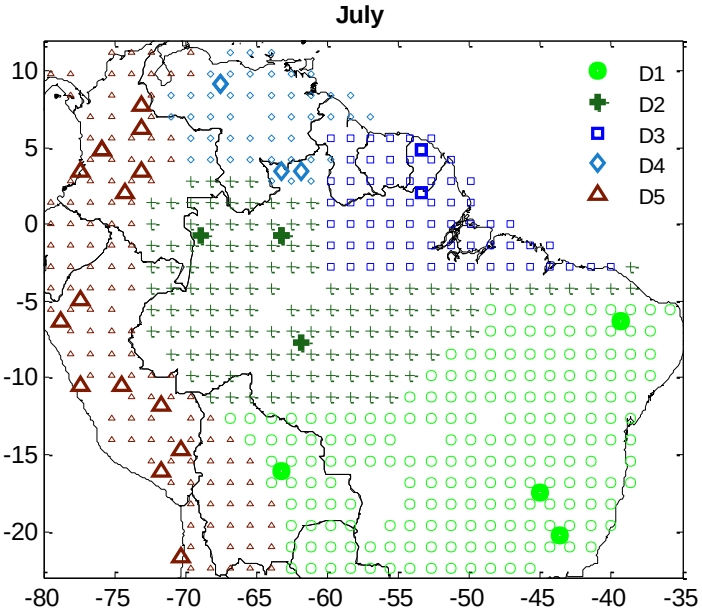

Figure 5.10. Same as Fig. 5.2 but for July.

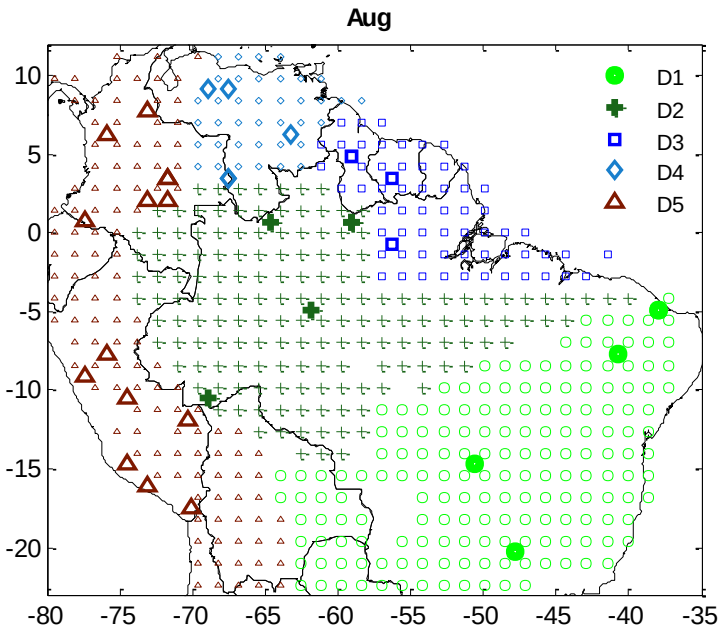

Figure 5.11. Same as Fig. 5.2 but for August.

The number of training pixels for D1, D2, D3, D4, and D5 in July is 4, 3, 2, 3, and 14, respectively (Fig. 5.10). The number of independent training pixels is 51 in this month. In August, D1, D2, D3, D4, and D5 need 4, 4, 3, 4, and 13 training pixels, respectively (Fig. 5.11). The number of independent training pixels is 49 in this month.

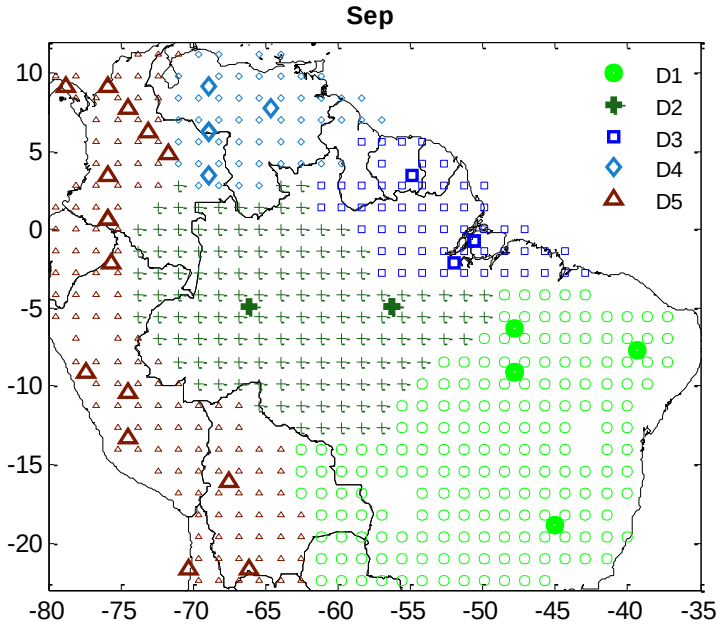

Figure 5.12. Same as Fig. 5.2 but for September.

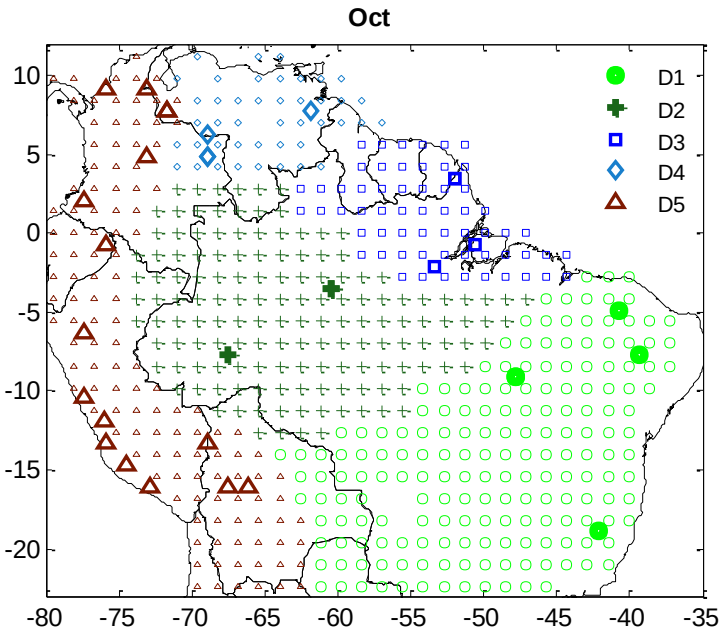

Figure 5.13. Same as Fig. 5.2 but for October.

The number of training pixels required for D1, D2, D3, D4, and D5 in September is 4, 2, 3, 4, and 14 training pixels, respectively with 27 independent training pixels (Fig. 5.12). A close scrutiny of the figures illustrates that independent training pixels are usually at the coast of the study domain, borders of the delineated domains, and D5. A complex and strong interaction between the land-ocean-atmosphere over the coast and the heterogeneity in D5 are most probably the cause of the increase in the number of independent training pixels. In October, D1, D2, D3, D4, and D5 need 4, 2, 3, 3, and 16 training pixels, respectively (Fig. 5.13). The number of independent training pixels is 46 in this month.

Figure 5.14 shows that the number of training pixels required for D1, D2, D3, D4, and D5 in November is 4, 3, 3, 4, and 14 training pixels, respectively and 28 independent training pixels.

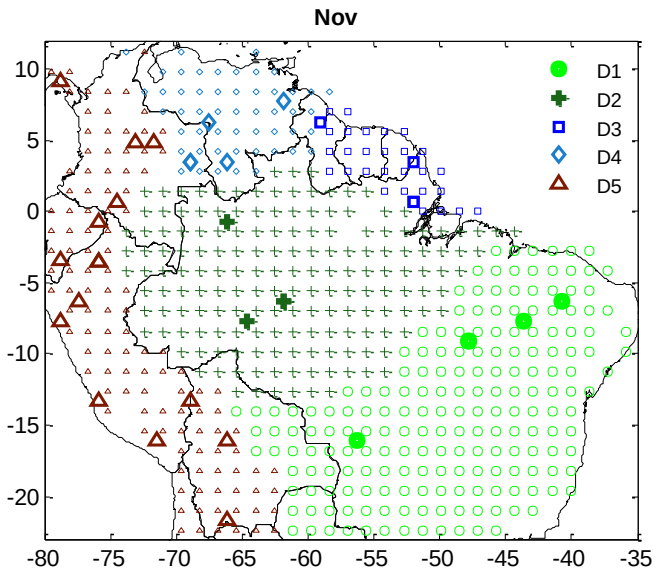

Figure 5.14. Same as Fig. 5.2 but for November.

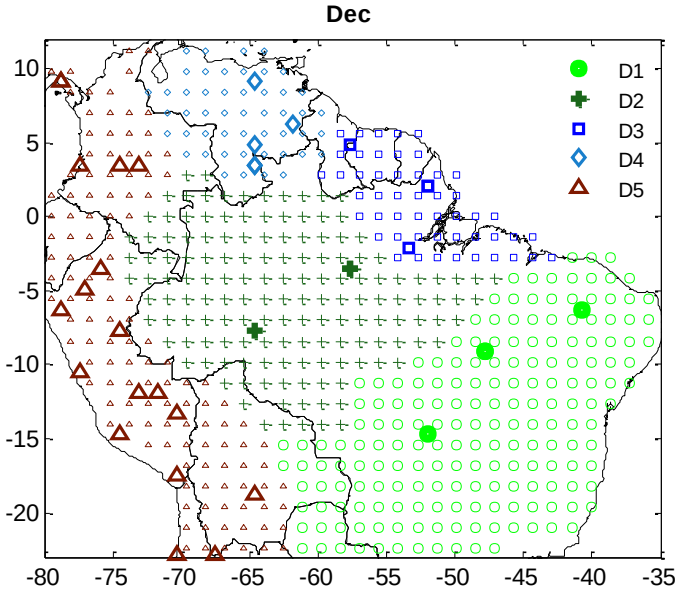

Figure 5.15. Same as Fig. 5.2 but for December.

In December, D1, D2, D3, D4, and D5 need 3, 2, 3, 4, and 17 training pixels, respectively (Fig. 5.15). As we can see, the high density of the training pixels is in D5, which is heterogeneous with higher elevation. The rest of the study domain is almost flat. The number of independent training pixels is 36 in this month, which is the minimum number compared to those required for the other months.

Table 5.1 summarizes the number of required training pixels to validate all pixels in the delineated domains for all months.

Table 5.1. The Number of training (TrP), independent training (IndTrP), and validating (VlP) pixels in each delineated domain (D1, D2, D3, D4, D5) for all months.

	Jan		**Feb**		**Mar**		**Apr**		**May**		**June**	
	No. TrP	**No. VlP**	**No. TrP**	**No. VlP**	**No. TrP**	**No. VlP**	**No. TrP**	**No. VlP**	**No. TrP**	**No. VlP**	**No. TrP**	**No. VlP**
D1	2	177	2	164	3	190	2	172	4	205	4	175
D2	2	179	2	186	3	181	2	192	3	158	3	162
D3	3	23	6	52	3	28	3	24	3	34	2	46
D4	4	53	4	36	3	40	4	34	4	43	2	38
D5	10	125	10	121	9	115	11	132	16	108	12	120
IndTrP	43		41		46		46		52		59	
	July		**Aug**		**Sep**		**Oct**		**Nov**		**Dec**	
	No. TrP	**No. VlP**	**No. TrP**	**No. VlP**	**No. TrP**	**No. VlP**	**No. TrP**	**No. VlP**	**No. TrP**	**No. VlP**	**No. TrP**	**No. VlP**
D1	4	186	4	171	4	176	4	180	4	192	3	186
D2	3	131	4	160	2	134	2	145	3	168	2	149
D3	2	65	3	61	3	55	3	60	3	28	3	50
D4	3	46	4	38	4	52	3	43	4	51	4	50
D5	14	121	13	121	14	130	16	126	14	116	17	129
IndTrP	51		49		53		46		45		36	

The results show that a relatively small number of observations can construct a robust model for bias correction of temperature at the other pixels with a good level of performance. The monthly average number of training pixels (including IndTrP) required to validate the entire study domain (600 pixels) is 73, which is only about 12% of the all pixels.

5.2.2. Precipitation

Similarly to temperature, we evaluate the possible regionalization of the bias correction of precipitation. We first examine the number of training pixels needed for season MAM under performance criteria of 70%, 80%, and 90% of bias error of the pixel-based correction (see Eq. 5.1). Figures 5.16, 5.17, and 5.18 show the training pixels for each delineated domain (D1, D2, D3, D4, D5) in MAM for 70%, 80%, and 90% performances, respectively.

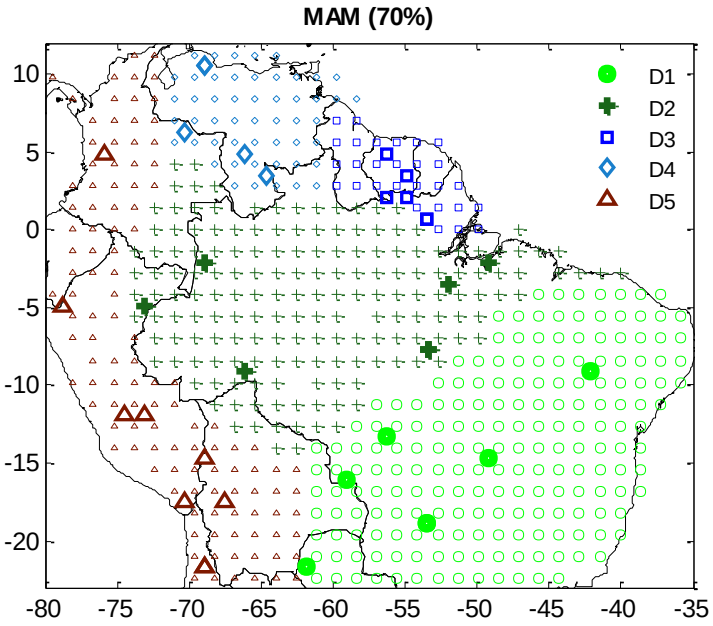

Figure 5.16. Training pixels (shown by the larger marker symbols) in the delineated domains; D1 (circle), D2 (cross), D3 (square), D4 (diamond), and D5 (triangle) at 70% performance during MAM.

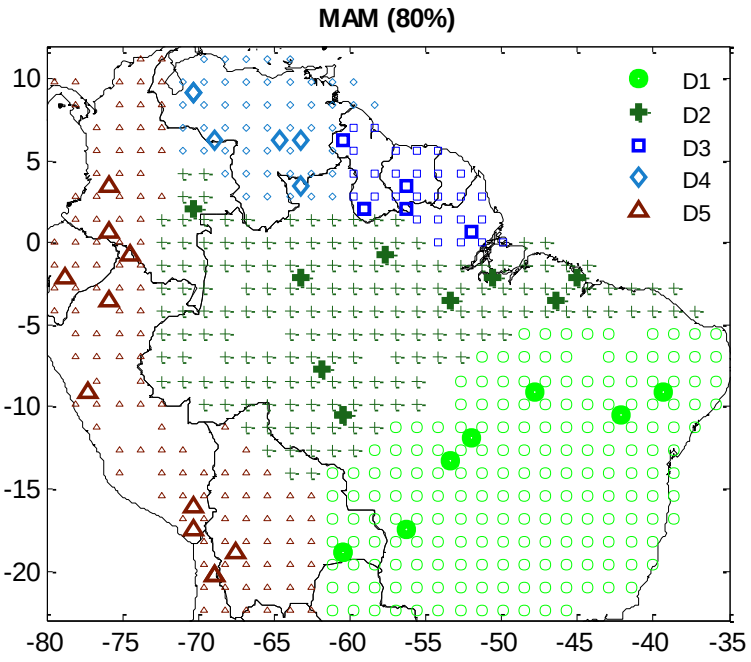

Figure 5.17. Same as Fig. 5.16 but for 80% performance.

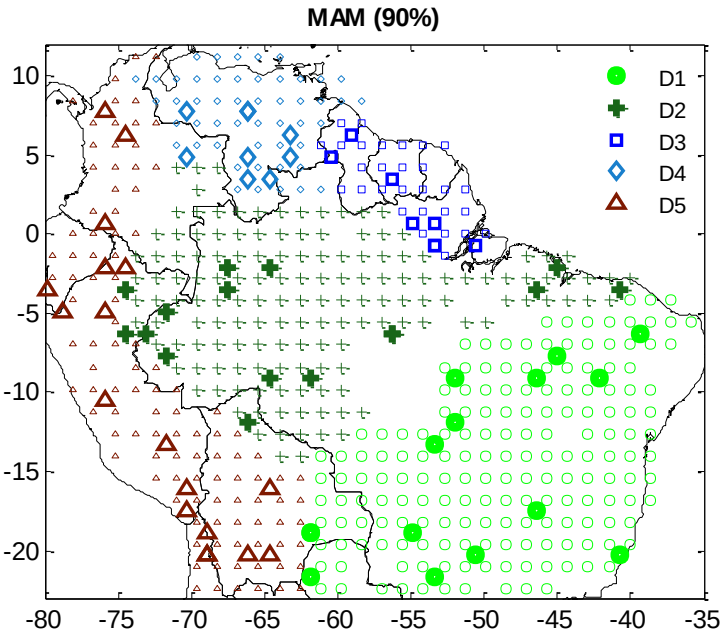

Figure 5.18. Same as Fig. 5.16 but for 90% performance.

Locations (latitude and longitude) of the training pixels in each delineated domain (D1, D2, D3, D4, D5) during MAM for 70%, 80%, and 90% performances are presented in Appendix D. The number of IndTrPs for precipitation regionalization during MAM for 70%, 80%, and 90% performance criteria is 37, 47, and 88, respectively. The results show that the regionalization of the model to reduce the precipitation biases at 70%, 80%, and 90% levels of performance needs more training pixels than the regionalization model for bias correction of temperature. This is consistent with the fact that precipitation is a highly complex and nonlinear process with higher variability and uncertainty. Note that using a small number of training pixels to correct the biases of precipitation at all domain pixels noticeably reduces the computational requirements, time, and memory usage. Figure 5.19 shows the number of validating pixels as a function of training pixels and performance criteria.

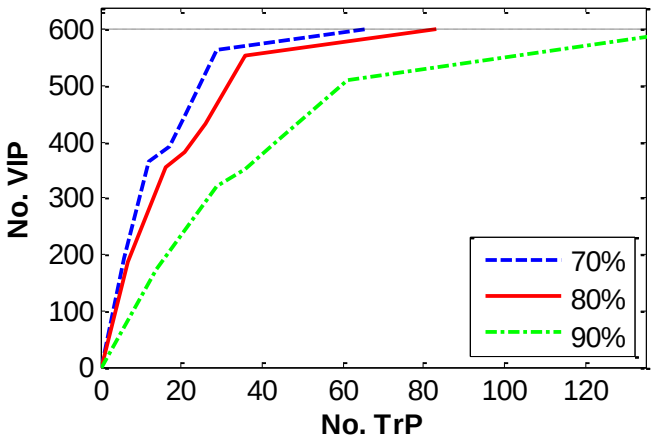

Figure 5.19. Performance curve. A comparison between the numbers of training pixels (No. TrP) vs. validating pixels (No. VlP) over the study domain for 70% (green dash-dot line), 80% (red solid line), and 90% (blue dashed line) performances in MAM.

The total number of training pixels (including IndTrP) required to establish a reliable relationship between the input-output to correct the precipitation biases over the entire study domain (600 pixels) for 70%, 80%, and 90% performances is 66, 83, 149, respectively. Lots of observations are not needed to construct a robust model. A small

number of good observations is able to satisfactorily regionalize the model (e.g., 11%, 14%, and 25% of all pixels for 70%, 80%, and 90% performances, respectively). The performance curve (Fig. 5.19) illustrates that the number of required training pixels is close for performance at 70% and 80% levels while the number rises considerably for a 90% performance level.

A performance level of 80% is used in what follows to define the number of training pixels required to regionalize bias correction over the other seasons. Figures 5.20 to 5.22 show the training pixels for the delineated domains (D1, D2, D3, D4, D5) in all seasons. Locations (latitude and longitude) of the training pixels are provided in Appendix D.

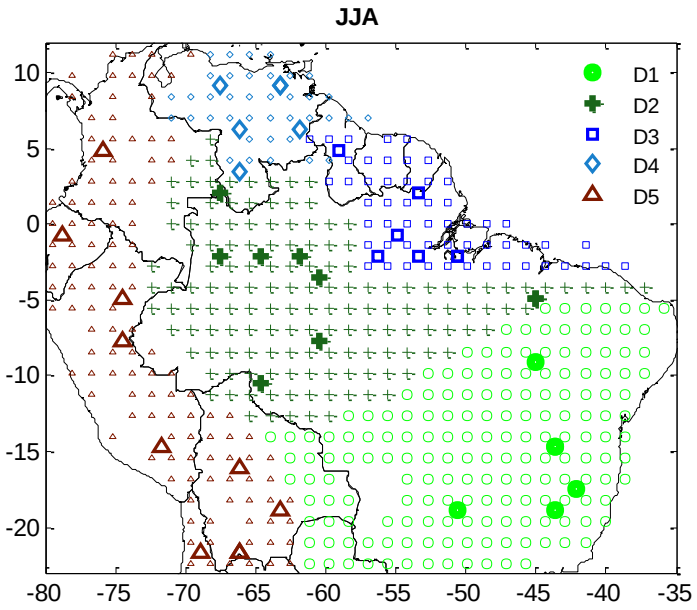

Figure 5.20. Same as Fig. 5.17 but for JJA.

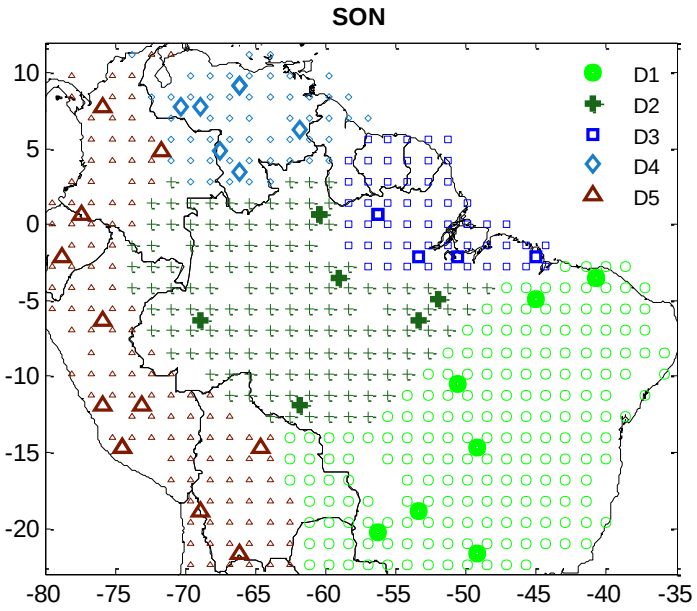

Figure 5.21. Same as Fig. 5.17 but for SON.

Season JJA needs the maximum number of training pixels, including IndTrP (97), to achieve the 80% performance at all domain pixels (Fig. 5.20). This can be due to the fact that most of the study domain is dry in JJA (with many zero or low values of precipitation). As a result, we need more training pixels and corresponding observations to construct a robust model. The number of training pixels for D1, D2, D3, D4, and D5 is 5, 8, 6, 5, and 9, respectively with 64 independent training pixels.

In SON, domains of D1, D2, D3, D4, and D5 need 7, 6, 4, 6, and 11 training pixels, respectively (Fig. 5.21). The number of independent training pixels is 53 in this season. A close scrutiny of the figures shows that the independent training pixels are mostly located at the coast of the study domain, borders of the delineated domains, and D5, which agrees with the results obtained from the regionalization of the temperature bias correction. The delineation and density of the training pixels can be related to the physical features of the study domain (such as topography, land cover, and climatology over the region), which are studied in the following section.

Figure 5.22 shows that DJF needs the minimum number of training pixels (including IndTrP) to regionalize the results at the desired performance (73). The

required minimum number of training pixels in D1, D2, D3, D4, and D5 is 5, 5, 4, 4, and 7, respectively. The number of independent training pixels is 48 in this season.

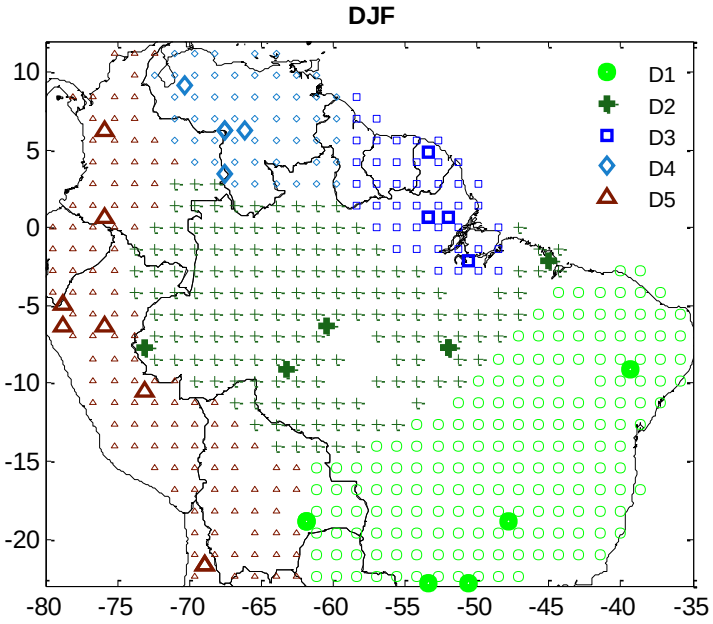

Figure 5.22. Same as Fig. 5.17 but for DJF.

Table 5.2 summarizes the number of required training pixels to validate all pixels in the delineated domains for all seasons. The seasonal average number of training pixels (including IndTrP) required to validate the entire study domain (600 pixels) is 85, which is only about 14% of the all pixels.

Table 5.2. The Number of training (TrP), independent training (IndTrP), and validating (VlP) pixels in each delineated domain (D1, D2, D3, D4, D5) for all seasons.

	MAM		**JJA**		**SON**		**DJF**	
	No. TrP	**No. VlP**	**No. TrP**	**No. VlP**	**No. TrP**	**No. VlP**	**No. TrP**	**No. VlP**
D1	7	187	5	172	7	184	5	174
D2	9	167	8	149	6	134	5	157
D3	5	27	6	55	4	54	4	44
D4	5	52	5	38	6	53	4	56
D5	10	120	9	122	11	122	7	121
IndTrP	47		64		53		48	

The results indicate that although the regionalization of the precipitation bias correction needs more calibrated pixels than that of temperature, a small number of the pixels in the study domain suffices to regionalize the results of bias correction for both temperature and precipitation with a prescribed accuracy. Furthermore, the results can demonstrate a reliable linkage between the delineation of the domain (density of the training pixels) and physical features of the regions, which is evaluated in the following section.

5.3. Physical Origins of the Regionalization

Here we investigate if the regionalization resulting from the statistical analysis can be related to features like land cover type, elevation, and temperature and precipitation as indicators for climatology.

The land cover data is from the Land Cover Type Climate Modeling Grid (CMG) product derived from Terra and Aqua MODIS data (publically available at https://lpdaac.usgs.gov/products/modis_products_table/mcd12c1). The product has 17 land cover classes, including 11 natural vegetation classes, 3 developed and mosaicked land classes, and 3 non-vegetated land classes defined by the International Geosphere Biosphere Programme, IGBP (see Fig. 5.23).

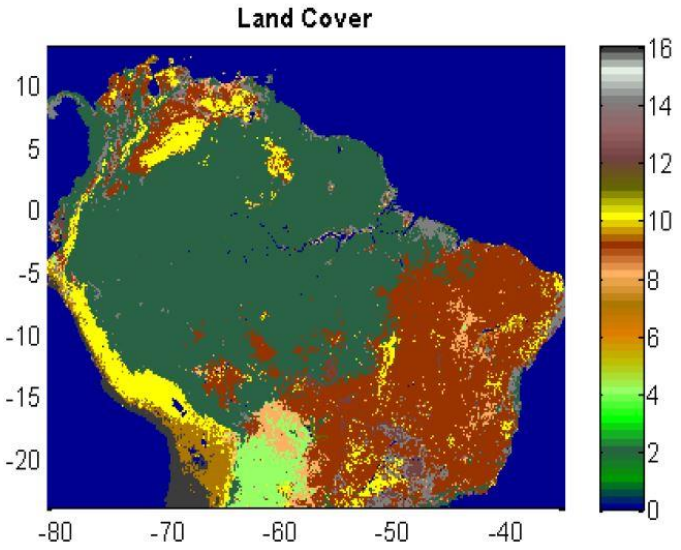

Group	Class
16	barren or sparsely vegetated
15	snow and ice
14	cropland/natural vegetation mosaic
13	urban and built-up
12	croplands
11	permanent wetlands
10	grasslands
9	savannas
8	woody savannas
7	open shrub lands
6	closed shrub land
5	mixed forests
4	deciduous broadleaf forest
3	deciduous needleleaf forest
2	evergreen broadleaf forest
1	evergreen needleleaf forest
0	water

Figure 5.23. Land cover classifications defined by the IGBP over the study domain.

Temperature and precipitation data are from MFD (see section 1.3.2), which were used as targets for bias correction of temperature. The elevation data are obtained from 30 arc-second Digital Elevation Model (DEM) of South America, provided by the U.S. Geological Survey's (USGS) EROS Data Center in Sioux Falls, South Dakota (publically available at http://databasin.org/datasets/d8b7e23f724d46c99db1421623fd1b4f). The average temperature, total precipitation, and elevation are illustrated in Figures 5.24, 5.25, and 5.26, respectively.

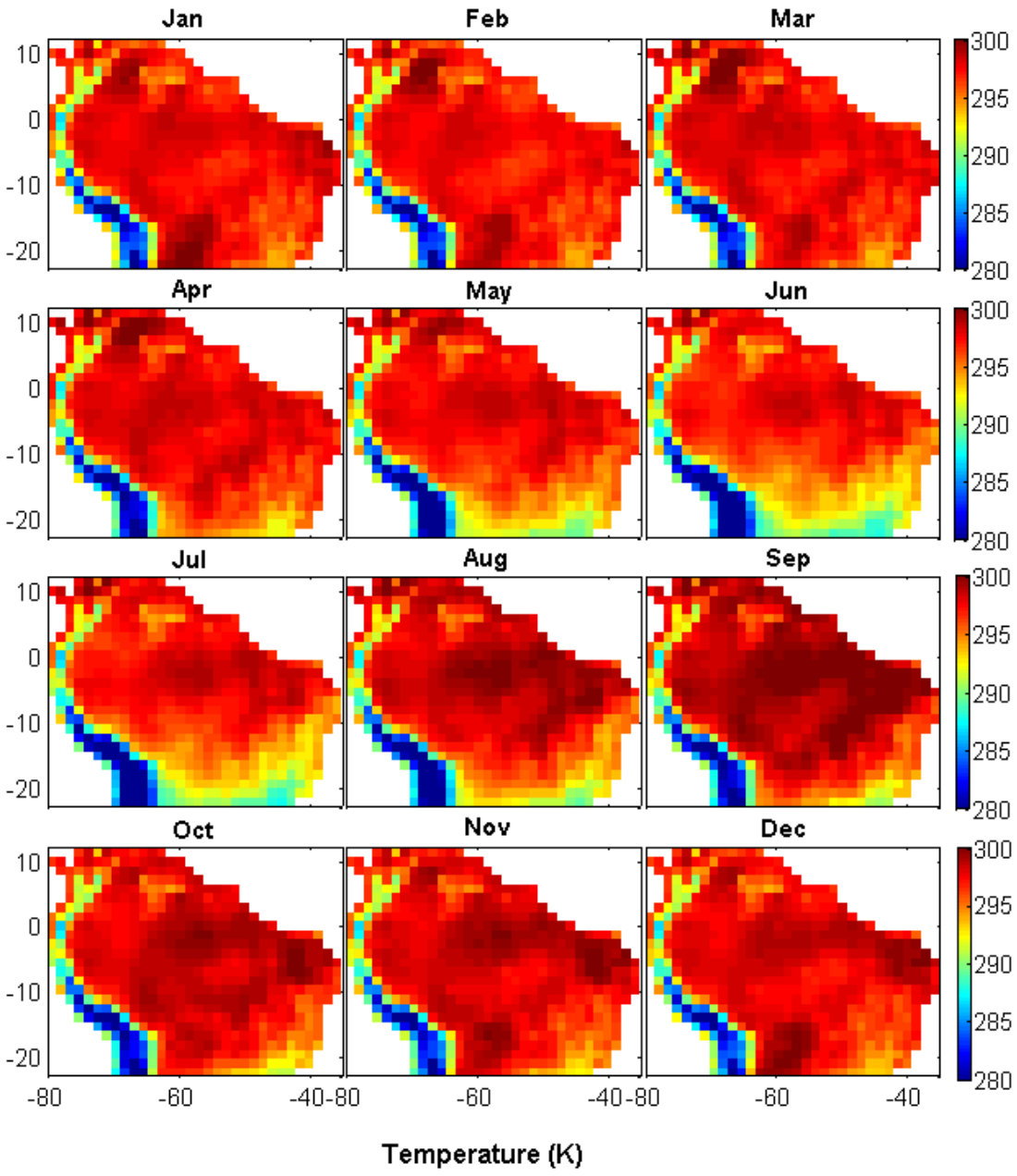

Figure 5.24. MFD temperature for the months over the study domain.

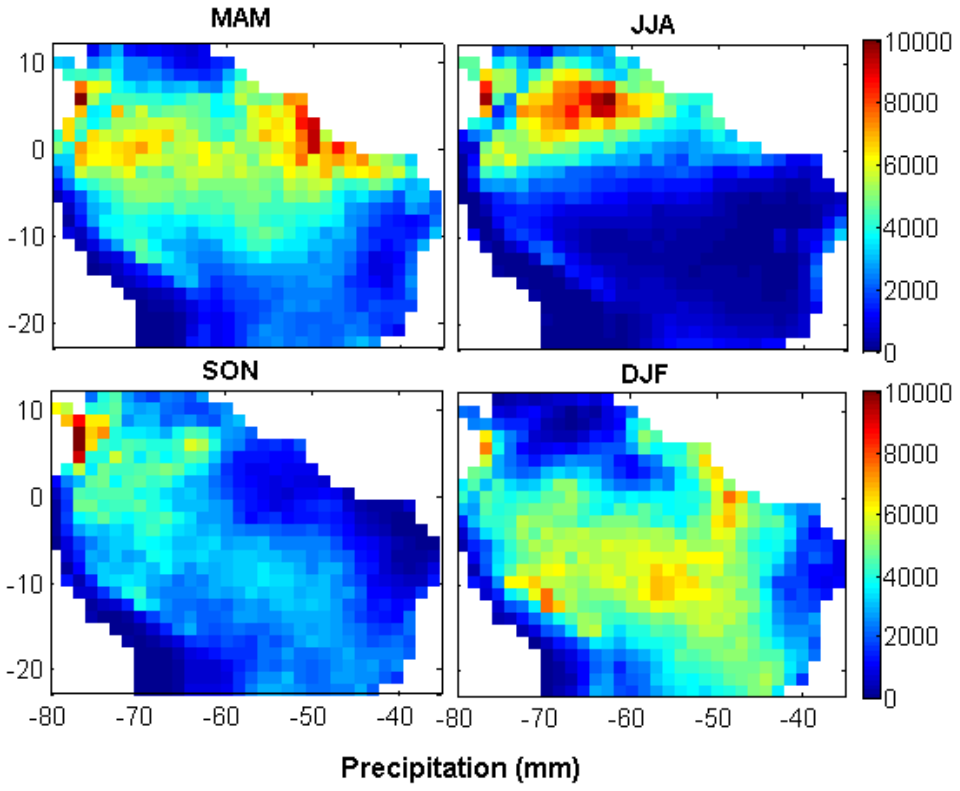

Figure 5.25. MFD precipitation for the seasons over the study domain.

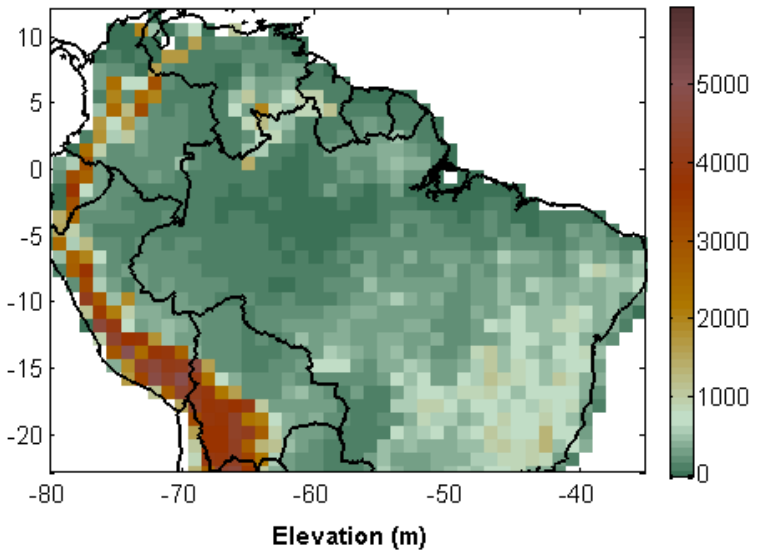

Figure 5.26. Elevation (30 arc-second DEM of South America by USGS) over the study domain.

Different patterns of weather and climate variability are evident over the study domain, which are linked to the land cover, topographic features, and wind-driven circulation by the trades over the tropics and the adjacent oceans. The trade winds over the tropics, sea surface temperature over the Atlantic Ocean, and El Niño Southern Oscillation (ENSO) have strong and profound impacts on the climate and rainfall patterns of the study domain. The Andes Mountains along the west coast with average height of about 4000m have the coolest temperature in all months. The mountains act as a barrier and block the tropospheric flow. This causes a dry climate over the west and moist climate over the east side of the mountains. The maximum rainfall usually occurs during December to June over the Amazon basin and the driest season during June to August. The peak of wet and dry seasons in the central part of the Amazon is DJF and JJA, respectively, which is in contrast to the peak of wet (JJA) and dry seasons (DJF) over the northern of the study domain (see Fig. 5.25). Convective activity generates large amount of rainfall over the basin, the largest rainforest in the world. Precipitation over the east of the basin is usually higher than the west side, with maximum rainfall occurring around the Amazon River Delta region ARD (mouth of the Amazon River, the northeast of the study domain). The boundary effects of the adjacent oceans can lead to large amounts of rainfall over the ARD and also over the northern part of the study domain. Examination of the delineated domains confirms that the specific physical features in each region correspond to the delineated domains as follows:

D1 and D2 mostly cover Brazil. D1, over the southeast Brazil (outside the Amazon basin), is mostly covered by savannas, and also small patches of deciduous broadleaf forest (over the southwest of D1) and sparse grassland. D2, over the majority of the Amazon basin in Brazil, is mostly covered by the evergreen broadleaf forest. D2 has on average wetter-warmer climate than D1. Similar to D2, the evergreen broadleaf forest covers D3. This domain over the ARD region is influenced by the strong interaction of the land-atmosphere-ocean system, leading to the large amount of rainfall and vast

estuarine wetlands. The different boundary conditions provided by the adjacent oceans, the Andes Mountains, and the trade winds affect the climate in D4 over the northern part of the study domain. Domains D4 and D5 have various types of land cover. The evergreen broadleaf forest, grasslands, savannas, and cropland/natural vegetation are found in D4 and evergreen broadleaf forest, deciduous broadleaf forest, grasslands, savannas, open shrub lands, cropland/natural vegetation, and barren or sparsely vegetated types in D5. D5 covers the west coast and contains the Andes Mountains and a small west part of the Amazon basin. This heterogeneous region has on average the driest-coolest climate.

To further explore the physical differences between the delineated domains, we also compare the spatial average of the mean and standard deviation of precipitation, temperature, and elevation in the five domains (Figs. 5.27 to 5.29).

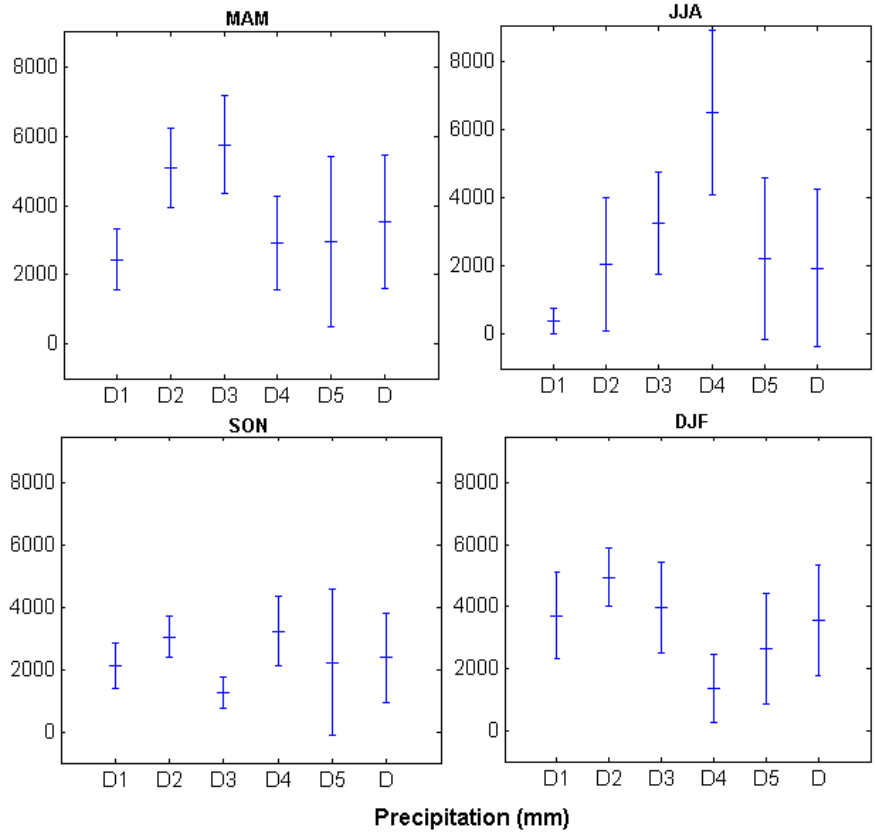

Figure 5.27. Spatial average of mean and standard deviation of precipitation in the delineated domains (D1, D2, D3, D4, D5) and the entire study domain (D).

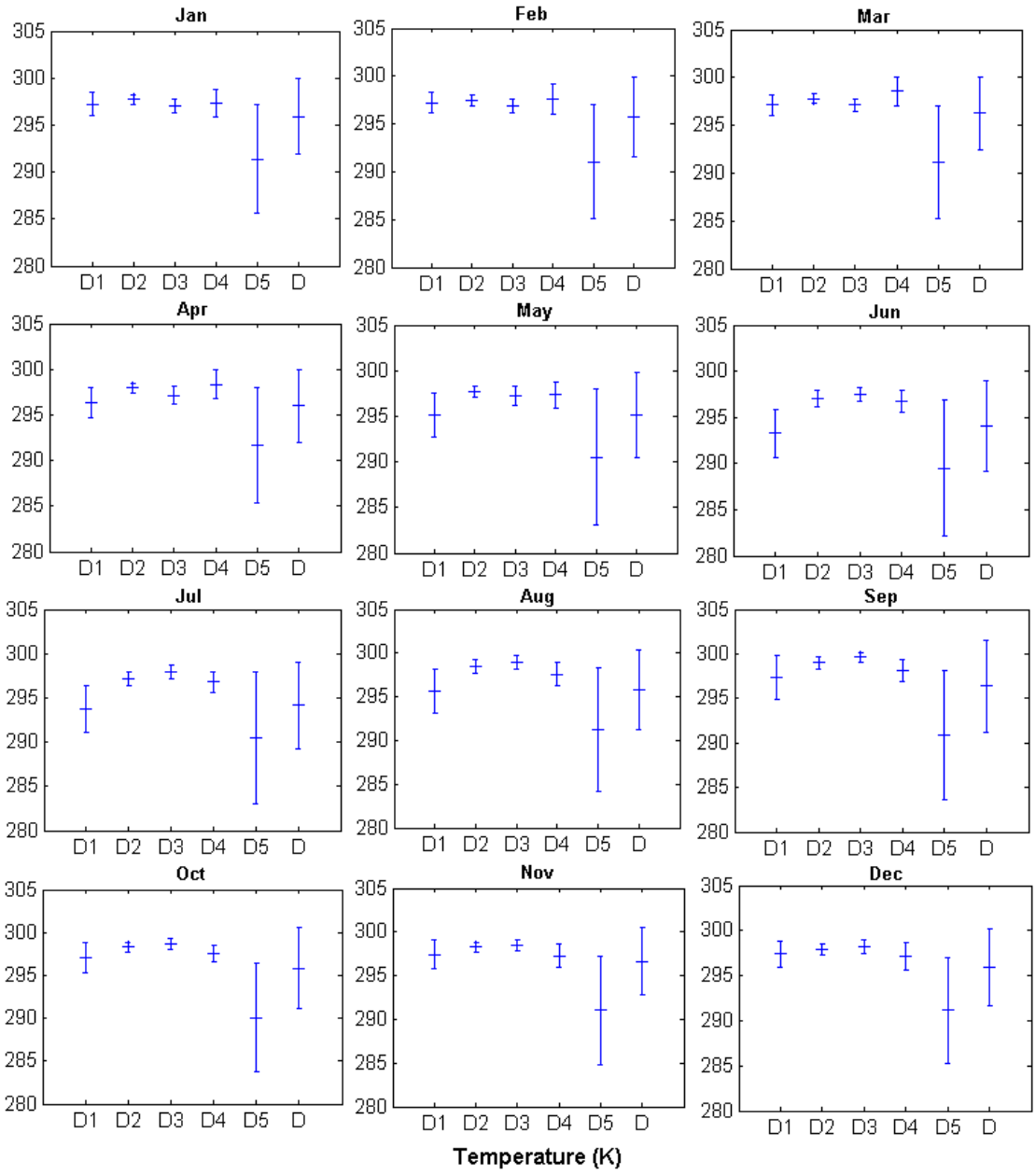

Figure 5.28. Same as Fig. 5.27 but for temperature.

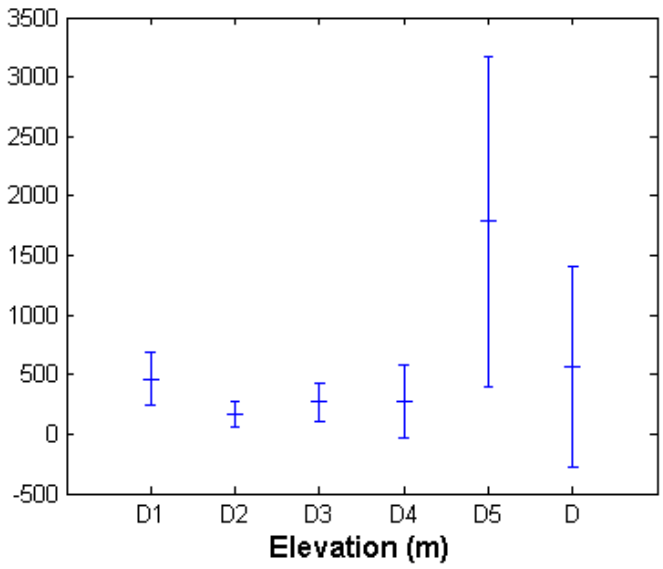

Figure 5.29. Same as Fig. 5.27 but for elevation.

As we can see the seasonal cycle of precipitation is evident in the delineated domains (see Fig. 5.27). However the change of temperature over D1, D2, D3, and D4 is smooth, small temperature variation in those domains can be observed during different months (see Fig. 5.28). This can be due to the fact that high moisture content over the tropic and the Amazon basin moderates variability of temperature. The coldest temperature and the highest elevation with the largest variability is D5, clearly distinguishable from the other domains.

The statistical delineation of the domain clearly follows physical and climatic features of the domain. This is consistent with the fact that the skill of schemes and parameterizations used in CCSM3 to simulate temperature and precipitation varies over regions with different topography, land cover, and climatology, which can produce the different systematic errors over the regions. We identified the minimum number of training pixels (model calibrations) required to achieve a domain regionalization response sufficiency close to the performance attained by the calibration at all domains' pixels.

The results show that in general the homogeneous regions (e.g., D1, D2) need fewer numbers of training pixels than the heterogeneous regions (e.g., D4 and D5).

Up to this point, we have discussed and elaborated on the regionalization ability of the linear regression model and reliable associations between the delineations and the land-atmospheric features of the regions. The performance of the trained ANN model at the defined training pixels to correct the biases of climate variables (temperature and precipitation) at the validating pixels is evaluated in the following section.

5.4. Regionalization of the Neural Network model

We delineated the study domain and determined the training pixels for each month/season using the linear regression model, now we train (calibrate) the ANN model at the defined training pixels and apply the trained model to reproduce bias-corrected temperature/precipitation at all pixels within the delineated domains with a desired accuracy. Note that the desired performance of all pixels is at least 80% of that of pixel by pixel correction (Chapter 4).

5.4.1. Temperature

Figures 5.30 to 5.41 show the regionalization ability of the ANN and LR to improve the results in terms of MSE, Bias, ρ, and KS.

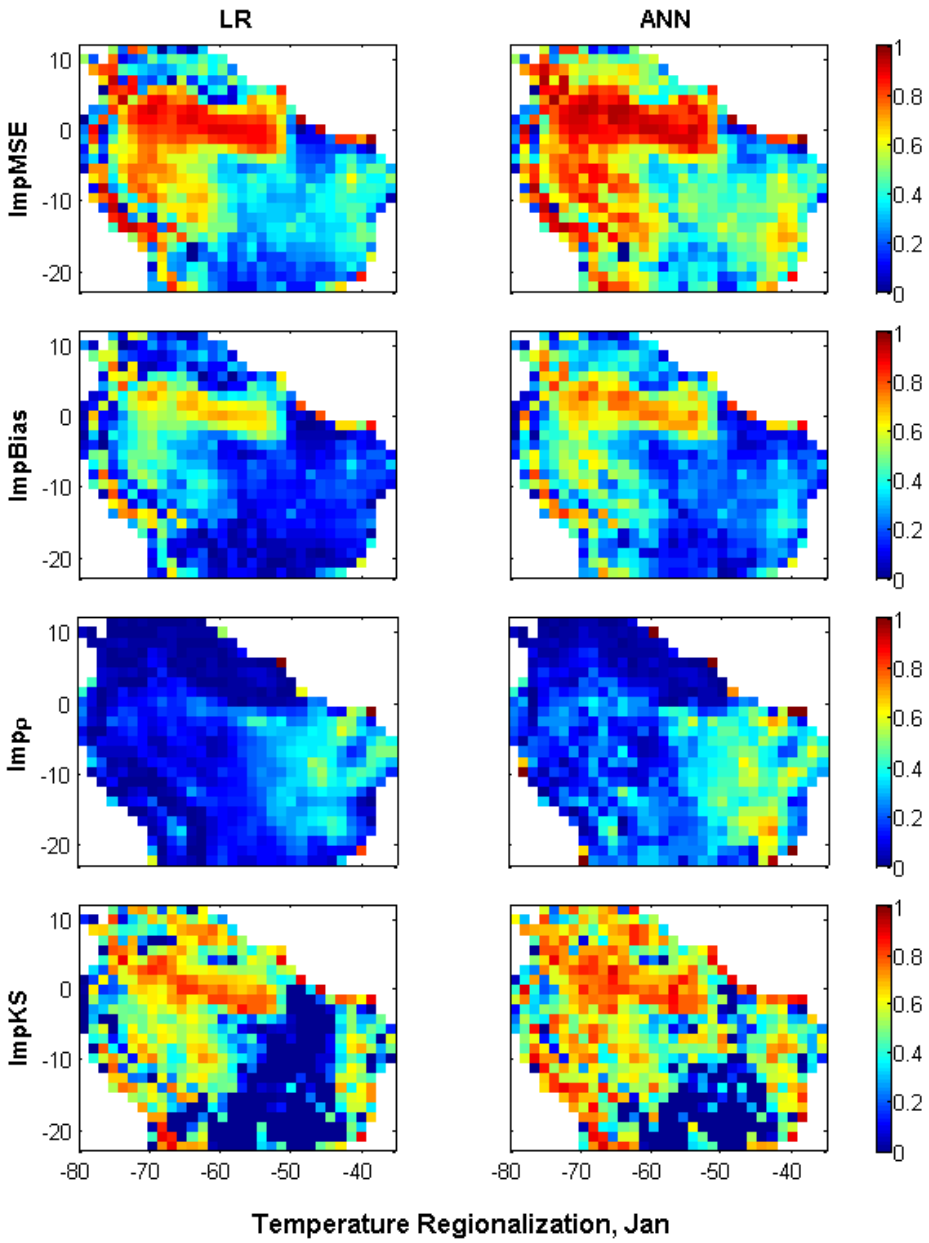

Figure 5.30. From top-to-bottom: Improvements of the MSE (ImpMSE), Bias (ImpBias), ρ (Impρ), and KS (ImpKS) by the linear (LR) and nonlinear (ANN) methods for 80% performance in January.

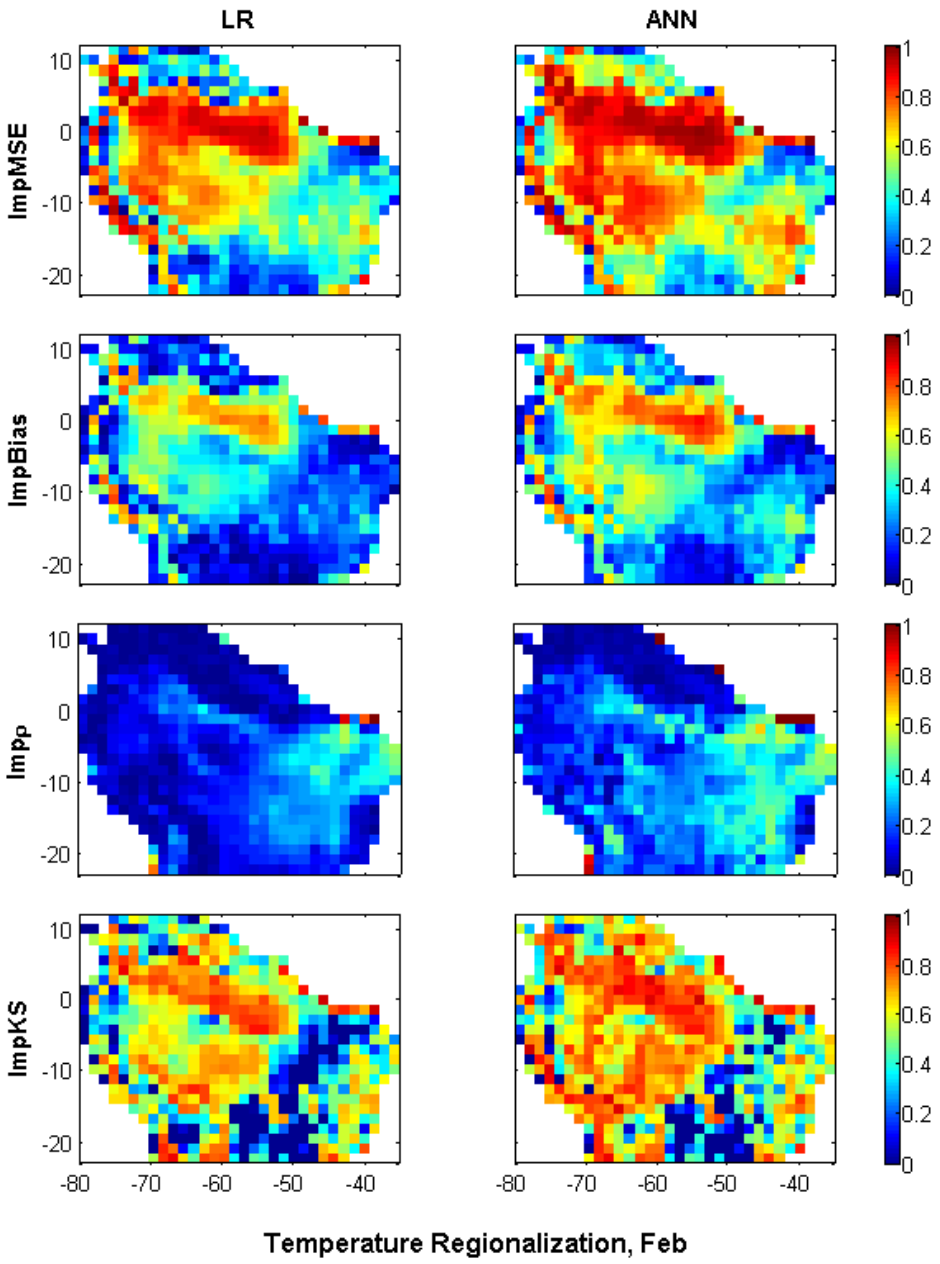

Figure 5.31. Same as Fig. 5.30 but for February.

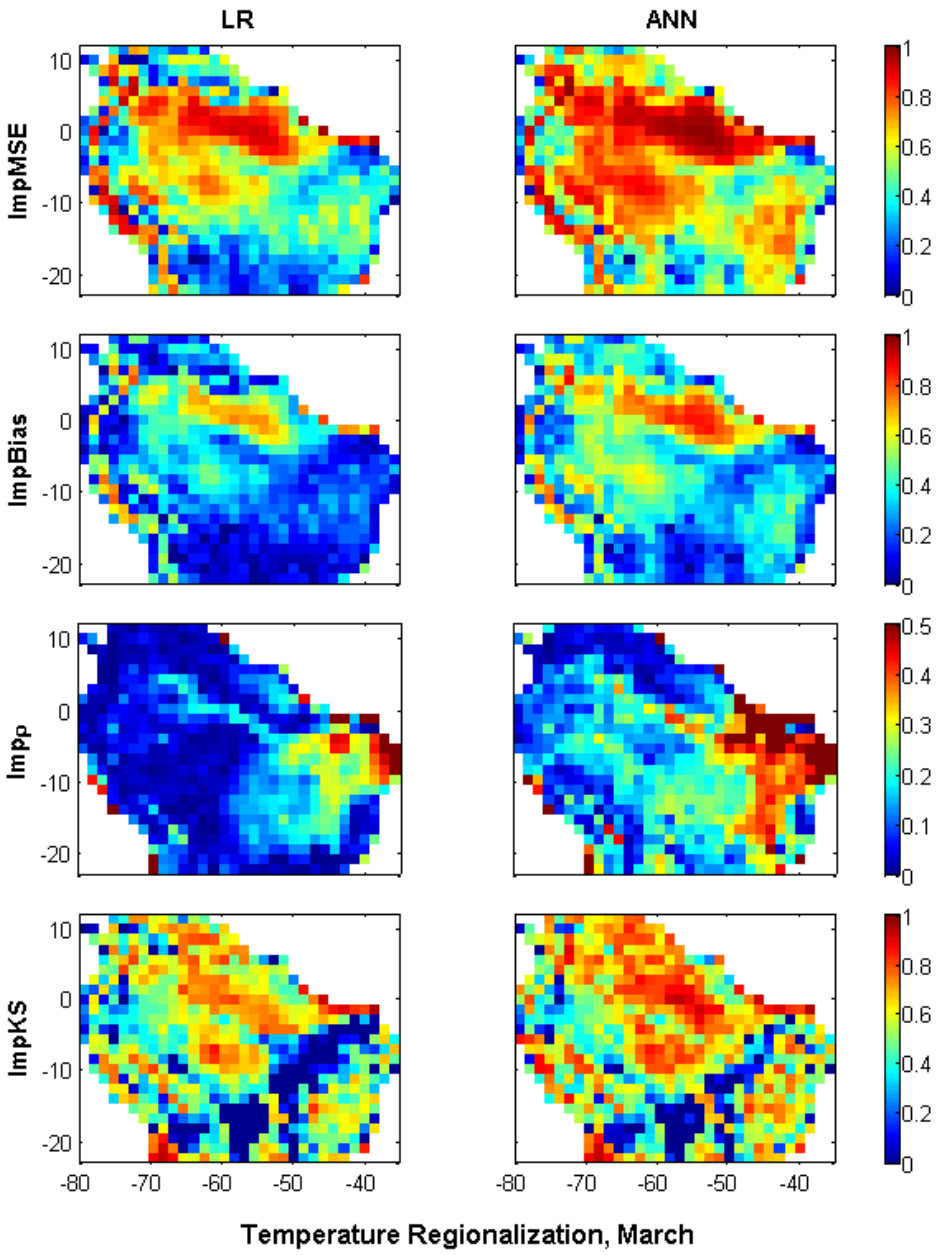

Figure 5.32. Same as Fig. 5.30 but for March.

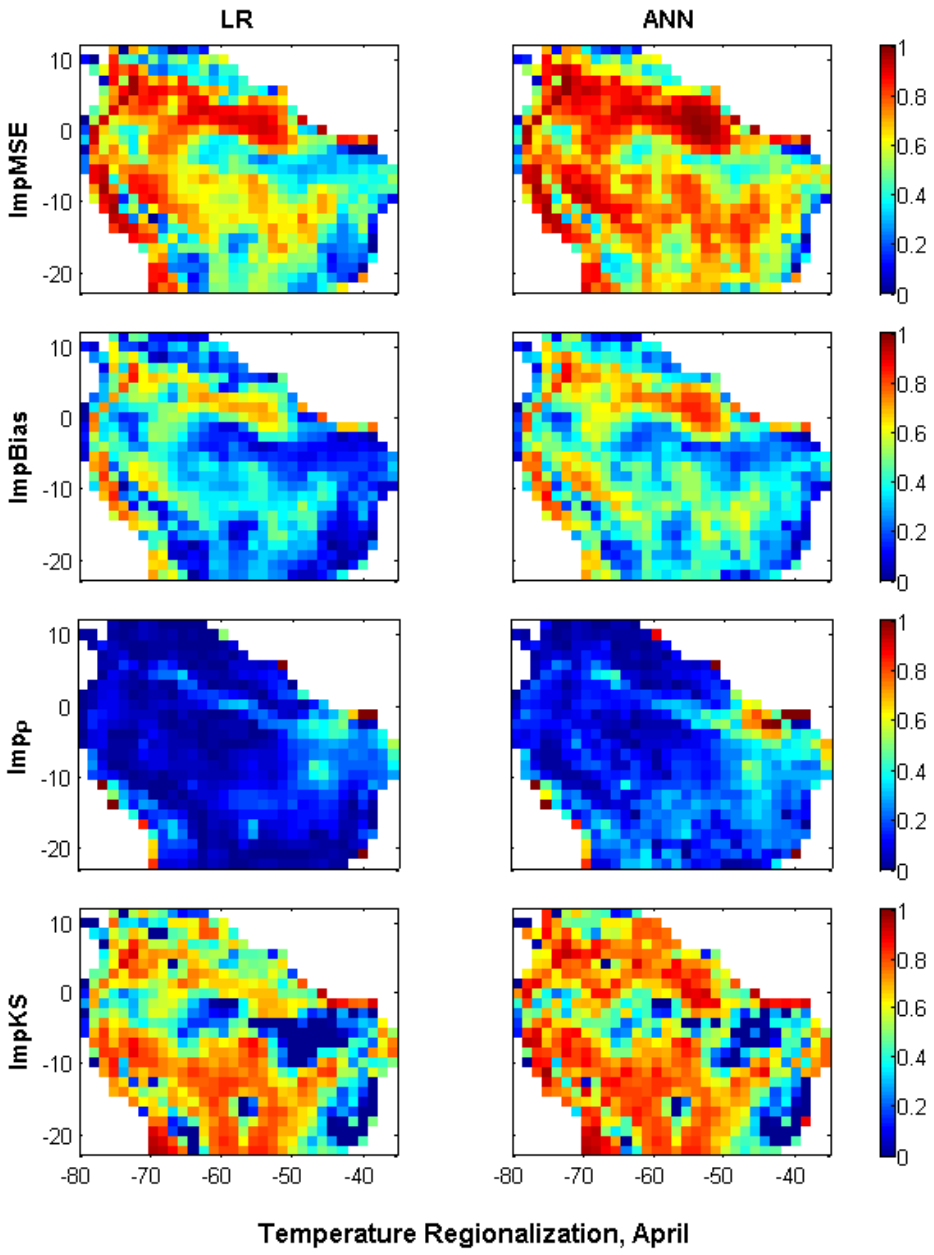

Figure 5.33. Same as Fig. 5.30 but for April.

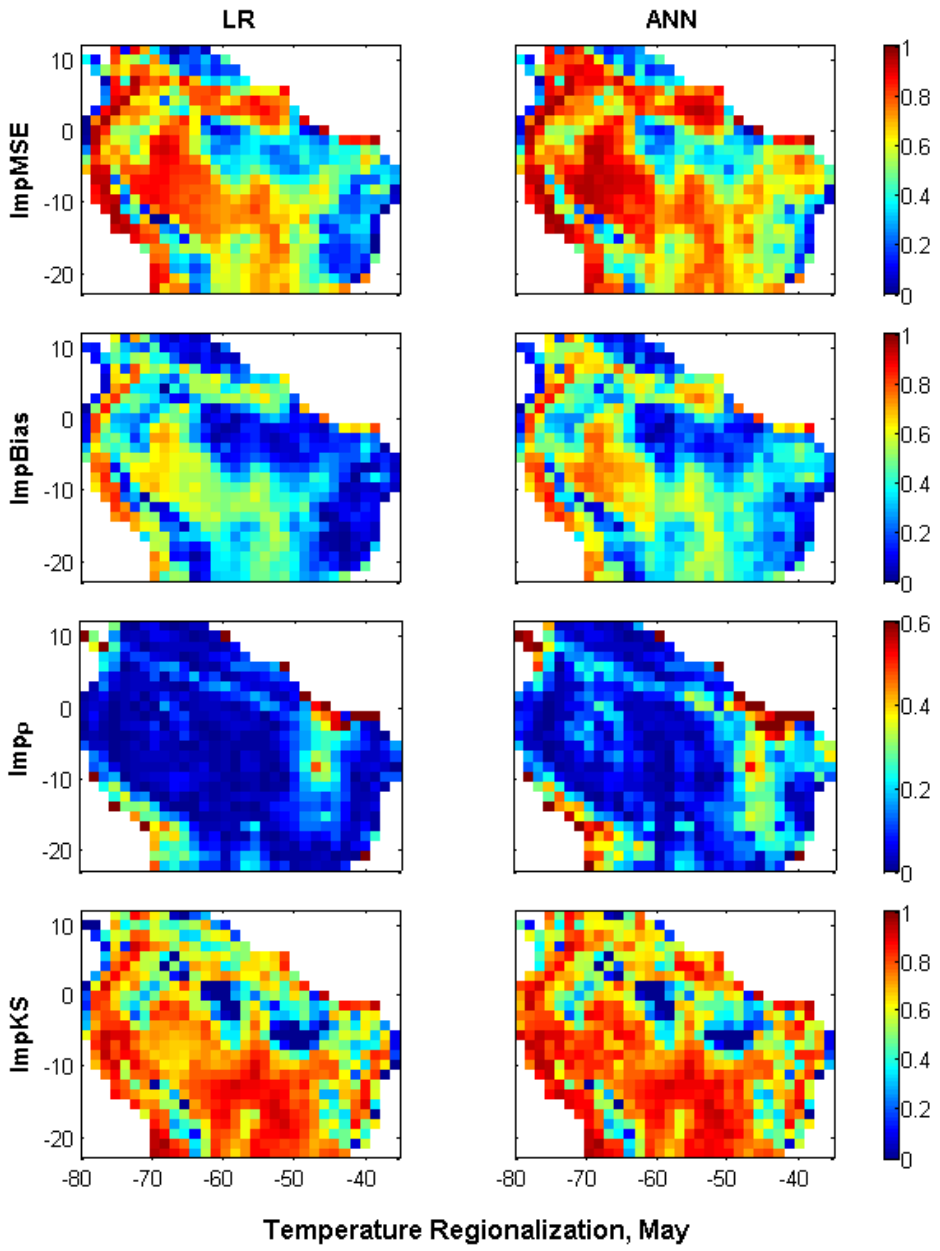

Figure 5.34. Same as Fig. 5.30 but for May.

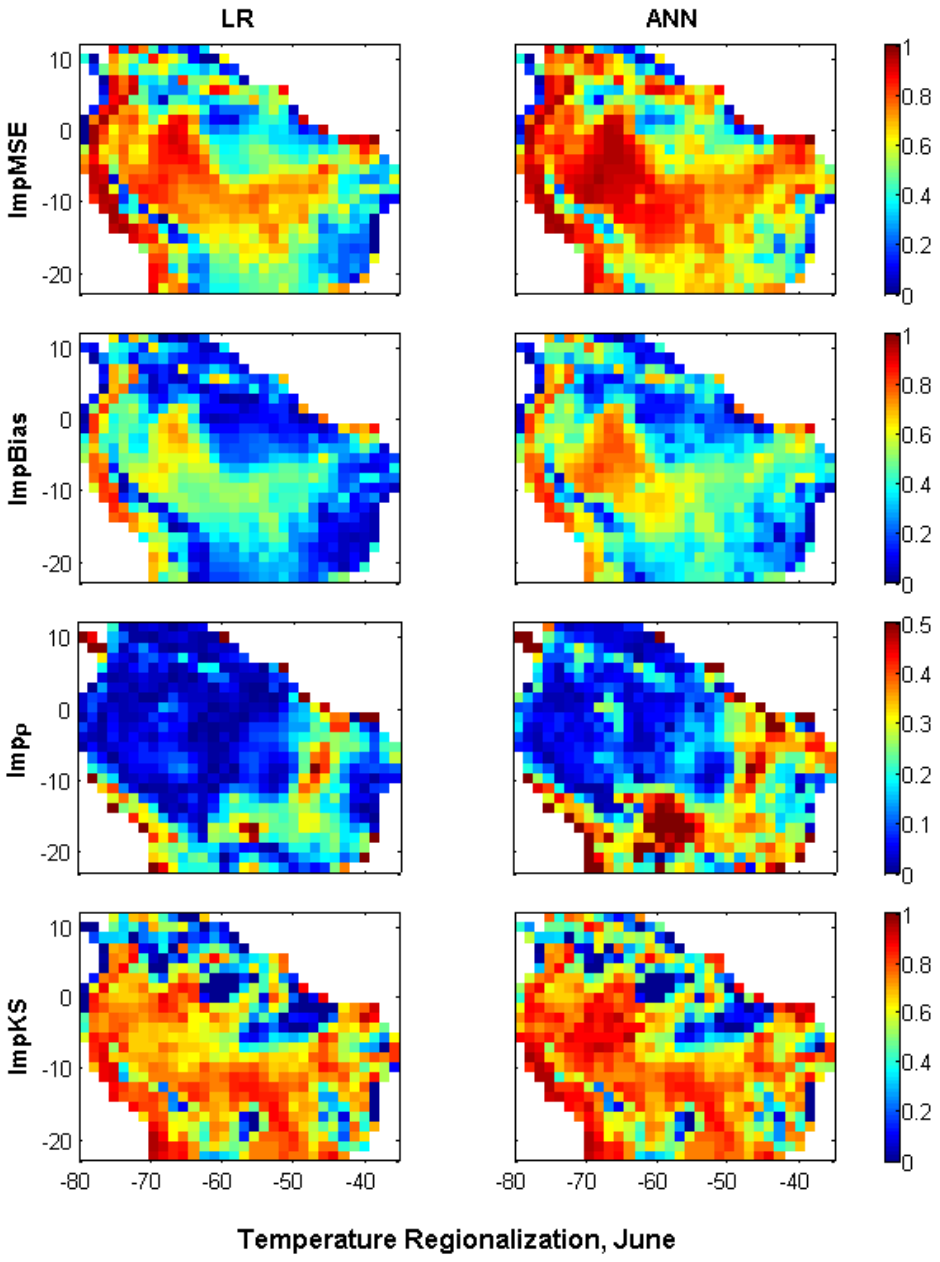

Figure 5.35. Same as Fig. 5.30 but for June.

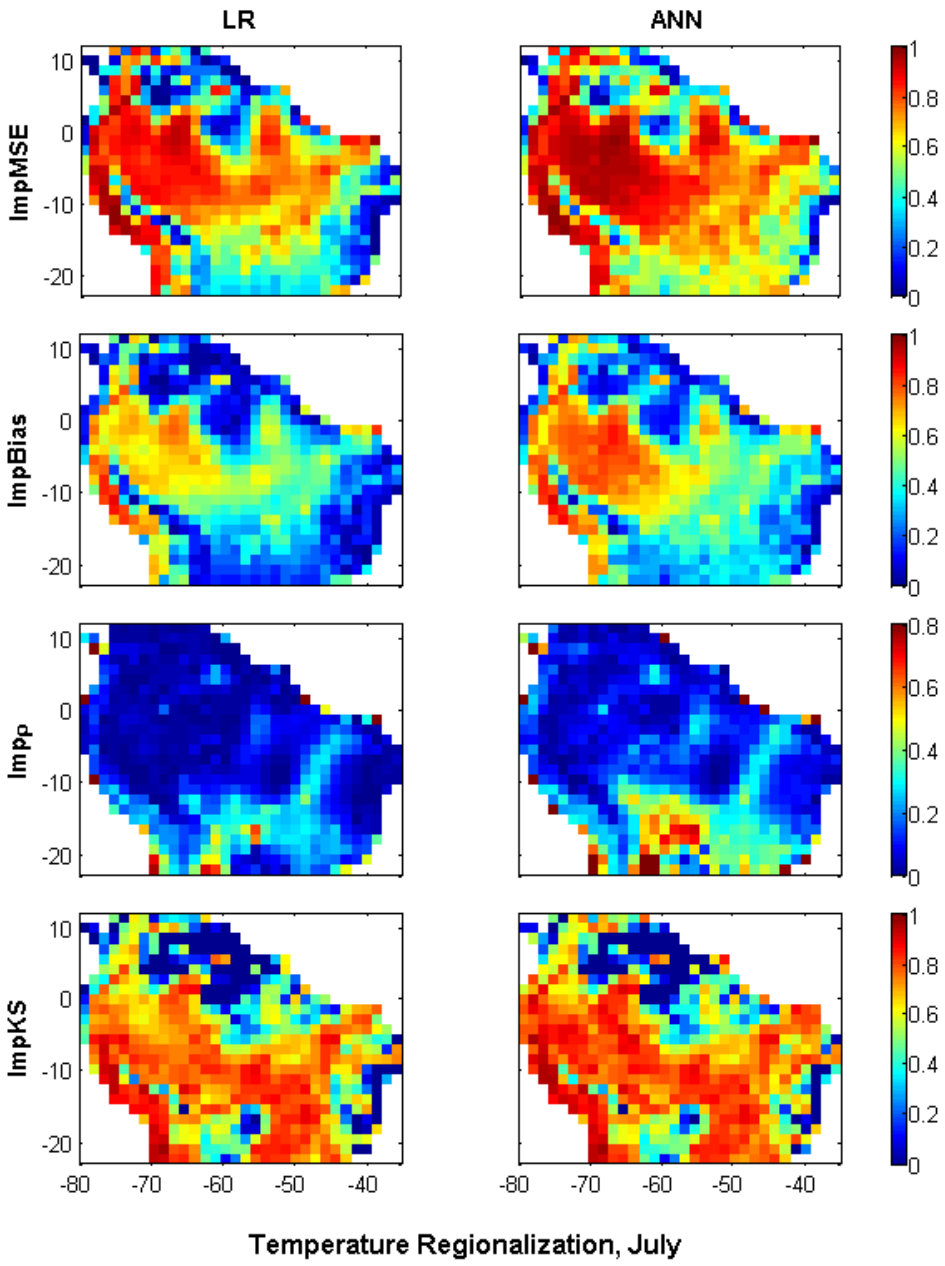

Figure 5.36. Same as Fig. 5.30 but for July.

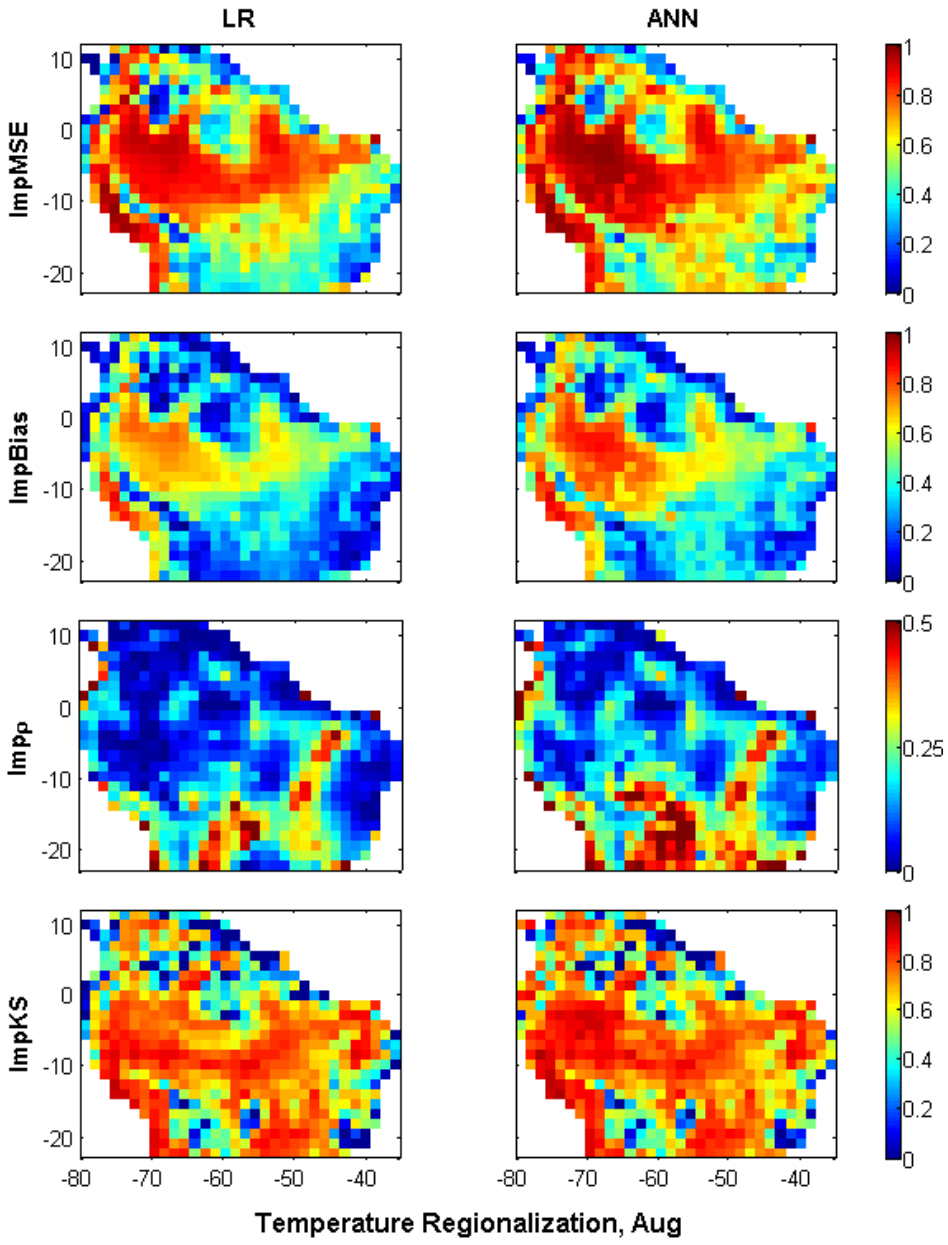

Figure 5.37. Same as Fig. 5.30 but for August.

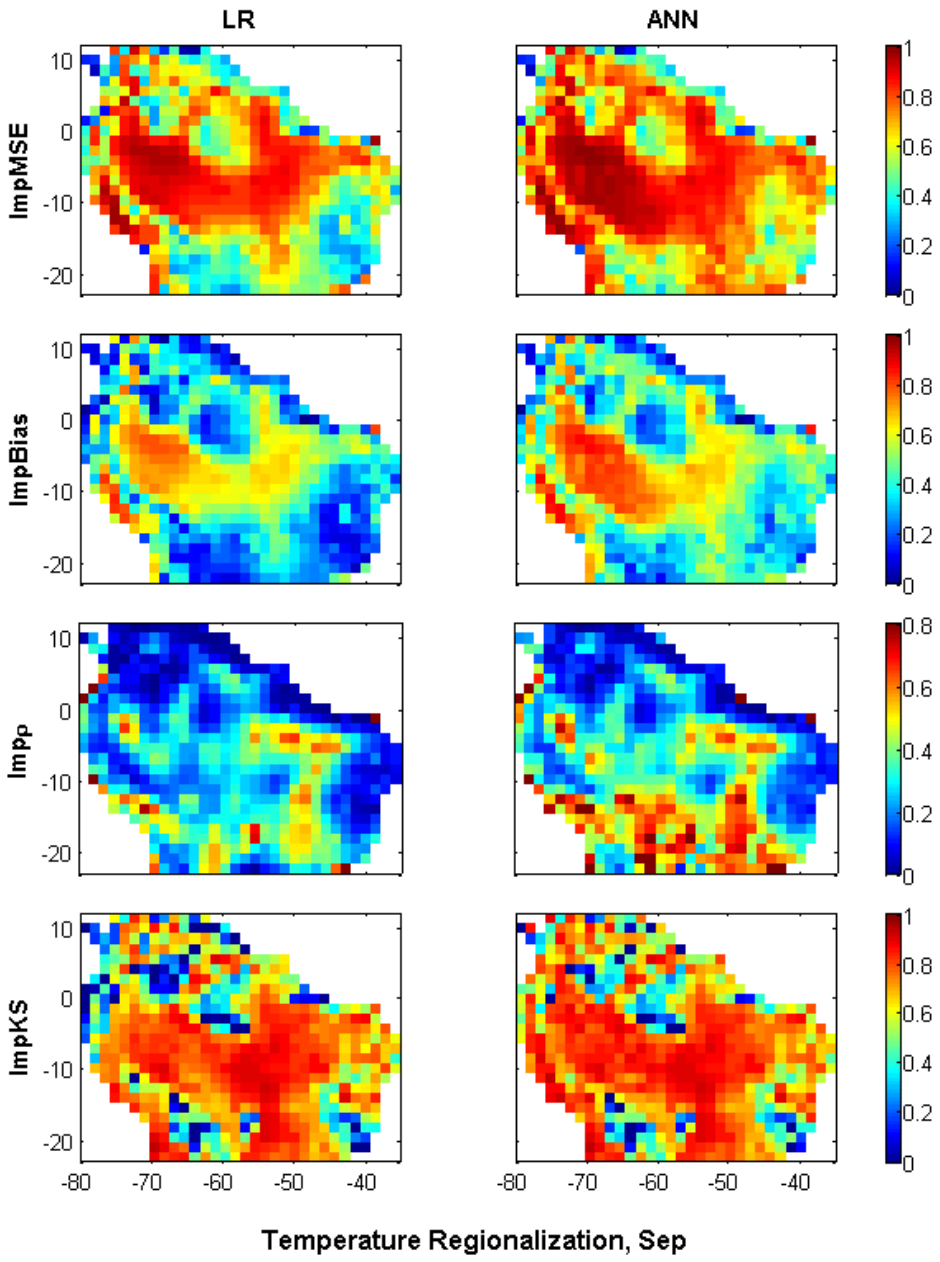

Figure 5.38. Same as Fig. 5.30 but for September.

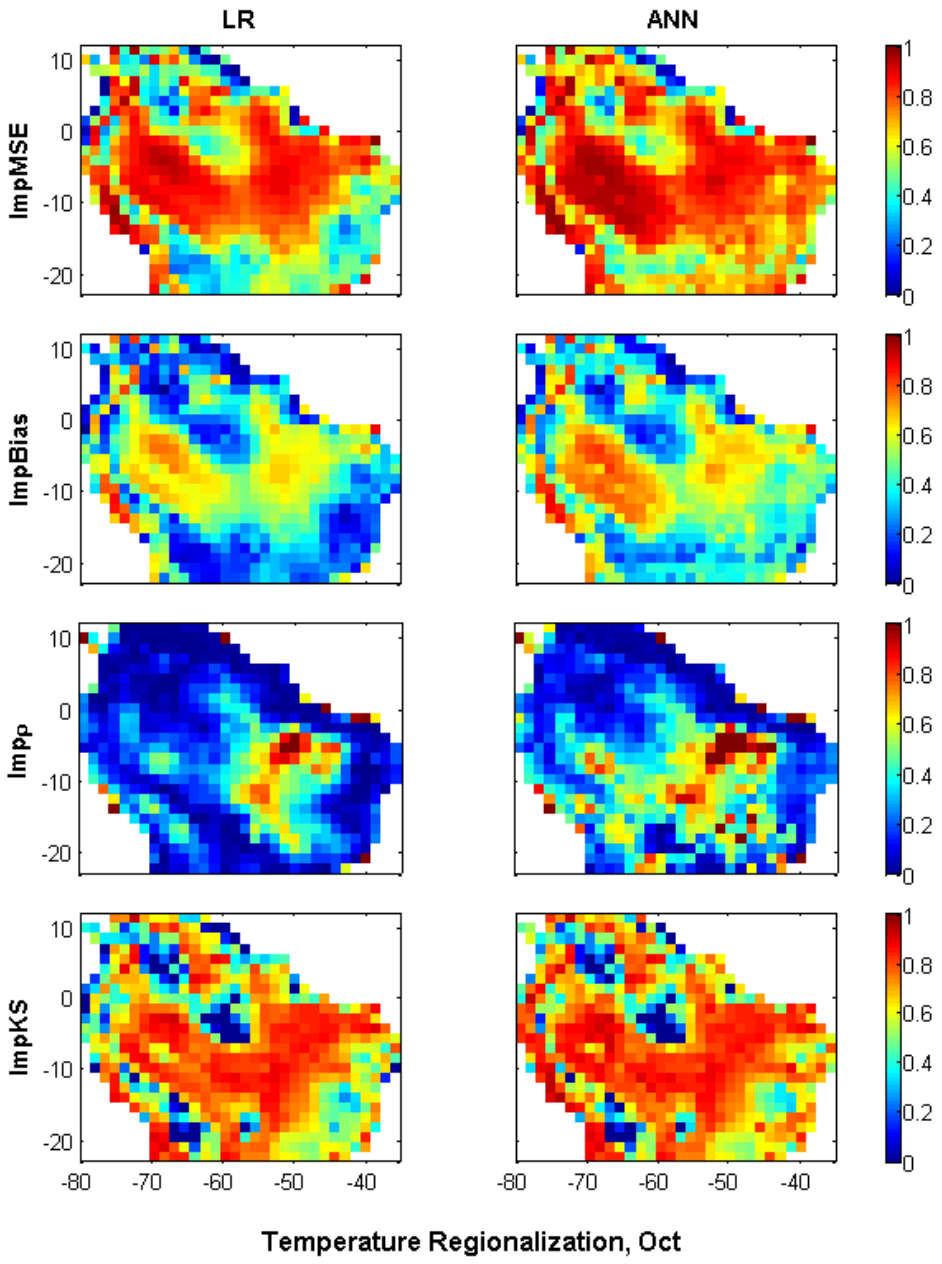

Figure 5.39. Same as Fig. 5.30 but for October.

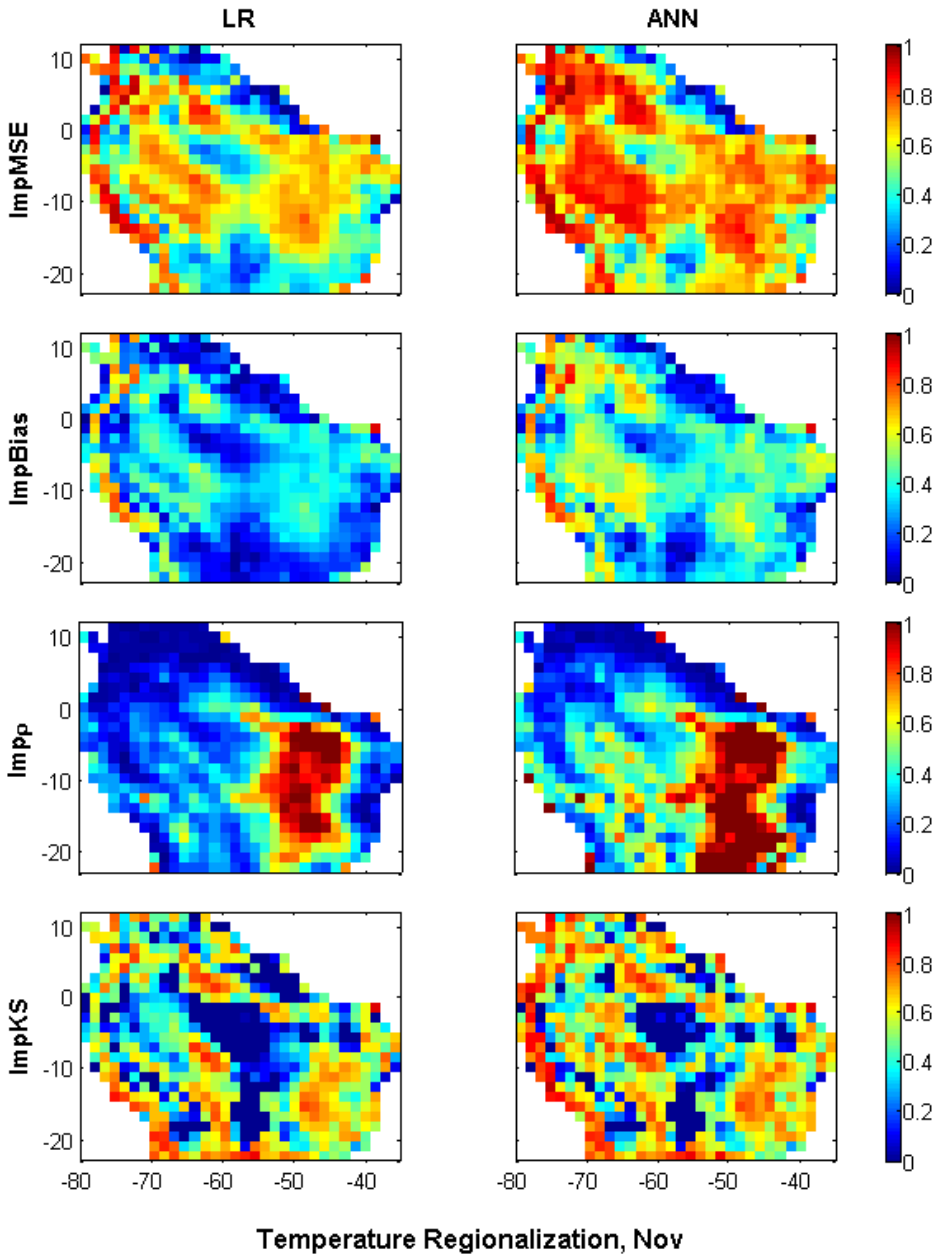

Figure 5.40. Same as Fig. 5.30 but for November.

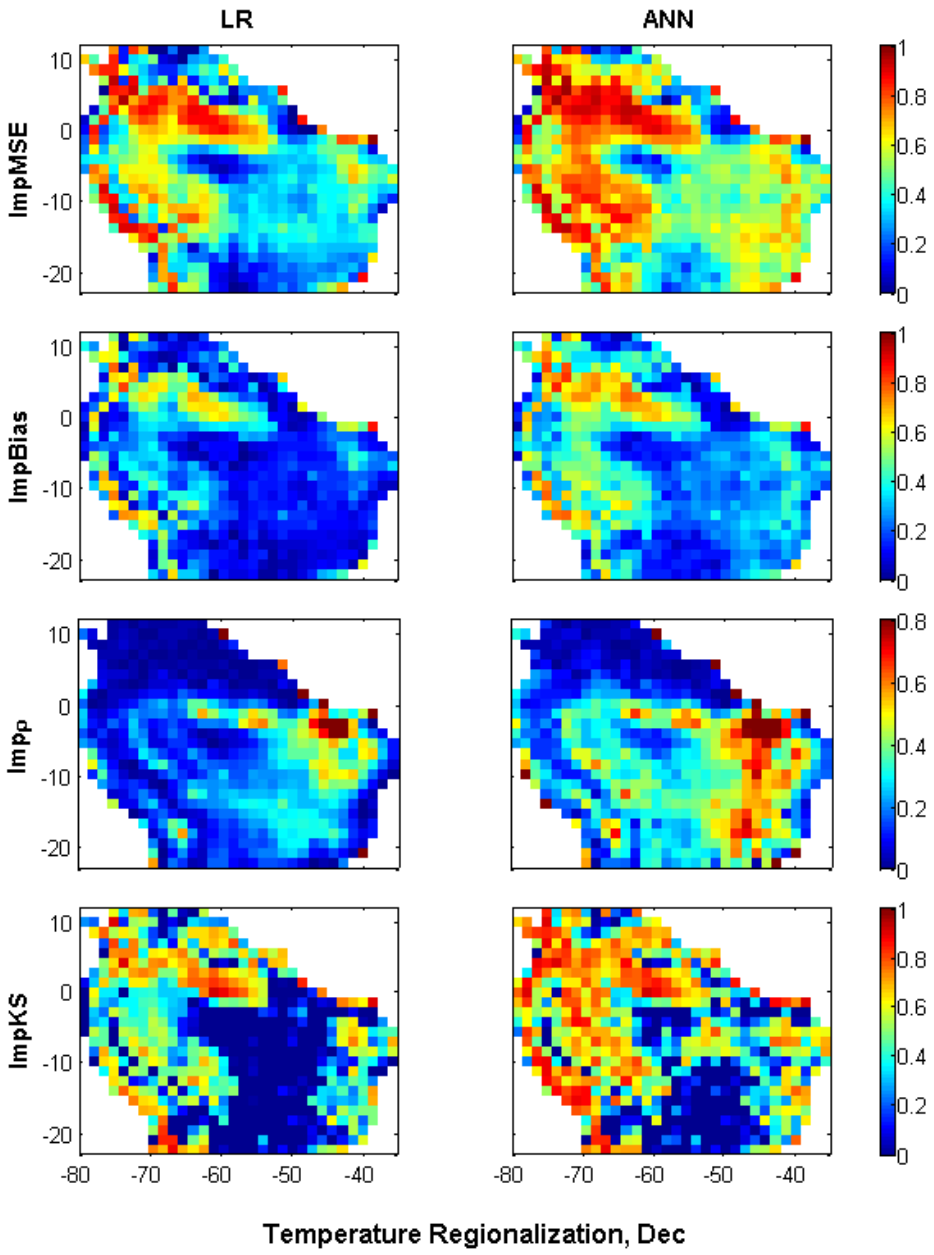

Figure 5.41. Same as Fig. 5.30 but for December.

We can see that the LR and ANN models have generalization ability to reduce biases of temperature with a desired accuracy. It is also evident that the ability of the ANN model to improve all terms of statistics is better than that of the LR. The results indicate that we do not need many observations to construct a robust model. On average, observations from 12% of the all domain pixels are sufficient to train a model that can perform well for the entire study domain. This generalization can save significant time and memory usage particularly for the ANN model. Although the LR and ANN can improve the results all over the domain, the performance of the model is more dominant over the regions that have larger original error such as the west coast (shown with the red color in the first and second rows of the figures above). The smaller improvements are over the regions (shown by the blue color in the Figures above) where the original error/KS (ρ) is small (high).

5.4.2. Precipitation

Similar to temperature, the regionalization ability of the ANN and LR to improve the results in terms of MSE, Bias, ρ, and KS is illustrated in Figures 5.42 to 5.45.

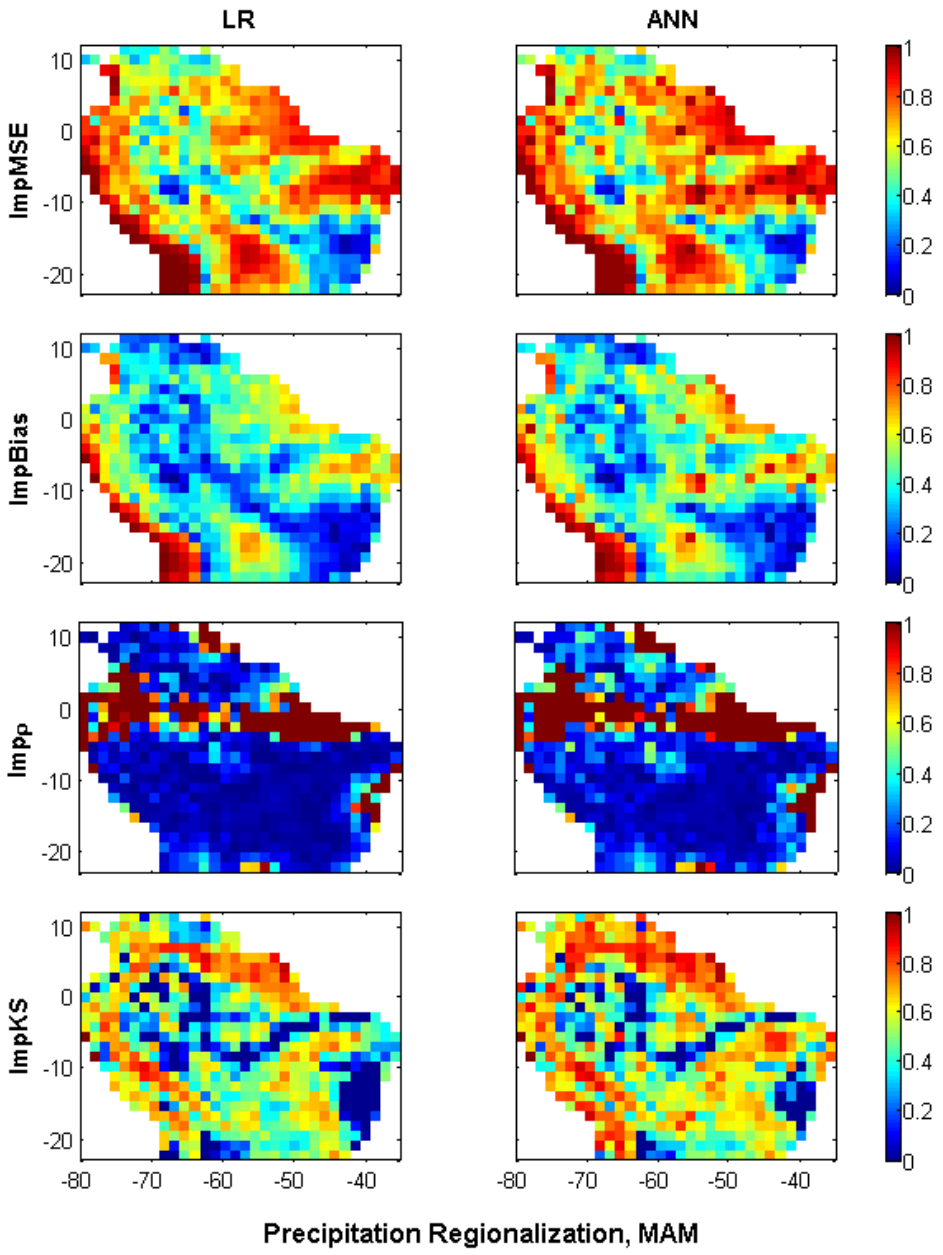

Figure 5.42. From top-to-bottom: Improvements of the MSE (ImpMSE), Bias (ImpBias), ρ (Impρ), and KS (ImpKS) by the linear (LR) and nonlinear (ANN) methods for 80% performance in MAM.

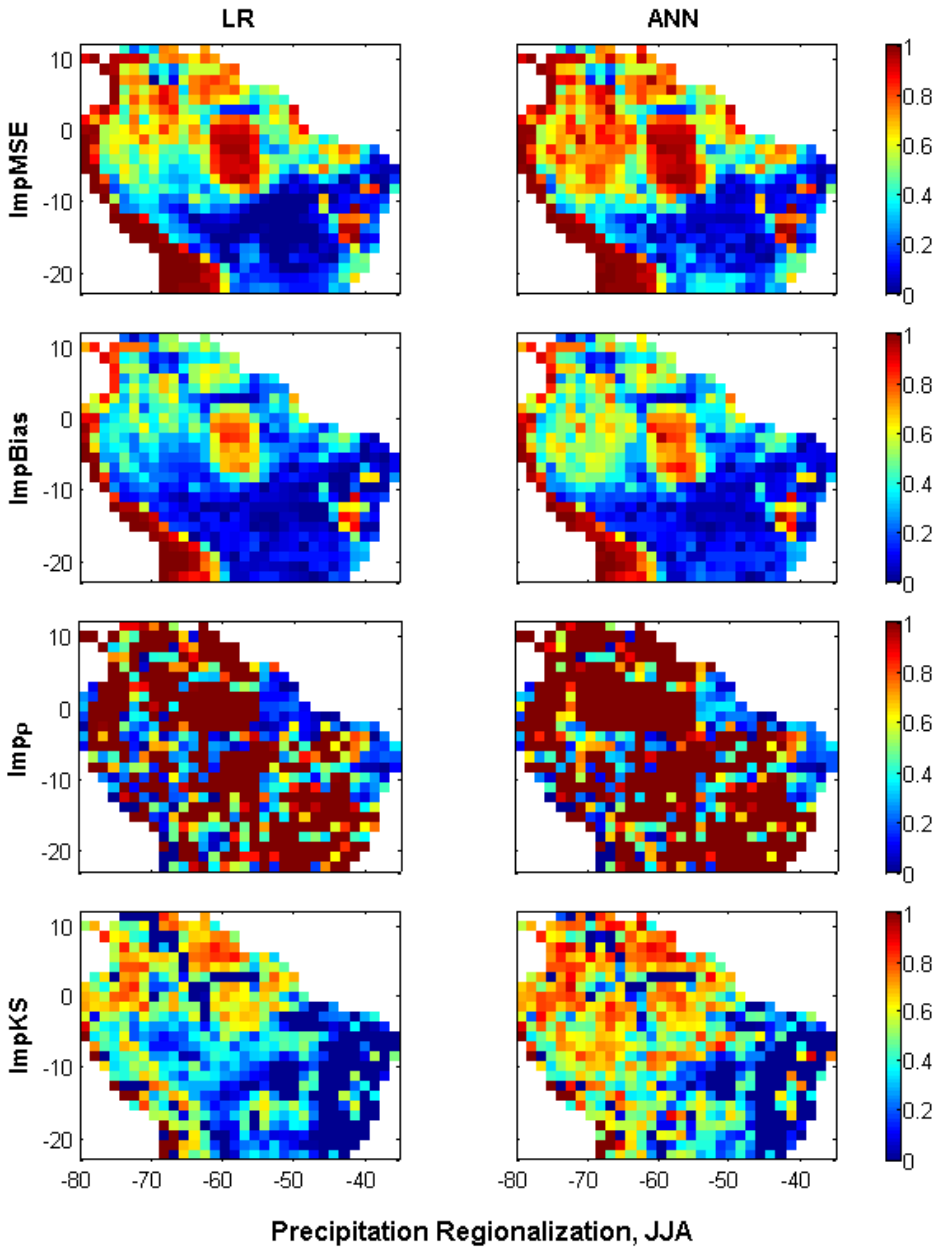

Figure 5.43. Same as Fig. 5.42 but for JJA.

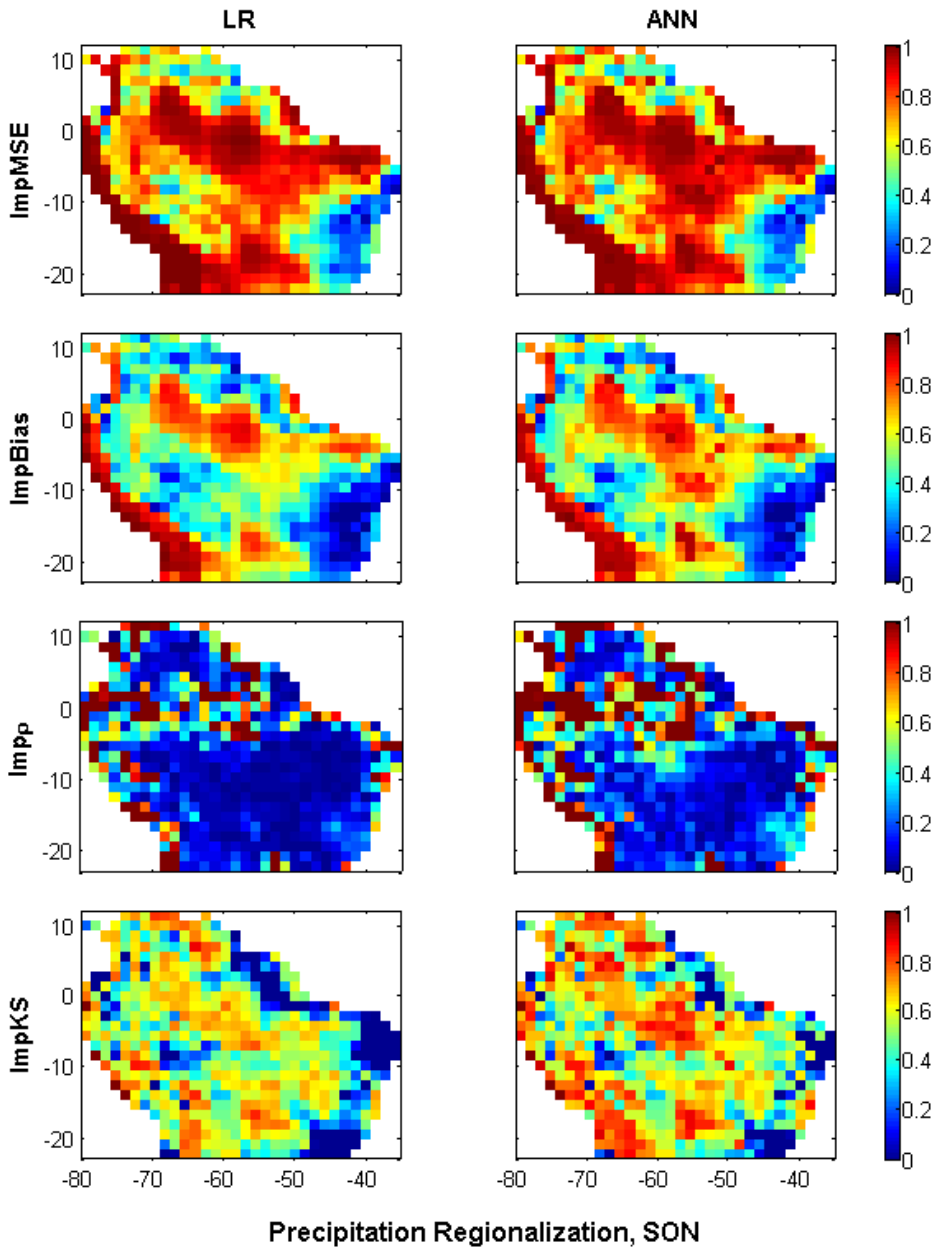

Figure 5.44. Same as Fig. 5.42 but for SON.

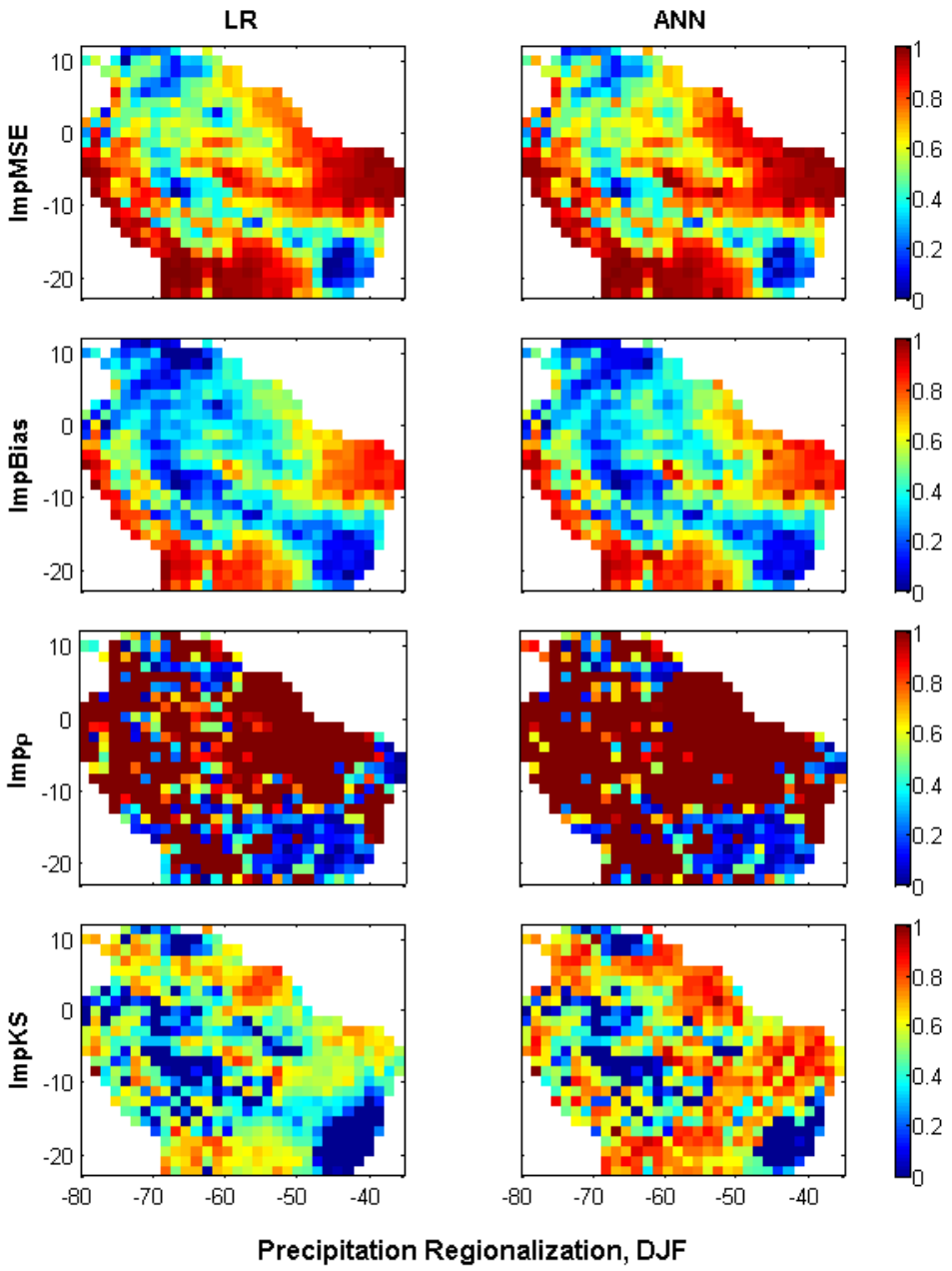

Figure 5.45. Same as Fig. 5.42 but for DJF.

The results confirm that the trained ANN and LR at the certain number of training pixels can be generalized to reduce precipitation biases at all pixels. The ANN outperforms the LR in improving all terms of statistics. Using observations from only 14% of the pixels to train the model for all domain pixels is a computationally efficient procedure in particular for the ANN. Similar to temperature, higher improvement of the results by the LR and ANN occurs over the regions that have larger (smaller) original error/ KS (ρ). While the smaller improvement is over the regions with smaller (larger) original error/ KS (ρ).

5.5. Summary

Calibration of the ANN model like other bias correction methods needs observations that are limited in space. In other words, it is not feasible to find accurate and reliable observations for all geographic locations. An efficient bias correction method uses available observations to construct a proper relationship between the input-output that performs well for other locations as well. The skill of CCSM3 to simulate climate variables such as temperature and precipitation varies over the regions with different topography and climatology, which leads to different systematic errors over the regions. These systematic errors can be used to delineate regions in the study domain.

The procedure of delineation can be implemented using LR or ANN models. Given the significantly lower computational efforts and smoother response of the LR, it is used to delineate regions in the study domain and identify required training pixels. The delineation of domains using the LR is consistent with the topography, land features, and atmospheric patterns over the study domain. This is consistent with the variable skill of CCSM3 to simulate temperature and precipitation over different regions. The study domain is divided into five domains: D1 over the southeast, D2 over the center, D3 over the northeast coast, D4 over the north, and D5 over the west coast of the study domain. Three indicators including temperature, precipitation, and elevation were used to clarify

the differences in the delineated domains. Although precipitation was the best indicator of the domains, a smooth variation of temperature can be also recognized in D1, D2, D3, and D4. The highest variability of temperature and elevation in D5 can clearly separate this domain from the other domains. D5 has the coldest temperature and the highest elevation in the study domain.

A small number of pixels in each delineated domain were used as the training pixels, where the ANN model was trained to re-produce the bias-corrected climate variables (temperature and precipitation) at other pixels within the delineated domains with a desired accuracy. The results confirmed that a few model calibrations at selected training pixels within the target domain are sufficient to regionalize the bias correction procedure. The number of calibration pixels in each delineated domain depends on the accuracy criterion (70%, 80%, 90% of the performance achieved with the model calibrated at all domain pixels), topography of the domain, and climatology over the regions. The number of training pixels increases considerably in going from a performance of 80% to 90%. The number of training pixels also increases over the heterogeneous region (e.g., D5). In general, the regionalization of the bias correction for precipitation needs more training pixels than that of temperature. This is due to the fact that the change of temperature is smooth and the variability and uncertainty of the precipitation values are higher than temperature.

The LR and ANN models were calibrated (trained) at the defined training pixels and were subsequently applied at other pixels within the delineated domains. The results showed that the trained ANN outperforms the LR model in terms of the chosen metrics (MSE, Bias, ρ, and KS) of the bias-corrected temperature and precipitation. The results also indicated that the model calibration at a small number of the all pixels would be sufficient to achieve a good accuracy for the entire domain. This generalization ability represents significant computational, time, and memory savings in particular for the ANN model.

CHAPTER 6

CONCLUSIONS

We developed a new method to correct the biases of climate variables (temperature and precipitation) using an Artificial Neural Network. We also investigated the generalization ability of the method to see if the method is applicable when the observations are not available at all times or locations (regionalization procedure).

6.1. Concluding Remarks

We used a three layer feedforward neural network to construct a valid relationship between a set of inputs and (the bias-corrected temperature or precipitation). Since the proposed method is a data driven method, which relies on the supervised learning approach, choosing a proper set of inputs is fundamental. A set of inputs including skin temperature, specific humidity, net longwave and shortwave radiation with raw temperature (before bias correction) had the best performance to reduce the temperature biases. Lag zero, one, two, three precipitation, and the standard deviation from 3 by 3 neighbors around the pixel of interest were the best predictor inputs to reduce the precipitation biases. The use of the standard deviation of precipitation from the neighbouring pixels as the input can improve the variance of precipitation at the pixel of interest. Since the change of temperature is smooth in time and space, adding lag-time temperature or variance of temperature from the neighbours does not improve the results. Although ANN like other statistical bias correction methods cannot completely explain the underlying physics of the process, a main impact of input selection on the ANN performance indicates that it is not totally a “black-box” model. Due to the nature of the ANN structure, even a small increase in the number of parameters such as inputs, hidden

layer, and hidden nodes can significantly increase computational time and memory usage during optimization of weights. It also increases the complexity and uncertainty of the model and decreases the generalization ability of the network. Thus, we attempted to construct a proper network that is large enough to capture the underlying relationships in the data, but not too large that leads to degradation of the generalisation ability of the network. The constructive algorithm (achieving a desired performance by progressively adding nodes to the hidden layer) indicated that 10 and 8 nodes in the hidden layer were sufficient for the temperature and precipitation networks, respectively. The hyperbolic tangent-linear transfer functions for the hidden-output layers and the BPGDR training algorithm for the optimization of the weights established a proper internal structure of the network to correctly model the functional relationship between the input-output. Since observations are limited in time and space, a proper network should perform well in response to the new and unseen dataset without any need for recalibration, which is identified as the generalization ability.

To evaluate the generalization ability of the network in time, we used two independent intervals of the datasets as:

- For temperature: 1970-1988 as a training set and 1989-2008 as a validation set.
- For precipitation: 1901-1956 as a training set and 1957-2013 as a validation set.

The ANN model was compared with the linear regression model (LR) in producing the bias-corrected temperature and precipitation. The results revealed that the trained model in the calibration period is able to improve all terms of MSE, Bias, ρ, and KS of the results in both calibration and validation periods. While the widely-used bias correction methods such as the delta change and the quantile-based mapping approaches only adjust the first or second order moment of the data and they may not able to improve the lump error metrics. In addition, they cannot improve the correlation of the bias-corrected data with the observations. The main feature of the ANN method is that it can improve all metric (statistics) even when the original correlation between the modeled data and the

observations is low. Although the ANN model does not directly take into account any specific information about the distribution of the underlying variables of interest, its performance in preserving distributional properties as reflected in the KS statistic was comparable with that of distribution mapping approach in the validation period.

The ANN outperformed the LR in improving all metrics/statistics for both temperature and precipitation. Similar improvements in the results for the calibration and validation periods indicated that the trained model has the generalization ability. Although the ANN improved the results all over the study domain, the larger improvements occurred over the regions that have larger original error and KS or smaller original ρ. The Andes Mountains over the west coast of the study domain were one of the regions where CCSM3 showed large error in temperature and precipitation. The large error extends to the other regions in different months. Parameterizations in CCSM3 produce different systematic errors over different regions and months. These systematic errors can be used to delineate the domain and evaluate the generalization ability of the ANN in space.

To evaluate the regionalization ability of the ANN in space, the study domain was divided into five domains; D1 over the southeast, D2 over the center, D3 over the northeast coast, D4 over the north, and D5 over the west coast of the study domain. The LR was used to delineate the regions due to its smoother response and computational efficiency compared to the ANN. The ANN model was calibrated (trained) at training pixels defined by the LR model and used at other pixels within the delineated regions without any recalibration (retraining). The results confirmed that the network does not need all observations from the entire domain pixels to construct a robust functional relationship between the input-output. Indeed, the constructed ANNs at a few training pixels suffice to regionalize the results with a prescribed accuracy for bias correction of temperature and precipitation. The regionalization of the precipitation network needs more training pixels than the temperature network due to higher uncertainty and

variability of precipitation. A comparison between the ANN and LR results showed that the trained ANN outperforms the LR in improving all metrics: MSE, Bias, ρ, and KS over the entire domain.

There is a reliable association between the derived delineated regions and required density of the training pixels and the physical/climatic features of the regions such as topography, land cover, elevation, dominant climatology (indicated by precipitation and temperature). Although precipitation was the best indicator of regions, a smooth variation of temperature can also be recognized in D1, D2, D3, and D4. The highest variability of temperature and elevation in D5 can clearly separate this domain from the others. A summary of the specific features in the delineated domains is:

- D1 is over the southeast of Brazil (outside the Amazon basin) mostly covered by savannas, and also small patches of deciduous broadleaf forest and sparse grassland with on average drier-cooler climate than D2
- D2 is over the majority of the Amazon basin in Brazil mostly covered by the evergreen broadleaf forest with on average wetter-warmer climate than D1.
- D3 is over the Amazon River Delta region (ARD, mouth of the Amazon River, the northeast of the study domain), covered by evergreen broadleaf forest. This region is influenced by the strong interaction of the land-atmosphere-ocean circulation, leading to the large amount of rainfall and vast estuarine wetlands.
- D4 is over the northern part of the study domain. The different boundary conditions provided by the adjacent oceans, Andes Mountains, and the trade winds affect the climate in D4. There is a stark contrast in rainfall regime between D4 and D2 (D3), with an extreme wet climate in JJA and extreme dry climate in DJF over D4. This domain is covered by different types of land cover including evergreen broadleaf forest, grasslands, savannas, and cropland/natural vegetation mosaic types.

- D5 is over the western part of the study domain, which contains the Andes Mountains and different land cover types such as evergreen broadleaf forest, deciduous broadleaf forest, grasslands, savannas, open shrub lands, cropland/natural vegetation mosaic types, and barren or sparsely vegetated types. As a result, this heterogeneous region has different climate e.g., the dry-cool weather on the west side of the mountains, the wetter-warmer weather over the east side, the tropical weather over the northern part of this domain. On average, D5 has the driest-coolest climate and the highest elevation in the entire study domain.

The delineation of the domain revealed that although more training pixels are concentrated in the heterogeneous region (e.g., D5), model calibration at about 12% to 14% of all pixels would achieve performance in bias correction of temperature and precipitation sufficiently close to that of the model calibrated at all domain pixels. This reduces the overall computational requirements, time and memory usage significantly.

This study suggests a methodology to correct model biases of precipitation and temperature over northern South America – and potentially over other locations. The new approach is capable of improving the error, correlation, and the probabilistic structure of the climate model outputs using an ANN model. The flexible and powerful predictive capacity of the ANN allows us to effectively employ the trained model for bias correction with unseen datasets in time and space.

6.2. Future Research

Accurate and high-resolution climate datasets are essential for effective and efficient long-term environmental management and climate change assessment.

Continuous developments of bias correction methods remain important to the climate research community. Promising future research includes:

- Apply the proposed bias correction method to output from other climate models and also under different climate scenarios.
- Apply the ANN model to correct the biases of the climate variables simultaneously in order to improve the preservation of cross-correlation between bias-corrected precipitation and temperature.
- Test the regionalization ability of the ANN to improve the biases of the climate variables over other domains.
- Evaluate the performance of the ANN using other training (learning) approaches, which are able to determine the structure of the ANN and the weights simultaneously (e.g., stochastic approaches such as genetic, simulated annealing methods).

APPENDIX A

RETRIEVAL OF HOURLY RECORDS OF SURFACE HYDROMETEOROLOGICAL VARIABLES

(Moghim et al., 2015)

A.1. Introduction

Global and regional climate models and remotely sensed data are commonly used to study the climate change. Adaption and impact assessments require high resolution hydrometeorological data to capture fine-scale regional climate variability (Mearns et al., 2009; Georgakakos et al., 2012). The available data products do not always have desired space and time resolutions, and hence need to be downscaled by statistical and dynamical approaches to meet the demands of applications. Dynamical downscaling often uses regional climate models (RCMs) to simulate high-resolution variables. The biases of General Circulation Model (GCM) outputs that are used to drive the RCM affect the performance of the RCM (Miller et al., 1999; Xue et al., 2007; Liang et al., 2008). The computational cost of dynamical downscaling makes it "essentially impossible" to produce long-term records (Maurer and Hidalgo, 2008). As a result, statistical downscaling methods are often an alternative to generate high-resolution variables. The statistical downscaling is based on the derived relationship or transfer function between modeled outputs and the corresponding observations during the same periods of time assuming that the transfer function derived from historical data remains unchanged for future times (Mearns et al., 1999; Murphy, 1999). Yet, this stationarity assumption for the transfer function may not always hold. Mathematically, a transfer function relates predictands to predictors. For example, predictors can be large-scale atmospheric variables and predictands can be the corresponding local surface variables, the parameters

of the distributions of local variables, and the frequencies of the extreme local variables (Pfizenmayer and Storch, 2001; Katz et al., 2002). Weather classification, regression models, and weather generators are the common statistical downscaling methods, which are mainly used in the Intergovernmental Panel on Climate Change Third Assessment Report IPCC TAR (Giorgi et al., 2001). For a complete explanation and review of dynamical and statistical downscaling techniques, the reader is referred to (Fowler et al., 2007; Wilby et al., 2004; Wilby and Wigley, 1997; Xu, 1999, among many others).

However Statistical downscaling methods are computationally advantageous over dynamical downscaling methods (Hay and Clark, 2003; Wilby and Wigley, 2000; Wood et al., 2004), they do have drawbacks. First, statistical relationships between predictors and predictands may be difficult to identify. Second, transfer functions do not always capture the underlying physical mechanisms and variability of climate system. This appendix proposes a new algorithm to disaggregate daily surface hydrometeorological variables into hourly variables using physically and statistically based models with input data from satellite remote sensing observations complemented by ground observations (Moghim et al., 2015). The work was sponsored by the Andes-Amazon Initiative of the Gordon and Betty Moore Foundation. Funding was also provided by NSF grant EAR-1138611 and ARO grant W911NF-07-1-0126.

A.2. Methodology

The retrieval algorithm of hourly meteorological variables from hourly satellite data and in-situ daily air temperature is based on three models: (1) surface net radiation (R_n) is estimated using hourly albedo derived from channel one (visible) of the GOES satellite (Bisht and Bras, 2010); (2) partition of net radiation into fluxes (sensible, latent, and ground heat fluxes) is estimated using the maximum entropy production (MEP) model (Wang and Bras, 2011); (3) hourly surface air temperature is retrieved from

sensible heat flux obtained from (2) using the half-order integral model (Wang and Bras, 1999).

A.2.1. Net Radiation Model

Surface net radiation R_n is expressed as

$$R_n = R_S^{\downarrow} - R_S^{\uparrow} + R_L^{\downarrow} - R_L^{\uparrow} \quad \text{(A.1)}$$

where $R_S^{\downarrow}$, $R_S^{\uparrow}$, $R_L^{\downarrow}$, and $R_L^{\uparrow}$ are downwelling shortwave, reflected shortwave, downweling longwave, and upwelling longwave radiation, respectively. Components of the surface energy budget can be parameterized using near-surface air temperature, humidity, and surface temperature (Brutsaert, 1975; Diak and Gautier, 1983; Idso, 1981; Prata, 1996; Zillman, 1972; Bisht and Bras, 2010). Downwelling shortwave radiation for clear sky ($R_S^{\downarrow clear}$) is expressed as (Zillman, 1972)

$$R_S^{\downarrow clear} = \frac{S_0 cos^2\theta}{1.85\, cos\theta + e_0(2.7+cos\theta)\times 10^{-3} + \beta} \quad \text{(A.2)}$$

where S_0 is the solar constant (1367 W m^{-2}), θ the solar zenith angle, e_0 (mb) the near-surface vapor pressure, and β an empirical coefficient set to be 0.1. It has been shown that Eq. A.2 tends to overestimate $R_S^{\downarrow clear}$ (Niemelä et al., 2001a,b; Bisht et al., 2005). In this study, β is set to be 0.2 to correct the overestimation (Bisht and Bras, 2010). e_0 is approximated as the saturated vapor pressure at air temperature T_a. The second term in denominator of Eq. A.2 plays a minor role on $R_S^{\downarrow clear}$ as it is at least one order of magnitude smaller than the first and third term, allowing a convenient approximation when surface humidity data are not available.

Surface downwelling and reflected shortwave radiation are expressed in terms of cloud and surface albedo, α_c and α_s, respectively as

$$R_S^{\downarrow} = (1 - \alpha_c)\, R_S^{\downarrow clear} \quad \text{(A.3)}$$

and

$$R_S^{\uparrow} = \alpha_s\, R_S^{\downarrow} \quad \text{(A.4)}$$

Albedo data used in this study are derived from the GOES visible images. α_c is obtained under cloudy condition and α_s is obtained under clear sky condition. Since the temporal variability of α_s is relatively low (Tsvetsinskaya et al., 2006), the obtained α_s is assigned as the time-invariant parameter for each site.

The other components of net radiation, downwelling and upwelling longwave radiation, are calculated based on the Stefan-Boltzmann's law as

$$R_L^{\downarrow} = \varepsilon_a \sigma T_a^4 \tag{A.5}$$

and

$$R_L^{\uparrow} = \varepsilon_s \sigma T_s^4 \tag{A.6}$$

where σ is the Stefan-Boltzmann constant (5.67×10^{-8} W m^{-2} K^{-4}); T_a is assumed to be equal to surface temperature (T_s) as an approximation when hourly T_s is not available. Surface emissivity (ε_s) is taken as unity due to its small variability over the land (Dickinson et al., 1986). Air emissivity (ε_a) is parameterized using e_0 (mb) and T_a (K) as (Prata, 1996)

$$\varepsilon_a = 1 - (1 + \zeta)\exp(-\sqrt{1.2 + 3\zeta}) \tag{A.7}$$

where the dimensionless parameter ζ is calculated as

$$\zeta = 46.5 \frac{e_0}{T_a} \tag{A.8}$$

A.2.2. Sensible Heat Flux Model

The recently developed maximum entropy production (MEP) model of evapotranspiration ET (Wang and Bras, 2011) provides a parameterization of sensible heat flux used in this study. The theory and formulation of the MEP model are described in detail in (Wang and Bras 2009; Wang and Bras, 2011). The MEP model predicts the partition of net radiation R_n into sensible H, latent E, and ground G heat fluxes according to

$$R_n = H + E + G \tag{A.9}$$

$$G = \frac{B(\sigma)}{\sigma}\frac{I_s}{I_0} H|H|^{-\frac{1}{6}} \quad \text{(A.10)}$$

and

$$E = B(\sigma)H \quad \text{(A.11)}$$

where I_s is the thermal inertia of the soil, I_0 is the apparent thermal inertia of the air, and B, the inverse Bowen ratio, is given as

$$B(\sigma) = 6\left(\sqrt{1+\frac{11}{36}\sigma} - 1\right) \quad \text{(A.12)}$$

and

$$\sigma = \frac{L_v^2}{c_P R_v}\frac{q_s}{T_s^2} \quad \text{(A.13)}$$

where c_P is the specific heat of air at constant pressure, L_v is the latent heat of vaporization of liquid water, R_v is the gas constant for water vapor, and q_s is the surface specific humidity at surface (skin) temperature T_s. For a saturated soil, a dimensionless parameter σ may be expressed as

$$\sigma = \frac{\Delta}{\gamma} \quad \text{(A.14)}$$

where Δ is the slope of the saturation vapor pressure at T_s according to the Clausius-Clapeyron equation and γ is the psychrometric constant (Brunt, 1939; Brutsaert, 1982).

A.2.3. Air Temperature Model

The diurnal variation of near-surface air temperature may be expressed in terms of a weighted time average (i.e. half-order integral) of sensible heat flux analogous to the half-order integral model of soil temperature and ground heat flux (Wang and Bras, 1999; Bennett et al., 2008)

$$T_a(t) = T_0 + \frac{1}{I}\int_{-\infty}^{t}\frac{H(s)ds}{\sqrt{\pi(t-s)}} \quad \text{(A.15)}$$

where T_0 is a reference temperature. In this study, T_0 is determined in such a way that the modeled daily mean air temperature $\overline{T_a}$, according to Eq. A.15, is equal to the observed

daily mean air temperature. *I* is the thermal inertia of air, which is treated as a fitting parameter to the model in this study (the details are described in subsection A.3.1).

A.3. Tests of the Algorithm

The proposed algorithm was tested at two sites in Brazil, Caxiuana (Cax) and Reserva Pe-de-Gigante (PDG), during January and February 2002 and two sites in Arizona, Kendall (Ken) and Lucky Hills (LKH), during January 2002. Table A.1 presents the characteristics of the sites used in the study.

Table A.1. General characteristics of the sites. Caxiuana and Reserva Pe-de-Gigante are sites of the LBA project; Kendall and Lucky Hills are sites of the Walnut Gulch Experimental Watershed.

Site	Location	Lat	Lon	Elev(m)	Biome Type
Caxiuanã	Para, Brazil	1.72°S	51.46°W	23	Forest
Reserva Pé-de-Gigante	São Paulo, Brazil	21.62°S	47.65°W	690	Savanna
Kendall	Arizona, US	31.74°N	109.94°W	1526	Grass
Lucky Hills	Arizona, US	31.74°N	110.05°W	1372	Shrub

Observations of hourly air temperature for the two sites in Brazil are from the Large Scale Biosphere-Atmosphere Experiment in Amazonia (LBA) project (de Goncalves et al., 2013). More detailed information about the data is available at http://dx.doi.org/ 10.3334/ORNLDAAC/1177. Observations of net radiation, sensible heat flux, air temperature, and other meteorological and hydrological data at the two sites in Arizona are from the Walnut Gulch Experimental Watershed (Emmerich and Verdugo, 2008). Data products are publicly available at http://www.tucson.ars.ag.gov/dap/. Daily mean air temperature required as an input to the proposed algorithm is obtained by averaging the observed hourly air temperature at the sites. Satellite-based remote sensing data as the other input used in this study come from the Geostationary Operational Environmental Satellite (GOES) of the National Oceanic and Atmospheric Administration (NOAA)

(publicly available at http://www.class.ngdc. noaa.gov). Visible images of GOES 8 centered at 0.65 μm with 1 km and hourly spatial-temporal resolution are used for the retrieval of hourly records of meteorological variables in the study.

A.3.1. Procedure

The hydrometeorological variables including hourly net radiation, sensible heat flux, and air temperature are estimated through three steps. In step one, mean daily air temperature and cloud albedo are used to calculate the components of radiation (longwave and shortwave radiation). Albedo, as an input to the algorithm, is assigned to each site based on the closest distance of the GOES images to the coordinates (longitude and latitude) of the site; sensible heat flux is computed for a given net radiation using the MEP model; and hourly air temperature is estimated using the half-order integral model. In step two, the same process is repeated by using the estimated hourly temperature as the input to update the calculated radiation and heat flux from step one. In step one and two, I is set at 3000 tiu (J m^{-2} K^{-1} $s^{-1/2}$) as an initial guess. In step three, the hourly temperature and sensible heat flux obtained from step two are used to estimate I as the regression coefficient between diurnal amplitudes of air temperature (ΔT_a) and sensible heat flux (ΔH) according to the following equation (Wang et al., 2010)

$$I = \frac{\Delta H}{\Delta T_a \sqrt{\omega_0}} \tag{A.16}$$

where $\omega_0 = \frac{2\pi}{d}$ with d being the length of day (24 hours). In step three, the estimated I is used to re-calculate the hourly temperature. The schematic diagram of the procedure is illustrated in Figure A.1.

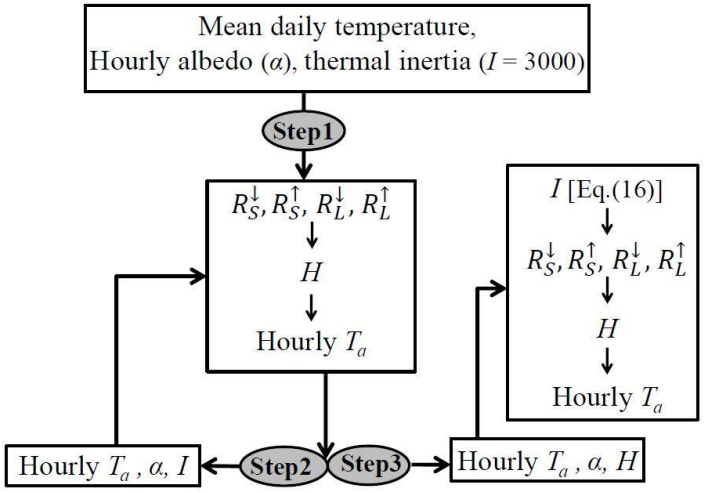

Figure A.1. The schematic diagram of the three-step algorithm.

A.3.2. Results

Estimated hourly net radiation and sensible heat flux at two sites in Brazil are illustrated in Figure A.2.

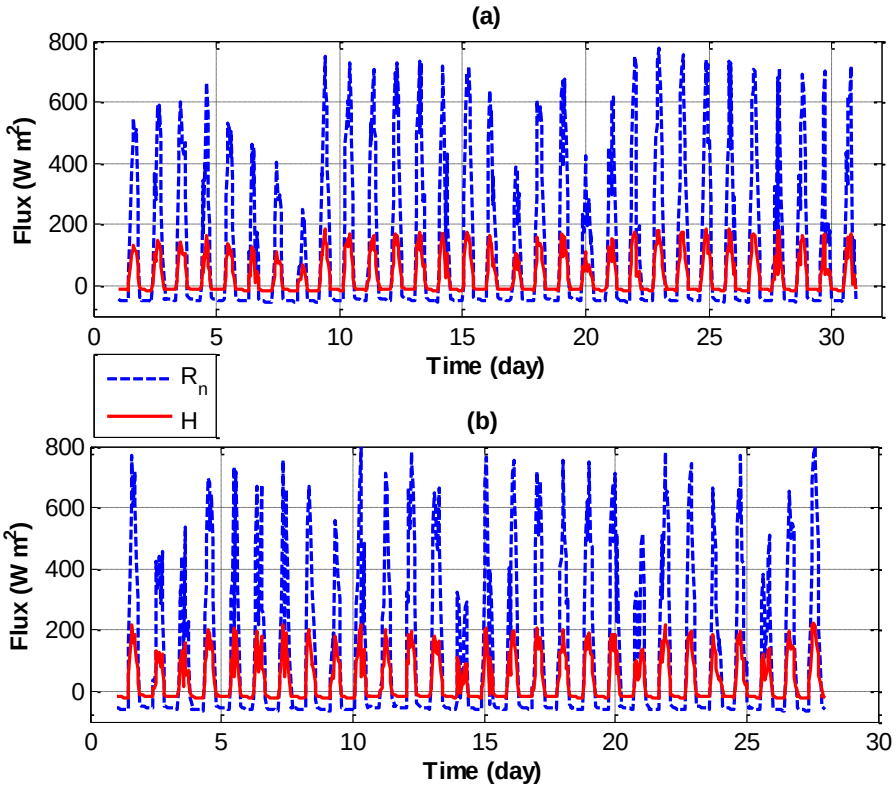

Figure A.2. Estimated hourly net radiation (blue dashed line) and sensible heat flux (red solid line) at (a) Cax in January 2002 and (b) PDG in February 2002.

The lower negative net longwave radiation at Cax agrees with the fact that more (thicker) clouds over Cax block more surface emitted longwave radiation from escaping to the space. It suggests that the average cloud albedo over Cax is greater than that over PDG during the test period. Note that a narrowband albedo data derived from one visible channel of the GOES satellite centered at 0.65 μm (0.55-0.75 μm) is essentially equivalent to "broadband" since the channel covers the range of the high intensity of shortwave radiation energy. Average sensible heat flux over PDG is higher than that over Cax. This is consistent with the fact that lower humidity over the savanna site (PDG) results from higher sensible heat flux compared to those over the forest site (Cax). Figure A.3 compares estimated hourly air temperature with the corresponding observations at the two sites.

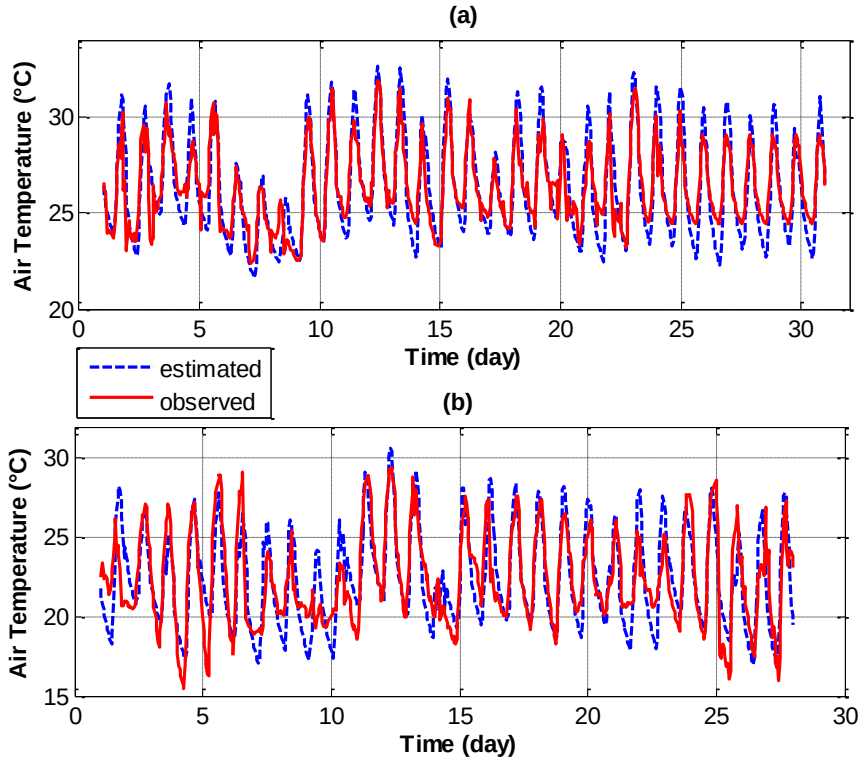

Figure A.3. Estimated hourly air temperature (blue dashed line) compared with observations (red solid line) from the LBA project at (a) Cax in January 2002 and (b) PDG in February 2002.

The field tests suggest that the proposed algorithm is able to retrieve hourly records of surface hydrometeorological variables using satellite remote sensing data supplemented by in-situ daily mean temperature. The performance of the algorithm is further illustrated through scatter plots in Figure A.4 at the two sites.

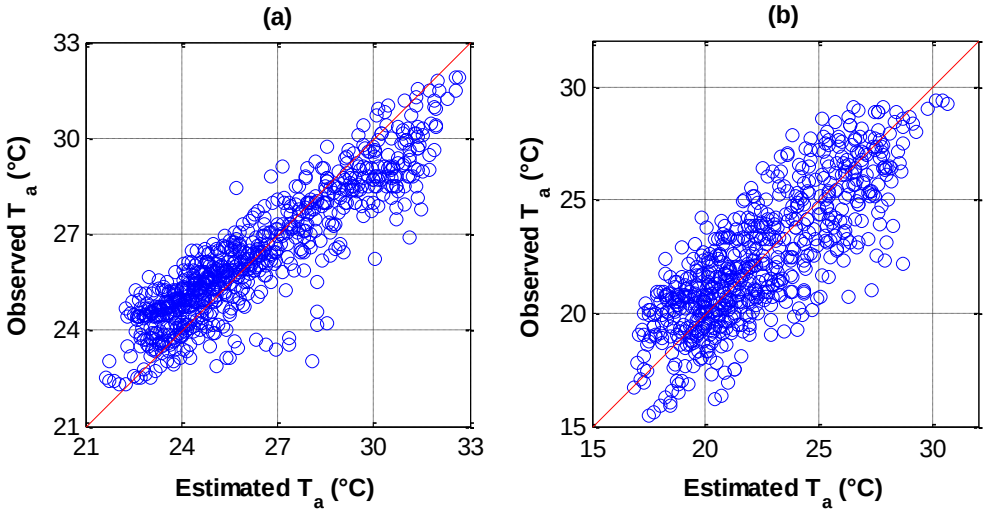

Figure A.4. Estimated vs observed air temperature corresponding to Fig. A.3 for (a) Cax (ρ = 0.90) and (b) PDG (ρ = 0.81).

Correlation coefficients (ρ) between observed and estimated air temperature of Cax and PDG are 0.90 and 0.81, respectively. The algorithm tends to underestimate lower temperatures and overestimate higher temperatures at Cax, but no apparent biases in the estimated temperature at PDG. This may be due to the fact that the stability of the atmosphere over the forest (Cax) is lower than that over the Savanna (PDG). It implies that improvement of parameterization of the thermal inertia is needed over forest sites with more unstable atmosphere. Since observations of R_n and H at Cax and PDG sites were not available to the authors, the radiation and flux models were tested using field observations from the Walnut Gulch Experimental Watershed. Figure A.5 compares estimated hourly net radiation with the corresponding observations at Ken and LKH sites for January 2002.

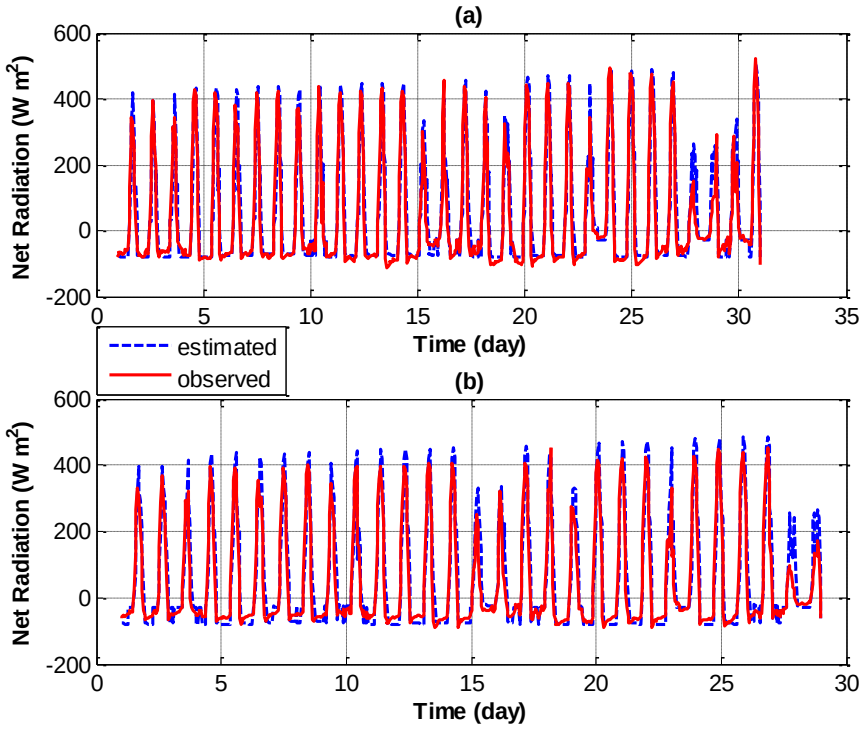

Figure A.5. Estimated hourly net radiation (blue dashed line) compared with observations (red solid line) from the Walnut Gulch Experimental Watershed at (a) Ken and (b) LKH in January 2002.

This Figure indicates that the estimated hourly R_n is in close agreement with the observed ones. The slightly overestimated R_n in particular at LKH site may be caused by the use of air temperature as a surrogate of surface temperature, leading to a decrease in $R_L^{\uparrow}$ and an increase in R_n (see Eqs. A.1,6). Figure A.6 shows a close agreement between the modeled and observed H.

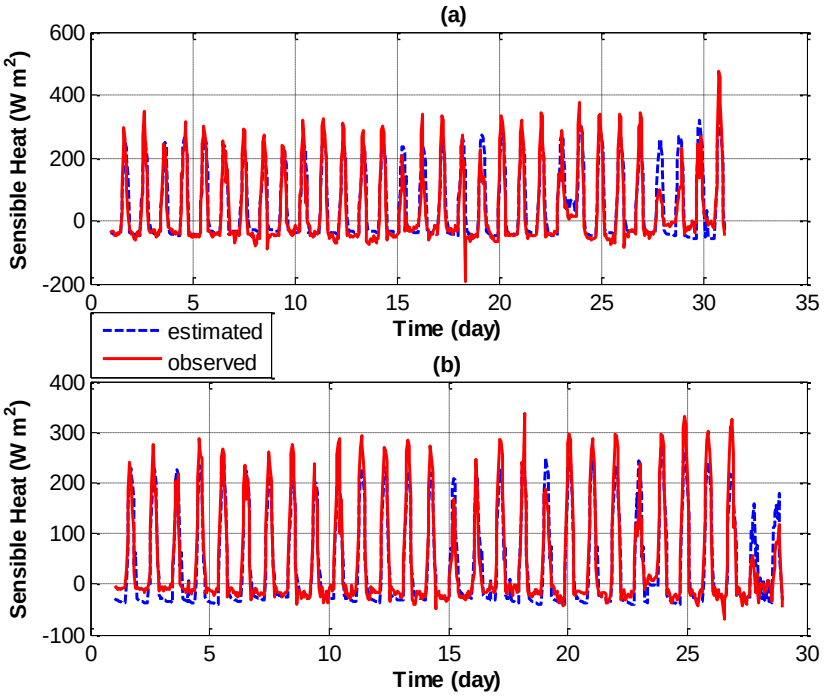

Figure A.6. Estimated hourly sensible heat flux (blue dashed line) compared with observations (red solid line) from the Walnut Gulch Experimental Watershed at (a) Ken and (b) LKH in January 2002.

Unrealistic values of observed H appeared by spurious spikes in Figure A.6. Bowen ratio energy balance technique was used to measure sensible heat flux in the Walnut Gulch Experimental Watershed (Emmerich and Verdugo, 2008). To overcome this issue, the other field experiment is required to measure heat fluxes (such as the eddy-covariance method). The corresponding scatter plots of R_n and H in Figures A.7 and A.8 indicate close agreement between the estimated and observed fluxes.

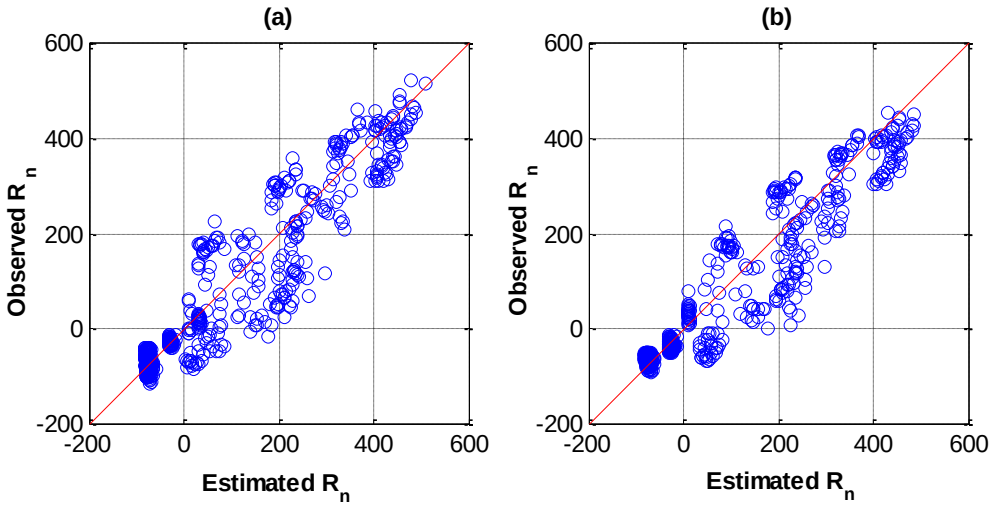

Figure A.7. Estimated vs observed net radiation corresponding to Fig. A.5 for (a) Ken and (b) LKH.

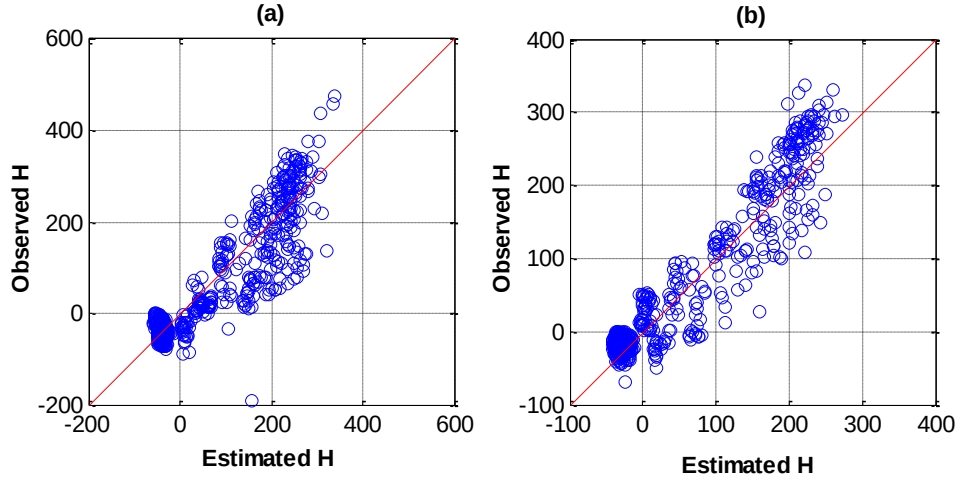

Figure A.8. Estimated vs observed sensible heat flux corresponding to Fig. A.6 for (a) Ken and (b) LKH.

Note that any uncertainty of the results may be caused by the uncertainty of the remote sensing data and the way that albedo is assigned to each site, which is based on the closest distance of the GOES images to the coordinate of the site. Figure A.9 indicates that the estimated air temperature agrees closely with the observations.

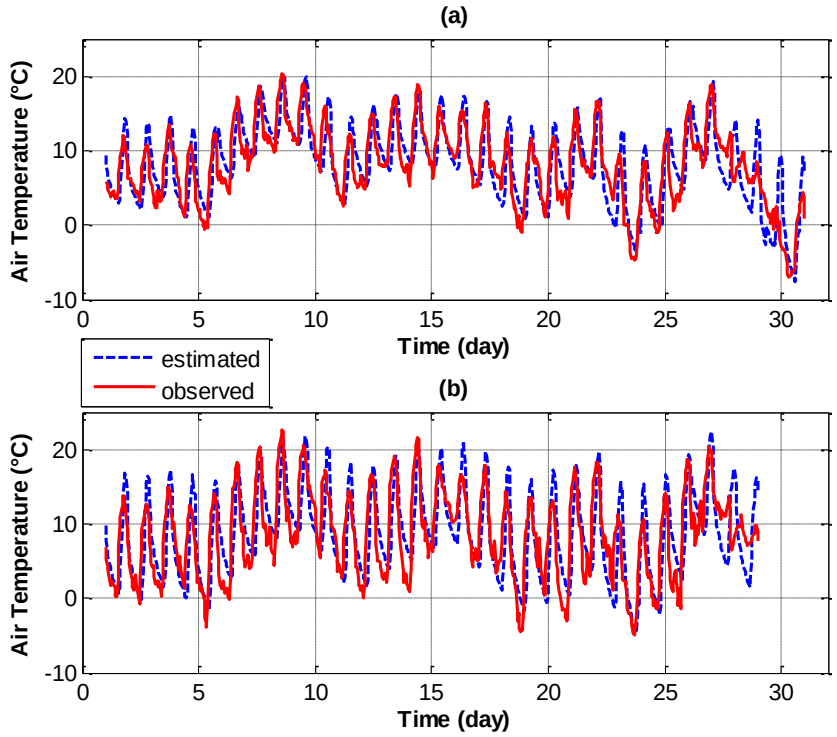

Figure A.9. Estimated hourly air temperature (blue dashed line) compared with observations (red solid line) from the Walnut Gulch Experimental Watershed at (a) Ken and (b) LKH in January 2002.

Correlation coefficients (ρ) between observed and estimated air temperature of Ken and LKH are 0.80 and 0.74, respectively shown in Figure A.10.

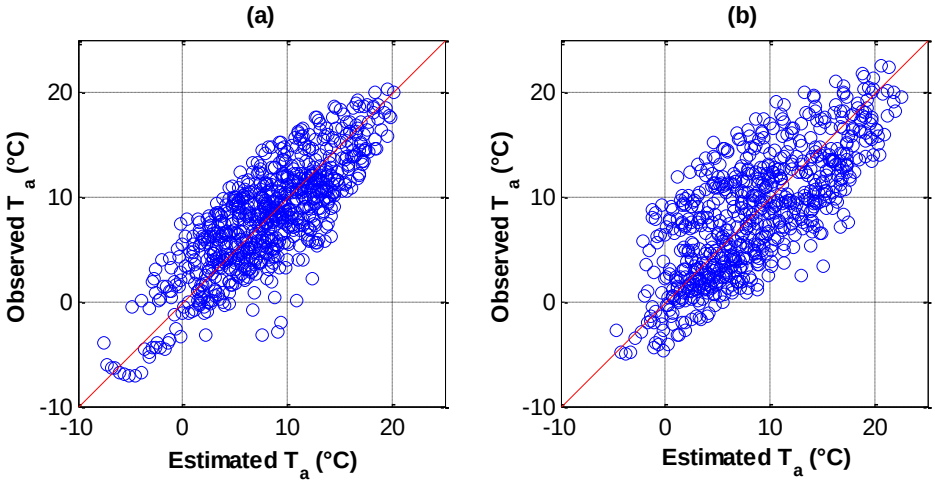

Figure A.10. Estimated vs observed air temperature corresponding to Fig. A.9 for (a) Ken (ρ = 0.80) and (b) LKH (ρ = 0.74).

The differences between estimated and observed R_n and H obtained from the Net Radiation and the Sensible Heat Flux Models may cause the discrepancies between estimated and observed T_a because the Air Temperature Model requires sensible heat flux obtained from the Sensible Heat Flux Model and net radiation from the Net radiation Model. The disaggregated hourly air temperature is affected by the thermal inertia parameter, daily mean air temperature, and GOES images as inputs to the algorithm. For any given sensible heat flux, greater thermal inertia leads to smaller diurnal amplitude of air temperature and vice versa (see Eq. A.15). Daily mean temperature affects diurnal variations of air temperature through longwave radiation. When daily mean temperature decreases, upward longwave radiation decreases, leading to an increase in net radiation and sensible heat flux, and a greater amplitude of the diurnal variation of air temperature and vice versa.

A.4. Summary and Conclusions

This study develops a new physically and statistically based algorithm for retrieving hourly surface hydrometeorological variables including air temperature, radiation, and heat flux. The close agreement between the observed and estimated air temperature over the sites with different climate (see Table A.1) suggests that the MEP and the half-order time integral models used in the proposed algorithm have potential to improve the estimates of the variability and magnitude of air temperature globally. Although the physically-based models (e.g. transfer based models) often use gradients of the variables such as temperature and humidity, the MEP model uses only one level of the inputs and the vertical profiles of the inputs are avoided. A major advantage of the algorithm is that the algorithm requires only mean daily temperature and satellite-based single level observations as inputs. The algorithm has lower computational cost compared to other existing dynamical downscaling methods. Decision makers and water resources

planners may use the retrieved hourly data to drive other land, ecosystem, and coupled climate-hydrology-water resources models.

APPENDIX B

BIAS CORRECTION OF THE CLIMATE MODEL OUTPUTS OVER AMAZONIA

(Moghim et al., 2015)

B.1. Introduction

This appendix explains the process of correcting biases of the variables including temperature T, precipitation P, specific humidity Q, and downwelling longwave radiation LW_d over Amazonia (Moghim et al., 2015). The data are obtained from the global and regional climate models, the Climate System Model (CCSM3) and the Regional Climate Model driven by the Hadley Centre Coupled Model (RegCM3), for historical (under 20C3M scenario) and future (under A2 scenario) period over the Amazon Basin extending from 74.5°W to 49.5°W and from 17.5°S to 3.5°N (Fig. B1). The regional Eta-CPTEC Model nested in HadCM3 (RegCM3) is used to provide the data over South America (Chou et al., 2012). The standard (unperturbed) HadCM3 was used as boundary conditions of RegCM3 at every 6 hour and updated linearly along the boundaries for each time step. We used 1960-1990 and 1940-2009 modeled datasets as the historical time for the RegCM3 and CCSM3, respectively and 2010-2099 as the projection time. The final long-term unbiased climate datasets can be used as forcing of ecosystem and hydrologic models to study climate changes and impact assessments over the Amazon Basin (Zhang et al., 2015). This work was supported by the Andes-Amazon Initiative of the Gordon and Betty Moore Foundation (http://www.oeb.harvard.edu/faculty/moorcroft/andes-amazon/).

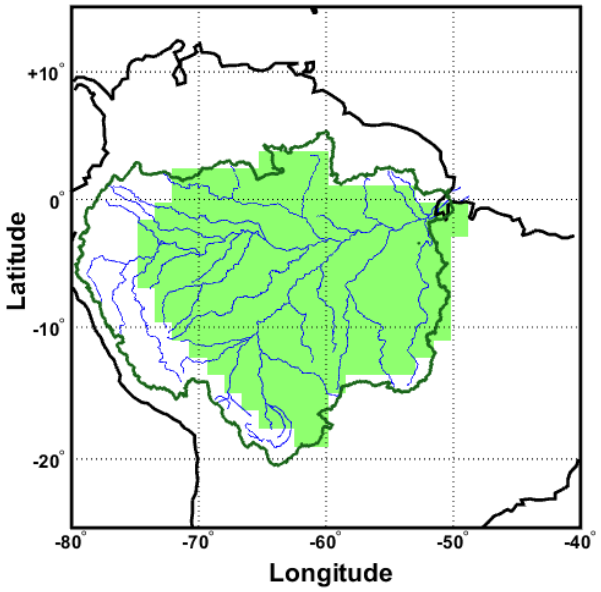

Figure B.1. Northern of South America. The Amazon Basin is bounded by the green line and the study domain is shaded by green color.

B.2. Methodology

The EDCDF method was used to reduce the biases of 6-hourly temperature and precipitation for the historical period and projection (under A2 scenario). Then specific humidity and downwelling longwave radiation were adjusted to be physically consistent with the bias-corrected temperature values. The correction methods of the climate variables are described in detail as follows:

B.2.1. Precipitation and Temperature

The differences between the empirical CDFs of the observations and the modeled outputs in the historical period at each percentile of the future projection (Δ) were used to correct the biases of the monthly model projections. We considered 1940-2009 and 1960-1990 as the historical periods for CCSM3 and RegCM3, respectively and 2010-2099 as the future projection period. We used the Climate Research Unit dataset (CRU) as the reference observations. To unify the spatial scales of this dataset with the spatial resolution of the studied model outputs, the monthly CRU data with original resolution of

0.5° were averaged to the models resolution. The years of the observations were selected based on available years of the historically modeled data (1940-2009 for CCSM3 and 1960-1990 for RegCM3). The longer record of the CCSM3 data, in particular years of 1991-2009, resulted in a better representative CDF of the modeled historical period compared to the RegCM3. Indeed, this recent period was reported by the IPCC as the beginning of a significant warming regime (Third Assessment Report, TAR 2001). For the temperature and precipitation variables, first we obtained bias-corrected values using the explained EDCDF method in a monthly basis. Then we multiplicatively adjusted hourly data (P^h) to conserve the bias-corrected monthly mean precipitation ($\tilde{P}^m$) as follows:

$$\tilde{P}^h = P^h \times \frac{\tilde{P}^m}{P^m} \quad \text{(B.1)}$$

where P^m is originally modeled monthly precipitation and $\tilde{P}^h$ denotes the bias-corrected values. Analogous to precipitation, we used an additive adjustment scheme (Eq. B.2) to assure that the bias-corrected mean monthly temperature ($\tilde{T}^m$) is properly conserved.

$$\tilde{T}^h = T^h + (\tilde{T}^m - T^m) \quad \text{(B.2)}$$

where T^m is originally modeled mean monthly values, while T^h and $\tilde{T}^h$ denotes hourly temperature before and after bias correction, respectively.

B.2.2. Specific Humidity

Adjustments of the temperature values can cause supersaturation and inconsistency between temperature and specific humidity. To resolve this inconsistency, specific humidity is adjusted (Sheffield et al., 2006; Cosgrove et al., 2003). In particular, the saturated vapor pressure E_{sat} as a function of air temperature for pure water vapor was expressed as (Buck, 1981)

$$E_{sat} = a \times exp\left[\frac{\left(b - \frac{T}{d}\right) \times T}{T + c}\right] \quad \text{(B.3)}$$

where a, b, c, d are empirical parameters defined in Table A.1 and T is modeled temperature before bias correction in Celsius. Buck (1981) also suggested an enhancement factor f, that is used to account for moist air as follow:

$$f = 1 + \alpha + PS \times (\beta + \gamma \times T^2) \quad \text{(B.4)}$$

where PS is modeled surface pressure (in millibar) and α, β, and γ are empirical constants reported in Table B.1. Thus, the modified saturated vapor pressure ($E_{sat,mod}$) can be computed as

$$E_{sat,mod} = E_{sat} \times f \quad \text{(B.5)}$$

and the saturated specific humidity Q_{sat} can be computed as

$$Q_{sat} = \frac{0.622 E_{sat,mod}}{(PS - 0.378 E_{sat,mod})} \quad \text{(B.6)}$$

and thus, the corresponding relative humidity as follows:

$$RH = \frac{E}{E_{sat,mod}} = \frac{Q \times (0.622 + 0.378 Q_{sat})}{Q_{sat} \times (0.622 + 0.378 Q)} \leq 1 \quad \text{(B.7)}$$

where Q denotes the modeled specific humidity. To adjust specific humidity, bias-corrected temperatures were plugged into all of the above equations. The new calculated saturated specific humidity was called $Q_{sat,adj}$. Then the bias-corrected specific humidity $\tilde{Q}$, was expressed as

$$\tilde{Q} = Q_{sat,adj} \times RH \quad \text{(B.8)}$$

The above steps were used to adjust specific humidity values for CCSM3. The RegCM3 provided dew point temperature and not the specific humidity. Therefore, one additional step was required to convert dew point temperature to specific humidity in this model outputs. To this end, given the dew point temperature, the water vapor pressure E was calculated using Eq. B.3 and then was used in Eq. B.6 to obtain the specific humidity.

Table B.1. Empirical parameters for calculation of vapor pressure as a function of temperature in Eqs. B.3 and B.4 (Buck, 1981).

Parameters	**a**	**b**	**c**	**d**	**α**	**β**	**γ**
T > 0°C	6.1121	18.729	257.87	227.3	7.2×10^{-4}	3.2×10^{-6}	5.9×10^{-10}
T < 0°C	6.1115	23.036	279.82	333.7	2.2×10^{-4}	3.83×10^{-6}	6.4×10^{-10}

B.2.3. Downwelling Longwave Radiation

Changes in air temperature values influence downwelling longwave radiation. To have a consistent bias-corrected temperature with downwelling longwave radiation values, we adjust longwave radiation using modeled emissivity values ϵ. The implied emissivity is computed using the modeled longwave radiation LW_d and the biased temperature T based on the Stefan-Boltzmann law as

$$\epsilon = \frac{LW_d}{\sigma T^4} \tag{B.9}$$

where σ is the Stefan-Boltzmann constant (5.67×10^{-8} W m^{-2} K^{-4}). Then bias-corrected downwelling longwave radiation ($\widetilde{LW_d}$) was identified using the modeled emissivity values computed in Eq. B.9 and bias-corrected temperatures $\tilde{T}$ as

$$\widetilde{LW_d} = \epsilon\sigma\tilde{T}^4 \tag{B.10}$$

It is important to note that changes in the temperature values play a more dominant role than changes in the emissivity values due to the fourth power temperature dependence in the Stefan-Boltzmann law. Thus, we adjusted downwelling longwave radiation only based on the changes in temperature values.

B.3. Results

To illustrate the spatial and temporal performance of the models, we use differences between original and statistically bias-corrected variables (hereafter estimated differences) in the historical and future periods. Figure B.2 illustrates the temporal

average of estimated differences for CCSM3 and RegCM3 variables at 1° by 1° spatial resolution.

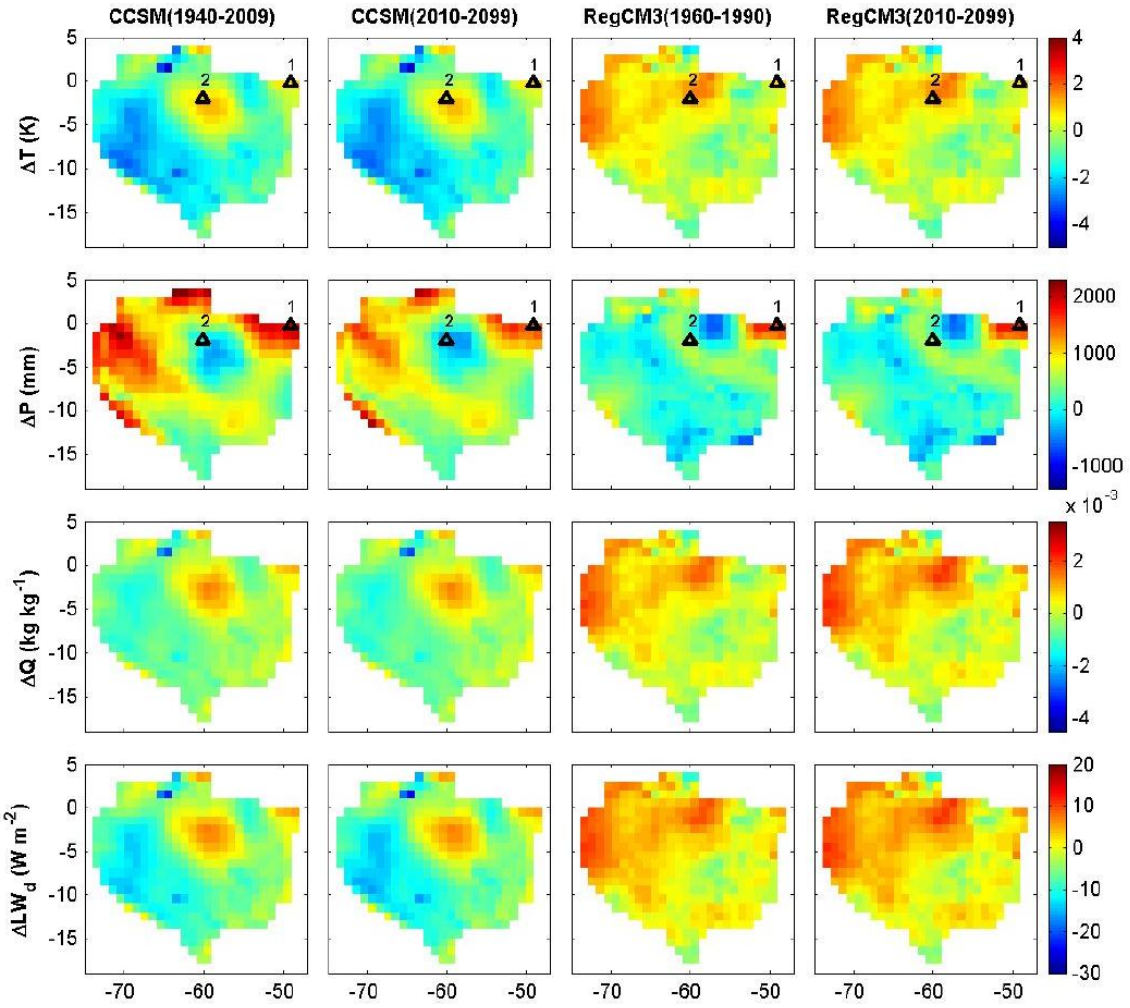

Figure B.2. From left-to-right panels: The temporal average of estimated differences of CCSM3 (first and second columns) and RegCM3 (third and fourth columns) in historical and future periods, respectively. From top-to-bottom: The estimated differences for temperature ΔT (K), precipitation ΔP (mm), specific humidity ΔQ (kg kg^{-1}), and downwelling longwave radiation, ΔLW_d (W m^{-2}), respectively. The outlet of the Amazon Basin and the city of Manaus are illustrated by numbers 1 and 2, respectively.

In this figure, the rows from top to bottom show the spatial fields of the estimated differences over all grid cells for temperature (ΔT), precipitation (ΔP), specific humidity (ΔQ), and downwelling longwave radiation (ΔLW_d), respectively. The first two columns

demonstrate the estimated differences in CCSM3 while the last two columns show the estimated differences for RegCM3 in the historical and future periods. The first row demonstrates that CCSM3 overestimates temperature in major parts of the domain, in particular over the western edge of the study domain (ΔT is negative). In contrast, RegCM3 underestimates temperature over most of those areas (ΔT is positive). We also see that both CCSM3 and RegCM3 show a small underestimation over the city of Manaus in the State of Amazonas (see Figure B.2).

The second row indicates that precipitations is generally underestimated by CCSM3 particularly over west, north, and around the outlet of the basin (see Figure B.2). Note that, CCSM3 shows a potential wet cool bias over Manaus. The estimated differences in the precipitation fields are smaller in RegCM3 compared to CCSM3 almost over the entire study domain. Precipitation is also underestimated by RegCM3 around the outlet. A poor performance of the model in simulating temperature and precipitation fields can be caused by inappropriate schemes and parametrizations used in the model over the above regions. Land cover representation can also contribute to the imperfect performance of the models. Differences between the land surface parameters of the models and land cover from remotely sensed MODIS product are reported by Tian et al. (2004); Oleson et al. (2003); Wang et al. (2004).

Since Q and LW_d are adjusted based on the bias-corrected temperature values, the patterns of spatial differences for specific humidity and downwelling longwave radiation, shown in the third and the fourth rows, are relatively analogous to the patterns of the temperature differences shown in the first row. For instance, where ΔT is negative, the estimated difference for longwave radiation (ΔLW_d) is also negative and vice versa. We can also observe that the patterns of the differences in all fields for the historical and future periods are very similar because in the bias correction method we assumed that the differences between the CDFs of observed and modeled values are stationary over time.

Figure B.3 illustrates the mean monthly domain average of the estimated differences between bias- corrected and the original time series for CCSM3 and RegCM3 outputs in the historical and future periods.

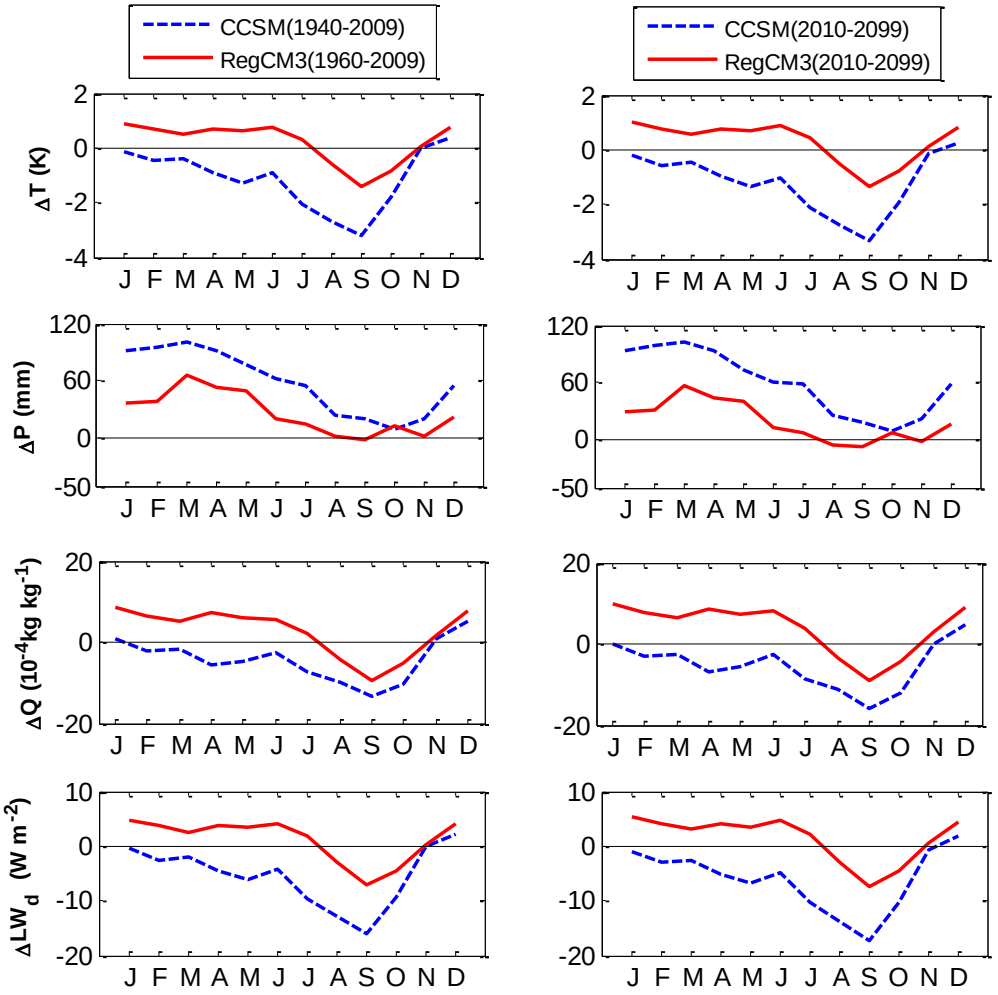

Figure B.3. The mean monthly domain average of estimated differences for CCSM3 and RegCM3 in the historical and future period. Blue dashed and red solid lines are CCSM3 and RegCM3, respectively. The first to fourth rows are the estimated differences for temperature ΔT (K), precipitation ΔP (mm), specific humidity ΔQ (kg kg^{-1}), and downwelling longwave radiation, ΔLW_d (W m^{-2}), respectively.

The Figure illustrates the temporal performance of the models over the study domain. The first to fourth rows show estimated differences for temperature (ΔT), precipitation (ΔP), specific humidity (ΔQ), and downwelling longwave radiation (ΔLW_d), respectively. The first column shows the results in the historical period and the second column is

referred to the future period. From the first row, it can be inferred that the CCSM3 overestimates temperature in almost all months while small underestimation can be seen during December. Furthermore, RegCM3 underestimates temperature in all months except for August, September, and October. The results show that both models tend to have a warm bias during the dry-warm season (Aug., Sep., Oct.). The largest estimated difference of temperature for both CCSM3 and RegCM3 occurs in September, which is more significant in CCSM3.

The second row indicates that, on average, the underestimation in the CCSM3 monthly precipitation fields is more significant than those by RegCM3 for all months. It is seen that the highest difference occurs during the rainy months in the Amazon (January to June) and the smaller difference is during the dry months (July through December) for both CCSM3 and RegCM3.

As expected, the patterns of ΔQ and ΔLW_d in the third and fourth rows follow the same pattern as of temperature. We can also observe that the patterns of future differences are similar to those of the historical differences although the magnitudes are slightly different.

As we previously mentioned, there are uncertainties regarding the predicted effects of climate change on the Amazon Basin and its ecosystem as a result of uncertainties in different GCMs' outputs. Therefore, using multiple models can perhaps shed more light on the existing uncertainties. To better understand the inter-annual trends of the domain average values of the climate variables of interest, Figure B.4, from top to bottom, shows the annual bias-corrected values of CCSM3 and RegCM3 temperature, precipitation, specific humidity, and long-wave radiation, respectively. We compared the datasets with bias-corrected PCM1 data (Sheffield et al., 2006 and Li et al., 2010), which used the same bias correction method (EDCDF) and the CRU as the reference dataset. The monthly CRU data, used to reduce the biases of the modeled temperature and precipitation, are also shown for comparison purposes in Figures B.4a,b.

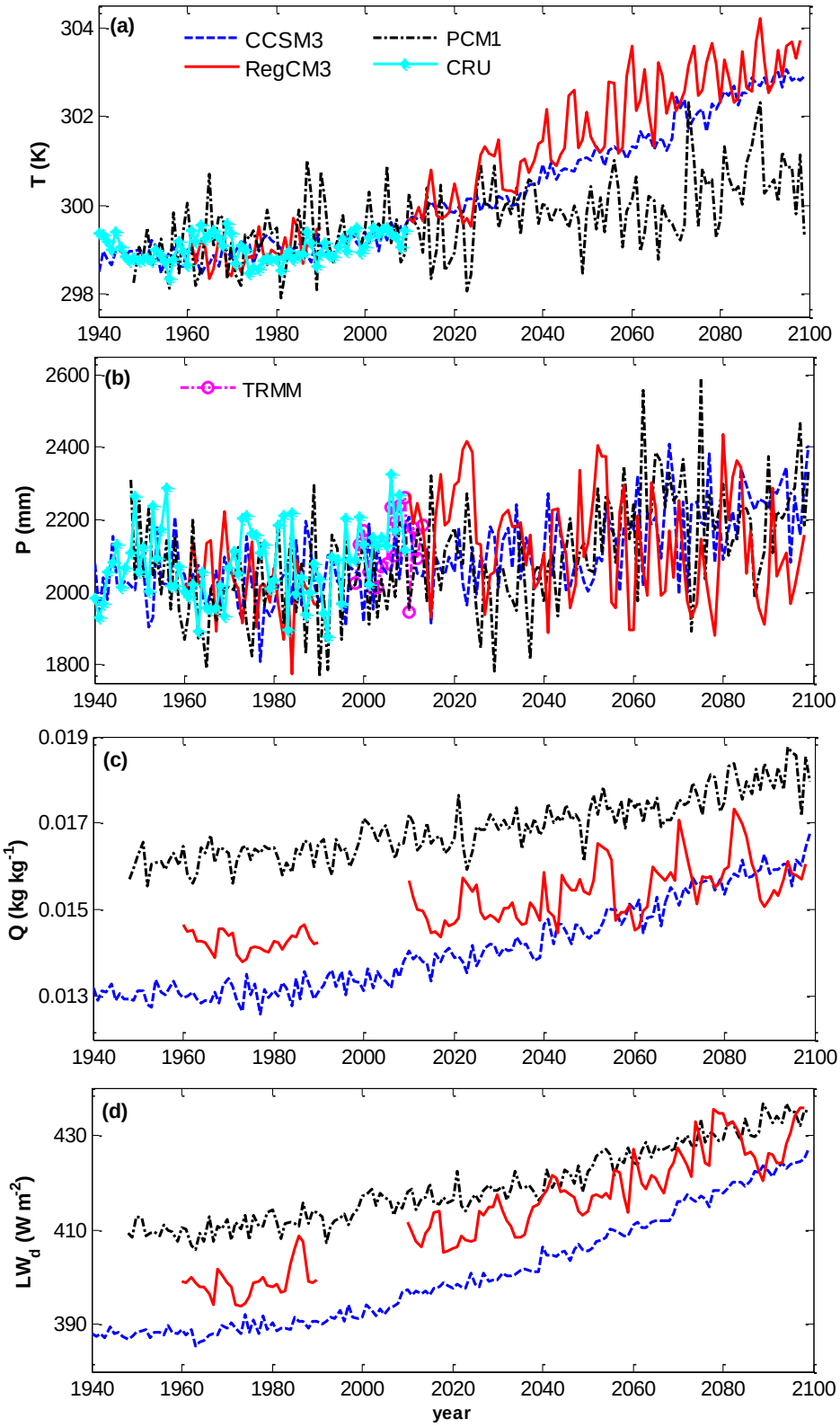

Figure B.4. Annual domain average of bias-corrected (a) temperature T, (b) precipitation P, (c) specific humidity Q, and (d) downwelling longwave radiation LW_d for the models (CCSM3, RegCM3, PCM1).

To evaluate the statistical significance of the results, Table B.2 presents p-value of the linear trend in the modeled variables (T, P, Q, LW_d) for the historical and future periods. The measured p-value smaller than 0.05 or 0.01 is conventionally defined "statistically significant" or "very significant", respectively (Nuzzo, 2014).

Table B.2. The statistical significance (p-value) of the linear trend in the modeled variables (T, P, Q, LW_d) for the historical and future periods.

Models		T	P	Q	LW_d
CCSM3	His	$P < 0.0001$	$P = 0.29$	$P < 0.0001$	$P < 0.0001$
	Fut	$P < 0.0001$	$P < 0.0001$	$P < 0.0001$	$P < 0.0001$
RegCM3	His	$P = 0.02$	$P = 0.04$	$P = 0.75$	$P = 0.04$
	Fut	$P < 0.0001$	$P = 0.02$	$P < 0.0001$	$P < 0.0001$
PCM1	His	$P = 0.02$	$P = 0.72$	$P < 0.0001$	$P < 0.0001$
	Fut	$P < 0.0001$	$P < 0.0001$	$P < 0.0001$	$P < 0.0001$

Figure B.4a indicates that all models have a long-term trend of rising temperature over the domain, which is significant (p-value is smaller than 0.05 for the entire period). A clear warming trend is apparent for the future (2010-2099), which is more significant than historical period in all models (p-value is smaller than 0.0001). The trend of rising temperature over the Amazon Basin has been previously reported (e.g., Malhi et al., 2009). All models show a similar skill to represent the CRU reference temperature. For precipitation (Fig. B.4b) the monthly data from the Tropical Rainfall Measuring Mission (TRMM_3B43) product from 1998 to 2013 is also used as an independent dataset for comparison purposes. The TRMM product (publicly available at http://trmm.gsfc.nasa.

gov/) is known as one of the best estimates of precipitation, resulting from integrating multi-sensor precipitation datasets across different remote sensing platforms and ground-based rain gauges (Huffman et al., 2007). The TRMM data at spatial resolution of 0.25° by 0.25 are averaged onto the horizontal grids used for the disaggregated GCM outputs. Figure 5b shows that the models agree well with the CRU dataset and also the TRMM precipitation during the time that data are available. CCSM3 and PCM1 do not display a significant trend for precipitation in the historical time (p = 0.29 and 0.72, respectively). Also the upward trend in the TRMM and CRU precipitation is not significant (p = 0.24 and 0.07, respectively). While RegCM3 shows a weak downward trend in the historical time (p = 0.04). Although CCSM3 and PCM1 show a significant trend of increase in precipitation for the future ($p < 0.0001$), RegCM3 displays a downward trend of precipitation ($p = 0.02$). For specific humidity (Fig. B.4c) the models exhibit an upward trend, which is significant ($p < 0.0001$). Note that there is a weak downward trend in the RegCM3 specific humidity for the historical time, which is not significant ($p = 0.75$). The upward trend in specific humidity is consistent with the observed warming trend in atmospheric temperature that leads to increased moisture content. Furthermore, it can be seen that the models exhibit a significant upward trend in downwelling longwave radiation time series (Fig. B.4d), which is consistent with the observed warming trend in temperature. The upward trend of downwelling longwave radiation in CCSM3 and PCM1 is more significant than in RegCM3 during the historical time (see Table B.2). On average RegCM3 shows a higher inter-annual variability compared to the other models in particular in projection period.

Table B.3 compares temporally averaged values of the annual domain mean and standard deviation of temperature, precipitation, specific humidity, and longwave radiation from three models for the historical and future periods.

Table B.3. Comparison of the mean annual domain average of the statistics (mean μ and standard deviation σ) of the three modeled variables for the two historical and future periods.

Models		T(K)		P(mm)		Q(kg kg^{-1})		LW_d (W m^{-2})	
		μ	σ	μ	σ	μ	σ	μ	σ
CCSM3	His	299.01	0.28	2037.5	88.94	0.0132	2.60E-4	389.72	2.27
	Fut	301.23	1.05	2151.8	109.22	0.0149	8.21E-4	409.19	9.17
RegCM3	His	298.97	0.32	2019.6	91.90	0.0143	2.40E-4	398.96	3.48
	Fut	301.80	1.26	2136.5	143.13	0.0155	6.57E-4	419.29	8.30
PCM1	His	299.25	0.69	2029.7	125.81	0.0163	3.42E-4	411.63	2.98
	Fut	300.01	0.81	2146.5	148.66	0.0173	5.99E-4	424.39	6.39

In particular, on average, the mean temperatures increased by 2.22, 2.83, and 0.76 °K, while comparing the historical years (1940-2009, 1960-1990, 1948-2009) with the future period (2010-2099) for CCSM3, RegCM3, and PCM1, respectively. Precipitation also increased 114.3, 116.9, and 116.8 mm in the bias corrected datasets, respectively. We need to note that the average RegCM3 precipitation has increased from historical to future period- conditioned to the fact that the data are missing from 1991 to 2009, which may affect the interpretation of the trends.

The potential impact of climate change varies over the region. To highlight the potential regional impacts of climate change, Figure B.5 shows the difference of temporal averages of the bias-corrected modeled variables (T, P, Q, LW_d) in the future from the corresponding ones in the historical period.

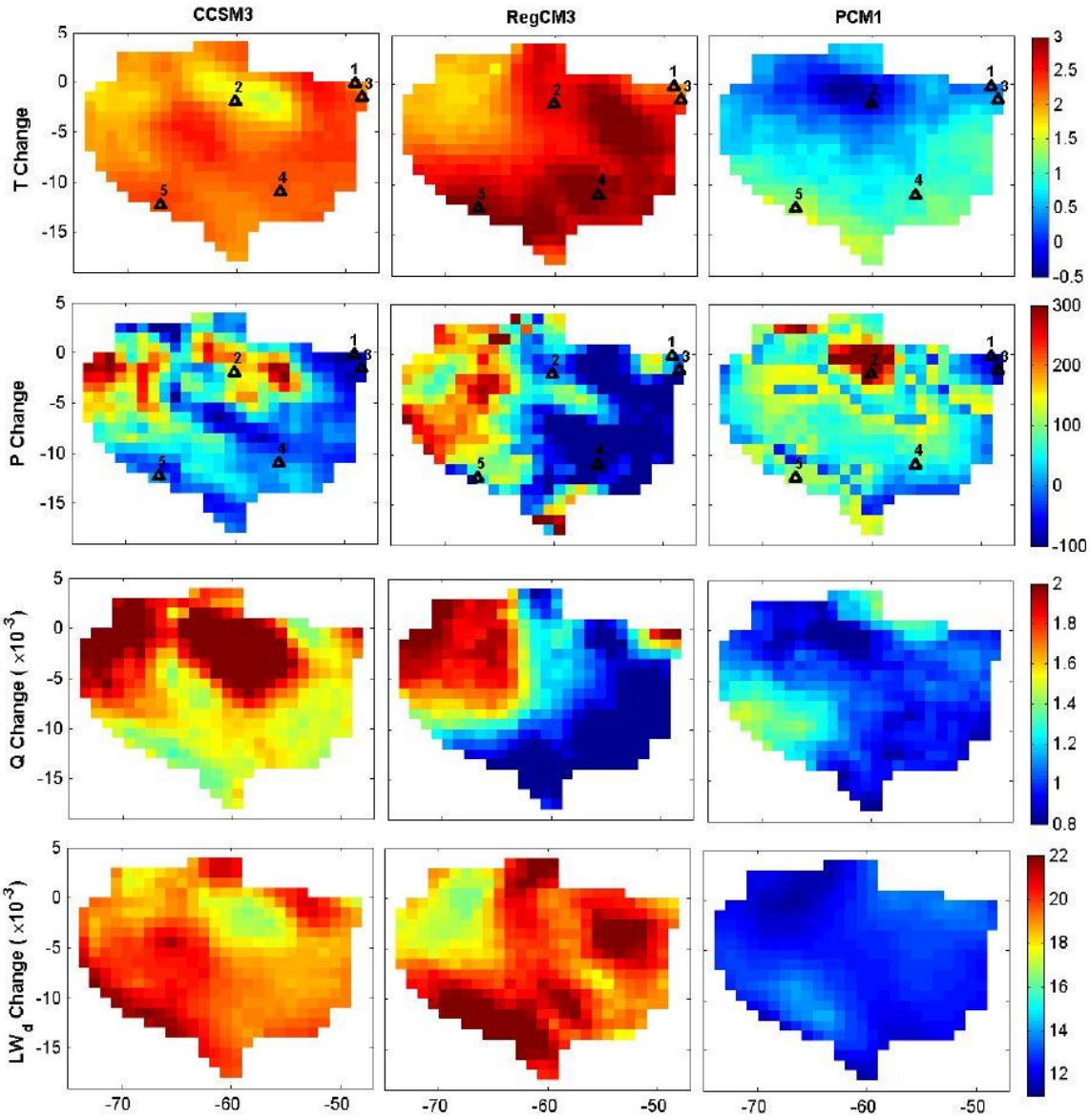

Figure B.5. From top-to-bottom: changes in temperature (T change), precipitation (P change), specific humidity (Q change), and downwelling longwave radiation (LW_d change). From left-to-right columns: changes in CCSM3, RegCM3, and PCM1. The outlet of the Amazon Basin, Manaus, Belem, Mato Grosso, and Bolivia are illustrated by numbers 1, 2, 3, 4, and 5, respectively.

This figure indicates that the potential impact of climate change on the differences is not evenly distributed over the study domain. The CCSM3, RegCM3, and PCM1 results show warmer areas over the eastern and the southern part of the Amazon Basin, while the

magnitude of the changes in the models are different. The strongest, intermediate, and moderate warming trends are in RegCM3, CCSM3, and PCM1, respectively. The warming effect is reported to be related to the deforestation trend over those regions (Davidson et al., 2012). The warmer areas are smaller over the northwest of the study domain. The PCM1 results indicate that temperature may decrease over the northern regions of the basin, where CCSM3 also shows a smaller increase of the surface temperature over the same northern regions.

The CCSM3 and RegCM3 results show that precipitation may increase over the western parts of the study domain while it may decrease over the eastern and central parts, in particular over the Bolivia and Mato Grosso (see Figure B.5), where the vast areas of the Amazon rainforest are deforested (Bagley et al., 2014). A decrease in precipitation over the eastern part of the Amazon Basin is also reported by Paiva and Clarke (1995); Reboita et al. (2014); Bombardi and Carvalho (2009). The PCM1 and CCSM3 results show large precipitation decreases around the Belem and large precipitation increases around the Manaus region (see Figure B.5), which is consistent with the results by Chu et al. (1994). This increase in precipitation occurs over the areas with the smaller increase in temperature.

The models produce different patterns of changes in specific humidity. The pattern of changes in specific humidity is similar to those of precipitation in CCSM3 and RegCM3. This similarity can indicate that higher water content of the air can potentially increase the rainfall amount with the condition that the atmosphere has sufficient convective energy. For LW_d the variability of changes is smaller in PCM1 compared to the other models. The CCSM3 and RegCM3 results exhibit a relatively large positive change of LW_d over the southwest (e.g. Bolivia), where the changes in temperature are large over that regions. Also the smaller changes of LW_d over the northwest of the study domain agree with the smaller changes in temperature. While the changes of LW_d is small over the southeast of the domain, where the temperature changes are large over the same

southeast regions. This might be due to the fact that LW_d depends not only on temperature but also on air emissivity and clouds.

B.4. Summary and Conclusions

Efficient and effective long-term environmental management plans over the Amazon Basin require accurate climate datasets. This study provides bias-corrected climate datasets using the probability matching technique (EDCDF), which can be used as forcing for ecosystem and land surface modeling over Amazonia. It is important to note that the EDCDF method cannot explicitly correct biases for particular years (e.g., El Niño or La Niña years). In other words, if the model is unable to properly simulate a specific phenomenon, the EDCDF method is not capable to correct the biases associated with that specific phenomenon. A limitation of most bias correction methods, including distribution mapping, is the stationarity assumption. The advantage of using the EDCDF method is that it incorporates information from the projection period of the models to at least partially accommodate some features of potential future changes (Li et al., 2010). The use of a long record of observation (CRU) from the historical period does add robustness to the method.

In general, CCSM3 tends to have a dry warm bias in most parts of the domain, while RegCM3 mostly shows a tendency to have a dry cool bias. These tendencies imply the presence of systematic errors in the models. Various schemes and parameterizations of the models may influence their performances over different months and locations. On average, RegCM3 exhibits smaller bias corrections (estimated differences) than those of CCSM3, for temperature and precipitation. This might be due to a better parameterization, for this domain, of clouds, and other related processes in RegCM3 compared to CCSM3 (Milton and Wilson, 1996; Gregory et al., 1998; Smith, 1990). Furthermore, a better simulation of mesoscale patterns and topographic effects on

precipitation in RegCM3, compared with the GCMs, is reported by many studies (e.g., Reboita et al., 2014; Frei et al., 2003, 2006; Intergovernmental Panel on Climate Change, 2007; Buonomo et al., 2007, among others).

Bias-corrected annual CCSM3, RegCM3, and PCM1 temperature showed a clear warming trend under the A2 simulation of the future. Warming over the Amazon Basin may have positive feedback. In other words, an increase in temperature can increase the risk of fire and drought over the Amazon Basin, possibly amplifying temperature increases. All models also exhibit an upward trend in specific humidity and downwelling longwave radiation, which agrees with the warming trend of temperature. Although no significant trend of precipitation is observed in the models' simulations of the historical period, the models do show different trends under the A2 simulation of the future. The RegCM3 results show a downward trend in precipitation while the CCSM3 and PCM1 results show an upward trend of precipitation. The upward trend of precipitation in CCSM3 and PCM1 is more significant than the downward trend of precipitation in RegCM3. The CCSM3 and PCM1 outputs mostly show lower inter-annual variability than the RegCM3 outputs, especially during the simulations of the future.

Results of the impacts of climate change at a regional scale revealed that the eastern and southern part of the region, where deforestation rate and risk of fire are high, experience a warmer and drier atmosphere under the A2 simulation of the future. Human activities such as deforestation and natural events such as El Niño may decrease precipitation over the Amazon (Malhi et al., 2008) and make it more susceptible to droughts and fires. The results, especially those of CCSM3 and RegCM3, indicate that north and northwestern parts of the region may experience an increasing trend in precipitation, which is strongly correlated with the observed increases in the air humidity.

APPENDIX C

BIAS CORRECTION OF CLIMATE VARIABLES IN THE CALIBRATION PERIOD USING THE ANN MODEL

The developed ANN (see section 4.2) is used to correct the biases of the climate variables (temperature and precipitation). The network is trained by the training set in the calibration period. Then the trained network is used in the validation period to check the generalization ability.

C.1. Temperature

To train and test the network, the 6-hourly historical CCSM data (ANN input) and MFD temperature (ANN target) from 1970 to 2008 are divided into two periods:

I) 1970-1988 as a training dataset to adjust the ANN synoptic weights (calibration).

II) 1989-2008 as a testing dataset to study the performance of the trained network (validation).

Figures C.1 to C.12 show the statistics MSE, Bias, ρ, and KS resulting from the LR and ANN models during the calibration period (1970-1988).

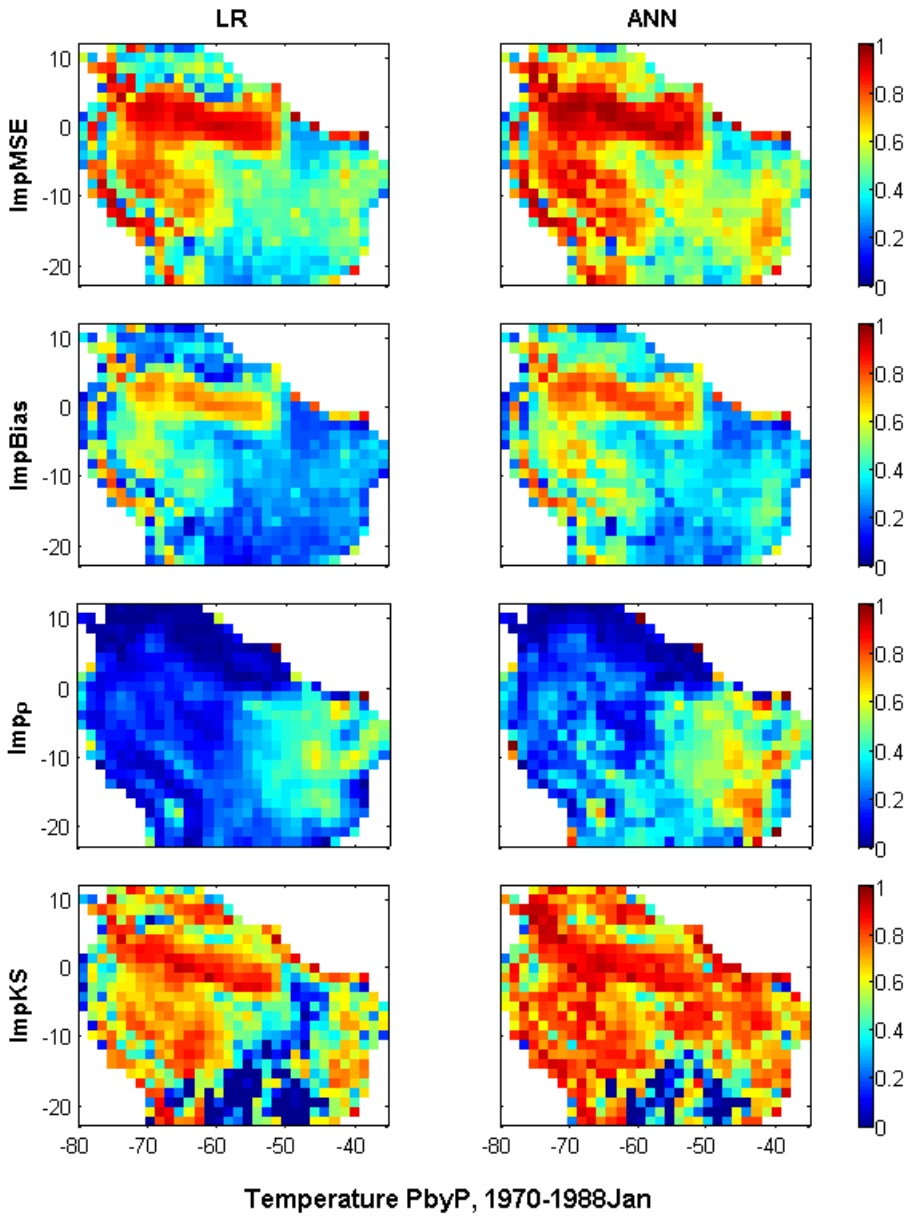

Figure C.1. From top-to-bottom: Improvements of the MSE (ImpMSE), Bias (ImpBias), ρ (Impρ), and KS (ImpKS) by the linear (LR) and nonlinear (ANN) methods for the calibration (Jan 1970-1998).

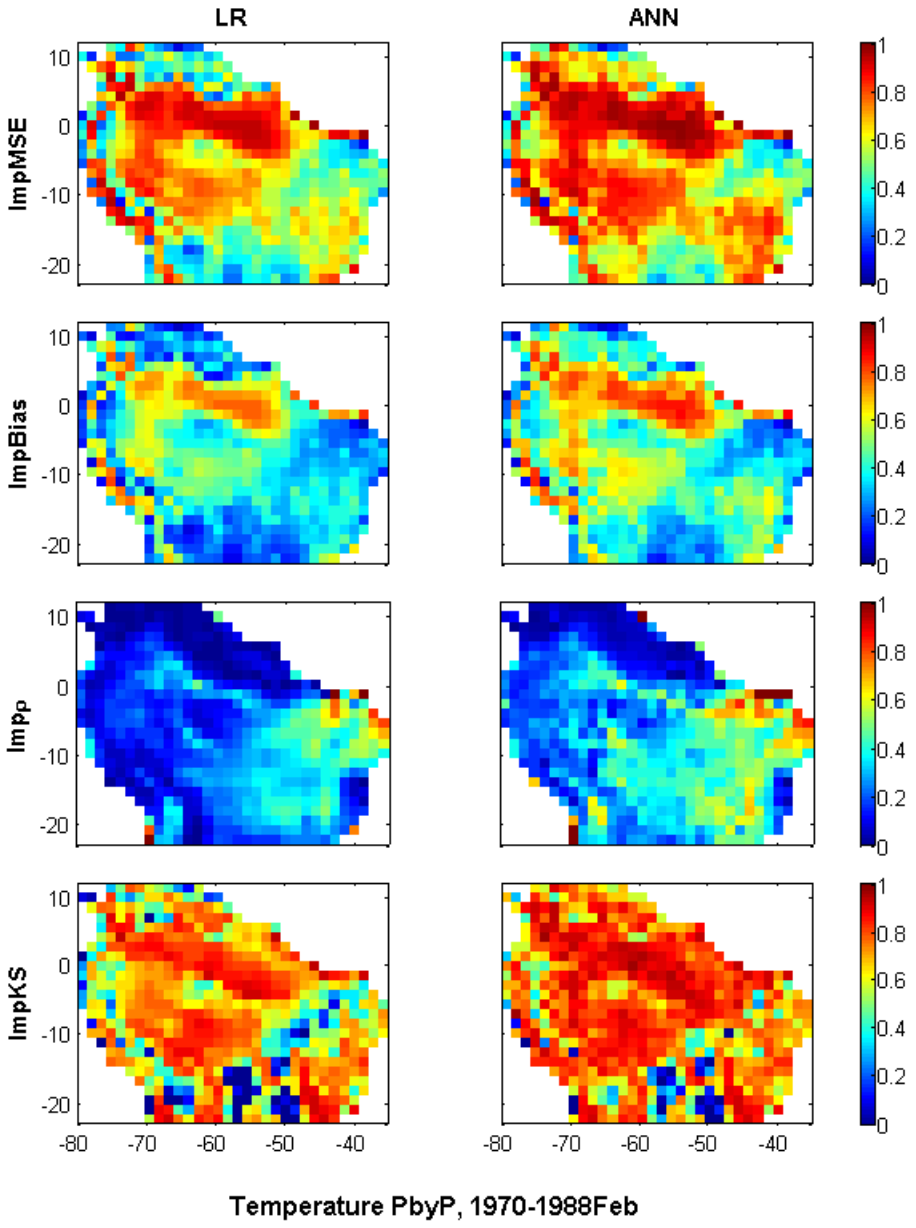

Figure C.2. Same as Fig. C.1 but for February.

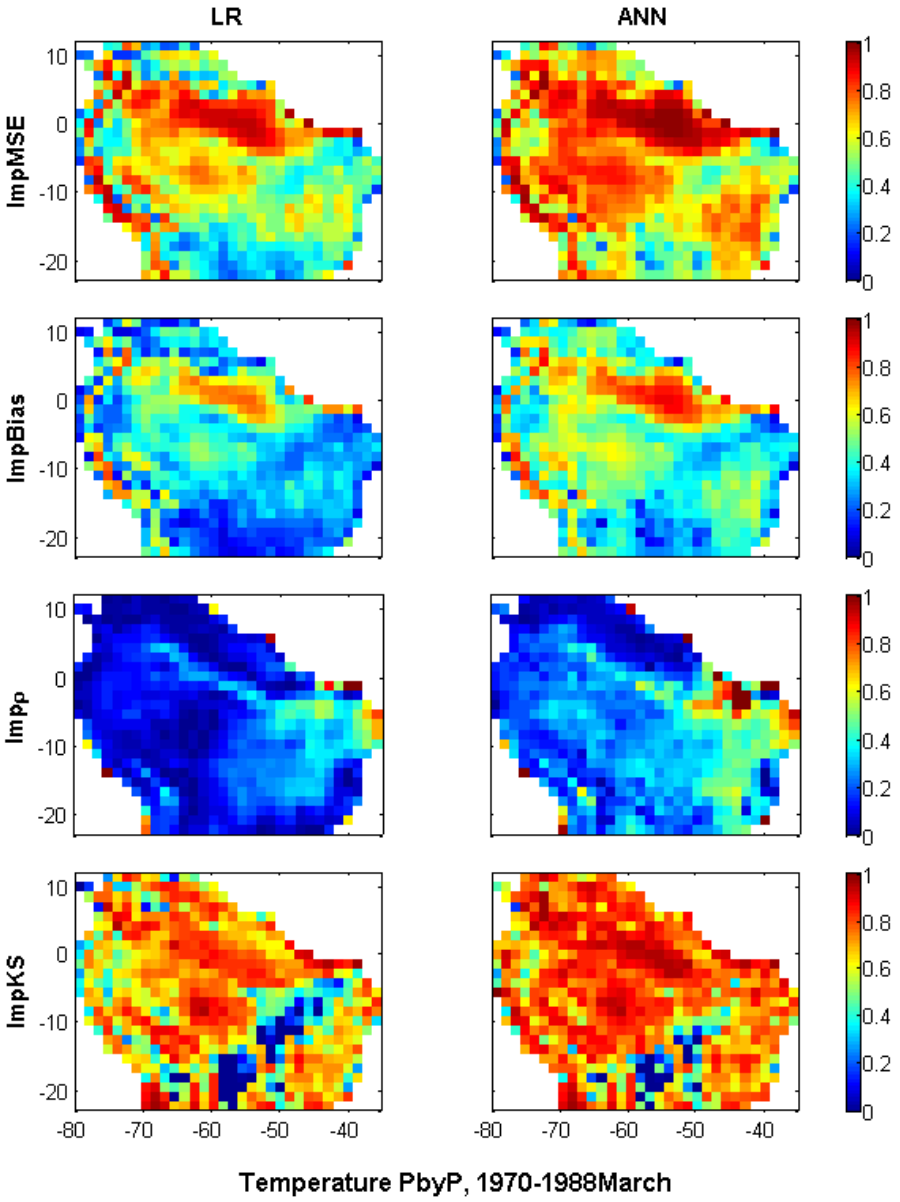

Figure C.3. Same as Fig. C.1 but for March.

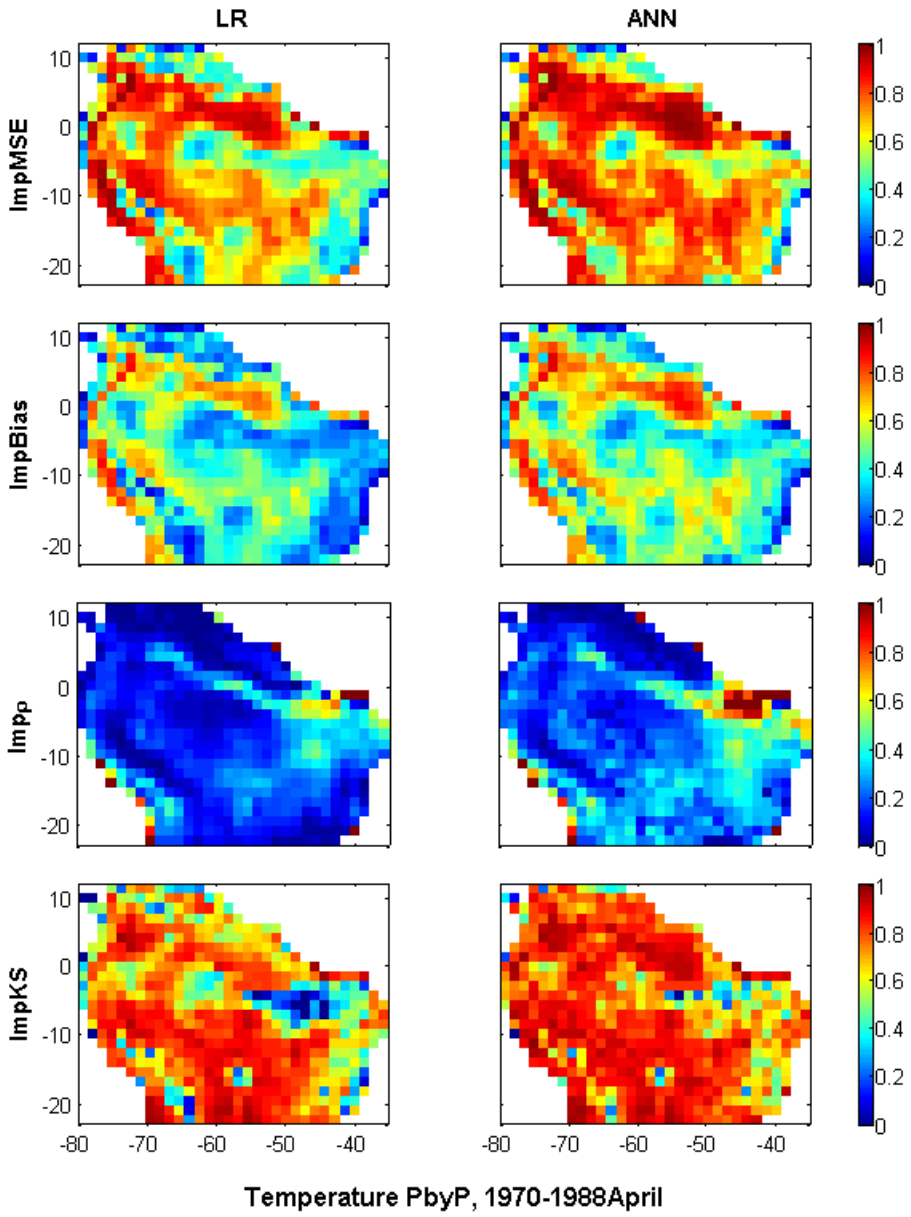

Figure C.4. Same as Fig. C.1 but for April.

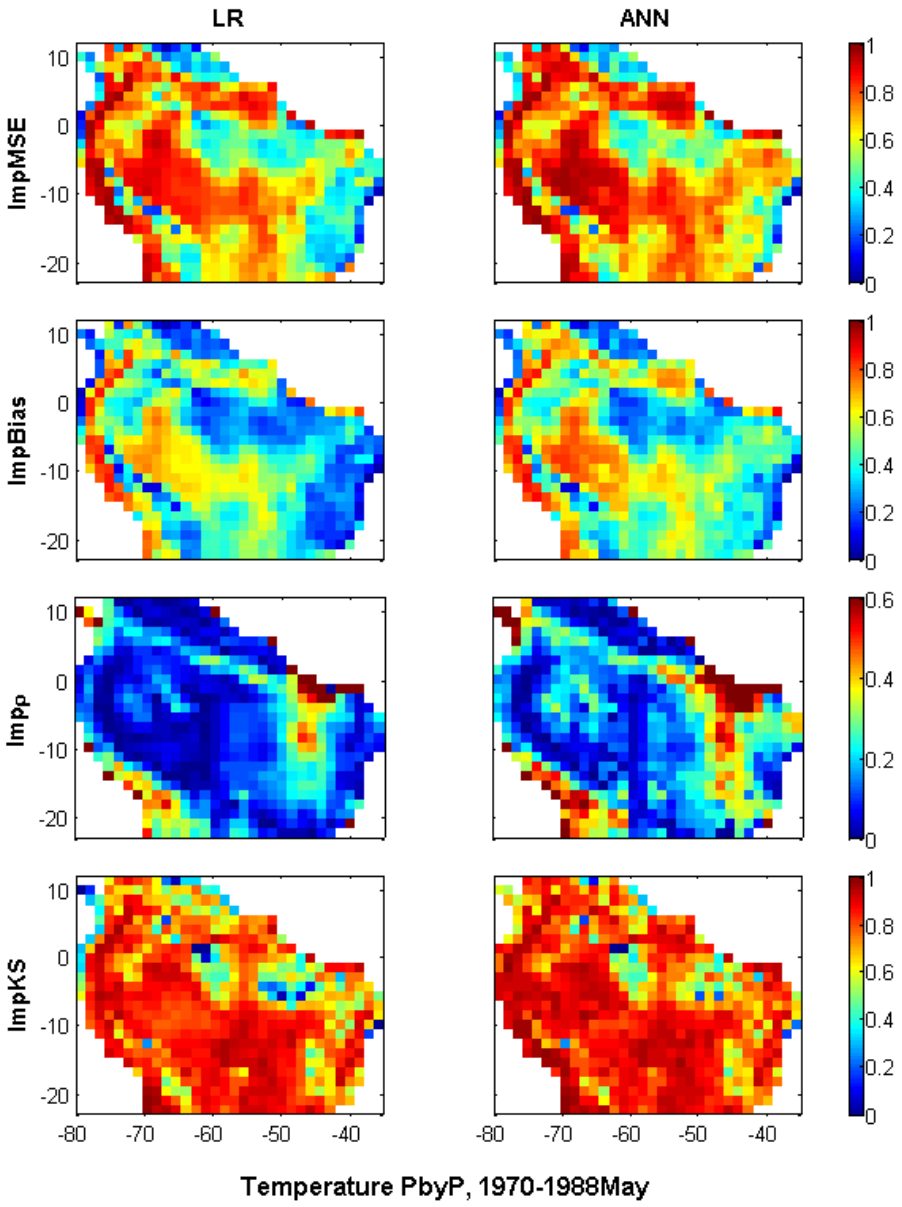

Figure C.5. Same as Fig. C.1 but for May.

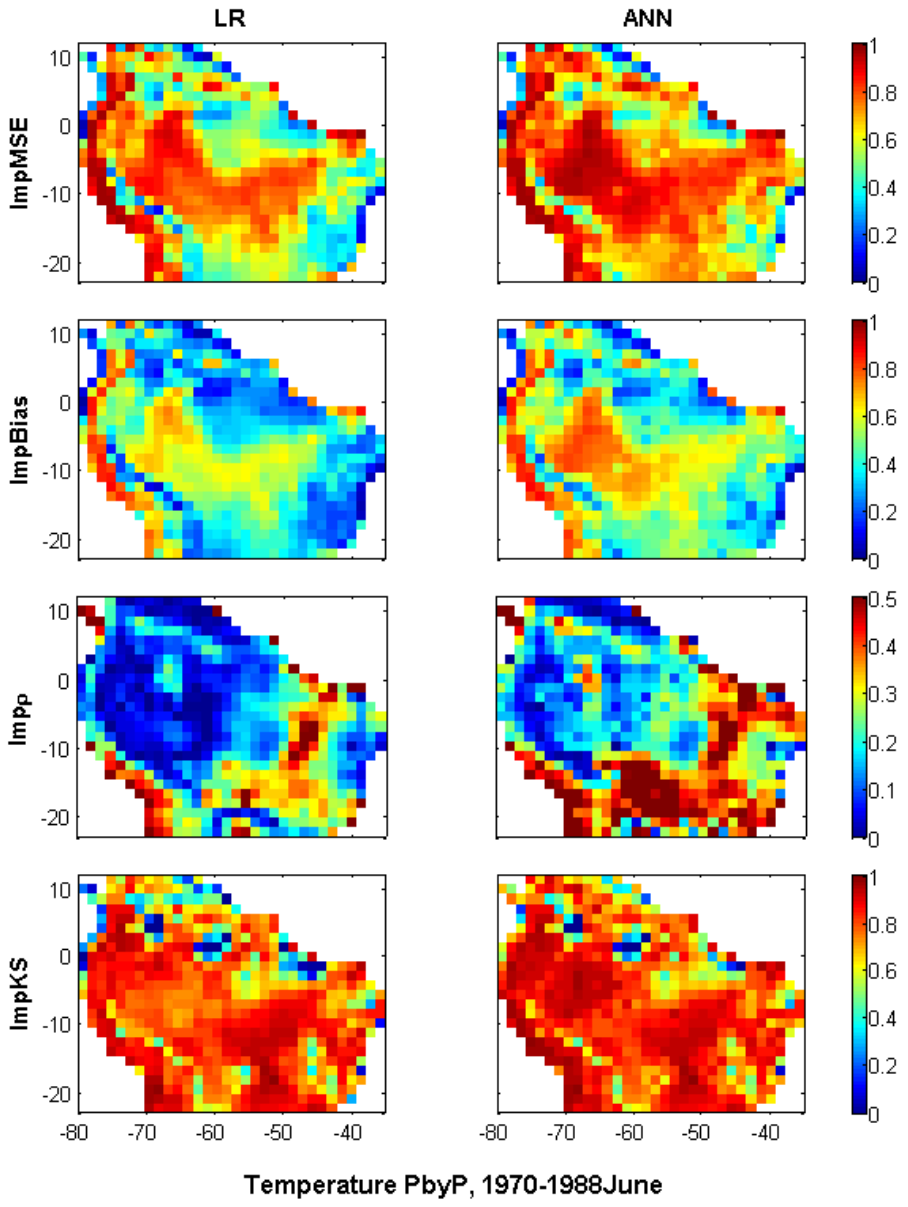

Figure C.6. Same as Fig. C.1 but for June.

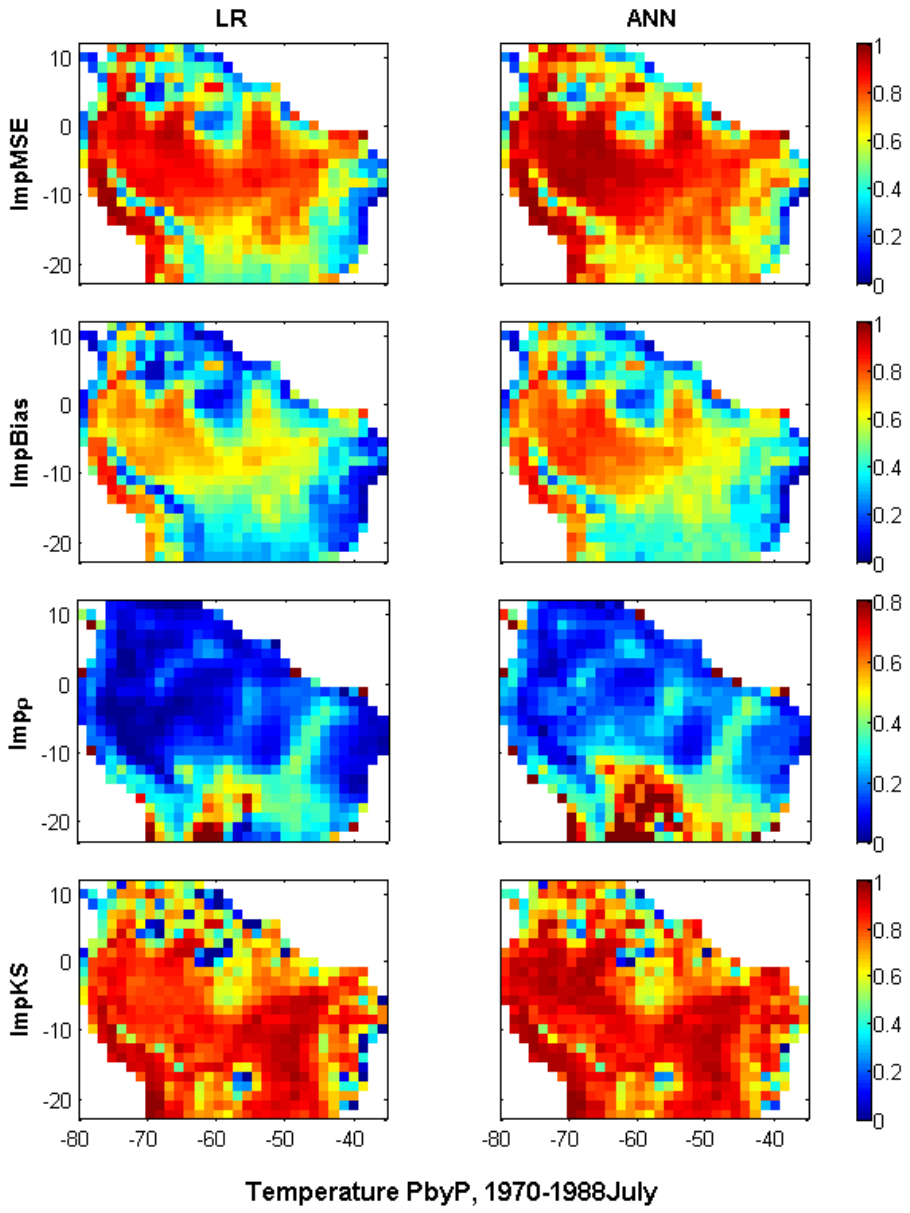

Figure C.7. Same as Fig. C.1 but for July.

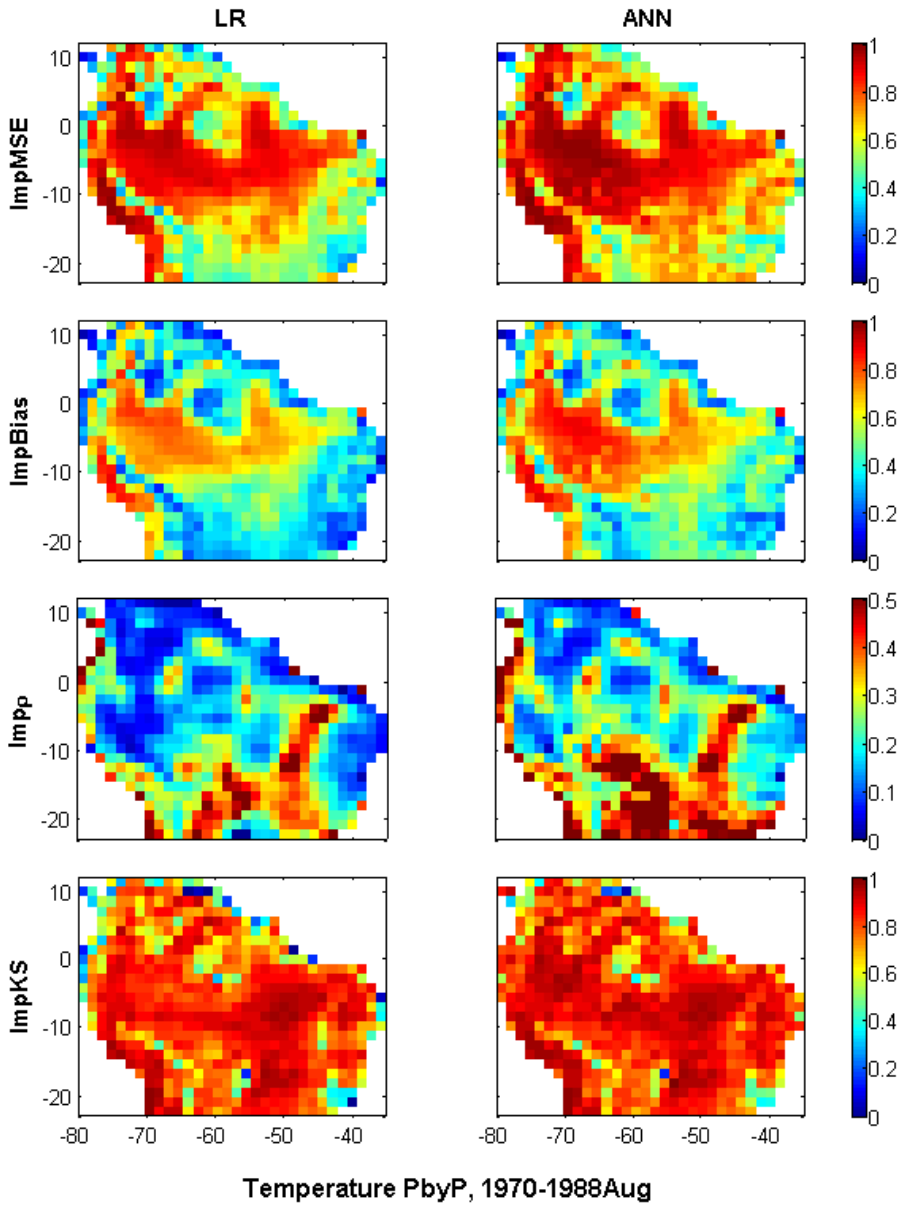

Figure C.8. Same as Fig. C.1 but for August.

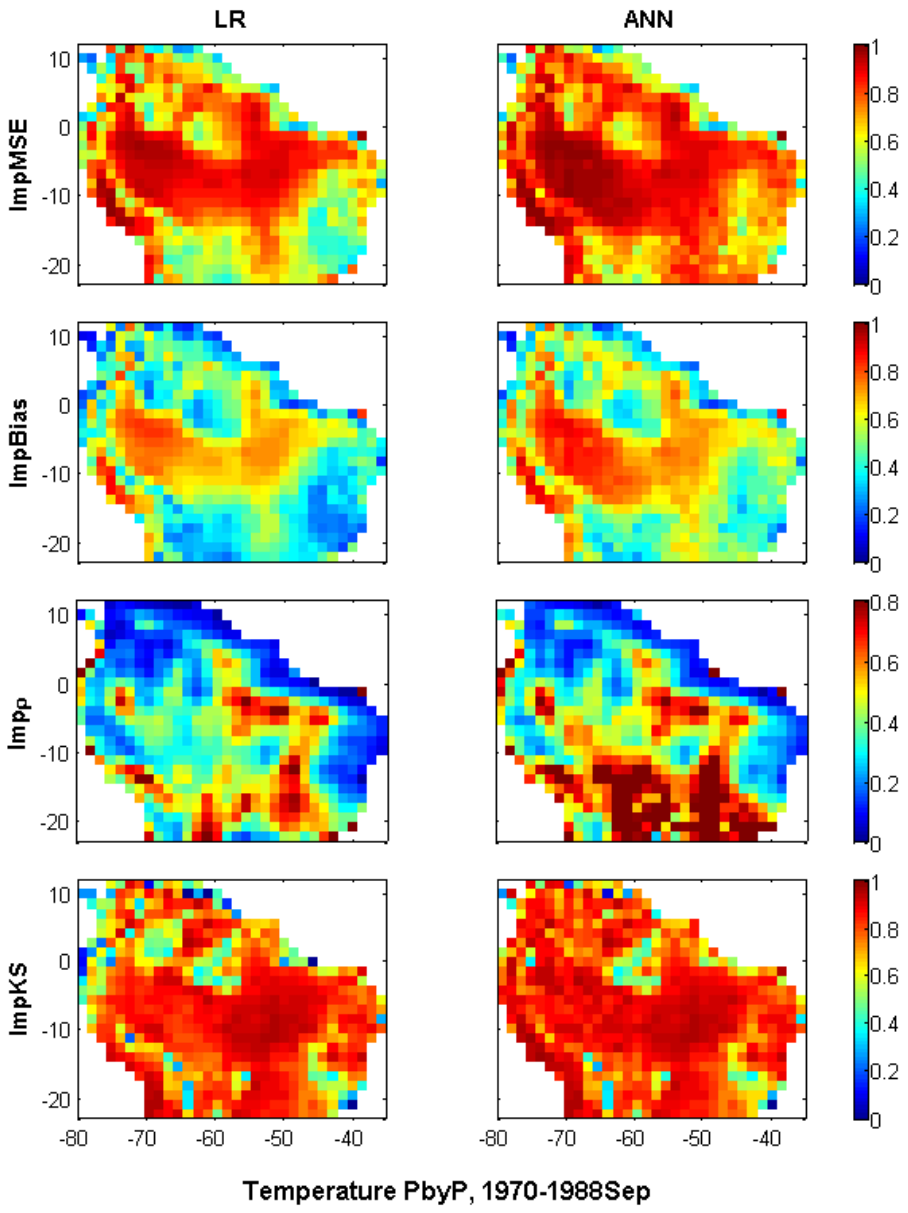

Figure C.9. Same as Fig. C.1 but for September.

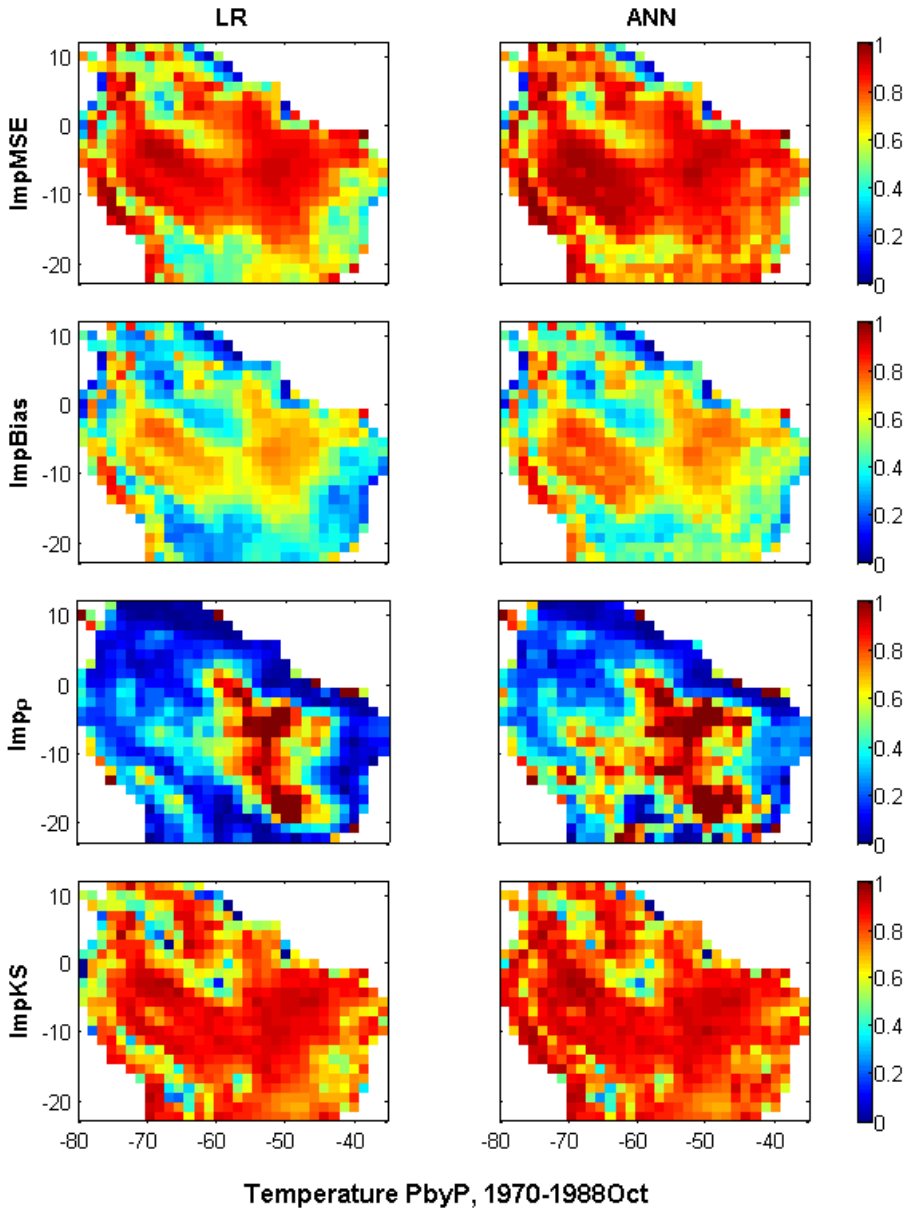

Figure C.10. Same as Fig. C.1 but for October.

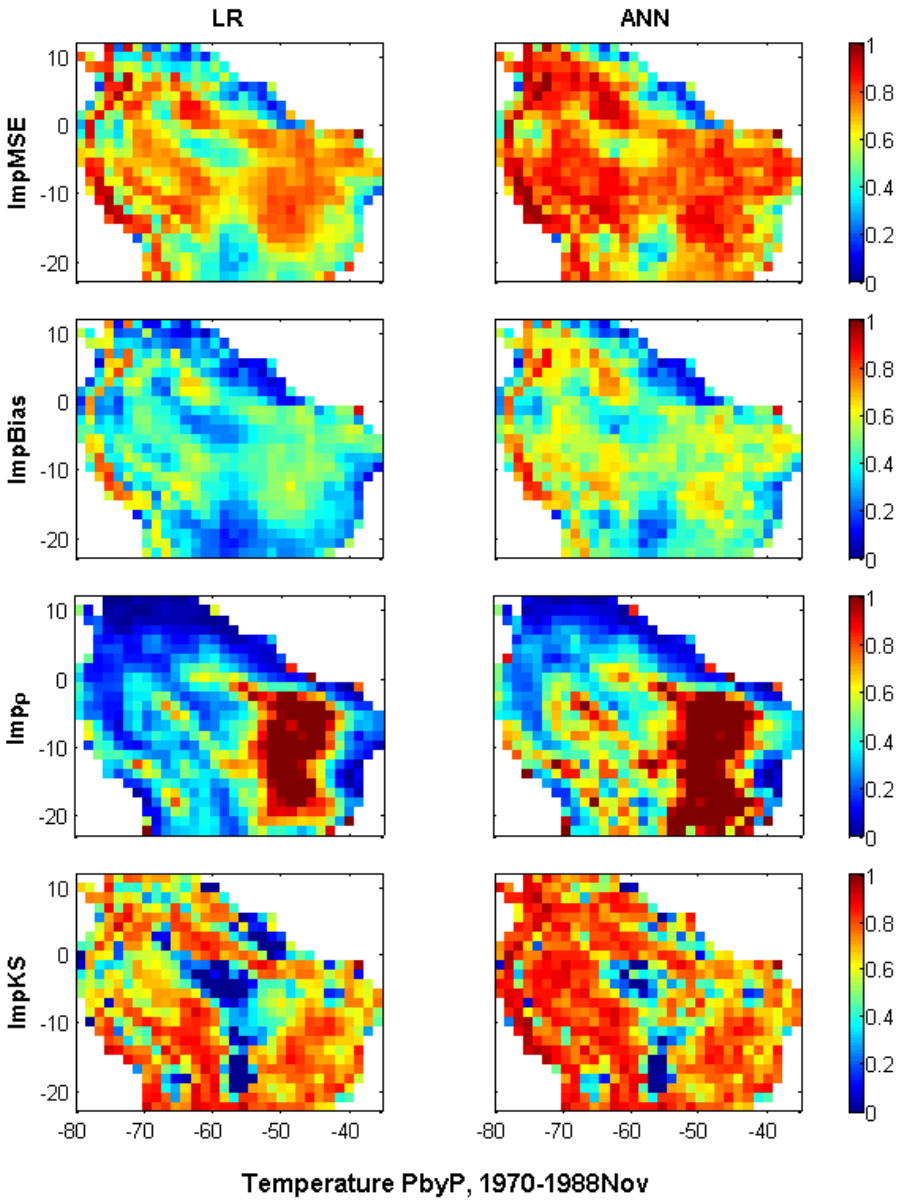

Figure C.11. Same as Fig. C.1 but for November.

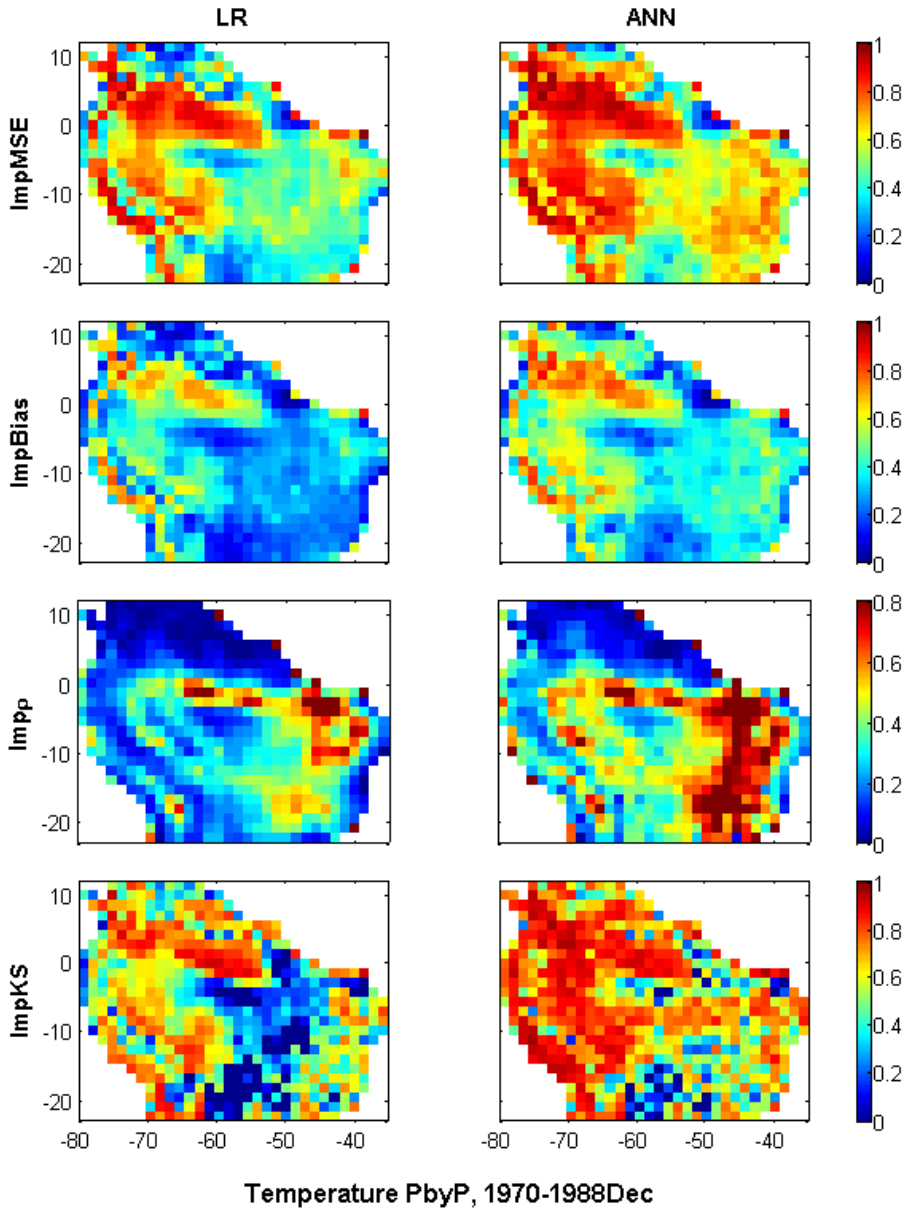

Figure C.12. Same as Fig. C.1 but for December.

C.2. Precipitation

To correct the biases of precipitation, we use seasonal historical CCSM precipitation (input to the ANN) and CRU precipitation (ANN target) from 1901 to 2013. The training set (the CCSM and CRU precipitation) is divided into two independent periods:

I) 1901-1956 as a calibration period, used to train the network.

II) 1957-2013 as a validation period, used to study the performance of the trained network.

Figures C.13 to C.16 show the statistics MSE, Bias, ρ, and KS resulting from the LR and ANN models during the calibration period (1970-1988).

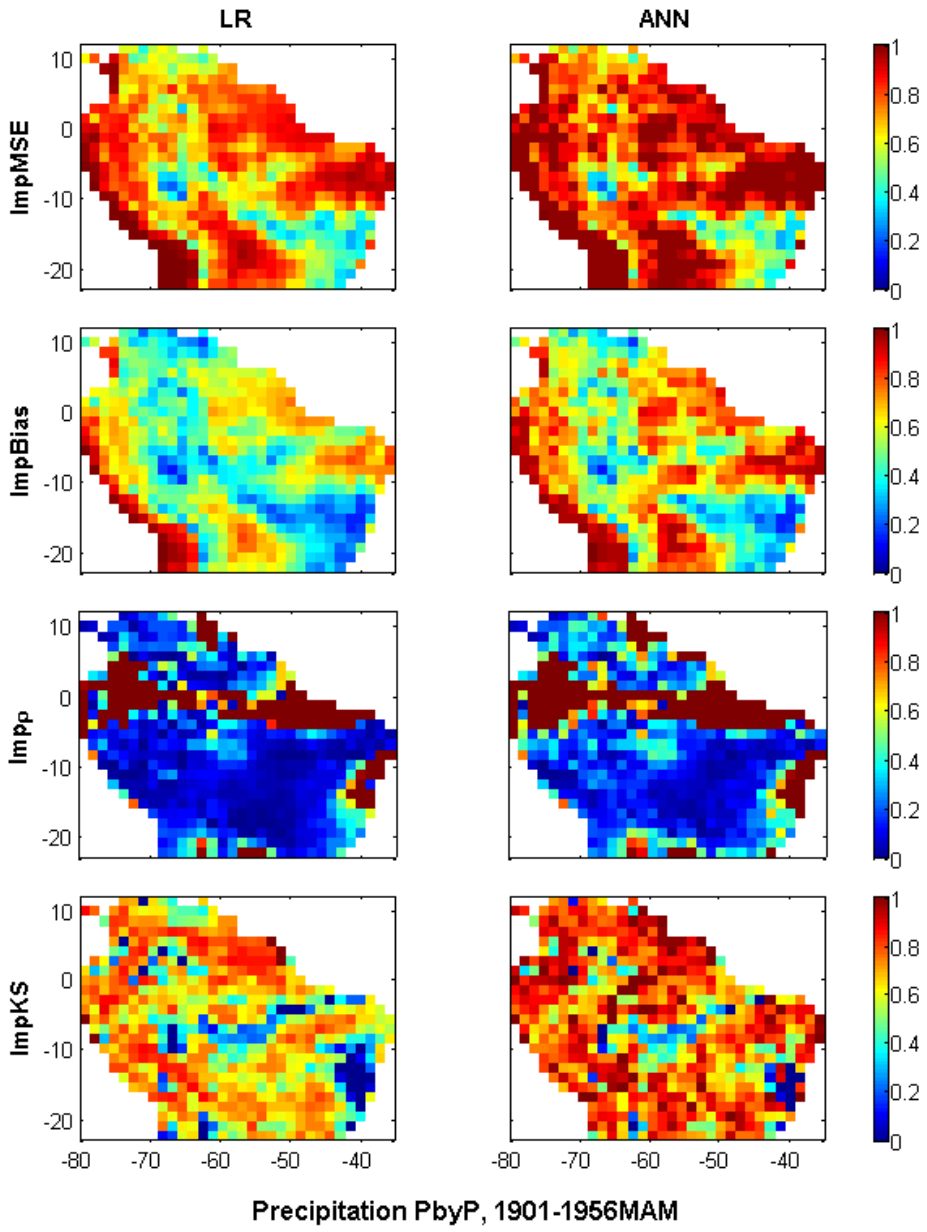

Figure C.13. From top-to-bottom: Improvements of the MSE (ImpMSE), Bias (ImpBias), ρ (Impρ), and KS (ImpKS) by the linear (LR) and nonlinear (ANN) methods for the validation (MAM 1957-2013).

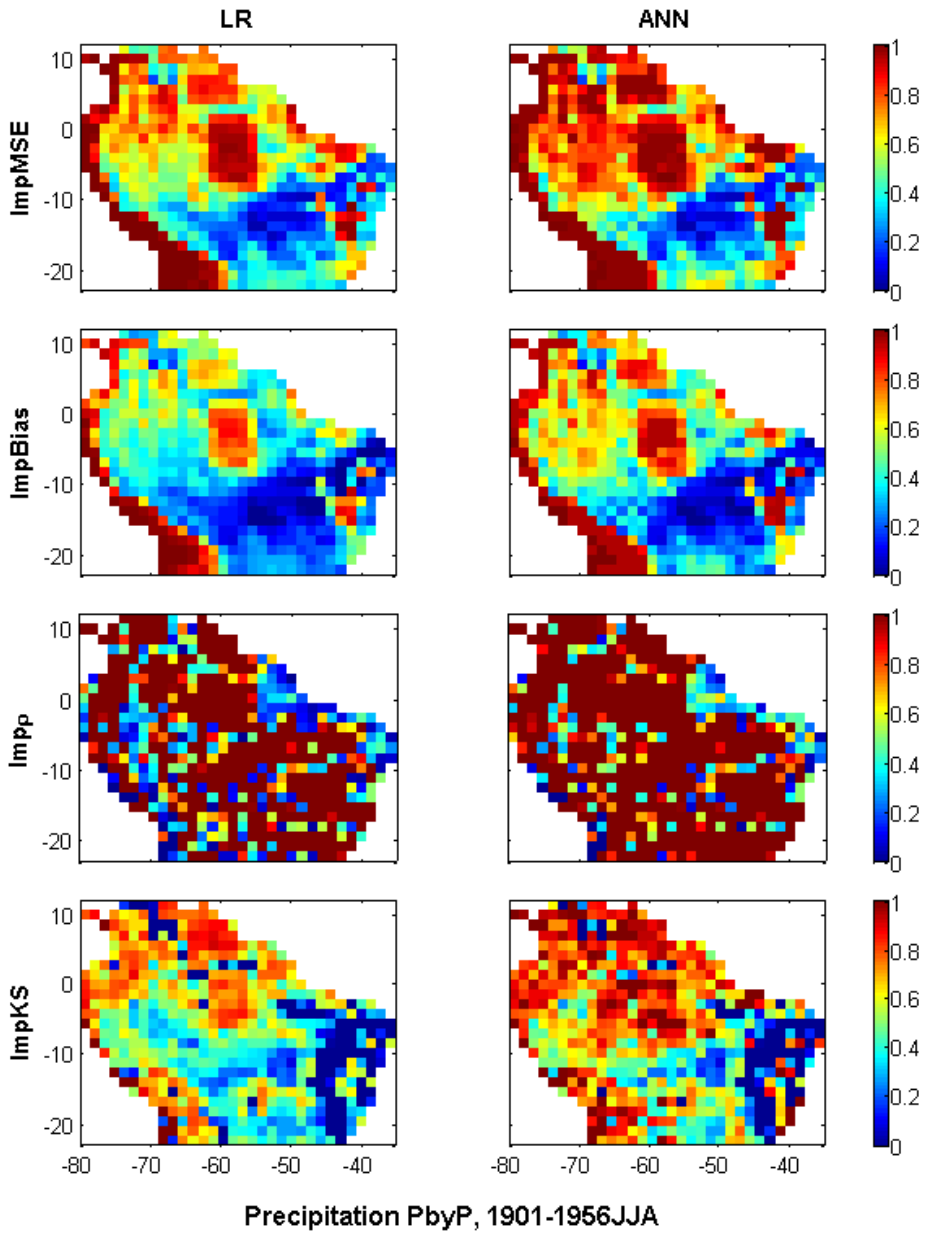

Figure C.14. Same as Fig. C.13 but for JJA.

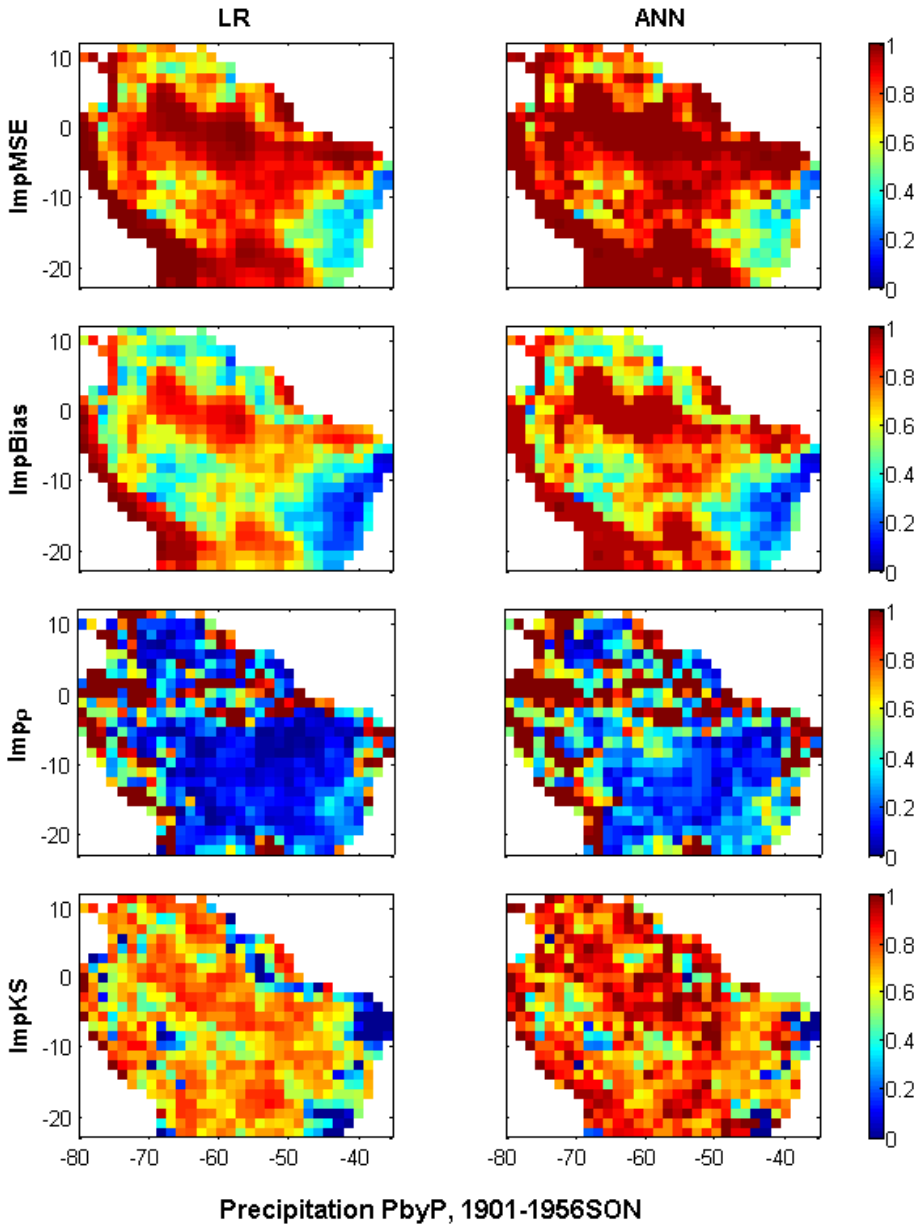

Figure C.15. Same as Fig. C.13 but for SON.

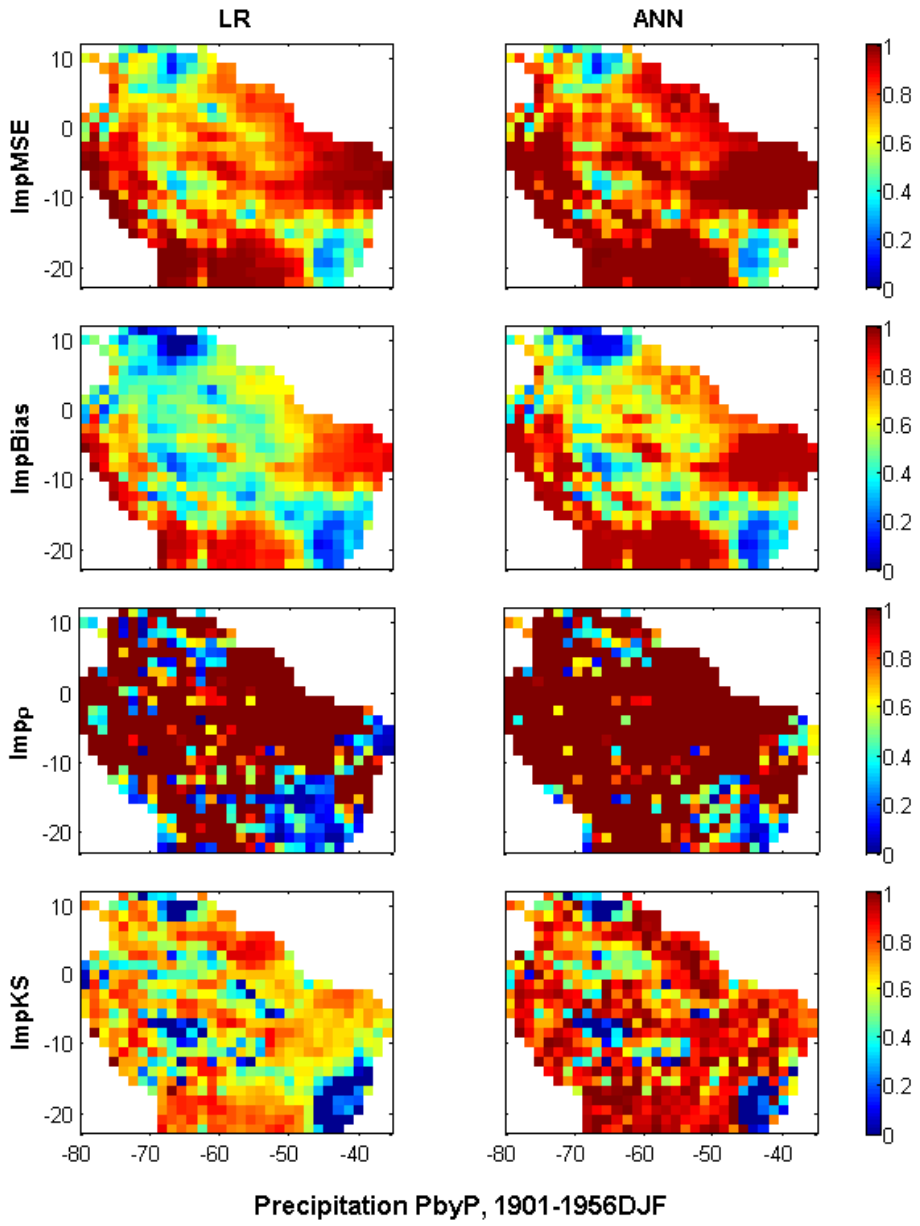

Figure C.16. Same as Fig. C.13 but for DJF.

APPENDIX D

LOCATIONS OF THE TRAINING PIXELS IN THE DELINEATED DOMAINS

The regression model is used to regionalize the study domain and identify the minimum number of training pixels necessary to achieve a good level of bias correction performance over the entire domain (see Chapter 5).

D.1. Temperature

Results in Chapter 5 confirm that a small number of training pixels suffices to regionalize the procedure with prescribed accuracy. Locations (latitude and longitude) of the training pixels in the delineated domains (D1, D2, D3, D4, D5) for 70%, 80%, and 90% performances in March and for 80% performance in other months are listed in the following tables.

Table D.1. Locations of the training pixels in the delineated domains for 70% performance corresponding to Fig. 5.1 in March.

Domain	Lat	Lon
D1	9.10S	47.81W
	18.91S	56.25W
D2	2.10S	57.66W
	6.30S	68.91W
D3	2.10N	53.44W
	4.91N	57.66W
D4	7.70N	64.69W
	4.91N	63.28W
D5	6.30N	74.53W
	10.50S	77.34W
	11.90S	73.125W
	7.70S	77.34W
	0.70S	75.94W
	20.31S	64.69W

Table D.2. Same as Table D.1 but for 80% performance corresponding to Fig. 5.2 in March.

Domain	Lat	Lon
D1	9.10S	47.81W
	16.11S	52.03W
	20.31S	45W
D2	0.70S	59.06
	10.51S	64.69W
	3.50S	68.91W
D3	4.90N	57.66W
	2.10N	54.84W
	3.50N	54.84W
D4	4.90	64.69W
	6.30N	64.69W
	9.10N	64.69W
D5	7.70S	75.94W
	4.90N	73.12W
	14.71S	73.12W
	10.51S	77.34W
	20.31S	68.91W
	0.70N	74.53W
	16.11S	66.09W
	13.31S	70.31W
	18.91S	66.09W

Table D.3. Same as Table D.1 but for 90% performance corresponding to Fig. 5.3 in March.

Domain	Lat	Lon
D1	9.10S	47.81W
	23.11S	50.625W
	17.51S	40.78W
	14.71S	52.03W
	7.70S	42.19W
	17.51S	57.66W
	23.11S	46.41W
D2	7.70S	70.31W
	3.50S	52.03W
	7.70S	57.66W
	3.50S	47.81W
	0.70N	56.25W
	0.70N	60.47W
	0.70S	56.25W
	10.51S	56.25W
	2.10S	52.03W
D3	4.90N	57.66W
	2.10N	57.66
	3.50N	56.25W
	3.50N	53.44W
D4	7.70N	64.69W
	9.10N	64.69W
	6.30N	68.91W
	6.30N	61.875W
	3.50N	64.69W
	3.50N	63.28W
D5	13.31S	74.53W
	4.90N	73.125W
	16.11S	71.72W
	7.70S	75.94W
	14.71S	66.09W
	6.30S	78.75W
	20.31S	70.31W
	0.70N	75.94W
	2.10S	75.94W
	20.31S	64.69W
	21.71S	66.09W
	18.91S	68.91W

Table D.4. Same as Table D.2 but for January corresponding to Fig. 5.5.

Domain	Lat	Lon
D1	9.10S	47.81W
	14.71S	50.625W
D2	4.90S	61.875W
	3.50S	52.03W
D3	4.90N	54.84W
	3.50N	54.84W
	2.10N	54.84W
D4	3.50N	68.91W
	4.90N	64.69W
	9.105N	66.09W
	10.51N	70.31W
D5	6.30N	77.34W
	0.70N	74.53W
	17.51S	70.31W
	3.50N	73.125W
	16.11S	68.91W
	6.30S	77.34W
	10.51S	74.53W
	3.50S	75.94W
	14.71S	74.53W
	14.71S	70.31W

Table D.5. Same as Table D.2 but for February corresponding to Fig. 5.6.

Domain	Lat	Lon
D1	9.10S	47.81W
	16.11S	56.25W
D2	4.90S	46.41W
	4.90S	59.0625W
D3	0.70N	50.625W
	3.50N	57.66W
	3.50N	56.25W
	4.90N	59.0625W
	7.70N	60.47W
	0.70S	54.84W
D4	4.90N	64.69W
	6.30N	66.09W
	9.105N	64.69W
	7.70N	63.28W
D5	9.105S	75.94W
	14.71S	68.91W
	3.50N	75.94W
	0.70N	75.94W
	7.70N	75.94W
	11.91S	71.72W
	3.50N	74.53W
	21.71S	64.69W
	23.11S	67.50W
	6.30S	78.75S

Table D.6. Same as Table D.2 but for April corresponding to Fig. 5.7.

Domain	Lat	Lon
D1	9.10S	47.81W
	14.705S	50.63W
D2	3.50S	54.85W
	11.90S	64.69W
D3	3.505N	57.66W
	2.10N	53.44W
	6.31N	60.47W
D4	3.505N	63.28W
	6.31N	67.50W
	6.31N	63.28W
	7.71N	67.50W
D5	4.90S	77.34W
	4.91N	74.53W
	13.30S	71.72W
	6.31N	74.53W
	0.70N	78.75W
	11.90S	74.53W
	20.31S	64.69W
	4.91N	73.125W
	16.106S	66.09W
	7.70S	78.75W
	11.90S	75.94W

Table D.7. Same as Table D.2 but for May corresponding to Fig. 5.8.

Domain	Lat	Lon
D1	9.10S	47.81W
	10.51S	37.97W
	16.11S	46.41W
	14.71S	61.875W
D2	4.90S	60.47W
	2.10S	66.09W
	10.51S	64.69W
D3	6.30N	60.47W
	3.50N	57.66W
	2.10N	54.84W
D4	6.30N	64.69W
	3.50N	64.69W
	10.51N	68.91S
	3.50N	61.875W
D5	6.30S	74.53W
	4.90S	75.94W
	6.30S	75.94W
	10.51S	78.75W
	3.50S	75.94W
	11.91S	74.53W
	21.71S	68.91W
	21.71S	66.09W
	7.70S	75.94W
	20.31S	70.31W
	2.10N	77.34W
	7.70S	77.34W
	6.30S	80.16W
	2.10N	75.94W
	7.70S	78.75W
	10.51S	77.34W

Table D.8. Same as Table D.2 but for June corresponding to Fig. 5.9.

Domain	Lat	Lon
D1	13.30S	45.00W
	9.10S	47.81W
	11.90S	39.38W
	20.31S	54.85W
D2	7.70S	61.88W
	3.50S	47.815W
	3.50S	66.09W
D3	4.906N	53.44W
	2.10N	53.44W
D4	4.906N	63.28W
	9.11N	66.09W
D5	14.705S	75.94W
	9.102S	75.94W
	2.098S	77.34W
	2.10N	77.34W
	4.90S	74.53W
	3.50S	80.16W
	13.30S	70.31W
	9.11N	74.53W
	9.102S	78.75W
	16.106S	66.09W
	11.90S	77.34W
	10.50S	77.34W

Table D.9. Same as Table D.2 but for July corresponding to Fig. 5.10.

Domain	Lat	Lon
D1	6.30S	39.38W
	17.51S	45.00W
	20.31S	43.60W
	16.106S	63.28W
D2	0.70S	63.28W
	0.70S	68.91W
	7.70S	61.88W
D3	4.91N	53.44W
	2.10N	53.44W
D4	9.11N	67.50W
	3.505N	63.28W
	3.505N	61.88W
D5	4.91N	75.94W
	6.31N	73.125W
	3.505N	77.34W
	3.505N	73.125W
	4.90S	77.34W
	2.10N	74.53W
	7.71N	73.125W
	21.71S	70.31W
	11.90S	71.72W
	10.50S	74.53W
	16.11S	71.72W
	14.705S	70.31W
	6.30S	78.75W
	10.50S	77.34W

Table D.10. Same as Table D.2 but for August corresponding to Fig. 5.11.

Domain	Lat	Lon
D1	4.90S	37.97W
	7.70S	40.78W
	14.705S	50.63W
	20.31S	47.815W
D2	0.70N	59.06W
	0.70N	64.69W
	4.90S	61.88W
	10.50S	68.91W
D3	4.906N	59.06W
	3.505N	56.25W
	0.70S	56.25W
D4	3.505N	67.50W
	6.31N	63.28W
	9.11N	68.91W
	9.11N	67.50W
D5	3.505N	71.72W
	7.71N	73.125W
	2.10N	71.72W
	6.31N	75.94W
	11.90S	70.31W
	17.51S	70.31W
	7.70S	75.94W
	2.10N	73.125W
	0.70N	77.34W
	16.106S	73.125W
	10.50S	74.53W
	14.705S	74.53W
	9.102S	77.34W

Table D.11. Same as Table D.2 but for September corresponding to Fig. 5.12.

Domain	Lat	Lon
D1	9.10S	47.81W
	7.70S	39.38W
	6.30S	47.81W
	18.91S	45.00W
D2	4.90S	56.25W
	4.90S	66.09W
D3	0.70S	50.63W
	3.505N	54.85W
	2.098S	52.03W
D4	6.31N	68.91W
	7.71N	64.69W
	3.505N	68.91W
	9.11N	68.91W
D5	0.70N	75.94W
	9.11N	75.94W
	4.906N	71.72W
	7.71N	74.53W
	21.71S	70.31W
	2.098S	75.94W
	9.11N	78.75W
	3.505N	75.94W
	10.50S	74.53W
	6.31N	73.125W
	21.71S	66.09W
	16.106S	67.50W
	13.30S	74.53W
	9.102S	77.34W

Table D.12. Same as Table D.2 but for October corresponding to Fig. 5.13.

Domain	Lat	Lon
D1	9.10S	47.81W
	4.90S	40.78W
	18.91S	42.19W
	7.70S	39.38W
D2	3.50S	60.47W
	7.70S	67.50W
D3	3.505N	52.03W
	0.70S	50.63W
	2.098S	53.44W
D4	4.906N	68.91W
	7.71N	61.88W
	6.31N	68.91W
D5	7.71N	71.72W
	9.11N	75.94W
	6.30S	77.34W
	2.10N	77.34W
	4.906N	73.125W
	16.106S	73.125W
	0.70S	75.94W
	9.11N	73.125W
	10.50S	77.35W
	4.90S	80.16W
	11.90S	75.94W
	13.30S	68.91W
	14.705S	74.53W
	16.106S	66.09W
	13.30S	75.94W
	16.106S	67.50W

Table D.13. Same as Table D.2 but for November corresponding to Fig. 5.14.

Domain	Lat	Lon
D1	9.10S	47.81W
	6.30S	40.78W
	16.106S	56.25W
	7.70S	43.60W
D2	6.30S	61.88W
	0.70S	66.09W
	7.70S	64.69W
D3	0.70N	52.03W
	3.505N	52.03W
	6.31N	59.06W
D4	3.505N	68.91W
	3.505N	66.09W
	7.71N	61.88W
	6.31N	67.50W
D5	3.50S	75.94W
	4.906N	73.125W
	0.70N	74.53W
	6.30S	77.34W
	9.11N	78.76W
	16.106S	71.72W
	0.70S	75.94W
	4.906N	71.72W
	3.50S	78.75W
	13.30S	68.91W
	13.30S	75.94W
	7.70S	78.75W
	16.106S	66.09W
	21.71S	66.09W

Table D.14. Same as Table D.2 but for December corresponding to Fig. 5.15.

Domain	Lat	Lon
D1	9.10S	47.81W
	14.705S	52.03W
	6.30S	40.78W
D2	3.50S	57.66W
	7.70S	64.69W
D3	2.10N	52.03W
	4.906N	57.66W
	2.098S	53.44W
D4	3.505N	64.69W
	4.906N	64.69W
	6.31N	61.88W
	9.11N	64.69W
D5	9.11N	78.75W
	3.50S	75.94W
	7.70S	74.53W
	3.505N	77.34W
	3.505N	73.125W
	4.90S	77.34W
	23.11S	70.31W
	13.30S	70.31W
	18.91S	64.69W
	17.51S	70.31W
	23.11S	67.50W
	11.90S	71.72W
	3.505N	74.53W
	11.90S	73.125W
	14.705S	74.53W
	6.30S	78.75W
	10.50S	77.34W

D.2. Precipitation

The training pixels listed in the following tables can be considered as the minimum number of training pixels that are required to get a desired performance at the validating pixels (VlP) in precipitation regionalization.

Table D.15. Locations of the training pixels for 70% performance corresponding to Fig. 5.16.

Domain	Lat	Lon
D1	18.91S	61.88W
	21.71S	61.88W
	16.11S	59.06S
	9.10S	42.19W
	14.70S	49.22W
	13.30S	56.25W
D2	7.70S	53.44W
	4.90S	73.12W
	2.10S	68.91W
	3.50S	52.03W
	9.10S	66.09W
	2.10S	49.22W
D3	0.70N	53.44W
	2.10N	56.25W
	2.10N	54.85W
	4.91N	56.25W
	3.50N	54.85W
D4	10.51N	68.91W
	4.91N	66.09W
	3.50N	64.69W
	6.31N	70.31W
D5	21.71S	68.91W
	17.51S	70.31W
	17.51S	67.50W
	11.90S	74.53W
	14.70S	68.91W
	11.90S	73.12W
	4.90S	78.75W
	4.91N	75.94W

Table D.16. Same as Table D.15 but for 80% performance corresponding to Fig. 5.17.

Domain	Lat	Lon
D1	18.91S	60.47W
	9.10S	39.38W
	11.90S	52.03W
	10.50S	42.19W
	17.51S	56.25W
	13.30S	53.44W
	9.10S	47.81W
D2	10.50S	60.47W
	3.50S	53.44W
	2.10S	63.28W
	7.70S	61.88W
	2.10S	50.63W
	0.70S	57.66W
	2.10N	70.31W
	3.50S	46.41W
	2.10S	45.00W
D3	2.10N	59.06W
	0.70N	52.03W
	2.10N	56.25W
	6.31N	60.47W
	3.50N	56.25W
D4	9.11N	70.31W
	6.31N	68.91W
	6.31N	64.69W
	6.31N	63.28W
	3.50N	63.28W
D5	20.31S	68.91W
	18.91S	67.50W
	17.51S	70.31W
	16.11S	70.31W
	2.10S	78.75W
	9.10S	77.33W
	3.50N	75.94W
	3.50S	75.94W
	0.70S	74.53W
	0.70N	75.94W

Table D.17. Same as Table D.15 but for 90% performance corresponding to Fig. 5.18.

Domain	Lat	Lon
D1	18.91S	61.88W
	21.71S	61.88W
	11.90S	52.03W
	20.31S	50.63W
	21.71S	53.44W
	18.91S	54.85W
	20.31W	40.78W
	13.30S	53.44W
	9.10S	52.03W
	9.10S	42.19W
	17.51S	46.41W
	7.70S	45.00W
	9.10S	46.41W
	6.30S	39.38W
D2	6.30S	56.25W
	9.10S	61.88W
	11.90S	66.09W
	6.30S	74.53W
	4.90S	71.72W
	6.30S	73.12W
	9.10S	64.69W
	7.70S	71.72W
	3.50S	74.53W
	2.10S	67.50W
	2.10S	64.69W
	3.50S	67.50W
	3.50S	46.41W
	2.10S	45.00W
	3.50S	40.78W
D3	0.70S	53.44W
	0.70S	50.63W
	0.70N	54.85W
	4.91N	60.47W
	0.70N	53.44W
	3.50N	56.25W
	6.31N	59.06W
D4	7.71N	66.09W
	6.31N	63.28W
	4.91N	70.31W
	4.91N	66.09W
	3.50N	64.69W
	3.50N	66.09W
	7.71N	70.31W
	4.91N	63.28W

Table D.17. Continued.

D5	20.31S	68.91W
	18.91S	68.91W
	20.31S	66.09W
	17.51S	70.31W
	20.31S	64.69W
	13.30S	71.72W
	16.11S	70.31W
	10.50S	75.94W
	4.90S	78.75W
	7.71N	75.94W
	16.11S	64.69W
	4.90S	75.94W
	3.50S	80.16W
	2.10S	74.53W
	2.10S	75.94W
	6.31N	74.53W
	0.70N	75.94W

Table D.18. Same as Table D.16 but for JJA corresponding to Fig. 5.20.

Domain	Lat	Lon
D1	14.70S	43.60W
	9.10S	45.00W
	17.51S	42.19W
	18.91S	43.60W
	18.91S	50.63W
D2	4.90S	45.00W
	10.50S	64.69W
	7.70S	60.47W
	3.50S	60.47W
	2.10S	61.88W
	2.10S	64.69W
	2.10N	67.50W
	2.10S	67.50W
D3	2.10S	50.63W
	0.70S	54.85W
	2.10S	56.25W
	2.10S	53.44W
	2.10N	53.44W
	4.91N	59.06W
D4	9.11N	63.28W
	9.11N	67.50W
	6.31N	61.88W
	3.50N	66.09W
	6.31N	66.09W
D5	21.71S	66.09W
	14.70S	71.72W
	21.71S	68.91W
	18.91S	63.28W
	0.70S	78.75W
	7.70S	74.53W
	4.91N	75.94W
	16.11S	66.09W
	4.90S	74.53W

Table D.19. Same as Table D.16 but for SON corresponding to Fig. 5.21.

Domain	Lat	Lon
D1	3.50S	40.78W
	4.90S	45.00W
	18.91S	53.44W
	20.31S	56.25W
	21.71S	49.22W
	10.50S	50.63W
	14.70S	49.22W
D2	0.70N	60.47W
	11.90S	61.88W
	3.50S	59.06W
	6.30S	68.91W
	4.90S	52.03W
	6.30S	53.44W
D3	2.10S	45.00W
	0.70N	56.25W
	2.10S	53.44W
	2.10S	50.63W
D4	9.11N	66.09W
	7.71N	70.31W
	7.71N	68.91W
	6.31N	61.88W
	4.91N	67.50W
	3.50N	66.09W
D5	14.70S	74.53W
	18.91S	68.91W
	21.71S	66.09W
	11.90S	75.94W
	2.10S	78.75W
	11.90S	73.12W
	0.70N	77.34W
	6.30S	75.94W
	14.70S	64.69W
	7.71N	75.94W
	4.91N	71.72W

Table D.20. Same as Table D.16 but for DJF corresponding to Fig. 5.22.

Domain	Lat	Lon
D1	18.91S	61.88W
	9.10S	39.38W
	23.11S	53.44W
	23.11S	50.63W
	18.91S	47.81W
D2	7.70S	52.03W
	6.30S	60.47W
	7.70S	73.12W
	9.10S	63.28W
	2.10S	45.00W
D3	0.70N	53.44W
	2.10S	50.63W
	0.70N	52.03W
	4.91N	53.44W
D4	6.31N	67.50W
	6.31N	66.09W
	9.11N	70.31W
	3.50N	67.50W
D5	21.71S	68.91W
	6.30S	78.75W
	4.90S	78.75W
	6.31N	75.94W
	6.30S	75.94W
	0.70N	75.94W
	10.50S	73.12W

REFERENCES

Adam, J. C., and D. P. Lettenmaier, 2003: Adjustment of global gridded precipitation for systematic bias. *J. Geophys. Res.*, **108**, 4257, doi:10.1029/2002JD002499.

Amari, S.-i., N. Murata, K.-R. Muller, M. Finke, and H. H. Yang, 1997. Asymptotic statistical theory of overtraining and cross-validation. *IEEE Transactions on Neural Networks*, **8**, 985–996

Aragao, L., Y. Malhi, N. Barbier, L. Anderson, S. Saatchi, and E. Shimabukuro, 2008: Interactions between rainfall, deforestation and fires during recent years in the Brazilian Amazonia, *Phil. Trans. R. Soc. B.*, **363**, 1779–1785.

Arkin, P. A., and P. Xie, 1994: The global precipitation climatology project: First algorithm intercomparison project, *Bull. Am. Meteorol. Soc*., **75**, 401–419.

ASCE Task Committee on Application of Artificial Neural Networks in Hydrology, 2000: Artificial neural networks in hydrology. parts I and II, *J. Hydrol. Eng*., **5**, 115-137.

Avissar, R., and Y. Liu, 1996: Three-dimensional numerical study of shallow convective clouds and precipitation induced by land surface forcing. *J. Geophys. Res.-Atmos.*, **101**, D3, 7499–7518.

Bagley, J. E., A. R. Desai, K. J. Harding, P. K. Snyder, and J. A. Foley, 2014: Drought and deforestation: Has land cover change influenced recent precipitation extremes in the Amazon? *J. Climate*, **27**, 345–361, doi: dx.doi.org/10.1175/JCLI-D-12-00369.1.

Baigorria, G. A., J. W. Jones, D –W. Shin, A. Mishra, and J. J. O'Brien, 2007: Assessing uncertainties in crop model simulations using daily bias corrected Regional Circulation Model outputs. *Clim. Res*., **34**, 211-222.

Barber, C. P., 2009: Climate change, human land use and future fires in the Amazon, *Global Change Biol.*, **15**, 601–612, doi:10.1111/j.13652486.2008.01786.x.

Bárdossy, A., and H. J. Caspary, 1990: Detection of climate change in Europe by analyzing European atmospheric circulation patterns from 1881 to 1989. *Theor. Appl. Climatol.*, **42**, 155–167, doi:10.1007/BF00866871.

Bebis, G., M. Georgiopoulos, 1994: Feed-forward neural networks: Why network size is so important. *IEEE Potentials*, 27–31.

Bennett, W. B., J. Wang, and R. L. Bras, 2008: Estimation of global ground heat flux. *J. Hydrometeor*., **9**, 744–759, doi:10.1175/2008JHM940.1.

Berg, A. A., J. S. Famiglietti, J. P. Walker, and P. R. Houser, 2003: Impact of bias correction to reanalysis products on simulations of North American soil moisture and hydrological fluxes. *Geophys. Res. Lett*., **108**, D16(4490), doi:10.1029/2002J D003334.

Bergström, S., 1976: Development and application of a conceptual runoff model for Scandinavian Catchments. *Report RHO*, **7**, SMHI, Norrköping, Sweden.

Betts, R. A., P. M. Cox, M. Collins, P. P. Harris, C. Huntingford, and C. D. Jones, 2004: The role of ecosystem-atmosphere interactions in simulated Amazonian precipitation decrease and forest dieback under global climate warming. *Theor. Appl. Climatol*., **78**, 157–175, doi:10.1007/s00704-004-0050-y.

Bisht, G., and R. L. Bras, 2010: Estimation of net radiation from the MODIS data under all sky conditions: Southern Great Plains case study. *Remote Sens. Environ.*, **114**, 1522–1534, doi:10.1016/j.rse.2010.02.007.

Bisht, G., V. Venturini, S. Islam, and L. Jiang, 2005: Estimation of the net radiation using MODIS (Moderate Resolution Imaging Spectroradiometer) data for clear sky days. *Remote Sens. Environ*., **97**, 52–67, doi:10.1016/j.rse.2005.03.014.

Blum, E. K., and L. K. Li, 1991: Approximation theory and feedforward networks. *Neural Networks*, **4**, 511-515.

Boisvenue, C., and S. W. Running, 2006: Impacts of climate change on natural forest productivity evidence since the middle of the 20th century. *Global Change Biol*., **12**, 862–882, doi:10.1111/j.1365-2486.2006.01134.x.

Bombardi, R. J., and L. M. V. Carvalho, 2009: IPCC global coupled model simulations of the South America monsoon system. *Clim. Dyn*., **33**, 893-916.

Bonan, G. B., and S. Levis, 2006: Evaluating aspects of the Community Land and Atmosphere Models (CLM3 and CAM3) using a dynamic Global Vegetation Model. *J. Climate*, **19**, 2290–2301, doi:10.1175/JCLI3741.1.

Brent, R. P., 1971: An algorithm with guaranteed convergence for finding a zero of a function. *Comput. J*., **14**, 422–425.

Broomhead, D. S., and D. Lowe, 1988: Multivariate functional interpolation and adaptive networks. *Complex Systems*, **2**, 321–355.

Brunt, D., 1939: Physical and Dynamical Meteorology. *Cambridge University Press*, pp. 454.

Brutsaert, W., 1975: On a derivable formula for long-wave radiation from clear skies. *Water Resour. Res*., **11**, 742–744, doi:10.1029/WR011i005p00742.

Brutsaert, W., 1982: Evaporation into the Atmosphere: Theory, History and Applications. *Kluwer Academic*, pp. 299.

Buck, A. L., 1981: New equations for computing vapor pressure and enhancement factor. *J. Appl. Meteor. Climatol*., **20**, 1527–1532.

Buonomo, E., R. G. Jones, C. Huntingford, and J. Hannaford, 2007: On the robustness of changes in extreme precipitation over Europe from two high resolution climate change simulations. *Q. J. R. Meteorol. Soc*., **133**, 65–81.

Burger, G., 1996: Expanded downscaling for generating local weather scenarios. *Climate Res*., **7**, 111–128, doi:10.3354/cr007111.

Burke, E. J., S. J. Brown, and N. Christidis, 2006: Modeling the recent evolution of global drought and projections for the twenty-first century with the Hadley Centre Climate Model. *J. Hydrometeor*., **7**, 1113–1125.

Bush, M. B., M. R. Silman, C. McMichael, A. Restrepo-Correa, D. H. Urrego, A. Correa, and S. Saatchi, 2008: Fire, climate change, and biodiversity in Amazonia: A late-holocene perspective. *Phil. Trans. R. Soc. B.*, **363**, 1795–1802.

Butler, R. A., 2006: Amazon Destruction. Retrieved 9 January 2006, from Mongabay.com / A Place Out of Time: Tropical Rainforests and the Perils They Face. Web site:http://rainforests.mongabay.com/amazon/amazon_destruction.html

Carpenter, G. A., and S. Grossberg, 1987a: ART 2: Self-organization of stable category recognition codes for analog input patterns. *Applied Optics*, **26**, 4919-4930.

Carpenter, G. A., and S. Grossberg, 1987b: A massively parallel architecture for a self-organizing neural pattern recognition machine. *Computer Vision, Graphics and Image Processing*, **37**, 54-115.

Castellano, G., A. M. Fanelli, and M. Pelillo, 1997: An iterative pruning algorithm for feedforward neural networks. *IEEE Transactions on Neural Networks*, **8**, 519–531.

Castillo, C. K. G., and K. R. Gurney, 2012: Exploring Surface Biophysical-Climate Sensitivity to Tropical Deforestation Rates Using a GCM: A Feasibility Study. *Earth Interact.*, **16**, 1–23. doi: http://dx.doi.org/10.1175/2011EI390.1.

Chau, K.W., 2006: Particle swarm optimization training algorithm for ANNs in stage prediction of Shing Mun River. *J. Hydrol*., **329**, 363–367.

Chau, K. W., C. L. Wu, and Y. S. Li, 2005: Comparison of several flood forecasting models in Yangtze river. *J. Hydrol. Eng*., **10**, 485-491.

Cayan, D. R., E. P. Maurer, M. D. Dettinger, M. Tyree, and K. Hayhoe, 2008: Climate change scenarios for the California region. *Climatic Change*, **87**, S21–S42, doi:10.1007/s10584-007-9377-6.

Chen, J., F. P. Brissette, R. Leconte, 2011a: Uncertainty of downscaling method in quantifying the impact of climate change on hydrology. *J. Hydrol*., **401**, 190–202.

Chen, J., F. P. Brissette, A. Poulin, R. Leconte, 2011b: Overall uncertainty study of the hydrological impacts of climate change for a Canadian watershed. *Water Resour. Res*., **47**, W12509.

Chen, J., F. P. Brissette, D. Chaumont, and M. Braun, 2013: Finding appropriate bias correction methods in downscaling precipitation for hydrologic impact studies over North America. *Water Resour. Res*., **49**, 4187–4205, doi:10.1002/wrcr. 20331.

Chen, K., L. P. Yang, X. Yu, and H. S. Chi, 1997: A self-generating modular neural network architecture for supervised learning. *Neurocomputing*, **16**, 33–48.

Cheng, C. T., K. W. Chau, Y. G. Sun, and J. Y. Lin, 2005: Long-term prediction of discharges in Manwan reservoir using artificial neural network models. *Lect. Notes Comput. Sci*., **3498**, 1040-1045.

Chng, E. S., S. Chen, and B. Mulgrew, 1996: Gradient radial basis function networks for nonlinear and nonstationary time series prediction. *IEEE Transactions on Neural Networks*, **7**, 191–194.

Chou, S. C., J. A. Marengo, A. A. Lyra, G. Sueiro, J. F. Pesquero, L. M. Alves, G. Kay, R. Betts, D. J. Chagas, J. L. Gomes, J. F. Bustamante, and P. Tavares, 2012: Downscaling of South America present climate driven by 4-member HadCM3 runs. *Clim. Dyn*., **38**, 635–653.

Christensen, J. H., B. Hewitson, A. Busuioc, A. Chen, X. Gao, R. Held, R. Jones, R. K. Kolli, W. K. Kwon, R. Laprise, V. M. Rueda, L. Mearns, C. G. Menendez, J. Räisänen, A. Rinke, A. Sarr, P. Whetton, R. Arritt, R. Benestad, M. Beniston, D. Bromwich, D. Caya, J. Comiso, R. de Elia, and K. Dethloff, 2007: Regional climate projections, Climate Change, 2007. The Physical Science Basis, *Contribution of working group I to the fourth assessment report of the intergovernmental panel on climate change*, Cambridge University Press, Cambridge, United Kingdom.

Chu, P.-S., Z. P. Yu, and S. Hastenrath, 1994: Detecting climate change concurrent with deforestation in the Amazon basin: Which way has it gone? *Bull. Am. Meteorol. Soc*., **75**, 579–583

Churchill, P. S., 1986: Neurophilosophy: toward a Unified Science of the Mind-Brain. *MIT Press*, Cambridge, MA.

Churchland, P. S., and T. J. Sejnowski, 1993: The Computational Brain. MIT Press, Cambridge, MA.

Clerc, M., and J. Kennedy, 2002: The particle swarm—explosion, stability, and convergence in a multidimensional complex space. *IEEE Transactions on Evolutionary Computation*, **6**, 58–73.

Cline, H., 2003: Sperry and Hebb: oil and vinegar? *Trends in Neurosci.*, **26**, 655-661.

Cochrane, M. A., and C. P. Barber, 2009: Climate change, human land use and future fires in the Amazon. *Global Change Biol.*, **15**, 601–612, doi:10.1111/j.1365-2486.2008.01786.x.

Coelho, C. A. S., and L. Goddard, 2009: El Niño-induced tropical droughts in climate change projections. *J. Climate*, **22**, 6456–6476.

Collins, W. D., C. M. Bitz, M. L. Blackmon, G. B. Bonan, C. S. Bretherton, J. A. Carton, P. Chang, S. C. Doney, J. J. Hack, T. B. Henderson, J. T. Kiehl, W. G. Large, D. S. Mckenna, B. D. Santer, and R. D. Smith, 2006: The Community Climate System Model Version 3 (CCSM3), *J. Climate*, **19**, 2122–2143.

Conway, D., 1998: Recent climate variability and future climate change scenarios for Great Britain. *Prog. Phys. Geogr*., **22**, 350–374.

Corte-Real, J., B. Qian, and H. Xu, 1999: Circulation patterns, daily precipitation in Portugal and implications for climate change simulated by the second Hadley Centre GCM. *Clim. Dyn*., **15**, 921–935, doi:10.1007/s003820050322.

Crane, R. G., and B. C. Hewitson, 1998: Doubled CO2 precipitation changes for the Susquehanna Basin: Down-scaling from the Genesis general circulation model. *Int. J. Climatol*., **18**, 65–76, doi:10.1002/(SICI)1097-0088(199801)18:1,65::AID-JOC222.3.0.CO;2-9.

Cosgrove, B. A., D. Lohmann, K. E. Mitchell, P. R. Houser, E. F. Wood, J. C. Schaake, A. Robock, C. Marshall, J. Sheffield, Q. Duan, L. Luo, R. W. Higgins, R. T. Pinker, J. D. Tarpley, and J. Meng, 2003: Real-time and retrospective forcing in the North American Land Data Assimilation System (NLDAS) project. *J. Geophys. Res*., **108**, doi:10.1029/2002JD003118.

Costa, M. H., and G. F. Pires, 2010: Effects of Amazon and Central Brazil deforestation scenarios on the duration of the dry season in the arc of deforestation. *Int. J. Climatol*., **30**, 1970–1979.

Cox, P. M., D. Pearson, B. B. Booth, P. Friedlingstein, C. Huntingford, C. D. Jones, and C. M. Luke, 2013: Sensitivity of tropical carbon to climate change constrained by carbon dioxide variability. *Nature*, **494**, 341–344.

Dai, A., 2001a: Global precipitation and thunderstorm frequencies. Part i: Seasonal and interannual variations. *J. Climate*, **14**, 1092–1111.

Dai, A., 2001b: Global precipitation and thunderstorm frequencies. Part ii: Diurnal variations. *J. Climate*, **14**, 1112–1128.

Dai, A., 2006: Precipitation characteristics in eighteen Coupled Climate Models. *J. Climate*, **19**, 4605–4630.

Daley, R., 1993: Atmospheric Data Analysis. *Cambridge University Press*, pp. 457.

Davidson, E. A., A. C. de Araújo, P. Artaxo, J. K. Balch, I. F. Brown, M. M. C. Bustamante, M. T. Coe, R. S. DeFries, M. Keller, M. Longo, J. W. Munger, W. Schroeder, B. S. Soares- Filho, C. M. Souza, and S. C. Wofsy, 2012: The Amazon basin in transition. *Nature*, **481**, 321–328.

Dawson, C. W., and R. Wilby, 1998: An artificial neural network approach to rainfall-runoff modelling. *Hydrol. Sci.*, **43**, 47–66.

de Goncalves, L. G. G., N. Restrepo-Coupe, H. R. da Rocha, S. R. Saleska, and R. Stockli, 2013: LBA-ECO CD-32 LBA Model Intercomparison Project (LBA-MIP) forcing data. Oak Ridge National Laboratory Distributed Active Archive Center Data-set. [Available online at http://daac.ornl.gov/cgi-bin/dsviewer. pl?ds_id=1177.]

De Pesquisas Espaciais INPE, I. N., 2003: Monitoring of the Amazon forest by satellite 2001-2002. Technical paper, Sao Jose Dos Campos, Brazil.

de Szoeke, S. P., and S. P. Xie, 2008: The Tropical Eastern Pacific seasonal cycle: Assessment of errors and mechanisms in IPCC AR4 Coupled Ocean -Atmosphere General Circulation Models. *J. Climate*, **21**, 2573–2590.

Diak, G. R., and C. Gautier, 1983: Improvements to a simple physical model for estimating insolation from goes data. *J. Climate Appl. Meteor.*, **22**, 505–508.

Dickinson, R. E., A. Henderson-Sellers, P. J. Kennedy, and M. F. Wilson, 1986: Biosphere–Atmosphere Transfer Scheme (BATS) for the Community Climate Model. NCAR Tech. Note NCAR/TN-2751STR, 72 pp., doi:10.5065/D6668B58.

Dixon, R., S. Brown, R. Houghton, A. Solomon, M. Trexler, and J. Wisniewski: 1994: Carbon pools and flux of global forest ecosystems. *Science,* 185-190.

Durbin, R., and D. E. Rumelhart, 1989: Product units: A computationally powerful and biologically plausible extension to backpropagation networks. *Neural Computation*, **1**, 133-142.

Eltahir, E., and R. L. Bras, 1993: On the response of the tropical atmosphere to large-scale deforestation. *Q. J. R. Meteor. Soc*., **119**, 779–793.

Emmerich, W. E., and C. L. Verdugo, 2008: Long-term carbon dioxide and water flux database, Walnut Gulch Experimental Watershed, Arizona, United States. *Water Resour. Res*., **44**, W05S09, doi:10.1029/2006WR005693.

Fahlman, S. E., and C. Lebiere, 1990: The cascade-correlation learning architecture. In D. S. Touretzk (ed.), Advances in Neural Information Processing Systems 2. Morgan Kaufmann, San Mateo, CA.

Figueroa, S., P. Satyamurty, and P. S. Dias, 1995: Simulations of the summer circulation over the South American region with an eta coordinate model. *J. Atmos. Sci.,* 1573-1584.

Fowler, H. J., C. G. Kilsby, and P. E. O'Connell, 2000: A stochastic rainfall model for the assessment of regional water resource systems under changed climatic condition. *Hydrol. Earth Syst. Sci*., **4**, 263–281, doi:10.5194/hess-4-263-2000.

Fowler, H. J., S. Blenkinsop, and C. Tebaldi, 2007: Linking climate change modelling to impacts studies: Recent advances in downscaling techniques for hydrological modelling. *Int. J. Climatol*., **27**, 1547–1578, doi:10.1002/joc.1556.

Frei, C., J. H. Christensen, M. Deque, D. Jacob, R. G. Jones, and P. L. Vidale, 2003: Daily precipitation statistics in regional climate models: evaluation and intercomparison for the European Alps. *J. Geophys. Res*., **108**, 4124.

Frei, C., R. Scholl, S. Fukutome, J. Schmidli, and P. L. Vidale, 2006: Future change of precipitation extremes in Europe: Intercomparison of scenarios from regional climate models. *J. Geophys. Res.*, **111**, D06,105.

Funahashi, K. I., 1989: On the approximation realization of continuous mapping by neural networks. *Neural Networks*, **2**, 183-192.

Galkin, I, and U. M. Lowell, Crash Introduction to Artificial Neural Networks. *Materials for UML 91.531 Data Mining course*.

Georgakakos, A. P., H. Yao, M. G. Mullusky, and K. P. Georgakakos, 1998: Impacts of climate variability on the operational forecast and management of the upper Des Moines River basin. *Water Resour. Res*., **34**, 799–821, doi:10.1029/97WR03135.

Georgakakos, A. P., H. Yao, M. Kistenmacher, K. P. Georgakakos, N. E. Graham,F. Y. Cheng, C. Spencer, and E. Shamir, 2012: Value of adaptive water resources management in Northern California under climatic variability and change: Reservoir management. *J. Hydrol*., **412–413**, 34–46, doi:10.1016/j.jhydrol.2011. 04.038.

Giorgi, F., and Coauthors, 2001: Regional climate information-Evaluation and projections. Climate Change 2001: The Scientific Basis, J. T. Houghton et al., (eds.), *Cambridge University Press*, 583–638.

Goodison, B. E., P. Y. T. Louie, and D. Yang, 1998: WMO solid precipitation measurement intercomparison, final report. *World Meteorological Organization Tech. Doc.*, WMO TD872, Geneva, Switzerland, pp. 212.

Gregory, D., G. J. Shutts, and J. R. Mitchell, 1998: A new gravity wave drag scheme incor porating anisotropic orography and low level 654 wave breaking: Impact upon the climate of the UK Meteorological Office Unified Model. *Q. J. R. Meteor. Soc*., **124**, 463–493.

Grossberg, S., 1969: Embedding field: A theory of learning with physiological implications. *J. Math. Psychol*., **6**, 209–239.

Guilyardi, E., 2006: El Niño mean state-seasonal cycle interactions in a multi-model ensemble. *Clim. Dyn*., **26**, 329–348.

Hagan, M. T. and M. B. Menhaj, 1994: Training feedforward networks with the marquardt algorithm. *IEEE Transactions on Neural Networks*, **5**, 989-993.

Harding, R., M. Best, E. Blyth, S. Hagemann, P. Kabat, L. M. Tallaksen, T. Warnaars, D. Wiberg, G. P. Weedon, H. V. Lanen, F. Ludwig, and I. Haddeland, 2011: WATCH: Current knowledge of the terrestrial global water cycle, *J. Hydrometeor*., **12**, 1149–1156, doi:10.1175/JHM-D-11-024.1.

Harris, I., P. D. Jones, and T. J. Osborn, and D. H. Lister, 2013: Updated high-resolution grids of monthly climatic observations – the CRU TS3.10 Dataset. *Int. J. Climatol.*, **34**, 623-642.

Harris, I., P. D. Jones, 2014: CRU TS3.22: Climatic Research Unit (CRU) Time-Series (TS) Version 3.22 of High Resolution Gridded Data of Month-by-month Variation in Climate (Jan. 1901- Dec. 2013). NCAS British Atmospheric Data Centre, University of East Anglia Climatic Research Unit, doi:10.5285/ 18BE23F8-D252-482D-8AF9-5D6A2D40990C.

Hassoun, M. H., 1995: Fundamentals of Artificial Neural Networks. *MIT Press*, Cambridge.

Hay, L. E., 1991: Simulation of precipitation by weather type analysis. *Water Resour. Res*., **27**, 493–501, doi:10.1029/90WR02650.

Hay, L. E., R. L. Wilby, and G. H. Leavesley, 2000: A comparison of delta change and downscaled GCM scenarios for three mountainous basins in the United States. *J. Am. Water Resour. Assoc*., **36**, 387-397.

Hay, L. E., and M. P. Clark, 2003: Use of statistically and dynamically downscaled atmospheric model output for hydrologic simulations in three mountainous basins in the western United States. *J. Hydrol*., **282**, 56–75, doi:10.1016/S0022-1694(03)00252-X.

Hayhoe, K., D. Cayan, C. B. Field, P. C. Frumhoff, E. P. Maurer, N. L. Miller, S. C. Moser, S. H. Schneider, K. N. Cahill, E. E. Cleland, L. Dale, R. Drapek, R. M. Hanemann, L. S. Kalkstein, J. Lenihan, C. K. Lunch, R. P. Neilson, S. C. Sheridan, and J. H. Verville, 2004: Emissions pathways, climate change, and impacts on California. *Proc. Natl. Acad. Sci. U.S.A.*, **101**, 12,422–12,427, doi:10.1073/pnas.0404500101.

Hecht-Nielsen, R., 1987: Kolmogorov's mapping neural network existence theorem. In: Proceedings of the IEEE International conference on Neural Networks. IEEE Press, New York, 3, 11-13.

Hecht-Nielsen, R., 1990: Neurocomputing. *Addison-Wesley*, MA.

Heiss, M., and S. Kampl, 1996: Multiplication-free radial basis function network. *IEEE Transactions on Neural Networks*, **7**, 1461–1464.

Hidalgo, H. G., M. D. Dettinger, and D. R. Cayan, 2008: Downscaling with constructed analogues: Daily precipitation and temperature fields over the United States. *Report*, **2007-027**, California Climate Change Center, pp. 48, [Prepared For: Public Interest Energy Research (PIER) Program California Energy Commission].

Hinton, G. E., and T. J. Sejnowski, 1986: Learning and relearning in Boltzmann machines. In D. E. Rummelhart, and J. L. McClelland, (eds). *Parallel Distributed Processing*, **1**, MIT Press, Cambridge, MA.

Hirose, Y., K. Yamashita, and S. Hijiya, 1991: Back-propagation algorithm which varies the number of hidden units. *Neural Networks*, **4**, 61–66.

Hochreiter, S., and J. Schmidhuber, 1997: Long short-term memory. *Neural Computation*, **9**, 1735–1780.

Hornik, K., 1989: Multilayer feedforward networks are universal approximators. *Neural Networks*, **2**, 359-366.

Hornik. K., 1991: Approximation capabilities of multilayer feedforward networks. *Neural Networks*, **4**, 251-257.

Horton, R. M., V. Gornitz, D. A. Bader, A. C. Ruane, R. Goldberg, and C. Rosenzweig, 2011: Climate hazard assessment for stakeholder adaptation planning in New York City. *J. Appl. Meteor. Climatol.*, **50**, 2247–2266.

Hsu, K. L., H. V. Gupta, and S. Sorooshian, 1995: Artificial neural network modeling of the rainfall-runoff process. *Water Resour. Res.*, **31**, 2517–2530.

Hsu, K. L., X. Gao, S. Sorooshian, and H. V. Gupta, 1996: Precipitation estimation from remotely sensed information using artificial neural networks. *J. Appl. Meteor*., **36**, 1176-1190.

Hsu, K. L., H. V. Gupta, X. Gao, and S. Sorooshian, 1999: Estimation of physical variables from multichannel remotely sensed imagery using a neural network: Application to rainfall estimation. *Water Resour. Res*., **35**, 1605–1618.

Hsu, K. L., H. V. Gupta, X. Gao, S. Sorooshian, and B. Imam, 2002: Self-organizing linear output map (SOLO): An artificial neural network suitable for hydrologic modeling and analysis. *Water Resour. Res*., **38**, 1302, doi:10.1029/2001WR000795.

Huang, S. C., Y. F. Huang, 1991: Bounds on the number of hidden neurons in multilayer perceptrons. *IEEE Transactions on Neural Networks*, **2**, 47–55.

Huffman, G. J., D. T. Bolvin, E. J. Nelkin, D. B.Wolff, R. F. Adler, G. Gu, Y. Hong, K. P. Bowman, and E. F. Stocker, 2007: The TRMM multisatellite precipitation analysis (TMPA): Quasi-Global, multiyear, combined-sensor precipitation estimates at fine scales. *J. Hydrometeor*., **8**, 38–55.

Huth, R., 2002: Statistical downscaling of daily temperature in central Europe. *J. Climate*, **15**, 1731–1742, doi:10.1175/1520-0442(2002)015,1731:SDODTI.2.0.CO;2.

Idso, S. B., 1981: A set of equations for full spectrum and 8- to 14-mm and 10.5- to 12.5-mm thermal radiation from cloudless skies. *Water Resour. Res*., **17**, 295–304, doi:10.1029/WR017i002p00295.

Ines, A. V. M., and J. W. Hansen, 2006: Bias correction of daily GCM rainfall for crop simulation studies. *Agric. For. Meteor*., **138**, 44–53, doi:10.1016/j.agrformet.2006.03.009.

Johnson, F., S. Westra, A. Sharma, and A. J. Pitman, 2011: An assessment of GCM skill in simulating persistence across multiple time scales. *J. Climate*, **24**, 3609–3623.

Jones, P. D., M. Hulme, and K. R. Briffa, 1993: A comparison of Lamb circulation types with an objective classification scheme. *Int. J. Climatol*., **13**, 655–663, doi:10.1002/joc.3370130606.

Jones, P. G., P. K. Thornton, and J. Heinke, 2009: Generating characteristic daily weather data using downscaled climate model data from the IPCC's Fourth Assessment. Project Rep., International Livestock Research Institute, Nairobi, Kenya, 19 pp. [Available online at https://cgspace.cgiar.org/handle/10568/2482.].

Joorabchi, A., H. Zhang, and M. Blumenstein, 2007: Application of artificial neural networks inflow discharge prediction for the Fitzroy River, Australia. *J. Coastal Res*., **SI50**, 287-291.

Kalman, B. L., and S. C. Kwasny, 1992: Why Tanh? Choosing a sigmoidal function. *Neural Networks*, **4**, 578-581.

Kalnay, E., 2003: Atmospheric Modeling, Data Assimilation, and Predictability. *Cambridge University Press*, pp 341.

Kandel, E. R., 1991: Nerve cells and behavior. In E. R. Kandel, J. H. Schwartz, T. M. Jessell (eds.), *Principles of Natural Science*, 3rd ed. Elsevier, New York.

Katz, R. W., 1996: Use of conditional stochastic models to generate climate change scenarios. *Climatic Change*, **32**, 237–255, doi:10.1007/BF00142464.

Katz, R. W., M. B. Parlange, and P. Naveau, 2002: Statistics of extremes in hydrology. *Adv. Water Resour*., **25**, 1287–1304, doi:10.1016/S0309-1708(02)00056-8.

Khotanzad, A., R. Afkhami-Rohani, T- .L Lu, A. Abaye, M. Davis, and D. J. Maratukulam, 1997: ANNSTLF—a neural-network-based electric load forecasting system. *IEEE Transactions on Neural Networks*, **8**, 835–846.

Kidson, J. W., 2000: An analysis of New Zealand synoptic types and their use in defining weather regimes. *Int. J. Climatol*., **20**, 299–316, doi:10.1002/(SICI)1097-0088(20000315)20:3,299::AID-JOC474.3.0.CO;2-B.

Kilsby, C. G., P. S. P. Cowpertwait, P. E. O'Connell, and P. D. Jones, 1998: Predicting rainfall statistics in England and Wales using atmospheric circulation variables. *Int. J. Climatol*., **18**, 523–539, doi:10.1002/(SICI)1097-0088(199804)18:5,523:: AID-JOC268.3.0.CO;2-X.

Kirkpatrick, S., C. Gelatt, and M. Vecchi, 1989: Optimization by simulated annealing. *Science*, **220**, 671-680.

Kitano, H., 1994: Neurogenetic learning: an integrated method of designing and training neural networks using genetic algorithms," *Physica D Nonlinear Phenomena*, **75**, 225-238.

Knox, R. G., 2013: Land conversion in Amazonia and Northern South America : influences on regional hydrology and ecosystem response. Ph.D. thesis, Massachusetts Institute of Technology. Department of Civil and Environmental Engineering.

Kohonen, T., 1982: Self-organized formation of topologically correct feature maps. *Biological Cybernetics*, **43**, 59-69.

Kohonen, T., 1987: Adaptive, associative and self-organizing functions in neural computing. *Applied Optics*, **26**, 4910-4918.

Kohonen, T., 1988: Self organizing feature maps. Course notes from 1988 Conference on Neural Networks, San Diego, CA. Available from the IEEE.

Kolmogorov, A. N., 1957: On the representation of continuous functions of many variables by superpositions of continuous functions of one variable and addition. *Doklady Akademii Nauk SSSR*, **114**.

Koza, J. R., and J. P. Rice, 1991: Genetic generation of both the weights and architecture for a neural network. *Poc. IJCNN 91*, pp. II397-II404.

Kuligowski, R. J., and A. P. Barros, 1998a: Experiments in short-term precipitation forecasting using artificial neural networks. *Mon. Weather Rev*., **126**, 470–482.

Kuligowski, R. J., and A. P. Barros, 1998b: Localized precipitation forecasts from a numerical weather prediction model using artificial neural networks. *Weather and Forecasting*, **13**, 1194–1204.

Kuok, K. K., S. Harun, and S. M. Shamsuddin, 2010: Particle swarm optimization feedforward neural network for modeling runoff. *Int. J. Environ. Sci. Tech.*, **7**, 67-78.

Kwok, T.-Y., and D. -Y Yeung, 1997a: Constructive algorithms for structure learning in feedforward neural networks for regression problems. *IEEE Transactions on Neural Networks*, **8**, 630–645.

Kwok, T.-Y., and D. -Y Yeung, 1997b: Objective functions for training new hidden units in constructive neural networks. *IEEE Transactions on Neural Networks*, **8**, 1131–1148.

Lachtermacher, G., Fuller, J. D., 1994: Backpropagation in hydrological time series forecasting. In: Hipel, K.W., McLeod, A.I., Panu, U.S., Singh, V.P. (eds.), *Stochastic and Statistical Methods in Hydrology and Environmental Engineering*. Kluwer Academic, Dordrecht.

Lafon, T., S. Dadson, G. Buys, and C. Prudhomme, 2013: Bias correction of daily precipitation simulated by a regional climate model: a comparison of methods. *Int. J. Climatol*., **33**, 1367–1381.

Lammering, B., and I. Dwyer, 2000: Improvement of water balance in land surface schemes by random cascade disaggregation of rainfall. *Int. J. Climatol*., **20**, 681–695.

Lattin, J., D. Carroll, and P. E. Green, 2003: Analyzing Multivariate Data. Cengage Learning, pp. 580.

Lawrence, D. M., P. E. Thornton, K. W. Oleson, and G. B. Bonan, 2007: The Partitioning of Evapotranspiration into Transpiration, Soil Evaporation, and Canopy Evaporation in a GCM: Impacts on Land–Atmosphere Interaction. *J. Hydrometeor*., **8**, 862–880. doi: http://dx.doi.org/10.1175/JHM596.1

Leander, R., and T. A. Buishand, 2007: Resampling of regional climate model output for the simulation of extreme river flows. *J. Hydrol*., **332**, 487–496.

Lettenmaier, D. P., and D. Rind, 1992: Hydrological aspects of global climate change – preface. *J. Geophys. Res*., **97**, 2675–2676.

Li, H., J. Sheffield, and E. F. Wood, 2010: Bias correction of monthly precipitation and temperature fields from Intergovernmental Panel on Climate Change AR4 models using equidistant quantile matching. *J. Geophys. Res*., **115**, D10,101, doi:10.1029/ 2009JD012882.

Liang, S., Ed., 2008: Advances in Land Remote Sensing. *Springer*, pp. 497.

Liang, X.-Z., K. E. Kunkel, G. A. Meehl, R. G. Jones, and J. X. L. Wang, 2008: Regional climate models downscaling analysis of general circulation models present climate biases propagation into future change projections. *Geophys. Res. Lett*., **35**, L08709, doi:10.1029/2007GL032849.

Liong, S., W. Lim, and G. Paudyal, 2000: River stage forecasting in Bangladesh: Neural Network Approach." *J. Comput. Civ. Eng.*, **14**, 1–8.

Lorentz, G. G., 1976: The 13th problem of Hilbert. *Proc. Symp. Pure Math*., **28**, 419-430.

Maier, H. R., and G. C. Dandy, 1998: The effect of internal parameters and geometry on the performance of back-propagation neural networks: An empirical study. *Environ. Model. Softw*.,,**13**, 193–209.

Maier, H. R., G. C. Dandy, 2000: Neural networks for the prediction and forecasting of water resources variables: a review of modelling issues and applications. *Environ. Model. Softw*., **15**, 101-124.

Maier, H. R., A. Jain, G. C. Dandy, and K. P. Sudheer, 2010: Methods used for the development of neural networks for the prediction of water resource variables in river systems: Current status and future directions. *Environ. Model. Softw*., **25**, 891-909

Malhi, Y., E. Pegoraro, A. D. Nobre, M. G. P. Pereira, J. Grace, A. D. Culf, and R. Clement, 2002: Energy and water dynamics of a central Amazonian rain forest. *J. Geophys. Res*., **107**, 8061, doi:10.1029/2001JD000623.

Malhi, Y., J. T. Roberts, R. A. Betts, T. J. Killeen, W. Li, and C. A. Nobre, 2008: Climate change, deforestation, and the fate of the Amazon. *Science*, **319**, 169–172.

Malhi, Y., L. E. O. C. Aragao, D. Galbraith, C. Huntingford, R. Fisher, P. Zelazowski, S. Sitch, C. McSweeney, and P. Meir, 2009: Exploring the likelihood and mechanism of a climate change-induced dieback of the Amazon rainforest. *PNAS*, **106**, 20,610–20,615.

Maltarollo, V. G., K. M. Honório, and A. B. F. da Silva, 2013: Applications of Artificial Neural Networks in Chemical Problems. Chapter 10, K. Suzuki (ed), doi: 10.5772 /51275.

Maren, A., C. Harston, R. Pap, 1990: Handbook of Neural Computing Applications. *Academic Press*, San Diego, CA.

Marengo, J. A., J. Tomasella, L. M. Alves, W. R. Soares, and D. A. Rodriguez, 2011: The drought of 2010 in the context of historical droughts in the Amazon region. *Geophys. Res. Lett*., **38**, L12703, doi: 10.1029/2011GL047436.

Marengo, J. A., S. C. Chou, G. Kay, L. M. Alves, J. F. Pesquero, W. R. Soares, D. C. Santos, A. A. Lyra, G. Sueiro, R. Betts, D. J. Chagas, J. L. Gomes, J. F. Bustamante, and P. Tavares, 2012: Development of regional future climate change scenarios in South America using the Eta CPTEC/HadCM3 climate change projections: climatology and regional analyses for the Amazon, Sao Francisco and the Parana River basins, *Clim. Dyn*., **38**, 1829–1848.

Martin, E., B. Timbal, and E. Brun, 1996: Downscaling of general circulation model outputs: Simulation of the snow climatology of the French Alps and sensitivity to climate change. *Clim. Dyn*., **13**, 45–56, doi:10.1007/s003820050152.

Masters, T., 1993: Practical Neural Network Recipes in C + +. *Academic Press*, San Diego, CA.

Maurer, E. P., A. W. Wood, J. C. Adam, D. P. Lettenmaier, and B. Nijssen, 2002: A long-term hydrologically-based data set of land surface fluxes and states for the conterminous United States. *J. Climate*, **15**, 3237–3251.

Maurer, E. P., L. Brekke, T. Pruitt, and P. B. Duffy, 2007: Fine-resolution climate projections enhance regional climate change impact studies. *Eos, Trans. Amer. Geophys. Union*, **88**, 504, doi:10.1029/2007EO470006.

Maurer, E. P., and H. G. Hidalgo, 2008: Utility of daily vs. monthly large-scale climate data: An intercomparison of two statistical downscaling methods. *Hydrol. Earth Syst. Sci*., **12**, 551–563, doi:10.5194/hess-12-551-2008.

Maurer, E. P., H. G. Hidalgo, T. Das, M. D. Dettinger, and D. R. Cayan, 2010: The utility of daily large-scale climate data in the assessment of climate change impacts on daily streamflow in California. *Hydrol. Earth Syst. Sci*., **14**, 1125–1138, doi:10.5194/hess-14-1125-2010.

May, D. B., and M. Sivakumar, 2009: Prediction of urban stormwater quality using artificial neural networks. *Environ. Model. Softw*, **24**, 296-302.

McCulloch, W. S., and W. Pitts, 1943: A logical calculus of the ideas immanent in nervous activity. *Bull. Math. Bio*., **5**, 115-133.

Mearns, L. O., I. Bogardi, F. Giorgi, I. Matyasovszky, and M. Palecki, 1999: Comparison of climate change scenarios generated from regional climate model experiments and statistical downscaling. *J. Geophys. Res*., **104**, 6603–6621, doi:10.1029/1998 JD200042.

Mearns, L. O., W. Gutowski, R. Jones, R. Leung, S. McGinnis, A. Nunes, and Y. Qian, 2009: A regional climate change assessment program for North America. *EOS*, **90**, 311–312, doi:10.1029/2009EO360002.

Meehl, G. A., H. Teng, and G. Branstator, 2006: Future changes of El Niño in two global coupled climate models. *Clim. Dyn*., **26**, 549–566.

Meehl, G. A., T. F. Stocker, W. D. Collins, P. Friedlingstein, A. T. Gaye, J. M. Gregory, A. Kitoh, R. Knutti, J. M. Murphy, A. Noda, S. C. B. Raper, I. G. Watterson, A. J. Weaver, and Z. C. Zhao, 2007: Global climate projections. In: Climate Change 2007: The Physical Science Basis., *Contribution of working group I to the fourth assessment report of the intergovernmental panel on climate change*, Cambridge University Press, Cambridge, United Kingdom, and New York, NY, USA, Solomon, S., D. Qin, M. Manning, Z. Chen, M. Marquis, K. B. Averyt, M. Tignor, and H. L. Miller (eds.).

Miller, N. L., J. Kim, R. K. Hartman, and J. Farrara, 1999: Downscaled climate and streamflow study of the southwestern United States. *J. Amer. Water Resour. Assoc*., **35**, 1525–1537, doi:10.1111/j.1752-1688.1999.tb04235.x.

Milly, P. C. D., J. Betancourt, M. Falkenmark, R. M. Hirsch, Z. W. Kundzewicz, D. P. Lettenmaier, and R. J. Stouffer, 2008: Stationarity is dead: Whither water management? *Science*, **319**, 573–574, doi:10.1126/science.1151915.

Milton, S. F., and C. A. Wilson, 1996: The impact of parameterized sub-grid scale orographic forcing on systematic errors in a global NWP model. *Mon. Wea. Rev*, **124**, 2023–2045.

Minsky, M., and S. Papert, (1969): Perceptrons – An Introduction to Computational Geometry. *The MIT Press*, Cambridge, MA.

Moghim, S., A. J. Bowen, S. Sarachi, and J. Wang, 2015: Retrieval of Hourly Records of Surface Hydrometeorological Variables Using Satellite Remote Sensing Data. *J. Hydrometeor*., **16**, 147–157. doi: http://dx.doi.org/10.1175/JHM-D-13-0127.1

Moghim, S., S. L. McKnight, K. Zhang, A. M. Ebtehaj, R. G. Knox, R. L. Bras, P. R. Moorcroft, and J. Wang, 2015: A Bias-corrected Data set of Climate Model Outputs at Uniform Space-Time Resolution for Land Surface Modelling over Amazonia. *Int. J. Climatol*., (under review).

Murphy, J., 1999: An evaluation of statistical and dynamical techniques for downscaling local climate. *J. Climate*, **12**, 2256–2284, doi:10.1175/1520-0442(1999)012,2256: AEOSAD.2.0.CO;2.

Muttil, N., and K. W. Chau, 2006: Neural network and genetic programming for modelling coastal algal blooms. *Int. J. Environ. Pollut*., **28**, 223-238.

Nakicenovic, N., O. Davidson, G. Davis, A. Grübler, T. Kram, E. L. L. Rovere, B. Metz, T. Morita, W. Pepper, H. Pitcher, A. Sankovski, P. Shukla, R. Swart, R.Watson, and Z. Dadi, 2000: Emissions Scenarios, *A special report of working group III of the Intergovernmental Panel on Climate Change*, IPCC, [Summary for Policymakers].

Nelder, A. J., and R. Mead, 1965: A simplex method for function minimization. *Comput. J*., **7**, 308-313.

New, M., M. Hulme, and P. D. Jones, 1999: Representing twentieth century space-time climate variability. Part 1: Development of a 1961-90 mean monthly terrestrial climatology. *J. Climate*, 12, 829-856.

Niemelä, S., P. Risnen, and H. Savijrvi, 2001a: Comparison of surface radiative flux parameterizations: Part I: Longwave radiation. *Atmos. Res*., **58**, 1–18, doi:10.1016/S0169-8095(01)00084-9.

Niemelä, S., P. Risnen, and H. Savijrvi, 2001b: Comparison of surface radiative flux parameterizations: Part II: Shortwave radiation. *Atmos. Res*., **58**, 141–154, doi:10.1016/S0169-8095(01)00085-0.

Nobre, C. A., G. Fisch, H. R. da Rocha, R. F. F. Lyra, E. P. da Rocha, and B. N. Ubarana, 1996: Observations of the atmospheric boundary layer in Rondonia. *Amazonian Deforestation and Climate,J*., H. C. Gash et al., Eds., John Wiley, 413–424.

Nuzzo, R., 2014: Scientific method: Statistical errors. *Nature*, **506**, 150–152.

Oleson, K. W., G. B. Bonan, C. Schaaf, F. Gao, Y. Jin, and A. H. Strahler, 2003: Assessment of global climate model land surface albedo using MODIS data, *Geophys. Res. Lett*., **30**, 1443.

Olson, J., 1994: Global ecosystem framework-definitions. USGS EROS Data Center Internal Report, Sioux Falls, SD.

Oppenheimer, M., 2013: Climate change impacts: Accounting for the human response. *Climatic Change*, **117**, 439–449, doi:10.1007/s10584-012-0571-9.

Paiva, E. M. C. D., and R. T. Clarke, 1995: Time trends in rainfall records in Amazonia. *Bull. Am. Meteorol. Soc*., **76**, 2203–2209.

Panofsky, H. A., and G. W. Brier, 1968: Some Application of Statistics to Meteorology. pp. 224, University Park, Pa.

Park, S., S.-Y. Hong, and Y.-H. Byun, 2010: Precipitation in boreal summer simulated by a GCM with two convective parameterization schemes: Implications of the intraseasonal oscillation for dynamic seasonal prediction. *J. Climate*, **23**, 2801–2816. doi: http://dx.doi.org/10.1175/2010JCLI3283.1.

Pfizenmayer, A., and H. von Storch, 2001: Anthropogenic climate change shown by local wave conditions in the North Sea. *Climate Res*., **19**, 15–23, doi:10.3354/cr019015.

Piani, C., J. O. Haerter, and E. Coppola, 2010: Statistical bias correction for daily precipitation in regional climate models over Europe. *Theor. Appl. Climatol*., **99**, 187–192, doi:10.1007/s00704-009-0134-9.

Prata, A. J., 1996: A new long-wave formula for estimating downward clear sky radiation at the surface. *Quart. J. Roy. Meteor. Soc*., **122**, 1127–1151, doi:10.1002/qj.49712253306.

Randall, D. A., R. A. Wood, S. Bony, R. Colman, T. Fichefet, J. Fyfe, V. Kattsov, A. Pitman, J. Shukla, J. Srinivasan, R. Stouffer, A. Sumi, and K. Taylor, 2007: Cilmate Models and Their Evaluation. In: Climate Change 2007: The Physical Science Basis, *Contribution of working group I to the fourth assessment report of*

the intergovernmental panel on climate change, Cambridge University Press, Cambridge, United Kingdom, and New York, NY, USA, Solomon, S., D. Qin, M. Manning, Z. Chen, M. Marquis, K. B. Averyt, M. Tignor, and H. L. Miller (eds.).

Reboita, M. S., R. P. da Rocha, C. G. Dias, and R. Y. Ynoue, 2014: Climate projections for South America: RegCM3 driven by HadCM3 and ECHAM5. *Adv. Meteorol*., **2014**, 1–17.

Reed, R., 1993: Pruning algorithms—A review. *IEEE Transactions on Neural Networks*, **4**, 740–747.

Reichler, T., and J. Kim, 2008: How well do coupled models simulate today's climate. *Bull. Amer. Meteor. Soc*., **89**, 303–311, doi:10.1175/BAMS-89-3-303.

Rheenen, N. T. V., A. W. Wood, R. N. Palmer, and D. P. Lettenmaier, 2004: Potential implications of PCM climate change scenarios for Sacramento-Jan Joaquin River Basin hydrology and water resources. *Climatic Change*, **62**, 257–281.

Rojas, R., 1996: Neural Networks: A Systematic Introduction. *Springer-Verlag*, Berlin.

Rocha, M., P. Cortez, and J. Neves, 2005: Simultaneous evolution of neural network topologies and weights for classification and regression. *Lecture notes in computer science*, **2902**, pp. 5966.

Rosenblatt, F., 1959: Principles of Neurodynamics. *Spartan Books*, New York.

Rumelhart, D. E., 1995: Backpropagation: Theory, Architectures, and Applications. Y. Chauvin (ed), pp. 561.

Rumelhart, D. E., G. E. Hintont, and R. J. Williams, 1986: Learning representations by back-propagation errors. *Nature*, **323**.

Saleska, S. R., K. Didan, A. R. Huete, and H. R. da Rocha, 2007: Amazon forests green-up during 2005 drought. *Science*, **318**, 612–612.

Scalero, R. S., and N. Tepedelenlioglu, 1992: A fast new algorithm for training feedforward neural networks. *IEEE Trans. Signal Process*., **40**, 202-210.

Schalkoff, R. J., 1990: Artificial Intelligence: An Engineering Approach. *McGraw-Hill*, New York.

Schalkoff, R. J., 1997: Artificial Neural Network. *McGraw-Hill*, New York, pp. 422.

Schmidli, J., C. Frei, P. L. Vidale, 2006: Downscaling from GCM precipitation: a benchmark for dynamical and statistical downscaling methods. *Int. J. Climatol*., **26**, 679–689. http://dx.doi.org/10.1002/joc.1287.

Semenov, M. A., and E. M. Barrow, 1997: Use of a stochastic weather generator in the development of climate change scenarios. *Climatic Change*, **35**, 397–414, doi:10.1023/A:1005342632279.

Setiono, R., and L. C. K. Hui, 1995: Use of a quasi-Newton method in a feedforward neural-network construction algorithm. *IEEE Transactions on Neural Networks*, **6**, 273–277.

Shabalova, M. V., van Deursen, W. P. A., and Buishand, T. A., 2003: Assessing future discharge of the river Rhine using regional climate model integrations and a hydrological model. *Climate Res*., **23**, 233–246.

Sheffield, J., G. Goteti, and E. F. Wood, 2006: Development of a 50-year high-resolution global dataset of meteorological forcings for land surface modeling. *J. Climate*, **19**, 3088–3111.

Shin, S. I., Z. Liu, B. Otto-Bliesner, E. C. Brady, J. E. Kutzbach, and S. P. Harrison, 2003: A simulation of the last glacial maximum climate using the NCAR-CCSM. *Clim. Dyn*., **20**, 127–151.

Shukla, J., C. Nobre, and P. Sellers, 1990: Amazon deforestation and climate change. *Science*, **247**, 1322-1325.

Simon, P., 2013: Too Big to Ignore: The Business Case for Big Data. *Wiley*, pp. 89.

Skole, D. and C. Tucker, 1993: Tropical deforestation and habitat fragmentation in the Amazon: Satellite data from 1978 to 1988. *Science*, **260**, 1905-1910.

Smith, R. N. B., 1990: A scheme for predicting layer clouds and their water content in a general circulation model. *Q. J. R. Meteor. Soc*., **116**, 435–460.

Solomon, S., D. Qin, M. Manning, Z. Chen, M. Marquis, K. Averyt, M. Tignor, and H. Miller (eds.), 2007: Climate change 2007: The physical science basis, *Contribution of working group I to the Fourth Assessment Report of the Intergovernmental Panel on Climate Change*, IPCC WGI Fourth Assessment Report, [Cambridge University Press, Cambridge, United Kingdom and New York, NY, USA].

Sprecher, D. A., 1965: On the structure of continuous functions of several variables. *Trans. Am. Math. Soc*., **115**, 340-355.

Stamm, J. F., E. F. Wood, and D. P. Lettenmaier, 1994: Sensitivity of a GCM simulation of global climate to the representation of land-surface hydrology. *J. Climate*, **7**, 1218–1239, doi:10.1175/1520-0442(1994)007,1218:SOAGSO.2.0.CO;2.

Stone, M., 1974: Cross-validatory choice and assessment of statistical predictions. *J. Royal Statistical Society*, **B(36)**, 111–147.

Stott, P. A., S. F. B. Tett, G. S. Jones, M. R. Allen, J. F. B. Mitchell, and G. J. Jenkins, 2000: External control of 20th century temperature by natural and anthropogenic forcings. *Science*, **290**, 2133–2137.

Sun, Y., S. Solomon, A. Dai, and R. Portmann, 2005: How often does it rain. *J. Climate*, **19**, 916–934.

Takahashi, Y., 1993: Generalization and approximation capabilities of multi-layer networks. *Neural Comput*., **5**, 132-139.

Tamura, S. i., and M. Tateishi, 1997: Capabilities of a four-layered feedforward neural network: Four layers versus three. *IEEE Transactions on Neural Networks*, **8**, 251–255.

Tanaka, S. K., and Coauthors, 2006: Climate warming and water management adaptation for California. *Climatic Change*, **76**, 361–387, doi:10.1007/s10584-006-9079-5.

Taormina, R., K. Chau, and R. Sethi, 2012: Artificial neural network simulation of hourly groundwater levels in a coastal aquifer system of the Venice lagoon. *Engineering Applications of Artificial Intelligence*, **25**, 1670-1676.

Teutschbein, C. and J. Seibert, 2010: Regional climate models for hydrological impact studies at the catchment scale: A review of recent modeling strategies. *Geogr. Compass*, **4**, 834–860.

Teutschbein, C., and J. Seibert, 2012: Bias correction of regional climate model simulations for hydrological climate-change impact studies: Review and evaluation of different methods. *J. Hydrol.*, **456–457**, 12–29.

Tian, Y., R. E. Dickinson, L. Zhou, R. Myneni, M. Friedl, C. Schaaf, M. Carroll, and F. Gao, 2004: Land boundary conditions from MODIS data and consequences for the albedo of a climate model. *Geophys. Res. Lett*., **31**, L05, 504.

Tsvetsinskaya, E. A., C. B. Schaaf, F. Gao, A. H. Strahler, and R. E. Dickinson, 2006: Spatial and temporal variability in Moderate Resolution Imaging Spectroradiometer–derived surface albedo over global arid regions. *J. Geophys. Res*., **111**, D20106, doi:10.1029/2005JD006772.

van Oldenborgh, G. J., S. Y. Philip, 779 and M. Collins, 2005: El Niño in a changing climate: a multi-model study. *Ocean Science*, **1**, 81–95.

van Rheenen, N. T. V., A. W. Wood, R. N. Palmer, and D. P. Lettenmaier, 2004: Potential implications of PCM climate change scenarios for Sacramento–San Joaquin River basin hydrology and water resources. *Climatic Change*, **62**, 257–281, doi:10.1023/B:CLIM.0000013686.97342.55.

von Storch, H., 1999: On the use of inflation in statistical downscaling. *J. Climate*, **12**, 3505–3506, doi:10.1175/1520-0442(1999)012,3505:OTUOII.2.0.CO;2.

von Storch, H, E. Zorita, and U. Cubasch, 1993: Downscaling of global climate change estimates to regional scales: An application to Iberian rainfall in wintertime. *J. Climate*, **6**, 1161–1171, doi:10.1175/1520-0442(1993)006,1161:DOGCCE.2.0.CO;2.

Wang, G., 2000: The role of ecosystem dynamics in enhancing the low-frequency variability of the Sahel rainfall. *Water Resour. Res*., **36**, 1013-1021.

Wang, J., and R. L. Bras, 1999: Ground heat flux estimated from surface soil temperature. *J. Hydrol*., **216**, 214–226, doi:10.1016/S0022-1694(99)00008-6.

Wang, J., and R. L. Bras, 2009: A model of surface heat fluxes based on the theory of maximum entropy production. *Water Resour. Res*., **45**, W11422, doi:10.1029/ 2009WR 007900.

Wang, J., and R. L. Bras, 2011: A model of evapotranspiration based on the theory of maximum entropy production. *Water Resour. Res*., **47**, W03521, doi:10.1029/ 2010WR009392.

Wang, J., and R. L. Bras, G. Sivandran, and R. G. Knox, 2010: A simple method for the estimation of thermal inertia. *Geophys. Res. Lett*., **37**, L05404, doi:10.1029/ 2009GL041851.

Wang, Z., X. Zeng, M. Barlage, R. E. Dickinson, F. Gao, and C. Schaaf, 2004: Using MODIS BRDF and albedo data to evaluate global model land surface albedo, *J. Hydrometeorol*., **5**, 3–14.

Werth, D., and R. Avissar, 2004: The regional evapotranspiration of the Amazon. *J. Hydrometeor*., **5**, 100–109.

White, H., 1990: Connectionist nonparameteric regression: Multi-layer feed forward networks can learn arbitrary mappings. *Neural Networks*, **3**, 535-549.

Widrow, B., and M. E. Hoff, 1960: Adaptive switching circuits. *1960 IRE WESCON Convention Record*, Part 4, pp. 96-104.

Wilby, R. L., and T. M. L. Wigley, 1997: Downscaling general circulation model output: a review of methods and limitations, *Phys. Geogr*., **21**, 530–548, doi:10.1177/ 030913339702100403.

Wilby, R. L., and T. M. L. Wigley, 2000: Precipitation predictors for downscaling: Observed and general circulation model relationships. *Int. J. Climatol*., **20**, 641–661, doi:10.1002/(SICI)1097-0088(200005)20: 6,641::AID-JOC501.3.0.CO;2-1.

Wilby, R. L, O. J. Tomlinson, and C. W. Dawson, 2003: Multi-site simulation of precipitation by conditional resampling. *Climate Res*., **23**, 183–194, doi:10.3354/cr023183.

Wilby R. L., S. P. Charles, E. Zorita, B. Timbal, P. Whetton and L. O. Mearns, 2004: Guidelines for use of climate scenarios developed from statistical downscaling methods. *Prepared for consideration by the IPCC*. pp. 27.

Wilks, D. S., and R. L. Wilby, 1999: The weather generation game: A review of stochastic weather models. *Prog. Phys. Geogr*., **23**, 329–357, doi:10.1177/03091 3339902300302.

Wood, A.W., L. R. Leung, V. Sridhar, and D. P. Lettenmaier, 2004: Hydrologic implications of dynamical and statistical approaches to downscaling climate model outputs. *Climatic Change*, **62**, 189–216, doi:10.1023/B:CLIM.0000013685 .99609.9e.

Wu, C. L. and K. W. Chau, 2006: A flood forecasting neural network model with genetic algorithm", *Int. J. Environ. Pollut.*, **28**.

Xu, C., 1999: From GCMs to river flow: a review of downscaling methods and hydrologic modeling approaches, *Phys. Geogr*., **23**, 229–249, doi:10.1177/030913 339902300204.

Xue, Y., R. Vasic, Z. Janjic, F. Mesinger, and K. E. Mitchell, 2007: Assessment of dynamic downscaling of the continental U.S. regional climate using the Eta/SSiB regional climate model. *J. Climate*, **20**, 4172–4193, doi:10.1175/JCLI4239.1.

Zhang, F., and A. P. Georgakakos, 2012: Joint variable spatial downscaling. *Climatic Change*, **111**, 945–972, doi:10.1007/s10584-011-0167-9.

Zhang, K., A. D de A. Castanho, D. R. Galbraith, S. Moghim, N. Levine, R. Bras, M. Coe, M. H. Costa, Y. Malhi, M. Longo, R. G. Knox, S. McKnight, J. Wang, and P. R. Moorcroft, 2015: The Fate of Amazonian Ecosystems over the Coming Century Arising from Changes in Climate, Land-use and CO2. *Glob. Chang. Biol.* (recently accepted).

Zillman, J. W., 1972: A study of some aspects of the radiation and heat budgets of the Southern Hemisphere oceans. Meteorological Study 26, *Bureau of Meteorology*, pp. 562.

Zorita, E., and H. von Storch, 1999: The analog method as a simple statistical downscaling technique: Comparison with more complicated methods. *J. Climate*, **12**, 2474–2489, doi:10.1175/1520-0442(1999)012,2474:TAMAAS.2.0.CO;2.